Charles University in Prague

Faculty of Science

Study program: Physical chemistry

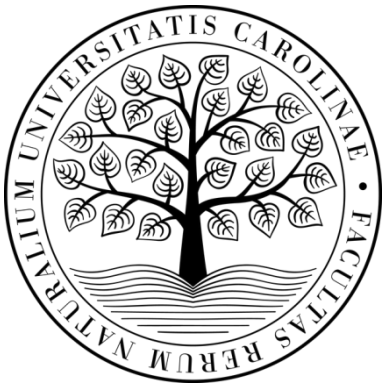

Mgr. Ondřej Veselý

Synthesis of novel zeolite materials and their application in catalysis

Dissertation thesis

Supervisor: Ing. Jan Přech, Ph.D.

Prague 2023

Univerzita Karlova v Praze

Přírodovědecká fakulta

Studijní program: Fyzikální chemie

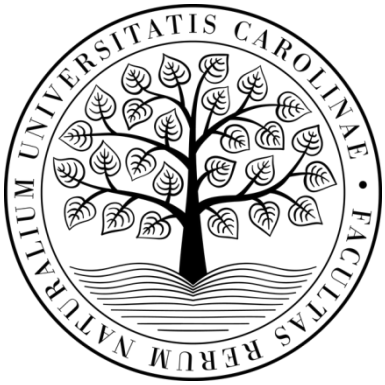

Mgr. Ondřej Veselý

Syntéza nových zeolitických materiálů a jejich aplikace v katalýze

Disertační práce

Školitel: Ing. Jan Přech, Ph.D.

Praha 2023

Prohlašuji, že jsem předloženou disertační práci vypracoval samostatně pod vedením Ing. Jana Přecha, Ph.D., Mgr. Pavly Eliášové, Ph.D. a prof. Ing. Jiřího Čejky, Dr.Sc. a že jsem řádně uvedl všechny použité zdroje. Tato práce ani její část nebyla nepředložena k získání jiného nebo stejného akademického titulu.

Hereby, I declare that I have prepared the submitted dissertation thesis independently under the supervision of Ing. Jan Přech, Ph.D., Mgr. Pavla Eliášová, Ph.D. and prof. Ing. Jiří Čejka, Dr.Sc., and that I have properly cited all the sources used. The work or part of has not been submitted to obtain another or the same academic degree.

Podpis

V Praze dne

Acknowledgement

First and foremost, I would like to thank my supervisor, Ing. Jan Přech, Ph.D., for his advice, guidance as well as trust and support throughout my doctoral study. I would also like to thank prof. Jiří Čejka, DrSc. for his suggestions, consultations and guidance.

In addition, I would like to thank prof. Russel Morris and prof. Wiesław Roth for sharing their insight and experience which were invaluable for my study.

Also, I would like to express my gratitude towards my colleagues, in particular to Pavla Eliášová, Ph.D., Mariya Shamzhy, Ph.D. and Kinga Gołąbek, Ph.D. for their time and fruitful scientific discussions that helped me understand my results in a wider context and inspired me with new scientific ideas.

Furthermore, I am grateful for the cooperation with Martin Kubů, Ph.D. whom I assisted in development of the methodology for water-vapour adsorption, and to Michal Mazur, Ph.D., Daniel Rainer, Ph.D. from the Charles University and David Miller, Ph.D., Aaron Naden, Ph.D. from the University of St. Andrews who trained me in operating the scanning electron microscope.

Last but not least, I would like to thank Zuzana Hrabalová for the assistance with organizing my internship in St. Andrews and Carlos V. Melo for the advice with conceptualisation and writing my articles.

List of abbreviations:

ADOR	- assembly, disassembly, organization, reassembly
AR	- aspect ratio
BET	- Brunauer-Emmett-Teller
D3R	- double three ring
D4R	- double four ring
DEDMS	- diethoxydimethyl silane
DETMDS	- 1,3-diethoxy-1,1,3,3-tetramethyl-disiloxane
DFT	- density functional theory
DMASD	- 2,6-dimethyl-5-azoniaspiro[4.5]decane
EASuD	- 7-ethyl-6-azoniaspiro[5.5]undecane
FCC	- fluid catalytic cracking
GC	- gas chromatography
GM	- growth modifier
H-K	- Horwath-Kawazoe pore size distribution
ICP-MS	- inductively coupled plasma - mass spectrometry
IPC-1P	- two-dimensional layered material prepared by hydrolysis of UTL zeolite
IPC-1TBA	- IPC-1P intercalated with tetrabutylammonium cations
IPC-2	- zeolite with OKO topology
IPC-4	- zeolite with PCR topology
IPC-6	- zeolite with *PCS topology (alternating IPC-2 and IPC-4 layers)
IPC-7	- zeolite alternating UTL and IPC-2 layers
MAS	- magic angle spinning
NMR	- nuclear magnetic resonance
p/p_0	- relative pressure
POSS	- octamethylsilsesquioxane
R	- universal gas constant
SDA	- structure directing agent

SEM - scanning electron microscopy

STEM - scanning transmission electron microscopy

S_{ext} - external surface area

TBAOH - tetrabutylammonium hydroxide

TEM - transmission electron microscopy

TEOS - tetraethylammonium silciate

TMCTS - 2,4,6,8-tetramethylcyclotetrasiloxane

V_{tot} - total pore volume

V_{mic} - micropore volume

χ - adsorption potential distribution

$\varepsilon(B)$ - extinction coefficient for Brønsted acid sites

$\varepsilon(L)$ - extinction coefficient for Lewis acid sites

List of publications:

The dissertation was completed based on the following publications:

J. Zhang, O. Veselý, Z. Tošner, M. Mazur, M. Opanasenko, J. Čejka, M. Shamzhy, *Toward Controlling Disassembly Step within the ADOR Process for the Synthesis of Zeolites*, **Chem. Mater.**, 33 (2021) 4 1228–1237

M. Jin, O. Veselý, C. J. Heard, M. Kubů, P. Nachtigall, J. Čejka, L Grajciar, *The Role of Water Loading and Germanium Content in Germanosilicate Hydrolysis*, **J. Phys. Chem. C**, 125 (2021) 43 23744–23757

O. Veselý, P. Eliášová, R. E. Morris, J. Čejka, *Reverse ADOR: reconstruction of UTL zeolite from layered IPC-1P*, **Mater. Adv.**, 2 (2021) 3862-3870

O. Veselý, M. Mazur, J. Přech, J. Čejka, *Modified reverse ADOR assembles Al-rich UTL zeolite from IPC-1P layers*, **Inorg. Chem. Front.**, 9 (2022) 5444-5453

Publications under revision:

O. Veselý, M. Shamzhy, W. J. Roth, R. E. Morris, J. Čejka, *Controlling crystal morphology of anisotropic zeolites with elemental composition*, 2023

Other publications:

D. Cvejn, I. Martausová, A. Martaus, J. Přech, O. Veselý, J. Čejka, Z. Lacný, J. Nedoma, R. Martínek, *Vermiculites catalyze unusual benzaldehyde and dioxane reactivity*, **Catal. Tod.** 366 (2021) 218-226

R. Bulánek, J. Vaculík, O. Veselý, J. Přech, M. Kubů, M. Rubeš, O. Bludský, *Reactivity of internal vs. external Brønsted acid sites in nanosponge MFI: H/D exchange kinetic study*, **Micropor. Mesopor. Mat.**, 332 (2022) 111717

A. Kurbanova, M. Nigríni, K. Gołąbek, O. Veselý, J. Veselý, *Preparation of functionalised tetrahydropyrans catalysed by isoreticular zeolites*, **Micropor. Mesopor. Mat.** (2023)

O. Veselý, R. E. Morris, J. Čejka, *Beyond traditional synthesis of zeolites: the impact of germanosilicate chemistry in the search for new materials*, **Micropor. Mesopor. Mat.** 358 (2023) 112385

O. Veselý, M. Opanasenko, J. Čejka, *Structural modifications on germanosilicates* (Chapter 5 in *Micro-Mesoporous Metallosilicates: Synthesis, Characterization, and Catalytic Applications*, Ed.: P. Wu), 2023

Abstract

Zeolites are crystalline microporous tectosilicates with acidic properties. The pore sizes of molecular dimensions restrict molecules from entering/exiting the pores based on the molecule size and geometry, or formation of certain (bulky) transition states within the pores. Accordingly, zeolites have become vital industrial catalysts, adsorbents and ion-exchangers. Zeolites are commonly synthesised by hydrothermal crystallization. However, this method provides only limited control over their crystal structure, morphology, or location of active sites within the framework. Some of these limitations can be overcome using an alternative synthetic method; the Assembly-Disassembly-Organisation-Reassembly (ADOR). The ADOR transforms a parent (germanosilicate) zeolite into a layered precursor and subsequently uses the layers as building blocks for a new zeolite framework. We aimed to develop methodology to control the crystal morphology of germanosilicate zeolite **UTL** (Assembly), determine the mechanism of the **UTL** hydrolysis (Disassembly), and to reconstruct the parent **UTL** zeolite from the ICP-1P layered material (Organisation and Reassembly) since the traditional ADOR yields zeolites of smaller channel size but the parent **UTL**.

We found the **UTL** crystal morphology progressively varies the Si/Ge molar ratio of the zeolite. Increase in the Si/Ge ratio from 0.79 to 12.8 resulted in enhanced crystal size along crystallographic *a*-axis (perpendicular to the two-dimensional pore system) from 0.17 μm to 5.39 μm. From comparison with **IWW** zeolite (exhibiting similar behaviour) we deduced that large cavities or building units along respective directions are crucial factor in the crystal which can be tuned by changing the Si/Ge ratio.

The mechanism of the **UTL** hydrolysis was studied using water-vapour adsorption. The experiments provided type V isotherms with wide hysteresis loops bellow relative pressure $p/p_0 = 0.35$ and with significant amount of irreversibly bound water after the adsorption-desorption cycle. We discovered that first, a small amount of water adsorbs reversibly at small relative pressures ($p/p_0 < 0.3$), followed by partially irreversible adsorption at higher relative pressures which induces structural changes to the zeolite framework due to the hydrolysis of labile Ge-O bonds. Germanium-rich **UTL** zeolites (Si/Ge = 2.5 and 4.5) lost their crystallinity upon water adsorption while germanium-poor **UTL** zeolites (Si/Ge = 18.5 and 53) retained the original structure. The germanium-rich **UTL** are susceptible to the hydrolysis and, thus, suitable for the ADOR transformation, while the germanium-poor **UTL** are hydrolysis-resistant. The critical Si/Ge = 8.5 corresponds to eight germanium atoms per unit cell of the **UTL** framework.

The hydrolysis of **UTL** in water is complete within minutes making it difficult to recover intermediate samples. We decelerated the hydrolysis by diluting the water with defined amount of alcohols which enabled controlling the hydrolysis rate by changing the alcohol content in the solution. Solution of HCl in ethanol also enabled slow disassembly of the **UTL** up to 20 days and additionally prevented undesired germanium deposition onto the samples. We observed a gradual decrease of pore size during the hydrolysis as follows: **UTL** (14-12R) – IPC-7 (14-12R & 12-10R) - **OKO** (12-10R) – IPC-6 (12-10R & 10-8R). Thus, the hydrolysis is a consecutive atom by atom leaching process.

Finally, we developed a method for converting the layered IPC-1P to the parent **UTL** zeolite by increasing the interlayer distance via intercalation of tetrabutylammonium hydroxide and subsequent reconstruction of the D4R units. The D4R reconstruction requires combination of silicon and

germanium sources or presence of fluoride anions. Alternatively, the **UTL** can be restored preformed D4R in form of octamethylsilsesquioxane without the presence of germanium or fluorides. This enabled preparation of high-silica **UTL** (Si/Ge = 481) which was hitherto not possible. The **UTL** reconstruction also enables incorporation of catalytically active heteroelements, such as aluminium up to Si/Al = 15 which cannot be achieved by the hydrothermal synthesis. These reconstructed Al-**UTL** samples outperformed directly synthetized one in tetrahydropyranylation of 1-decanol model reaction.

In summary, the thesis provides means to modify the crucial properties of a zeolite, including the crystal morphology, hydrolytic stability, and concentration of active sites.

Abstrakt

Zeolity jsou krystalické mikroporézní tektosilikáty s kyselými vlastnostmi. Velikosti pórů, srovnatelné s rozměry molekul, omezují molekulám vstup/výstup z pórů na základě velikosti a geometrie molekuly nebo tvorbu určitých (objemných) přechodových stavů v pórech. Proto se zeolity staly klíčovými průmyslovými katalyzátory, adsorbenty a iontoměniči. Zeolity se běžně syntetizují hydrotermální krystalizací. Tato metoda však poskytuje pouze omezenou kontrolu nad jejich krystalickou strukturou, morfologií nebo umístěním aktivních míst v krystalové mřížce. Některá z těchto omezení lze překonat pomocí alternativní syntetické metody; Assembly-Disassembly-Organisation-Reassembly (ADOR). ADOR transformuje mateřský zeolit (germanosilikát) na vrstevnatý prekurzor a následně používá tyto vrstvy jako stavební kameny pro novou zeolitovou strukturu. Naším cílem bylo vyvinout metodiku pro kontrolu morfologie krystalů germanosilikátového zeolitu **UTL** (Assembly), určit mechanismus hydrolýzy **UTL** (Disassembly) a rekonstruovat mateřský zeolit **UTL** z vrstveného materiálu ICP-1P (Organisation and Reassembly), jelikož tradiční ADOR poskytuje pouze zeolity menší velikosti kanálu než mateřský **UTL**.

Pozorovali jsme, že morfologie krystalů **UTL** se progresivně mění s molárním poměrem Si/Ge zeolitu. Zvýšení poměru Si/Ge z 0,79 na 12,8 mělo za následek zvýšení velikosti krystalu podél krystalografické osy *a* (kolmé na dvourozměrný systém pórů) z 0,17 µm na 5,39 µm. Ze srovnání se zeolitem **IWW** (vykazujícím podobné chování) jsme vyvodili, že velké dutiny nebo stavební jednotky v příslušných směrech jsou rozhodujícím faktorem pro morfologii krystalu, který lze vyladit změnou poměru Si/Ge.

Mechanismus hydrolýzy **UTL** byl studován pomocí adsorpce vodních par. Experimenty poskytly izotermy typu V se širokými hysterezními smyčkami od relativního tlaku $p/p_0 = 0,35$ a s významným množstvím ireverzibilně vázané vody po adsorpčním a desorpčním cyklu. Zjistili jsme, že nejprve se při malých relativních tlacích ($p/p_0 < 0,3$) reverzibilně adsorbuje malé množství vody, následované částečně nevratnou adsorpcí při vyšších relativních tlacích, která indukuje strukturní změny ve struktuře zeolitu v důsledku hydrolýzy labilních Ge-O vazeb. Zeolity **UTL** bohaté na germanium (Si/Ge = 2,5 a 4,5) ztratily svou krystalinitu při adsorpci vody, zatímco zeolity chudé na germanium (Si/Ge = 18,5 a 53) si zachovaly původní strukturu. **UTL** bohaté na germanium jsou citlivé na hydrolýzu, a tudíž vhodné pro transformaci ADOR, zatímco **UTL** s nízkým obsahem germania jsou odolné vůči hydrolýze. Kritický poměr Si/Ge = 8,5 odpovídá osmi atomům germania na základní buňku krystalické mřížky **UTL**.

Hydrolýza **UTL** ve vodě je obvykle kompletní během několika minut, což komplikuje izolaci intermediátů. Hydrolýzu jsme zpomalili zředěním vody definovaným množstvím alkoholů, což umožnilo regulovat rychlost hydrolýzy změnou obsahu alkoholu v roztoku. Roztok HCl v etanolu také umožnil pomalou hydrolýzu **UTL** až na dobu 20 dnů a dodatečně zabránil nežádoucímu usazování germania ve vzorcích. Během hydrolýzy jsme pozorovali postupný pokles velikosti pórů v následujícím pořadí: **UTL** (14-12R) – IPC 7 (14-12R & 12-10R) – **OKO** (12-10R) – IPC-6 (12-10R & 10-8R). Hydrolýza je tedy postupný proces odstraňování jednotlivých atomů.

Následně jsme vyvinuli metodu pro transformaci vrstvnatého IPC-1P na mateřský zeolit **UTL** zvýšením mezivrstvé vzdálenosti prostřednictvím interkalace hydroxidu tetrabutylamonného a následné rekonstrukce D4R jednotek. Rekonstrukce D4R vyžaduje kombinaci zdrojů křemíku a germania nebo přítomnost fluoridových aniontů. Alternativně lze **UTL** rekonstruovat pomocí předem syntetizovaných

D4R ve formě oktamethylsilsesquioxanu bez přítomnosti germania nebo fluoridů. To umožnilo přípravu **UTL** s vysokým obsahem křemíku (Si/Ge = 481), což dosud nebylo možné. Rekonstrukce **UTL** také umožňuje začlenění katalyticky aktivních prvků, jako je hliník až po Si/Al = 15, čehož nelze hydrotermální syntézou dosáhnout. Tyto rekonstruované Vzorky Al-**UTL** předčily přímo syntetizované vzorky v modelové reakci, tetrahydropyranylaci 1-dekanolu.

Shrnutím práce poskytuje prostředky pro modifikaci klíčových vlastností zeolitu, včetně morfologie krystalů, hydrolytické stability a koncentrace aktivních center.

Table of contents

1. Aims of the study 1
2. Introduction 2
3. Theoretical part 3
   3.1. Zeolites 3
      3.1.1. UTL 6
   3.2. Zeolite synthesis 8
      3.2.1. Hydrothermal crystallization 8
      3.2.2. ADOR method 11
4. Experimental part 15
   4.1. Synthesis of UTL zeolite 15
      4.1.1. Synthesis of organic structure directing agents 15
      4.1.2. Synthesis of UTL zeolites 16
   4.2. Hydrolysis and modification of UTL zeolites 16
      4.2.1. Treatment with Water−Alcohol solutions 16
      4.2.2. Treatment with HCl−Ethanol Solution 17
      4.2.3. Hydrolysis of UTL to IPC-1P 17
      4.2.4. Intercalation of IPC-1P and reconstruction of UTL 17
   4.3. Synthesis of IWW zeolites 18
   4.4. Characterization methods 19
   4.5. Adsorption of water vapour 20
   4.6. Catalytic experiments 21
5. Results and Discussion 22
   5.1. Assembly – modification of UTL germanosilicate morphology 22
   5.2. Disassembly – water-vapour adsorption on UTL germanosilicates 31
      5.2.1. Reversibility of adsorption 32
      5.2.2. Hydrolytic stability and germanium content 34
   5.3. Slow Disassembly of UTL germanosilicate 37
   5.4. Reverse ADOR – reconstruction of UTL framework from IPC-1P 40
      5.4.1. Expansion of interlayer space 41
      5.4.2. Reconstruction of D4R units 43
      5.4.3. Introduction of catalytically active elements 51
6. Conclusions 59

7. References 62
8. Appendix..... 69
9. Publications..... 70

1. Aims of the study

This dissertation thesis investigates new synthetic methods for preparation of zeolitic materials based on the Assembly-Disassembly-Organisation-Reassembly (ADOR) method. The ADOR protocol transforms a parent germanosilicate zeolite (Assembly) into new zeolite structures through disconnection of the 3D framework into 2D layers (Disassembly), deliberate alteration of the respective layer distance and orientation (Organisation) and re-condensation into a new 3D zeolite (Reassembly). The presented research focuses on the fundamental understanding of individual steps of the ADOR mechanism in order to develop new zeolitic materials and novel methods for preparation of zeolite-based catalysts with highly tuneable properties. The thesis aims to:

- Identify factors that influence the **UTL** zeolite crystal morphology using scanning electron microscopy and to develop a method to deliberately control the morphology.
- Investigate the nature of the interaction between the **UTL** germanosilicate and water molecules by water-vapour adsorption and
    - Determine its relationship to hydrolytic stability of the zeolite.
- Develop a method for slow and controllable hydrolysis of the **UTL** germanosilicate and to track the disassembly process and characterize the intermediates.
- Develop a method for reconstruction of the **UTL** zeolite from the layered material IPC-1P, the product of hydrolysis of **UTL**.
    - And use the method for incorporation of active sites into the **UTL** to produce a material with superior catalytic activity.

2. Introduction

Design and development of new advanced materials with distinctive properties impact diverse fields ranging from medicine, energy storage to biomass processing and chemical manufacturing. [1-9] In particular, chemical industry relies heavily on application of neatly designed materials in catalytic processes, separation or purification of chemicals. Careful tuning of the material properties increases the efficiency of the processes, reduces costs and decreases waste production and thus environmental impact. Ergo, the manufacturing becomes more efficient and causes less harm to the environment. [1, 2, 8-16] Significant portion of the chemical production utilize heterogeneous (*vide infra*) catalysts such as zeolites. [1, 4, 17]

The zeolites earned a key position in the chemical industry due to their versatility, safe-handling and relatively low-cost preparation. Zeolites are microporous crystalline metalosilicates which contain micropores of uniform sizes ranging from 4.1 to 12.5 Å, [18, 19] have surface area up to 1000 m^2/g [20] and can contain varying concentration and strength of acid sites. In some cases, the strength of zeolite acid sites is comparable to that of strong mineral acids. [10, 21] They are also chemically benign and thermally stable under temperatures up to 900 °C, depending on their composition, which makes them sufficiently durable to withstand even harsh reaction conditions; for instance, in fluid catalytic cracking process where the zeolite catalyst encounters temperatures up to 700 °C. [22] Zeolites can be both found in nature and prepared synthetically. Synthetic zeolites are most commonly prepared by hydrothermal crystallization due to its simplicity and universality. However, the mechanism of the zeolite hydrothermal crystallization is not entirely understood. Due to the limited understanding of the zeolite nucleation and growth, the discovery of new zeolites is based on empirical rules and trial and error approach rather than prediction and *in silico* design. Consequently, we lack generally applicable strategies for directly controlling key parameters such as crystal morphology, location of active sites within the framework or size of the micropores.

Alternative synthetic methods attempt to overcome the drawbacks of the hydrothermal method. For example, the Assembly-Disassembly-Organisation-Reassembly (ADOR) method transforms a parent zeolite into a layered intermediate, alters the relative spatial position of the layers and then re-condenses them into a new zeolite topology. [23] The new zeolite consists of the same layers; however, their connections and thereby the width of the pores in between them changes during the transformation. Thus, the ADOR can produce a zeolite with predictable structural features and enables direct control over its pore size by the synthesis conditions. [24] Nevertheless, up-to-now the ADOR can hitherto only decrease the pore size and provides limited control over the crystal morphology or location of active sites.

In the thesis, I describe a novel facile method for predicting and controlling the crystal morphology of a wide group of zeolites by altering their composition and demonstrate its principles on germanosilicate zeolite **UTL**. Furthermore, I provide an in-depth investigation of the disassembly of the **UTL** and the impact of experimental conditions on the transformation. Finally, I discuss the development of "Reverse ADOR" transformation which enables the preparation of extra-large pore zeolite **UTL** from a layered precursor with simultaneous incorporation of Brønsted acid sites in amount unattainable by the direct hydrothermal synthesis (i.e.-Si/Al = 15 by Reverse ADOR compared to minimum Si/Al = 35 by hydrothermal synthesis). [25]

3. Theoretical part

3.1. Zeolites

Zeolites are crystalline microporous silicate or metallosilicate (e.g. aluminosilicates, germanosilicate, titanosilicates, ferrosilicates) molecular sieves. The term “zeolite" originates from Swedish mineralogist Axel Cronsted. Cronsted observed that a mineral (probably stilbite) releases steam upon heating, without visible structural damage, which inspired him to name the mineral "zeolite" - a boiling stone (from Greek *zeo* = “to boil” and *lithos* = “stone”). This observation was later explained as a release of reversibly adsorbed water from the micropores of the zeolite. The first breakthrough in zeolite science came in late 1940s when R. M. Barrer succeeded in the preparation of the first synthetic zeolites. Barrer and his colleagues systematically studied the hydrothermal synthesis of zeolites from alkali solutions of silicon and aluminium oxides and established the foundation of modern synthetic methods. [22, 26] In the second half of the twentieth century, zeolite science underwent major advance with the introduction of organic templates (also called structure directing agents, SDAs). The SDAs can stabilize the zeolite framework under a wider range of synthetic conditions including pH or elemental composition. This enabled preparation of zeolites with larger pores as well as higher silicon content, such as the pure-silica **MFI**, silicalite-1. In contrast to natural zeolites, the Si-rich synthetic zeolites are hydrophobic making them more suitable for interaction with non-polar compounds. At the same time zeolites started attracting attention from the industry as prospective materials for gas drying and separation and as catalysts for fluid catalytic cracking (FCC) and petrochemical processes. [27] Further development led to discovery and commercialization of Lewis-acidic titanosilicates in 1980s. [22, 28, 29]

The zeolite framework comprises of tetrahedral TO_4 units (T = Si, Al, Ti, Fe…) linked through sharing their corners. The corners of the tetrahedra contain the oxygen atoms, whereas the T-atom resides in the centre. The tetrahedra assemble into wide range of geometries of larger building units such as rings, prisms or small cages varying in size and geometry which provides the zeolites with unprecedented structural variability. This manifests in the variation of pore diameters, channel connectivity, geometry and size of internal cavities or even stability of different zeolite structures. [30] To this day, the International Zeolite Association recognizes 260 distinct structures each designated by a unique three-letter code (e.g. **LTA**, **FAU**, **UTL**) along with numerous more published zeolite frameworks awaiting the approval. [19] The framework topology can be described using several different categories of building units such as secondary building units (SBUs), composite building units (CBUs) or natural tiles (e.g. cubes, labelled as *t-cub*, hexagonal prism labelled as *t-hpr* or truncated octahedrons as *t-toc*). [19, 31] While some of the building units genuinely form during the zeolite synthesis, others are purely theoretical tools to describe the structure geometry. Nevertheless, aside from studies addressing the zeolite crystal growth and formation, it is more common to classify different zeolites according to pore size and channel connectivity rather than building units. [32] We differentiate zeolites as either;

- small-pore (i.e. 8 ring “8R” channels up to 4 Å; e.g. **LTA**)
- medium-pore (i.e. 10R channels up to 5.5 Å; e.g. **MFI**)
- large-pore (i.e. 12R channels up to 7.5 Å; e.g. ***BEA**)
- extra-large pore (i.e. channels larger than 12R; e.g. **UTL**)

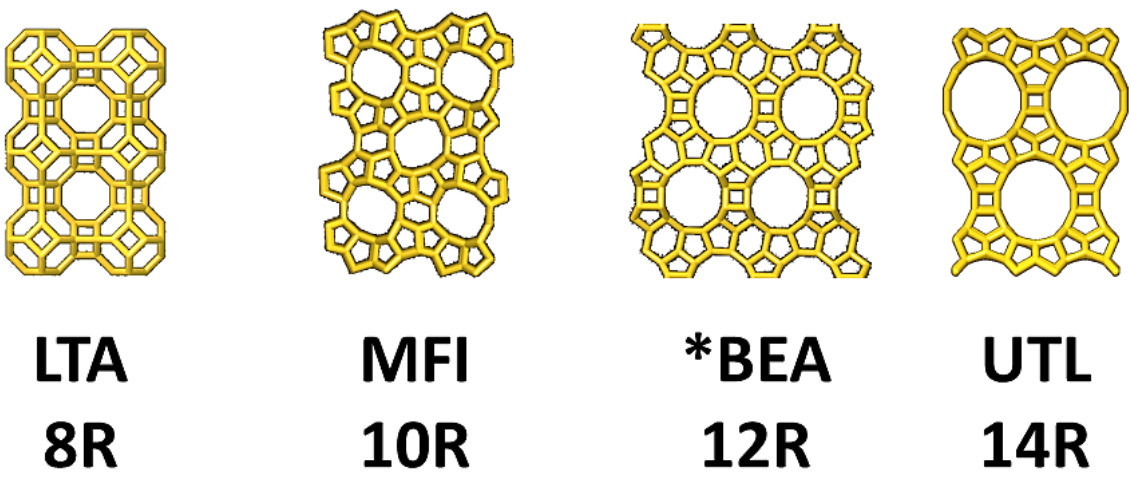

Figure 1: Examples of small-, medium-, large- and extra-large pore zeolites. [19]

If the channels run in parallel to only one crystallographic axis, they form a one-dimensional pore system (e.g. **MTW**). Whereas, if the channels run along multiple axes they may form intersections and create two-dimensional (e.g. **UTL**, **NES**) or three-dimensional channel system (e.g. **LTA**, ***BEA**). The channel size and connectivity determine the textural and molecular sieving properties of the zeolite. This unique set of properties makes zeolites excellent for adsorption, separation of small molecules or so-called shape-selective catalysis.

The molecular sieving embodies one of the pivotal properties of zeolites. Relatively narrow and precisely defined pore-windows of a zeolite can restrict the size and geometry of molecules that enter or exit the channels or reaction intermediates that form within the internal cavities. This effect, the molecular sieving, provides the zeolite with extraordinary separation and catalytic abilities. [33-35] For instance, the zeolite 5A (i.e. Na^+/Ca^{2+} **LTA** with average pore size 5 Å) selectively adsorbs water and, hence, is being used as a solid drying agent. [36-38] Na-FAU (Na^+ exchanged Faujasite; see below) finds use in gas-phase separation of CO_2 from N_2. [39-41] Other small-pore zeolites are currently investigated as an inexpensive alternative for propane/propene separation. [42, 43] More importantly, the shape-selectivity proves indispensable in catalytic reactions including large-scale petrochemical processes (e.g. xylene production) or biomass conversion as well as fine chemical production where it limits the formation of undesired side products. On one hand, small- or medium-pore zeolites are suitable for reaction of small molecules, while on the other hand, large- and extra-large pore zeolites can accommodate even large molecules and are thereby suitable for production of bulky fine chemicals including fragrances, flavourings or pharmaceuticals. [44-46] In essence, zeolites can provide a product distribution different from the thermodynamic equilibrium due to retention of sterically unfavourable compounds or restriction of formation of bulky transition states. As a result, the reaction provides higher yields of certain products, decreases the amount of waste products and decreases the overall cost of the process. [22, 44, 47-54]

The recognition of zeolites in the catalysis also originates from their acidic properties. The zeolite acid sites are formed by isomorphous substitution of silicon with other tetrahedrally coordinated trivalent (i.e. M^{3+}) or tetravalent (i.e. M^{4+}) or elements. [46] Trivalent elements such as Al^{3+}, Ga^{3+} or Fe^{3+} introduce a negative charge to the framework which requires compensation by extra-framework cations. Introduction of protons as the charge-balancing cations creates Brønsted acid sites (Figure 2).

The Brønsted acid sites of the aluminosilicate zeolites generally possess acid strength comparable to mineral acids. The strong acidity along with the shape-selectivity makes zeolites suitable for catalysing various reactions such as hydrocarbon cracking or Friedel-Crafts alkylation or acylation. [47, 55-58] Alternatively, Lewis acid sites also form in the proximity of defects associated with trivalent element (e.g. Al^{3+}). Tetravalent elements such as Ti^{4+}, Zr^{4+}, Ge^{4+} or Sn^{4+} possess free orbitals which provide Lewis acidity (Figure 2). For instance, the Lewis-acidic titanosilicates excel in oxidation and epoxidation reactions while the stannosilicates find use in Baeyer–Villiger oxidation of ketones or transformation of biomass. [59-63]

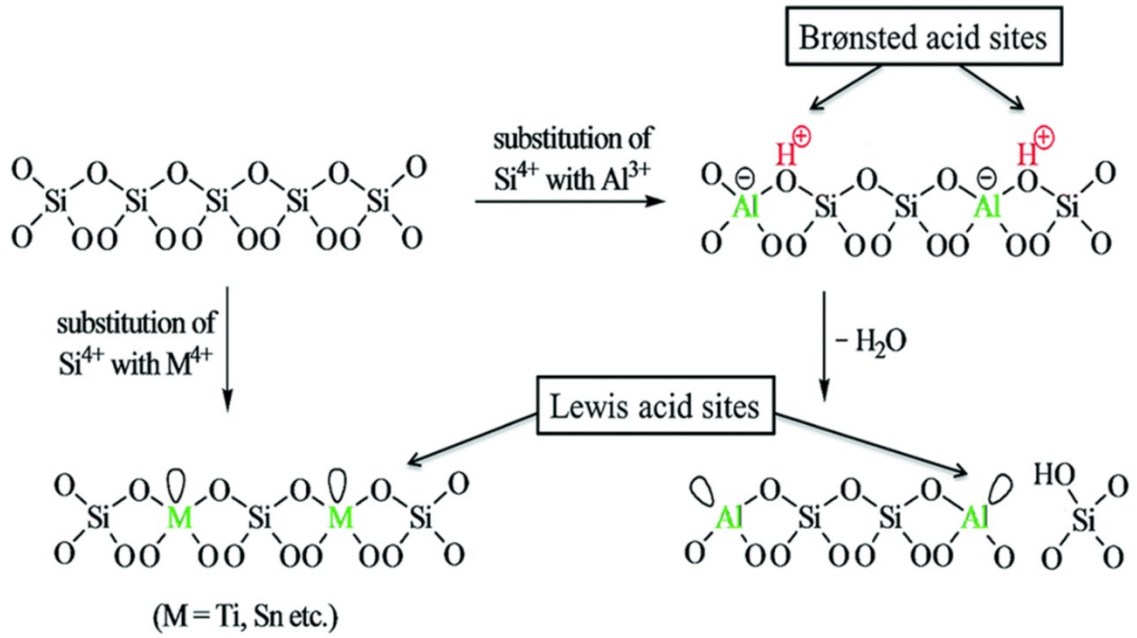

Figure 2: Representation of different types of acid sites in zeolites [64]

Germanosilicate zeolites

Among the substituting heteroelements, germanium stands out due to its unique structure-directing properties and chemical lability. The first property originates from the flexibility of Ge-O-Ge bond angles. The Ge-O-Si or Ge-O-Ge linkages can accommodate bond angles ranging from 120 to 180° in contrast to Si-O-Si with more narrow range from 137 to 180°. [65, 66] The increased flexibility permits the germanium to adopt more strained geometries and stabilise new building units which rarely appear in purely siliceous zeolites. Particularly, the germanium promotes formation of double-four ring (D4R) and double-three ring (D3R) units. [18, 67] The small units such as D4R and D3R are invaluable in preparation and stabilisation of zeolites with low framework density, including numerous extra-large pore zeolites such as **UTL**, ***CTH** or **IRR** (Figure 3). [18, 68, 69] The ability of germanium to stabilise the strained units also relates to its uneven distribution throughout the framework. The germanium preferentially locates in more strained framework positions; whereas, the less strained ones predominantly accommodate silicon atoms. For illustration, **IRR** germanosilicate contains 50% of the framework germanium located in the highly strained D3R and 37% in the D4R positions. In contrast, the rest of its framework contains only 13% of the germanium. [18, 70, 71]

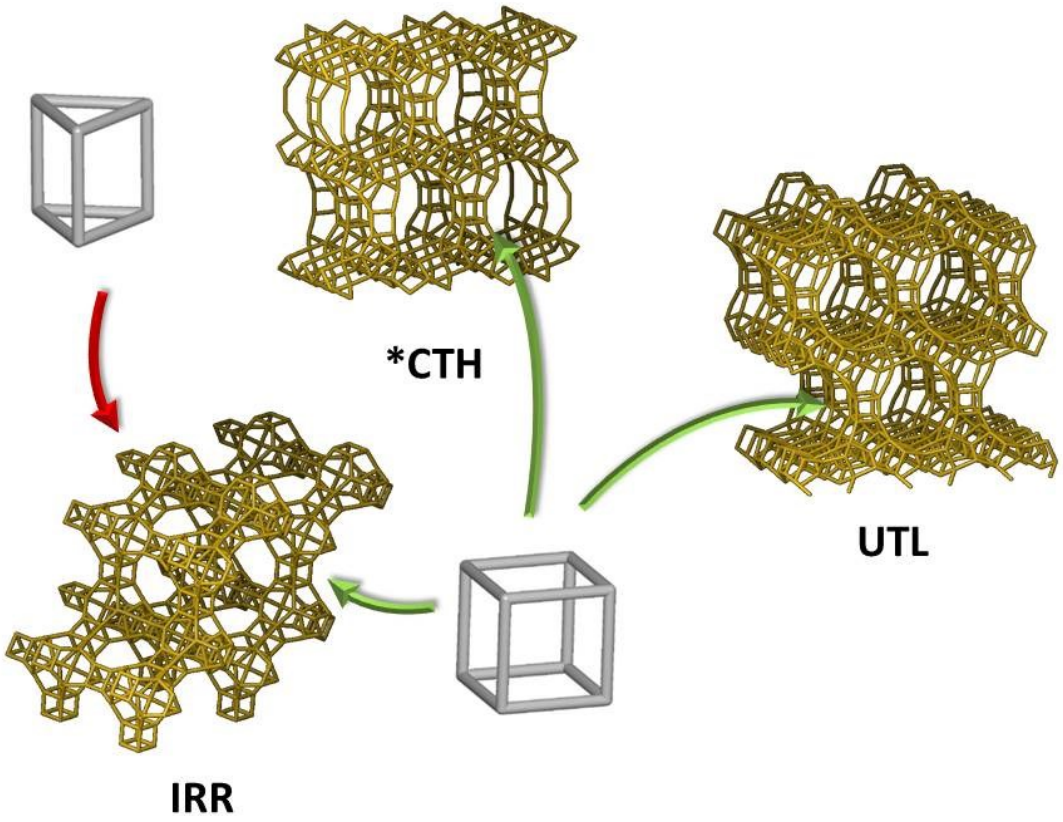

Figure 3: Location of D3R and D4R units in zeolites **UTL**, ***CTH** and **IRR**. [19]

The second key property of germanium stems from relative lability of Ge-O bonds. The Ge-O bonds are weaker than Si-O which makes them more prone to hydrolysis. Ergo, germanosilicate zeolites, without the support of the template, tend to gradually deteriorate in moist environments. [72-74] On the other hand, we can use aqueous solutions to selectively remove the germanium from the framework. The hydrolysis selectively removes the germanium which predominantly resides in the D4R or D3R units while leaving the rest of the framework intact. Roth et al. exploited this in selective hydrolysis of D4R units in the **UTL** germanosilicate transforming it into a layered IPC-1P material (see section 2.2.2.). [74]

3.1.1. UTL

The **UTL** (originally denoted as IM-12 or ITQ-15) is an extra-large pore germanosilicate zeolite with a system of intersecting 14R (9.5 x 7.1 Å) and 12R (8.5 x 5.5 Å) pores. [68, 75] The intersecting pores create a two-dimensional pore system interposed in between parallel non-porous *pcr* layers. The layers mostly consist of 5-rings and contain predominantly silica. On the other hand, the D4R units which connect the layers to the 3D framework contain predominantly germanium. Ergo, we can also imagine the **UTL** as a series of parallel Si-rich layers connected by Ge-rich D4R units (Figure 4). [76]

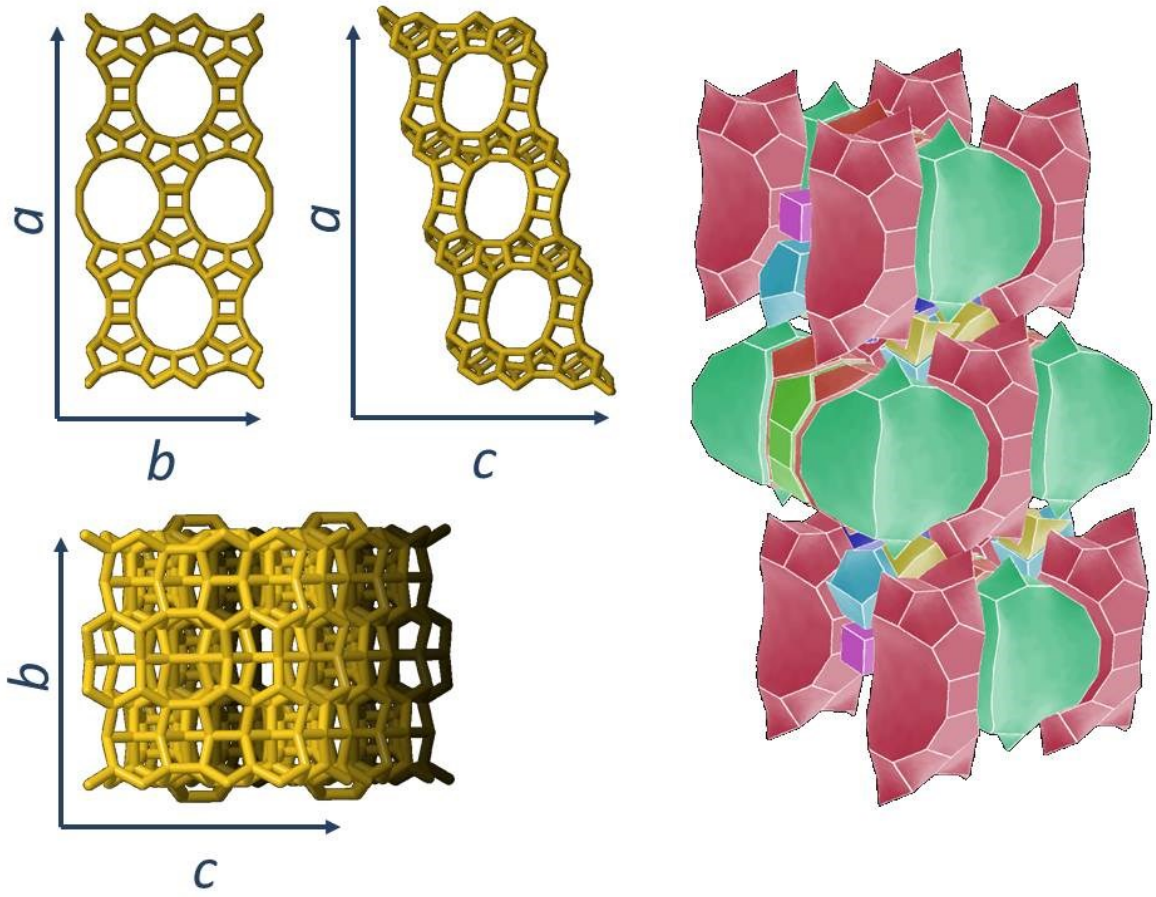

Figure 4: Structure of the **UTL** zeolite along *ab*-, *ac*-, and *bc*-planes and illustration of building units [19]

The 14R and 12R pores make the **UTL** attractive catalyst for transformation of bulky organic molecules such as fragrances, dyes or drugs. The catalytic activity of the **UTL** originates either from the germanium atoms or from other heteroelements (*vide supra*) which can be incorporated into the framework either during the hydrothermal synthesis or via post-synthetic modifications. The germanosilicate **UTL** can catalyse Baeyer-Villiger oxidation of ketones or ketalization of glycerol due to the Lewis acidic nature of the germanium sites. [77, 78] However, the germanium sites deteriorate upon contact with water released by the reaction. Therefore, numerous efforts have been employed to stabilise the **UTL** zeolite by post-synthetic substitution of germanium for silicon. The stabilisation commonly involves degermanation of the **UTL** under acidic conditions and subsequent or simultaneous incorporation of silicon into the newly formed vacancies. [79, 80]

Other heteroelements can also be incorporated into the **UTL** framework directly during the hydrothermal synthesis. Shamzhy et al. investigated the direct synthesis routes to **UTL** zeolite containing framework Al^{3+}, Fe^{3+} or Ga^{3+}. Their results show that the **UTL** can accommodate a range of trivalent elements which introduce Brønsted acid sites into the framework (*vide supra*). However, the content of the heteroelements in the framework is limited and the presence of certain elements narrows the pH range of the synthesis time and prolongs the required synthesis time. For example, germanosilicate **UTL** crystalizes in range of pH from 7.3 to 12.1 within 8 days; whereas aluminogermanosilicate **UTL** (Al-UTL) with molar ratio Si/Al = 65 crystalizes within pH range from 11.4 to 12 and takes 20 days to fully crystalize. [81]

Additionally, post-synthetic incorporation of other elements such as Al^{3+}, Ga^{3+} or Fe^{3+} into the vacancies not only stabilizes the zeolite but also introduces Brønsted acid sites. This increases the scope of reactions we can catalyse over the **UTL** zeolite to, for instance, alkylation of toluene, acylation of p-xylene and Beckmann rearrangement of 1-indanone oxime. [82, 83]

3.2. Zeolite synthesis

Synthetizing zeolites artificially provides numerous advantages including higher phase purity and variability of feasible crystal topologies compared to the zeolites obtained from nature. One can tailor the synthetic zeolite to contain required amounts of specific elements. Suitable synthesis conditions can also promote formation of desired framework topologies and impede formation of undesired side phases. [84] A number of diverse zeolite synthesis methods have been developed, including hydrothermal crystallization, dry-gel conversion, mechanochemical synthesis, high pressure transformation or the Assembly-Disassembly-Organisation-Reassembly (ADOR) method. In this chapter we will focus only on two of them which are relevant to the thesis: the hydrothermal crystallization and the ADOR method. [85-91]

3.2.1. Hydrothermal crystallization

The hydrothermal crystallization is the most straightforward preparation of synthetic zeolites. In essence, the hydrothermal synthesis involves dissolution or mixing of T-element source compounds (i.e. silicates, aluminates...) in a solution of alkali or organic hydroxide and crystallization in a closed vessel at elevated temperature (from 90 to 200 °C). The synthesis mixture also commonly contains organic structure directing agent (SDA). The SDA stabilizes the desired framework topology by filling the pores and cavities, by stabilizing certain building units through Coulombic interactions or, in rare cases, by promoting formation of specific structural features via templating. [87, 91, 92] The simplicity of the hydrothermal method makes it so widespread as well as relatively easy to scale up. On the other hand, the complexity of the synthesis mixture makes it difficult to describe the underlying processes and nearly impossible to tailor or design. Beneath the simple experimental protocol lies an intricate interplay of dissolution, precipitation, agglomeration, nucleation, polymerization as well as ionic interaction or solvation. However, regardless of the complexity of the zeolite crystallization mechanism, several key steps have been identified and extensively studied. [22, 26, 93]

Composition

The zeolite formation begins with mixing the source compounds to form a synthesis gel or a solution. The choice and combination of the source chemicals can already predetermine the properties of the final zeolite. For instance, numerous zeolite structures crystalize exclusively in the presence of specific alkali cations which behave as inorganic structure directing agents. The alkali cations can stabilize different building units by ionic interactions and promote formation of specific framework type rich in those units. For example, Na^+ favours coordination to aluminosilicate six-rings while K^+ prefers eight-rings. This results in crystallization of zeolites with high occurrence of six-rings such as **LTA** or **FAU** in presence of Na^+ while zeolites such as **TON** or **KFI** crystallize predominantly in K^+ media. [92, 94] Similarly, certain T-elements can affect the nature of the building units that form in the early stages of the synthesis. Most notably, the germanium promotes the formation of strained four-rings and double four-rings (D4R) present in germanosilicate extra-large pore zeolites. In contrast, zinc favours the formation of spiro [3,3] rings while gallium often acts as a linker between two existing silicate

species. Consequently, the presence of specific T-atom can promote the formation of certain building units and direct the synthesis towards frameworks with respective features. [95, 96]

The outcome of the synthesis also depends significantly on the molar Si/T ratio. Lower abundance of charged moieties such as Al^{3+} provides fewer sites for interaction with the extra-framework cations (i.a., that of the SDA) that stabilize the zeolite. Furthermore, it has been empirically shown that zeolite structures cannot contain Al-O-Al linkages (Loewenstein's rule) and ergo the Si/Al ratio of the zeolite cannot decrease bellow 1. Moreover, high aluminium content in the synthesis gel favours formation of even-rings with alternating Si-O-Al linkages while odd-rings become less favourable under the same conditions. As a result, zeolites with abundance of even-rings form more easily in high aluminium environment while odd-ring zeolites favour lower aluminium content. [92, 94, 97] Other heteroelements do not obey the same rules as aluminium; however, majority show certain upper limit for incorporation into the zeolite framework. For instance, Millini et al. showed that the TS-1 (i.e. Ti-MFI) can accommodate titanium only up to Si/Ti = 39 and any excessive titanium forms extra framework species. [98]

Supersaturation

The synthesis conditions and the composition of the synthesis gel do not only determine the phase selectivity but also the crystal size and morphology of the zeolite. The size of the crystals inversely correlates with the rate of nucleation and thereby with the degree of saturation of the synthesis mixture with the source compounds (i.e. Si, Al…). Highly saturated mixtures generate large number of nuclei during the synthesis. The crystal growth from these nuclei gradually depletes the synthesis gel of the source compounds until the crystal growth ceases. The large number of nuclei in highly saturated gels results in shorter crystal growth and formation of a large number of small crystals in the final material. In contrast, more diluted gels produce fewer nuclei which can consume grow to larger crystals. [99, 100] The degree of saturation depends on the overall gel concentration; however, also on the nature of the source compounds. Highly soluble compounds, such as TEOS (tetraethyl orthosilicate), saturate the synthesis gel more rapidly resulting in a faster nucleation. In contrast, compounds which dissolve more slowly, such as silica gel, cause a slower nucleation. Consequently, using different source chemicals in the same synthesis can result in zeolite crystals with diverse morphologies or Al distribution. [101-103]

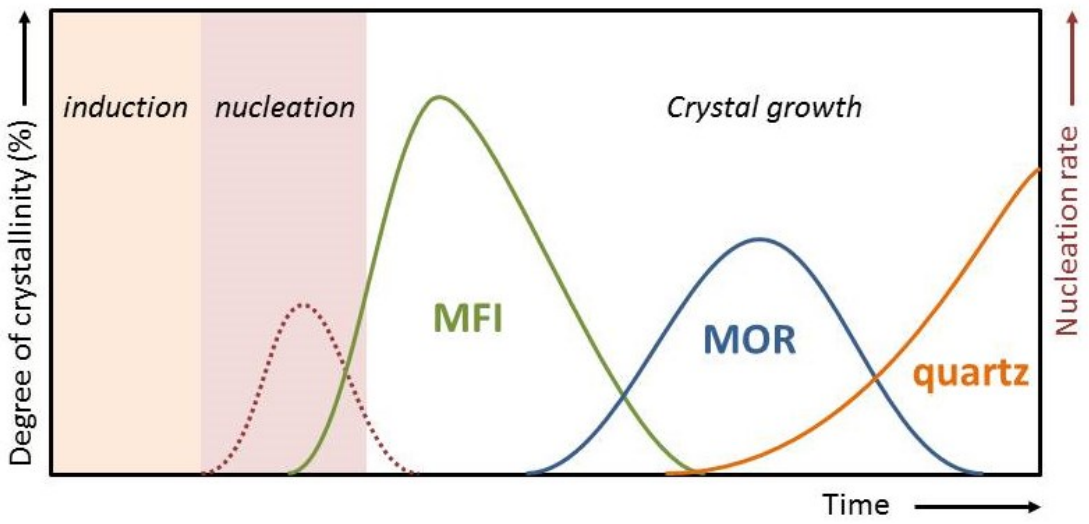

Figure 5: Stages of hydrothermal crystallization of zeolites from an alkaline mixture. [104]

Time and temperature

Zeolites are thermodynamically metastable phases. This means that any zeolite is essentially an intermediate phase which forms through a kinetically favoured pathway under the hydrothermal conditions and over time recrystallizes to energetically more favourable structure (Figure 5). Eventually, the recrystallization continues until the most stable (dense) phase, such as cristobalite or quartz, forms. Consequently, a particular zeolite structure can only be obtained in a distinct time window during the synthesis before it recrystallizes to a more stable material. [99, 105]

Another key factor for producing the desired crystal structure of the solid phase is the synthesis temperature. The temperature governs the rate of the synthesis and all its underlying processes. In general, increasing the temperature shortens the synthesis time. However, the change of temperature may also affect the complex interactions within the system and kinetics of the secondary processes (i.e. dissolution, condensation, mass transfer…) meaning that changing temperature may not only alter the synthesis time but also enable the crystallization of completely new phase. [90, 94] Altogether, these factors make the hydrothermal synthesis highly variable and tuneable. However, up to now the complexity of the system effectively prevented rational design of synthesis conditions with particular structure in mind.

Synthesis of UTL zeolite

I will illustrate the above-mentioned principles of hydrothermal synthesis on the zeolite **UTL**. The **UTL** crystallizes most commonly as germanosilicate or metalo-germanosilicate with a third T-element such as aluminium, gallium or tin. [81] High concentration of germanium in the synthesis gel is crucial because it promotes the formation of D4R units. Synthesis mixtures with Si/Ge from 1 to 5 yield pure **UTL** phase. However, synthesis mixture with Si/Ge higher than 10 provides mainly **STF** structure. Shvets et al. also observed that a decrease in the germanium content is accompanied by an increase in average crystal size. [106]

The **UTL** germanosilicate with Si/Ge = 2 generally requires from 4 to 7 days (depending on pH) to reach full crystallinity. Prolongation of the synthesis time results in recrystallization of the **UTL** to denser

***BEA**, **MTW** or **MEL** zeolites after 10 days and to quartz after 14 days. The crystallization time depends on the pH of the synthesis gel. Successful synthesis of **UTL** occurs within pH range from 7.2 to 11.5. Decrease in the synthesis pH generally prolongs the time required to achieve full crystallization. [106, 107]

Addition of the third element can significantly impact the synthesis time and range of conditions where the pure **UTL** phase forms. Most notably, aluminium in the synthesis mixture considerably slows down the **UTL** growth. Addition of the heteroelement presumably changes the equilibrium between different silicate, germanosilicate and metallosilicate species and impedes the aggregation of primary particles due to electrostatic repulsion. As a result, synthesis time of **UTL** with Si/Al = 66 increases to 20 days and with Si/Al = 44 further to 28 days. The presence of heteroelements also narrows down the synthesis pH range from 7.2 - 11.5 for germanosilicate UTL to 7.8 - 11.0 for B-UTL or 8.2 – 11.0 for Ga-UTL. [81, 108] Lastly, the successful incorporation of the element depends on the choice of the SDA used in the synthesis. The **UTL** can be synthesised using a broad range of spiro-azacompounds without clear impact on the formation of the zeolite. However, the SDA controls the upper limit for the heteroelement content in the framework. For example, the 7-ethyl-6-azoniaspiro[5.5]undecane (EASuD) enables incorporation of higher amounts of trivalent element into the UTL, in contrast to the 2,6-dimethyl-5-anizospiro[4.5]decane (DMASD), which is more suitable for preparation of pure germanosilicate UTL. For example, synthesis with EASuD can yield **UTL** with boron content up to 12 % molar content, while identical synthesis with DMASD can only yield **UTL** with 3 % boron content. [108]

3.2.2. ADOR method

The commonly used hydrothermal synthesis of zeolites is, on one hand, relatively facile and versatile in the choice of source materials and synthesis conditions. On the other hand, we do not fully understand its mechanism and thus lack a straightforward relationship between the synthesis conditions and the structure of the produced zeolite. This limits us to rely on verified recipes or tedious screening of synthesis conditions in search of new structures. As a result, development of new zeolites with specific structural features (e.g. chirality, extra-large pores, odd-ring channels) is rather challenging via the hydrothermal synthesis. [87]

The Assembly-Disassembly-Organisation-Reassembly (ADOR) method approaches this hurdle from a different perspective. Instead of using bottom-up crystallization from solution, the ADOR applies top-down approach to obtain building blocks from existing germanosilicate zeolites and uses them to form new frameworks. The new zeolite always contains the same building blocks, most commonly layers, originating from the parent material but connected via different linkages. The transformation replaces the original double-four ring (D4R) units with, e.g., single-four rings (S4R) or oxygen bridges (*vide supra*) and can yield a family of isoreticular zeolites from one parent material. The isoreticular zeolites possess the same structural features and pore connectivity but vary in the diameter of the pores. This makes them suitable for studying relationship between pore size and catalytic activity or separation properties. [83, 109-111]

The ADOR consists of four steps (Scheme 1); 1) Assembly - hydrothermal synthesis of the parent germanosilicate; 2) Disassembly - selective hydrolysis of the germanosilicate to produce a layered intermediate; 3) Organisation – adjustment of the spatial arrangement of the layers; 4) Reassembly - topotactic condensation of the layers into a new three-dimensional zeolite framework. [23, 24]

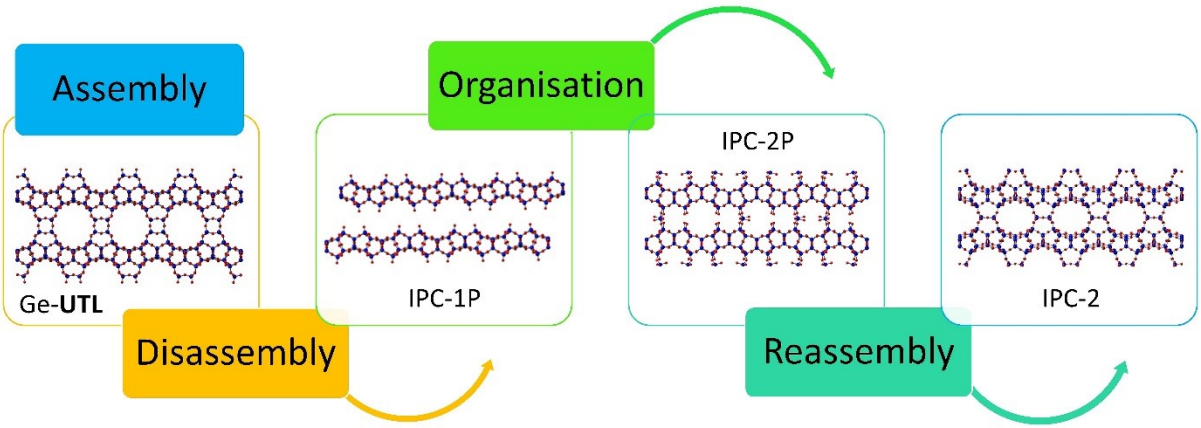

Scheme 1: Assembly-Disassembly-Organisation-Reassembly transformation of the **UTL** germanosilicate to layered precursors IPC-1P and IPC-2P, and to IPC-2 (**OKO**) zeolite. [112]

Assembly

The Assembly, first step of ADOR, refers to the hydrothermal crystallization of a suitable parent germanosilicate zeolite which possess germanium rich double-four rings (D4R) arranged in a planar manner. For instance, the **UTL** consists of silicon-rich *pcr* layers connected by the D4Rs which makes it a suitable parent material for the ADOR. [68] In contrast, zeolites such as **ASV** or **BEC** contain D4Rs connected by only small building units. Hence their hydrolysis causes amorphization of the material which makes them unsuitable for ADOR. [67, 113]

The distribution of the germanium within the framework, namely the occupation in the D4R positions, is crucial for the later steps of the ADOR. Particularly, the occupancy of the D4R with germanium increases with decreasing Si/Ge ratio. Furthermore, synthesis of the zeolite in OH^- medium encourages the clustering of germanium in the D4Rs. In contrast, presence of F^- in the synthesis gel favours more even distribution of the germanium, making the zeolite more resistant to the hydrolysis and less suitable for the ADOR transformation. [69, 72]

Disassembly

In the second step of the ADOR, the disassembly, the parent germanosilicate undergoes a transformation into a layered precursor. The disassembly step takes advantage of the relative lability of the Ge-O bonds compared to the Si-O bonds. The Ge-O bonds undergo hydrolysis in presence of water or in acidic environment resulting in leeching of the germanium from the framework and formation of vacancies. Since the germanium predominantly resides in the D4R units, the acidic hydrolysis enables to selectively remove the D4Rs while keeping the Si-rich part of the framework intact. In case of the **UTL**, the hydrolysis removes the D4Rs that connect the Si-rich *pcr* layers, resulting in the formation of the layered precursor. In order to disconnect the layers completely, it is imperative that at least 4 germanium atoms in suitable arrangement occupy each D4R unit. This corresponds to **UTL** with Si/Ge ratio 8.5. [74]

The degermanation of the **UTL** produces Ge and Si debris originating from the hydrolysed D4Rs. The debris can either de-intercallate from the interlayer space or re-insert into the framework to heal vacancies. Large amount of liquid in the system promotes the rate of de-intercallation and, therefore,

favours the hydrolysis and formation of the layered IPC-1P. In contrast, low-liquid system promotes re-insertion of the leeched species into the framework and slow formation of linked IPC-2P precursor (Scheme 1). [114, 115] The structure of the daughter zeolite also depends on the acidity of the solution during the treatment. The acidic environment promotes breaking and making of Si-O bonds and facilitates Si leeching and reinsertion. As a result, moderately acidic solutions (e.g. 7M HCl) favour Si reinsertion and formation of IPC-2P. In contrast, mildly acidic solutions (e.g. 1M HCl) or pure water favour the hydrolysis and formation of IPC-1P. [111]

In order to fully disassemble the **UTL** into the layered precursor, the D4Rs cannot contain any Si-O-Si linkages between the neighbouring layers. Each D4R need to contain at least four geranium atoms in suitable arrangement to ensure the D4Rs hydrolyse completely. [76] The removal of the D4Rs disconnects the layers and leaves unique silanol quadruplets on the layer surface in place of the missing D4Rs. These quadruplets facilitate the later re-condensation of the layers into the new structure or provide a foundation for functionalisation of the material. [24]

Organisation

Rapid hydrolysis of **UTL** in diluted acidic solution (e.g. 0.1 M HCl) produces a semi-ordered layered precursor which yields a disordered IPC-1 material upon direct condensation. [74] Therefore, the relative layer position needs to be adjusted into a proper arrangement prior to the condensation. The layers can either spontaneously re-arrange under favourable conditions or by intercalation of organic agents into the interlayer space. [114, 116] For instance, the intercalation of octylamine improves the ordering of the IPC-1P layers and the subsequent transformation produces ordered IPC-4 (**PCR**) zeolite instead of the disordered IPC-1. [23, 116]

The intercalation of organic agents not only improves the quality of the final material, but it also enables controlling the respective layer distance and position. Intercalation of large, substituted amines or surfactants can increase the interlayer spacing beyond that of the **UTL**. The intercalated precursor can be pillared by amorphous silica or organic linkers to fix the interlayer distance and produce hybrid semi-crystalline pillared materials with pore size up to 3.5 nm. [116, 117] Other intercalating agents can induce a mismatch in the relative layer position and provide a zeolite with new interlayer connectivity upon condensation. For example, intercalation of choline into the IPC-1P induces a shift of the layers by half of unit cell along the crystallographic *c*-axis. The subsequent condensation produces IPC-9 or IPC-10 zeolites with odd 7- and 9-ring channels. [118]

Reassembly

The last step involves the topotactic condensation of the layered precursor to the three-dimensional zeolite framework. The condensation significantly differentiates the ADOR from the hydrothermal synthesis. While the hydrothermal crystallization includes series of reversible processes (e.g. crystallization, dissolution) the condensation transforms the precursor in one irreversible step. [118] This opens the doors to formation of high-energy zeolite structures which do not obey the Local Interatomic distances (LID) criteria applied to zeolites prepared by the hydrothermal route. The set of LID rules is based on observations of existing zeolites and relate geometrical features of the framework (e.g. average T-T and T-O distances or T-O-T angles) with hydrothermal feasibility of the particular zeolite. [119] In short, the ADOR enables preparation of zeolites considered “unfeasible” by the

hydrothermal approach. This includes the IPC-9 and IPC-10 zeolites which contain odd 7- and 9-rings seldom found in zeolite structures. [118, 120]

In summary, the ADOR enables preparation of new zeolites, some of which are unfeasible by the hydrothermal route, in a predictable and controllable way.

4. Experimental part

Table1: List of used chemicals

Compound	Purity	Manufacturer
1,3-Diethoxy-1,1,3,3-tetramethyl-disiloxane	97%	Sigma Aldrich
1,4-Dibromobutane	≥98%	Alfa Aesar
1,5-Dibromopentane	≥98%	VWR Chemicals
1-Decanol	≥99%	Merck
2,4,6,8-Tetramethylcyclotetrasiloxane	≥99,5%	Sigma Aldrich
2-Ethylpiperidine	>98%	TCI Chemicals
2-Propanol, Isoropylalcohol	99,9%	VWR Chemicals
3,4-Dihydro-2H-Pyran	99%	Sigma Aldrich
Acetic acid, natural	≥99,5%	Sigma Aldrich
Acetonitrile, anhydrous	≥99.95%	VWR Chemicals
Aluminium hydroxide, extra pure, powder	100%	Acros Organic
Aluminium nitrate nonahydrate	≥98%	Sigma Aldrich
Ambersep 900(OH), ion exchange resin		Alfa Aesar
Ammonium fluoride, ACS reagent	≥98%	Sigma Aldrich
Ammonium nitrate	≥99%	Sigma Aldrich
cis-2,6-Dimethylpiperidine	98%	Sigma Aldrich
Diethoxydimethyl silane	≥97%	Sigma Aldrich
Diethyl ether	≥99%	VWR Chemicals
Ethanol absolute anhydrous	≥99.8%	VWR Chemicals
Germanium(IV) methoxide	≥95%	Sigma Aldrich
Germanium(IV) oxide	≥99,99%	Sigma Aldrich
Hydrogen chloride - ethanol solution, 1.25 M HCl		Sigma Aldrich
Ludox® AS-40 colloidal silica 40 wt.% suspension in H_2O	40%	Sigma Aldrich
Mesitylene	98%	Sigma Aldrich
Methanol for HPLC	≥99,9%	Sigma Aldrich
Potassium carbonate, anhydrous	≥99%	VWR Chemicals
PSS-Octamethyl substituted (Octamethylsilsesquioxane)		Sigma Aldrich
Pyridine	99,9%	Sigma Aldrich
Silica, fumed, powder	99.80%	Sigma Aldrich
Tetrabutylammonium hydroxide, aqueous solution	40%	Sigma Aldrich

4.1. Synthesis of **UTL** zeolite

4.1.1. Synthesis of organic structure directing agents

The germanosilicate **UTL** was synthetised by the hydrothermal method using the 2,6-dimethyl-5-anizospiro[4.5]decane (DMASD) bromide the SDA. [107] The synthesis of DMASD-Br involved mixing 60 mL of 1,4-dibromobutane, 82.9 g of K_2CO_3 and 500 mL of acetonitrile in a round-bottom flask. Subsequently, 67 mL of 2,6-dimethylpiperidine was added dropwise through addition funnel. The resulting mixture was heated to 85 °C and stirred for 16 h under reflux. Afterwards, the reaction mixture was cooled down and the acetonitrile was evaporated. The solid phase obtained by the evaporation was dissolved in ethanol and the insoluble fraction (leftover K_2CO_3) was removed by filtration. Next, the ethanol was evaporated to create an almost saturated solution. The DMASD-Br was precipitated from the solution by diethyl ether, recovered by filtration and dried under vacuum

overnight. The structure of the SDA was confirmed by ^{1}H NMR spectroscopy using D_2O as a solvent (see Appendix, Figure A1). The DMASD-Br was dissolved in water to prepare 1M solution. The solution was subsequently mixed with Ambersep 900(OH) ion exchange resin with a 2 : 1 SDA : resin w/w ratio for 24 hours to ion-exchange the SDA to the hydroxide form (DMASD-OH). The completeness of ion-exchange was verified by titration with 0.1 M HCl using phenolphthalein as indicator.

The alumino-germanosilicate **UTL** was synthetised using the 7-ethyl-6-azoniaspiro[5.5]undecane (EASuD) bromide as the SDA. [108] The EASuD-Br was synthesized via a procedure analogous to that used for DMASD-Br, with 1,5-dibromopentane and 2-ethylpiperidine as the starting compounds. The SDA structure was verified by ^{1}H NMR spectroscopy (see Appendix, Figure A2). This EASuD-Br was ion-exchanged to the hydroxide form (EASuD-OH) using the Ambersep 900 (OH) ion exchange resin using analogous procedure.

4.1.2. Synthesis of **UTL** zeolites

The germanosilicate **UTL** was prepared using the DMASD-OH as SDA and molar composition of the synthesis gel 0.67 SiO_2: 0.33 GeO_2: 0.4 DMASD-OH : 33.3 H_2O. [107] The **UTL** was also synthetised with different Si/Ge molar ratios ranging from 0.33 to 7. The proportions of Si/Ge were varied; however, the total Si + Ge molar content was kept constant.

First, germanium dioxide was dissolved in 0.6 M water solution of DMASD-OH. Second, fumed silica (Cab-O-Sil M5) was added. The mixture was stirred at room temperature until the silica completely dissolved. The synthesis gel was transferred into a 1000 mL Parr autoclave and heated to 175 °C for 6 days with rotation 200 rpm. The **UTL** zeolite was recovered by filtration, washed out with a copious amount of distilled water and dried in an oven at 60 °C. The SDA was removed by calcination in air at 550 °C for 6 h, with a temperature ramp of 1 °C.min^{-1}.

UTL germanosilicates modified with growth modifiers (GM) were prepared using identical method. The 1,5-pentanediol, 1,5-diaminopentane, pentanoic acid or L-lysine, used as GM, were added to the synthesis mixture in GM/Si = 0.21 molar ratio prior to the hydrothermal crystallization.

The alumino-germanosilicate **UTL** was prepared following an analogous synthesis using EASuD-OH as the SDA and aluminium hydroxide as the aluminium source. The synthesis mixture with a molar composition of 1 SiO_2 : 0.5 GeO_2 : 0.012 Al_2O_3 : 0.4 EASuD-OH : 33.3 H_2O was placed into 90 mL Teflon lined autoclave and heated under rotation at 175 °C for 28 days. The Al-UTL was recovered by filtration, washed with distilled water and dried at 60 °C and calcined in air at 550 °C for 6 hours with a ramp of 1 °C.min^{-1}.

4.2. Hydrolysis and modification of **UTL** zeolites

4.2.1. Treatment with Water−Alcohol solutions

The treatment of the germanosilicate **UTL** zeolite with pure alcohols (methanol, ethanol, i-propanol) or their respective 20, 40, and 60% solutions in water was carried out by immersing 1 g of calcined **UTL** into 160 mL of the respective solution pre-heated to 60 °C. Samples of the solution were collected with automatic pipette after 1, 3, 5, 18, and 24 h and centrifuged to separate the zeolite from the solution. The solid samples were washed with pure alcohol (respectively to the treatment solution), dried at room temperature and calcined at 550 °C for 6 h in an air flow.

4.2.2. Treatment with HCl−Ethanol Solution

Prior to the treatment of the germanosilicate **UTL** zeolite with solution of HCl in ethanol, 160 mL of the 1.25 M HCl/EtOH solution was cooled down to 0 °C in a thermostat. Subsequently, 1 g of calcined germanosilicate **UTL** was added to the solution and kept stirring. The samples were collected periodically for 60 days, separated by centrifugation, washed with absolute ethanol, and dried at room temperature. The dry samples were calcined at 550 °C for 6 h in an air flow.

4.2.3. Hydrolysis of **UTL** to IPC-1P

The IPC-1P was prepared by hydrolysis of calcined germanosilicate **UTL** zeolite in 1 M CH_3COOH. Typically, 250 mL of 1 M CH_3COOH were heated to 85 °C in a round-bottom flask equipped with a condenser. Subsequently, 1 g of a calcined **UTL** was added to the mixture and stirred for 24 h. The IPC-1P was recovered by filtration, washed with a copious amount of distilled water to achieve neutral pH and dried at 60 °C.

4.2.4. Intercalation of IPC-1P and reconstruction of **UTL**

The intercalation of IPC-1P was carried out using an aqueous solution containing 20 % (w/w) tetrabutylammonium hydroxide (TBAOH) and 15 % (w/w) colloidal silica (Ludox AS-40. Firstly, 0.5 g of IPC-1P was added to 15 mL of the solution and stirred for 6 hours at room temperature. Subsequently, the intercalated material IPC-1TBA was recovered by centrifugation at 4500 rpm for 15 minutes, washed with distilled water to neutral pH and dried at 60 °C.

In a typical experiment, 0.1 g of IPC-1TBA was mixed with 5 mL of 1.25 M HCl in ethanol in a 25 mL Teflon-lined steel autoclave. Subsequently, respective amounts (Table 2) of ammonium fluoride, selected source of silicon (e.g. diethoxydimethyl silane), germanium methoxide and aluminium nitrate were added to the mixture. The autoclave was subsequently heated to 170 °C for 20 hours under static conditions. The product was recovered by filtration, washed with absolute ethanol and dried at 60 °C. The samples were calcined in flow of air at 550 °C for 6 h with a temperature ramp of 1 °C.min^{-1}.

Table 2: Composition of the individual reaction mixtures for **UTL** reconstruction and their respective labelling.

Sample	$c_{HCl/EtOH}$ (mol/l)	DEDMS (mg)	DETMDS (mg)	TMCTS (mg)	POSS (mg)	$(MeO)_4Ge$ (mg)	NH_4F (mg)	$Al(NO_3)_3.9H_2O$ (mg)
rec Si1	1.25	65.8						
rec Si2	1.25		49.4					
rec Si4	1.25			26.7				
rec Si8	1.25				29.8			
rec Si–Ge (3 : 1)	1.25	49.4				21.9		
rec Si–Ge (1 : 1)	1.25	32.9				43.7		
rec Si–Ge (1 : 3)	1.25	16.5				65.6		
rec Ge	1.25					87.3		
rec F Si1	1.25	65.8						
rec F Si–Ge (1 : 1)	1.25	32.9				43.7		
rec F Ge	1.25					87.3		

3Si:1Al	1.25	49.4					2.1	41.6
1Si:1Al	1.25	32.9					2.1	83.3
1Si:3Al	1.25	16.5					2.1	124.9
Pure Al ≡ pHCl = -0.1 (F)	1.25						2.1	166.5
pHCl = 1(Ge)	10^{-1}	24.7				32.8		37.7
pHCl = 3(Ge)	10^{-3}	24.7				32.8		37.7
pHCl = 5(Ge)	10^{-5}	24.7				32.8		37.7
pHCl = 1 (F)	10^{-1}	50.9					2.1	37.7
pHCl = 3 (F)	10^{-3}	50.9					2.1	37.7
pHCl = 5 (F)	10^{-5}	50.9					2.1	37.7
Re-UTL (Al)	10^{-3}	50.9					2.1	37.7
Re-UTL (Al+Ge)	10^{-3}	24.7				32.8		37.7

DEDMS = Diethoxydimethylsilane; DETMDS = 1,3-diethoxy-1,1,3,3-tetramethyl-disiloxane; TMCTS = 2,4,6,8-tetramethylcyclotetrasiloxane; POSS = octamethylsilsesquioxane.

The ion-exchange of the reconstructed **UTL** samples to the H^+ form was performed using 0.5 M NH_4NO_3 solution in ethanol. 100 mL of the solution was added to 1 g of sample and stirred for 4 h at room temperature. Subsequently, the solid was recovered by centrifugation. The procedure was repeated four times. The exchanged samples were dried at 60 °C and subsequently activated at 450 °C for 90 min.

4.3. Synthesis of **IWW** zeolites

Germanosilicates with **IWW** structure were synthetized using 1,5-Bis-(methylpyrrolidinium)pentane dihydroxyde (MPP) as SDA.

MPP was prepared through reaction of 18.8 g of 1,5-dibromopentane with 20 g of N-methylpyrrolidine in 150 ml of acetone. The reaction mixture was refluxed for 20 h and the solid product was collected by filtration, washed with acetone and dried under vacuum overnight. The structure of the SDA was verified by ^{1}H NMR spectroscopy using deuterium oxide as a solvent. MPP was ion exchanged for hydroxide form using anionic exchange resin Ambersep 900(OH) ion exchange resin with a 2 : 1 SDA : resin w/w ratio for 24 hours. The degree of ion-exchange was verified by titration with 0.1 M HCl using phenolphthalein as indicator. The solution was subsequently concentrated on an evaporator to a hydroxide concentration 1.0 M.

The **IWW** zeolites were synthetised dissolving germanium dioxide in 1M solution of MPP. Subsequently, tetraethyl orthosilicate was added to the mixture and stirred till complete evaporation of ethanol formed by the hydrolysis of tetraethylorthosilicate. The final mixture possessed molar composition x SiO2: 1-x GeO_2: 0.25 MPP: 15 H_2O. The **IWW** was prepared with Si/Ge ratio 4 and 6. The crystallization was carried out in Teflon-lined stainless-steel autoclaves at 175 °C for 11 days. The final solid products were recovered by centrifugation, washed with water and dried at 60 °C overnight. Calcination was carried out at 580 °C for 6 h in air.

4.4. Characterization methods

X-ray powder diffraction (XRD) analyses of the solid samples were performed on a Bruker D8 Advance diffractometer equipped with a Linxeye XE-T detector in the Bragg–Brentano geometry using Cu Kα (λ = 0.15406 nm) radiation. Data were collected over the 2 θ range of 3–40° with 0.021° step size and 0.8 s time per step.

Scanning electron microscopy (SEM) imaging was carried out using a JEOL IT-200 microscope in secondary electron imaging mode using electron beam accelerating voltage 15kV and working distance 10 mm; or using a JEOL IT-800 microscope in secondary electron imaging mode using electron beam accelerating voltage 3kV and working distance 2 mm.

Aspect ratios, *AR*, of the crystals were by calculated using equation (3):

$$AR(x_1/x_2) = \frac{x_1(\mu m)}{x_2(\mu m)} \quad (3)$$

where x_1 and x_1 represent two of the crystallographic axes.

Scanning transmission electron microscopy (STEM) imaging was performed using a JEOL NeoARM 200 F microscope equipped with a Schottky-type field emission gun operated at an accelerating voltage of 200 kV. Microscope was aligned using a gold nanoparticles sample as the standard to reach atomic resolution. The EX-37001 energy dispersive X-ray analyser connected to the STEM was used for the EDX mapping of the samples. The Si/Al molar ratios of the reconstructed **UTL** samples were obtained from four separate crystals for each sample and calculated as an average Si/Al molar ratio.

Elemental composition of the samples was analysed using Agilent 7900 ICP-MS instrument (Agilent Technologies, Inc.). 50 mg of a sample were mixed with 1.8 mL of HNO_3 (67-69%, ANALPURE®), 5.4 mL of HCl (34-37%, ANALPURE®), 1.8 mL of HF (47-51%, ANALPURE®), then transferred into a closed Teflon vessel, placed in the Speedwave® XPERT microwave and heated at 210 °C with heating rate 5 °C/min for 25 min. After cooling down, the complexation of the excess HF was done by adding 12 mL of H_3BO_3 and further treatment in the microwave at 190 °C (5 °C/min) for 10 min. Finally, the obtained cooled down solutions were diluted for analysis.

The concentration and type of acid sites were determined by adsorption of pyridine as a probe molecule. The content of the adsorbed pyridine was quantified by an FTIR analysis using a spectrometer Nicolet 6700 AEM equipped with a DTGS detector. Prior to probe adsorption, the samples were pressed into self-supporting wafers at a density of ca. 10 mg cm^{-2} and activated in a quartz IR cell under vacuum (10^{-4} Pa) at 450 °C for 2 hours. Pyridine adsorption proceeded at 150 °C for 20 min at pyridine pressure of 3 Torr, followed by 20 min evacuation at 150 or 450 °C. The concentrations of Brønsted and Lewis acid sites in aluminosilicate samples were determined from the integral intensities of individual bands representing vibrations of pyridine ring interacting with Brønsted acid sites at 1545 cm^{-1} and with Lewis acid sites at 1455 cm^{-1} and using the molar absorption coefficients of ε(B) = 1.67 ± 0.1 cm μmol^{-1} and ε(L) = 2.22 ± 0.1 cm μmol^{-1}, respectively. [121] The spectra were recorded with a resolution of 4 cm^{-1} after collecting 128 scans for each spectrum.

The solid-state ^{27}Al NMR spectra were collected using a Bruker Advance III HD spectrometer with a 9.4 T standard bore superconducting magnet. The spectra were collected at a resonance frequency of 104.2 MHz using strong and short 1 µs pulses, with 1.5 s repetition time and 4000 scans. The samples

were packed into a 3.2 mm zirconia rotor and rotated at a MAS rate of 15 kHz using a Bruker 3.2 mm HX CP-MAS probe.

Argon adsorption-desorption isotherms were measured on a Micromeritics 3Flex volumetric Surface Area Analyser at −186 °C in liquid argon bath. Before analysis, the samples were degassed on a Micromeritics Smart Vac Prep instrument under vacuum at 250 °C for 8 hours with heating rate 1 °C min^{-1} under vacuum (3.10^{-2} mmHg minimum pressure). The specific surface area was evaluated using BET method in the relative pressure range from $p/p_0 = 0.05$ to $p/p_0 = 0.25$. The micropore volume (V_{mic}) was calculated using the t-plot method using the Harkins−Jura thickness equation. The total pore volume (V_{tot}) was calculated from the adsorbed amount at relative pressure $p/p_0 = 0.98$. The pore size distribution curves were calculated using Horwath–Kawazoe method and DFT pore size distribution using Kernel model for argon adsorption on oxidic surface with slit-shaped pore geometry.

4.5. Adsorption of water vapour

Water-vapour adsorption experiments were carried out using the Micromeritics ASAP 2020 volumetric adsorption analyser. Before analysis, the samples were outgassed under vacuum and gradual heating by 1 °C.min^{-1} from ambient temperature to 300 °C and for 8 h at the final temperature. The experiment consisted of interchanging N_2 and H_2O adsorption measurements in the following sequence: N_2−H_2O−N_2−H_2O−N_2. The outgassing was repeated after collecting each isotherm. The N_2 adsorption measurements were performed in a liquid nitrogen bath at −195.8 °C; whereas, the H_2O adsorption experiments were conducted at 20 °C in a thermostat. The sample BET area was evaluated by using the BET method from adsorption data in the relative pressure (p/p_0) range from 0.05 to 0.20. The volume of micropores (V_{mic}) and the external surface area (S_{ext}) were calculated by using the t-plot method using the Harkins−Jura thickness equation and the total pore volume (V_{tot}) was calculated from the adsorbed amount at $p/p_0 = 0.95$). The pore size of the samples was evaluated using the DFT pore size distribution using Kernel model for nitrogen adsorption on oxidic surface with slit-shaped pore geometry.

The amounts of irreversibly bound water molecules were calculated from the adsorbed amounts per unit cell at $p/p_0 = 0.008$ on the desorption branch of the isotherm. The maximum numbers of reversibly adsorbed water molecules were extrapolated from the “knee” of the adsorption branches of the isotherms, between the low and high water-intake regions. For quantifying the relative strength of interaction between the water and individual samples, the water adsorption potential distributions, χ, were calculated based on equation (1):

$$\chi = \frac{dn}{dA} \tag{1}$$

where n stands for the amount adsorbed and A is the adsorption potential. [122-124] The adsorption potential is described by equation (2):

$$A = -RT.\ln\left(\frac{p}{p_0}\right) \tag{2}$$

where T is the thermodynamic temperature of the measurement, R is the universal gas constant, and p_0 is the saturation pressure of water at 20 °C equal to 2.333 kPa.

4.6. Catalytic experiments

Tetrahydropyranylation of 1-decanol was used as a model reaction to test the catalytic performance of the reconstructed **UTL** samples. The experiments were performed in liquid phase under an atmospheric pressure at 60 °C on the Multi-experiment workstation Starfish™. The catalyst was activated at 450 °C in air for 90 min prior to each experiment. Typically, 50 mg of catalyst were added into a three-neck 25 mL bottle. The bottle was equipped with a condenser and a thermometer. Subsequently, 0.25 g of internal standard (mesitylene) and 10 mL (110 mmol) of 3,4-dihydro-2H-pyran were added. The reaction was initiated by adding 1-decanol (4.5 mmol). Samples of the reaction mixture were taken periodically, centrifuged to separate the catalyst, and analysed using Agilent 7890B GC gas chromatograph equipped with an autosampler, an HP-5 column (30 m length, 0.320 mm diameter, and 0.25 μm film thickness) and a flame ionization detector.

5. Results and Discussion

5.1. Assembly – modification of **UTL** germanosilicate morphology

We aimed to identify factors that affect the crystal growth of the UTL zeolite and develop a method for controlling its crystal morphology. As a reference, we first synthesised **UTL** germanosilicate zeolite from a synthesis gel with Si/Ge = 2 molar ratio. The elemental analysis of the resulting sample showed Si/Ge molar ratio in the zeolite 3.22, thus this reference sample is hereafter denoted **UTL** (Si/Ge = 3.22). Properties of the resulting sample including crystal structure, elemental composition, textural properties and morphology were characterized by X-Ray diffraction, ICP-MS analysis, argon adsorption-desorption and SEM, respectively. The powder XRD pattern of the sample (**UTL** (Si/Ge = 3.22)) exhibited reflections characteristic of **UTL** framework (Figure 6A). [19] Additionally, the XRD pattern revealed no sign of any secondary phases in the sample. The textural properties of the sample derived from the Ar adsorption isotherm (Figure 6B) were BET area 520 m^2/g and volume of micropores 0.21 cm^3/g, typical for **UTL** zeolites reported in literature. [106, 107] Scanning Electron Microscopy imaging of the **UTL** (Si/Ge = 3.22) revealed characteristic flat rectangular crystals with an average size 43.7 x 32.5 x 0.84 µm (Figure 7A) also in agreement with the literature. [68, 106] This sample was chosen as a reference for subsequent experiments with modification of the crystal morphology.

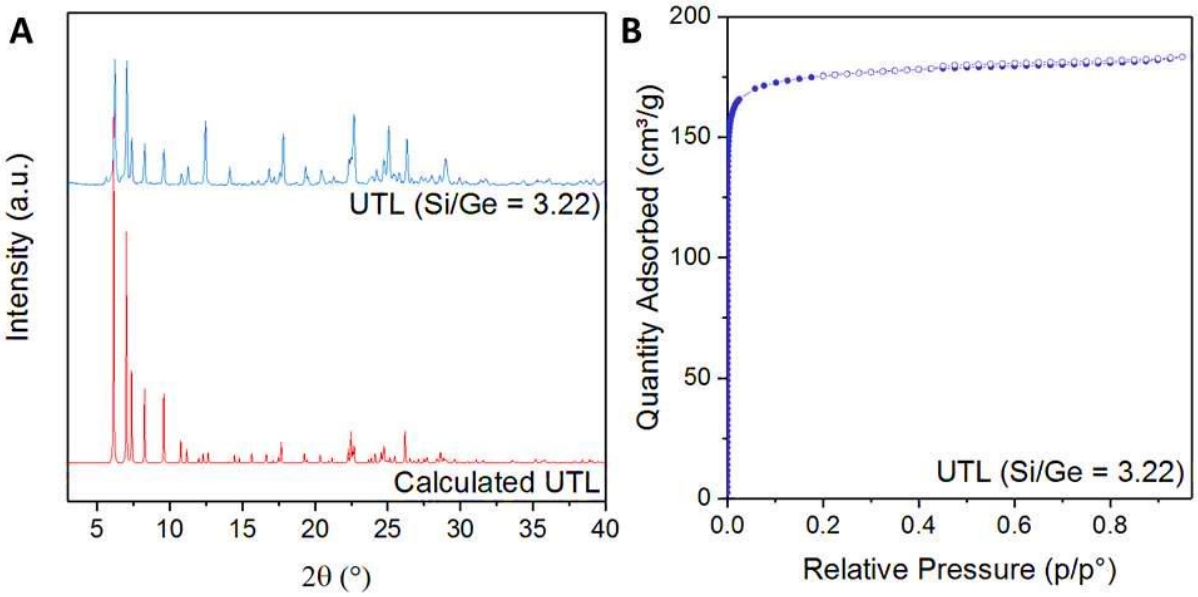

Figure 6: A) powder X-ray diffraction pattern and B) argon adsorption-desorption isotherm of the UTL (Si/Ge = 3.22) sample.

The commonly studied method for modifying zeolite crystal morphology uses growth modifiers as additives during the hydrothermal synthesis. The growth modifiers interact with specific crystal planes of the zeolite during synthesis and restrict the crystal growth along respective axis. This can be illustrated on the growth of zeolite **LTL** which provides flat or rod-like crystals when modified with butylamine and poly(diallyldimethylammonium chloride), respectively. [125] However, successful application of these growth modifiers has not been demonstrated on other zeolites beside **LTL**, raising doubts about their general applicability in zeolite synthesis.

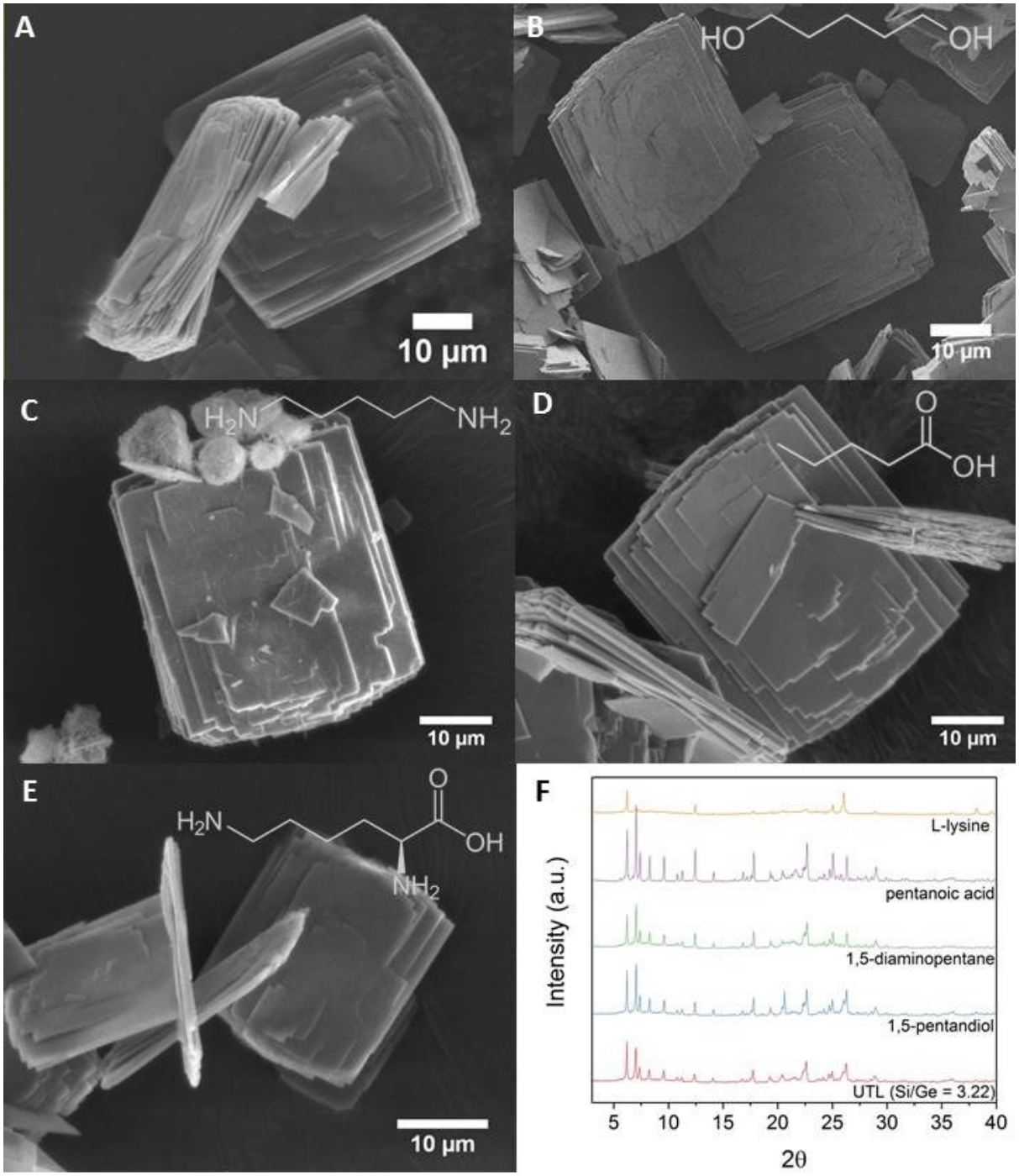

Figure 7: SEM images of A) unmodified **UTL** (Si/Ge = 3.22) and **UTL** samples modified with B) 1,5-pentanediol, C) 1,5-diaminopentane, D) pentanoic acid and E) L-lysine, and F) powder XRD pattern of respective samples.

We assessed the applicability of the method on synthesis of zeolite **UTL** by carrying out several synthesis batches containing 1,5-pentanediol, 1,5-diaminopentane, pentanoic acid and L-lysine as growth modifiers (GM) with GM/Si = 0.21 in otherwise identical synthesis mixtures. Each synthesis yielded flat **UTL** zeolite crystals 23 x 23 x 0.7 µm in size on average. The SEM imaging further showed that samples modified with 1,5-diaminopentane and L-lysine contained small particles of an amorphous matter (Figure 7C) likely due to different crystallization rate or impaired phase-selectivity

in the presence of the modifiers. However, no sample showed any significant change in crystal morphology compared to the unmodified synthesis (Figure 7). In summary, we conclude that the growth modifiers, despite showing great potential for modification of zeolite **LTL** are insufficient for modifying the morphology of **UTL**.

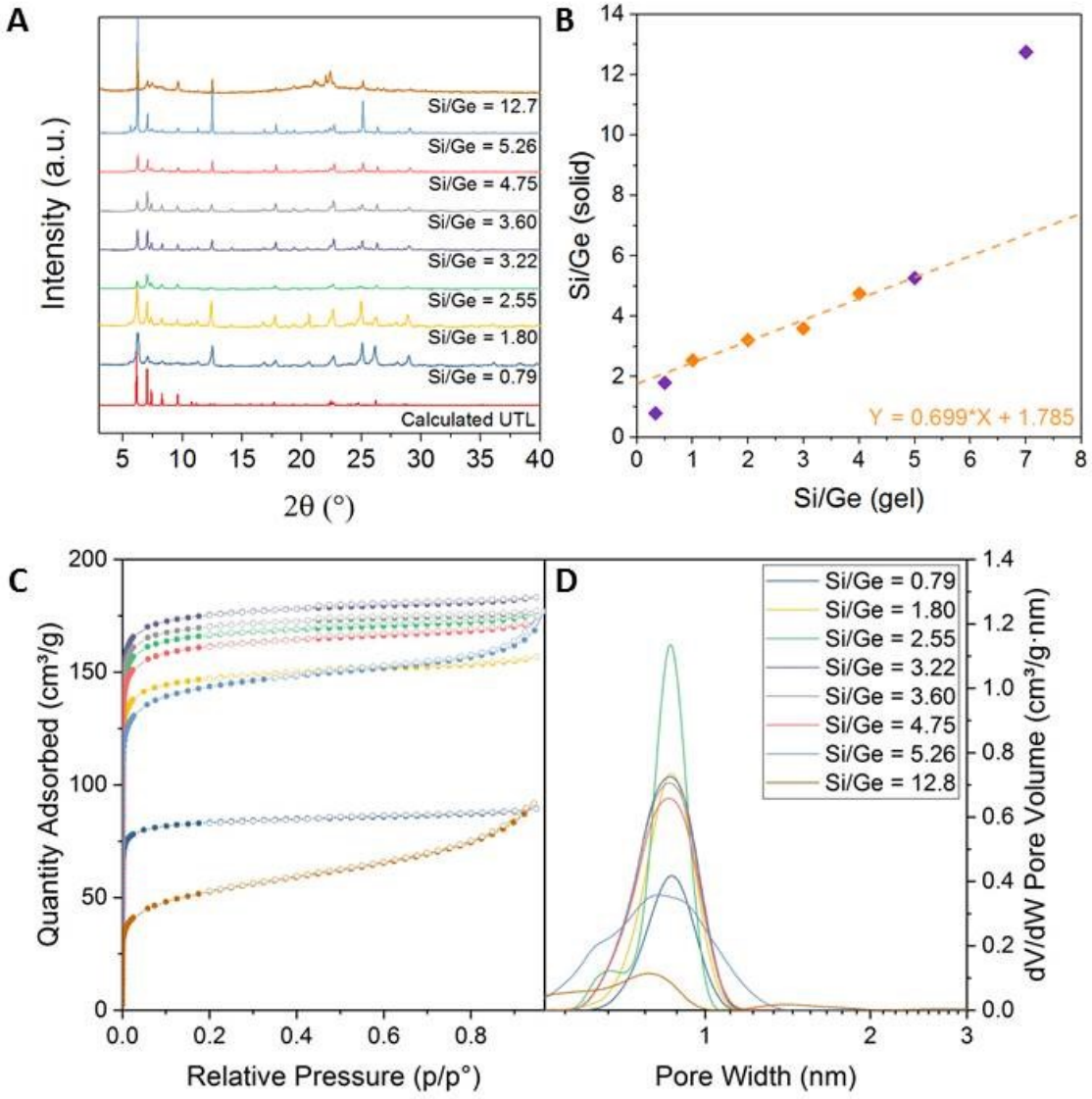

Figure 8: A) powder XRD patterns of **UTL** samples with varying Si/Ge ratio; B) correlation between the synthesis gel Si/Ge ratio and the Si/Ge of the solid sample; C) Argon adsorption-desorption isotherms and D) DFT pore size distributions of the **UTL** samples with varying Si/Ge.

Previously published studies on the synthesis of the **UTL** zeolite indicate that its Si/Ge ratio may influence the crystal morphology. Nevertheless, the assumption was never verified. [106] Hence, we prepared a set of **UTL** samples with varying Si/Ge ratios to test this hypothesis. Synthesis gels with Si/Ge ratio ranging from 0.33 to 7 yielded solid samples which possessed the **UTL** structure according to the powder XRD analysis (Figure 8A). The XRD of samples with synthesis gel Si/Ge < 1 also contained an impurity which we identified as germanium oxide (characteristic reflections at 2θ = 26.1°, 36.1°,

37.9° and 39.0° [126]). The elemental analysis revealed that the actual Si/Ge ratio of the solid samples ranged from 0.79 to 12.8. **UTL** samples with Si/Ge from 1.80 to 3.60 exhibited linear dependence between the Si/Ge ratio of the zeolite on the Si/Ge ratio of the synthesis mixture with the synthesis gel being slightly richer in germanium (Figure 8B, Table 3). Nevertheless, the **UTL** samples with solid Si/Ge ≤ 1.80 deviated from the trend and contained proportionally more germanium. We hypothesized that the excess of germanium originates from the competing germanium oxide phase. However, the ICP-MS elemental analysis cannot distinguish framework germanium from bulk germanium oxide leaving us no means to verify the assumption. On the opposite side, the sample with Si/Ge = 12.8 contained unexpectedly high amount of Si which we attributed to competing silicon oxide phase formation observed in SEM images (*vide infra*). The presence of non-porous secondary phases such as germanium or silicon oxide is apparent from the decreased pore volumes of respective samples (Figure 8C, D, Table 3) supporting our hypothesis. The occurrence of competing phases in samples with the highest and lowest Si/Ge delimitates the range of Si/Ge where pure **UTL** formation is feasible by the hydrothermal method.

Table 3: Elemental composition, textural properties (Ar adsorption-desorption) and average crystal size of **UTL** samples with varying Si/Ge ratio.

Si/Ge		**Textural properties**				**Crystal size**		
Synthesis	**Solid**	**BET (m^2/g)**	**$S_{external}$ (m^2/g)**	**V_{total} (cm^3/g)**	**V_{micro} (cm^3/g)**	***a* (µm)**	***b* (µm)**	***c* (µm)**
0.33	0.79	250	8.6	0.11	0.10	0.17	30.1	23.0
0.50	1.80	442	15	0.20	0.17	0.20	25.5	15.1
1.0	2.55	494	42	0.22	0.19	0.33	34.8	25.8
2.0	3.22	520	42	0.23	0.21	0.84	43.7	32.5
3.0	3.60	505	38	0.23	0.20	1.20	44.8	34.9
4.0	4.75	480	45	0.22	0.20	1.65	42.1	30.5
5.0	5.26	430	66	0.23	0.15	3.60	65.5	39.7
7.0	12.8	162	49	0.12	0.03	5.39	78.6	26.7

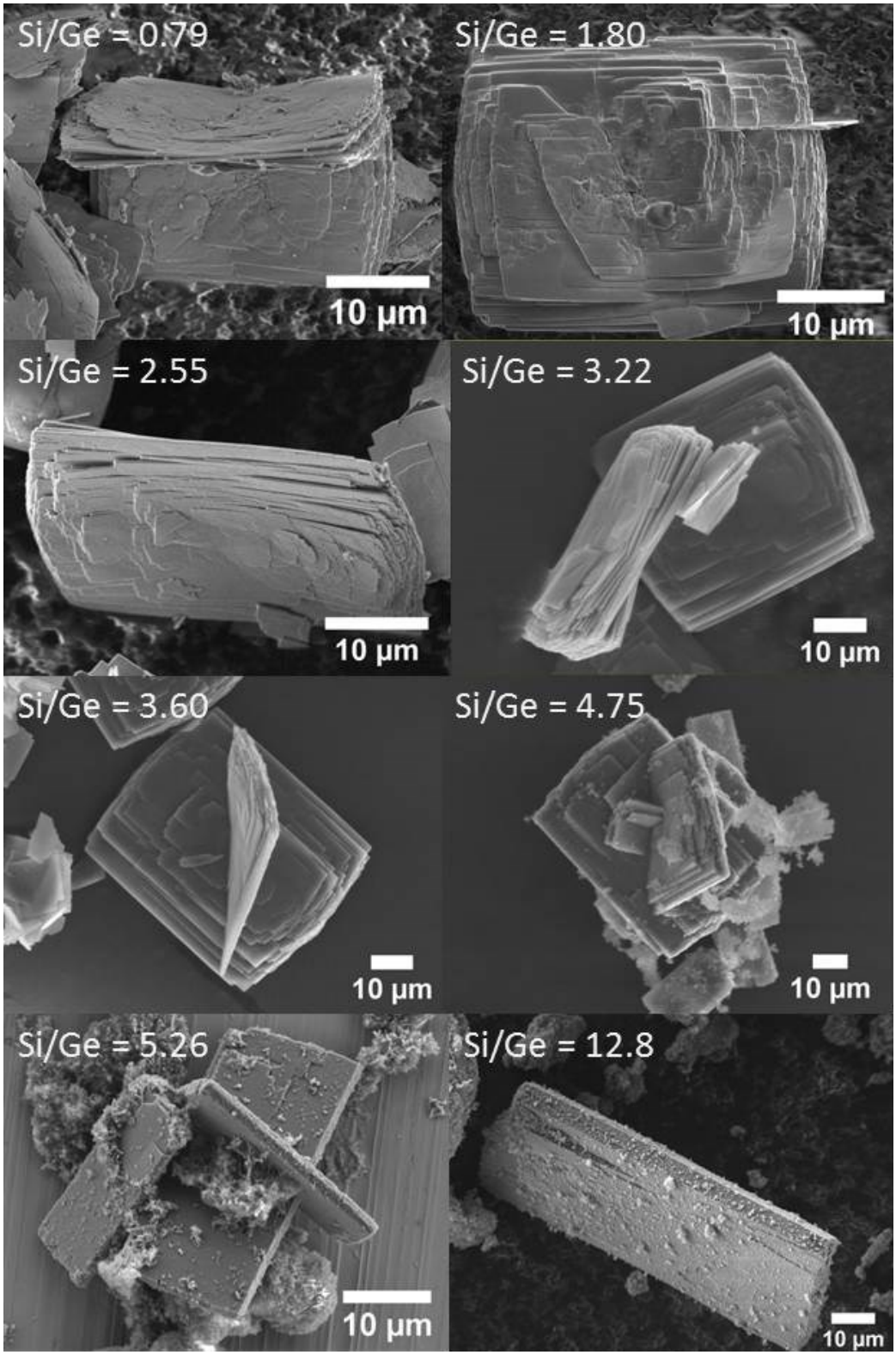

Figure 9: SEM images of **UTL** with Si/Ge varying from 0.79 to 12.8

We used the SEM to characterize the crystal size and morphology of the **UTL** samples. All **UTL** samples consisted of flat rectangular crystals of uniform size. Typical crystals consisted of smaller crystalline lamellas intergrown into larger flat crystals (Figure 9). Samples with Si/Ge > 4.75 also contained a second phase in a form of clumps without a definite shape. The second phase may either be a

precursor or competing phase in the **UTL** crystallization. The average size of the **UTL** crystals significantly increases along *a*-axis (thickness) from 0.17 µm to 5.39 µm with increase of Si/Ge ratio from 0.79 to 12.8. We calculated aspect ratios of the crystals in order to more rigorously assess the dependence of the crystal morphology on the Si/Ge ratio (Figure 10). The crystals showed the smallest variation in size along the *c*-axis; therefore, we used it as a reference for calculation of the aspect ratios.

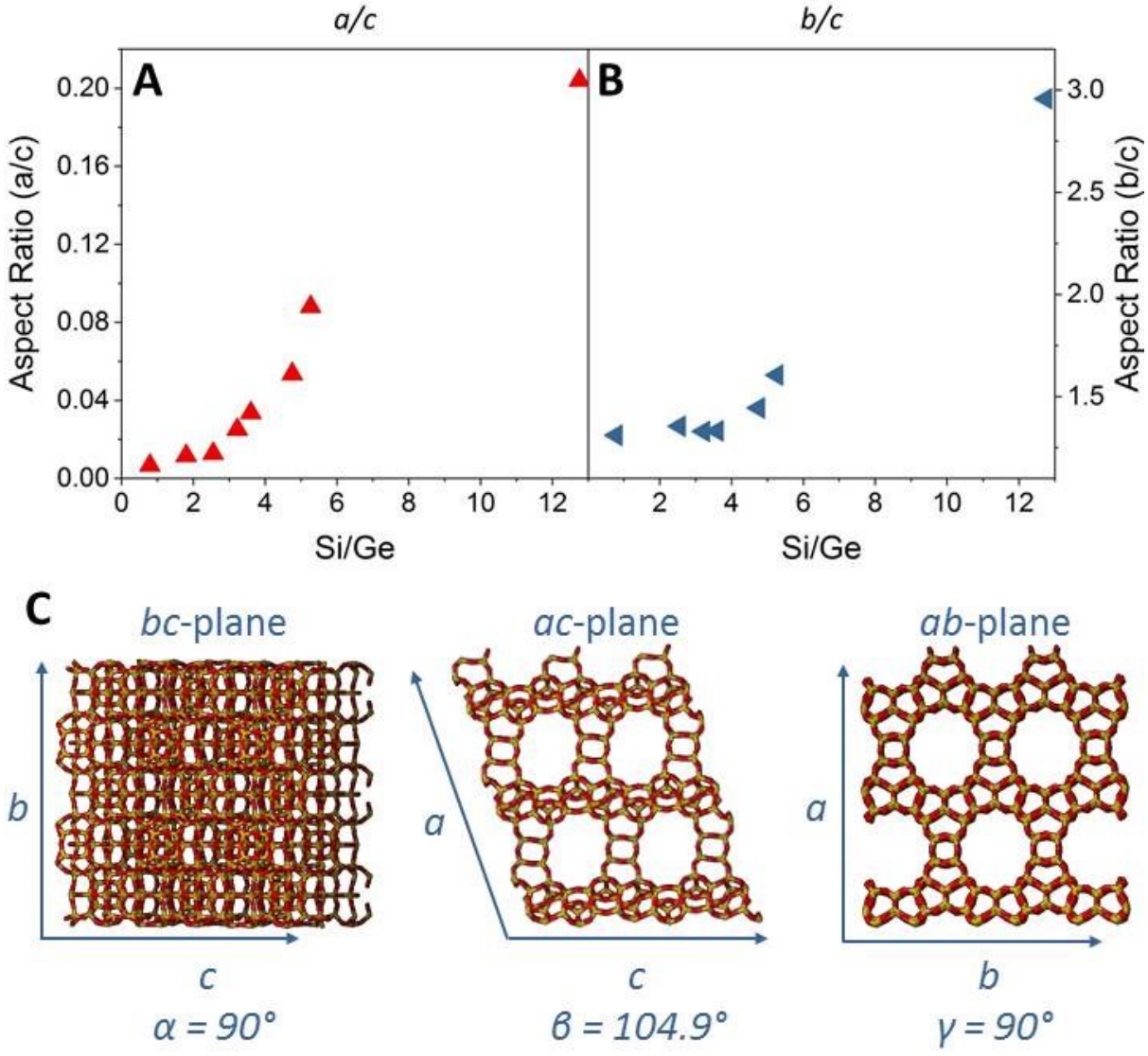

Figure 10: A) variation of *a*/*c* and B) *b*/*c* aspect ratios of the **UTL** crystals with Si/Ge; C) Schematic representation of **UTL** with projections along *a*-, *b*- and *c*-axes.

The **UTL** zeolite undergoes two major changes of crystal morphology with increasing Si/Ge ratio. First, the *b*/*c* aspect ratio increases with increasing Si/Ge (Figure 10). We attributed the pronounced growth along the *b*-axis to the lower density of *t-cub* (D4R) units along the *b*-axis. Germanium is crucial for the formation of D4Rs and therefore decreasing the germanium content (i.e. increasing the Si/Ge) favours the expansion of the crystal along the *b*-axis (less abundant in the D4Rs) relatively to the *c*-axis. Second, the *a*/*c* aspect ratio also increases with the increasing Si/Ge. This phenomenon stems from different relative growth rate of the *pcr* layers oriented along the *bc*-plane and the interlayer connections along the *a*-axis. For simplicity, we considered layer growth (along the *bc*-plane) and 3D

growth (along *a*-axis) separately. The layer growth proceeds through the formation of small *t-tes*, *t-pes* and *t-non* cages. In contrast, 3D growth consists of relatively rapid formation of D4R (*t-cub*) units and comparably slower formation of large cages in between the *pcr* layers (i.e., *t-utl-1*, *t-utl-2*, *t-utl-3* or *t-utl-4*). The presence of the large cages impedes the growth of the crystal along the a-axis, generating the typical flat **UTL** crystals. According to our observations, higher Si/Ge ratio (i.e. higher silicon content) encourages the formation of the large interlayer cages and thereby promotes the crystal growth in perpendicular to the *pcr* layers.

Literature provides several examples of other zeolites that exhibit similar change in crystal morphology in relation to Si/T ratio. Zeolite **LTL** (12R pores) crystalizes in a form of hexagonal rods elongated along the direction of the pores. Increased Si/Al ratio promotes crystal growth of the zeolite in perpendicular to the pores, resulting in thickening of the **LTL** crystals. [127] Analogously, **IFR** zeolite (12R pores) exhibits pronounced crystal growth in perpendicular to the direction of the pores in response to increasing Si/Al ratio. [128] **MWW** (10-10R) zeolite also displays a dependence of its crystal morphology on the Si/Al ratio. However, this case is more complicated, because the Si/Al influences not only the crystal morphology but also the structure of the **MWW**. Low aluminium content favours formation of MCM-22P, a semi-ordered layered precursor to **MWW**. On the other hand, high aluminium content promotes formation of disordered unilamelar MCM-56 as an intermediate which subsequently transforms to three-dimensional MCM-49 framework. Essentially, the aluminium facilitates formation of the interlayer connections. Nevertheless, the aluminium also decelerates the crystal growth in direction perpendicular to the layers. This causes the **MWW** crystals to become thinner with decreasing Si/Al ratio. [129-131]

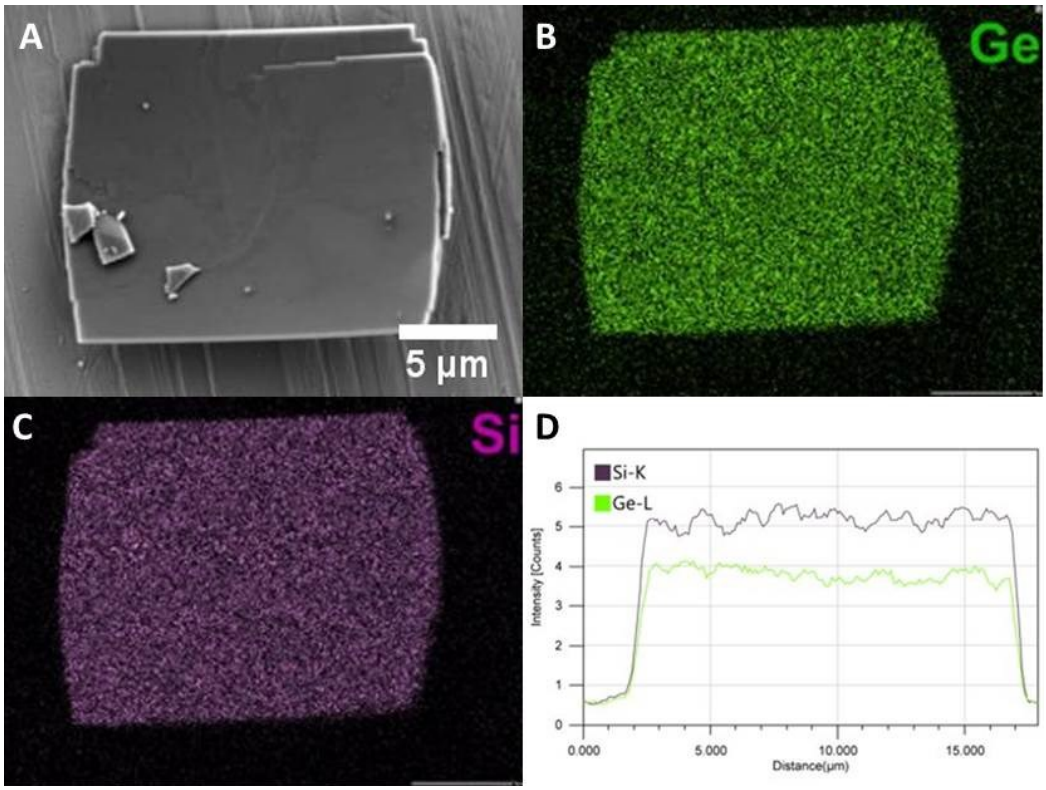

Figure 11: A) SEM image, B) EDX map of Ge and C) Si of a **UTL** (Si/Ge = 3.22) crystal; D) profile of the Si and Ge content across the crystal volume.

Additionally, Schunk et al. observed analogous behaviour on silico-aluminophosphate SAPO-5 with the **AFI** structure (12R pores). The hexagonal rod-like crystals of SAPO-5 also showed increased growth in perpendicular to the pores as a result of increased Si content. However, the relatively low content of Si in the SAPO-5 along with the aluminophosphate nature of the material raises doubts whether this observation can be related to our observation on the **UTL** and the other zeolites or whether the mechanism differs. The authors showed that the silicon resides predominantly in the outer zones of the SAPO-5 crystals while the core is depleted of silicon. They deduced that the silicon incorporates into the crystal in later stages of the synthesis and then slows down the growth rate along the direction of the pores. [132] We performed an elemental mapping of the **UTL** crystals to examine the silicon and germanium distribution throughout the crystals (Figure 11). However, our results showed no significant discrepancy in distribution of the elements throughout the crystal. This suggests that the evolution of **UTL** and SAPO-5 crystal morphology arise from a different mechanism.

The above examples demonstrate that zeolites with one- or two-dimensional pore system undergo predictable evolution of their crystal morphology with Si/T molar ratio. However, the data do not disclose whether the morphology evolution emerges due to the dimensionality of the channel system (one- or two-dimensional) or whether the uneven building units (presence of cavities etc.) of the zeolites affect the crystal growth. We hypothesized that if the uneven crystal growth originated from the geometry of the building units even zeolites with anisotropic (i.e. uneven pore size along different spatial directions) three-dimensional pore system would exhibit analogous behaviour. We chose the **IWW** zeolite with 12-10-8R pore system as test sample to verify our hypothesis. [133] Based on the topology of the **IWW** (Figure 12A), we estimated that the crystals will be elongated along c-axis in parallel to the largest 12R pores. Additionally, according to our hypothesis the row of large building units arranged long *bc*-plane (Figure 12B) should restrict the crystal growth along *a*-axis. SEM imaging of **IWW** zeolite with Si/Ge = 4 revealed intergrown 0.16 x 2.36 x 1.34 µm large rectangular crystals (Figure 12D). We identified the crystallographic axes using TEM imaging and confirmed that the crystal is elongated along *b*- and *c*-axes and narrowed along the *a*-axis (Figure 12C). In contrast, the IWW with the Si/Ge ratio 6 formed crystals with size 0.38 x 2.79 x 1.50 µm (Figure 12E). The thickness along the *a*-axis increased proportionally more than the *b*- and *c*-axis with increasing Si/Ge ratio and, thereby, confirmed our hypothesis.

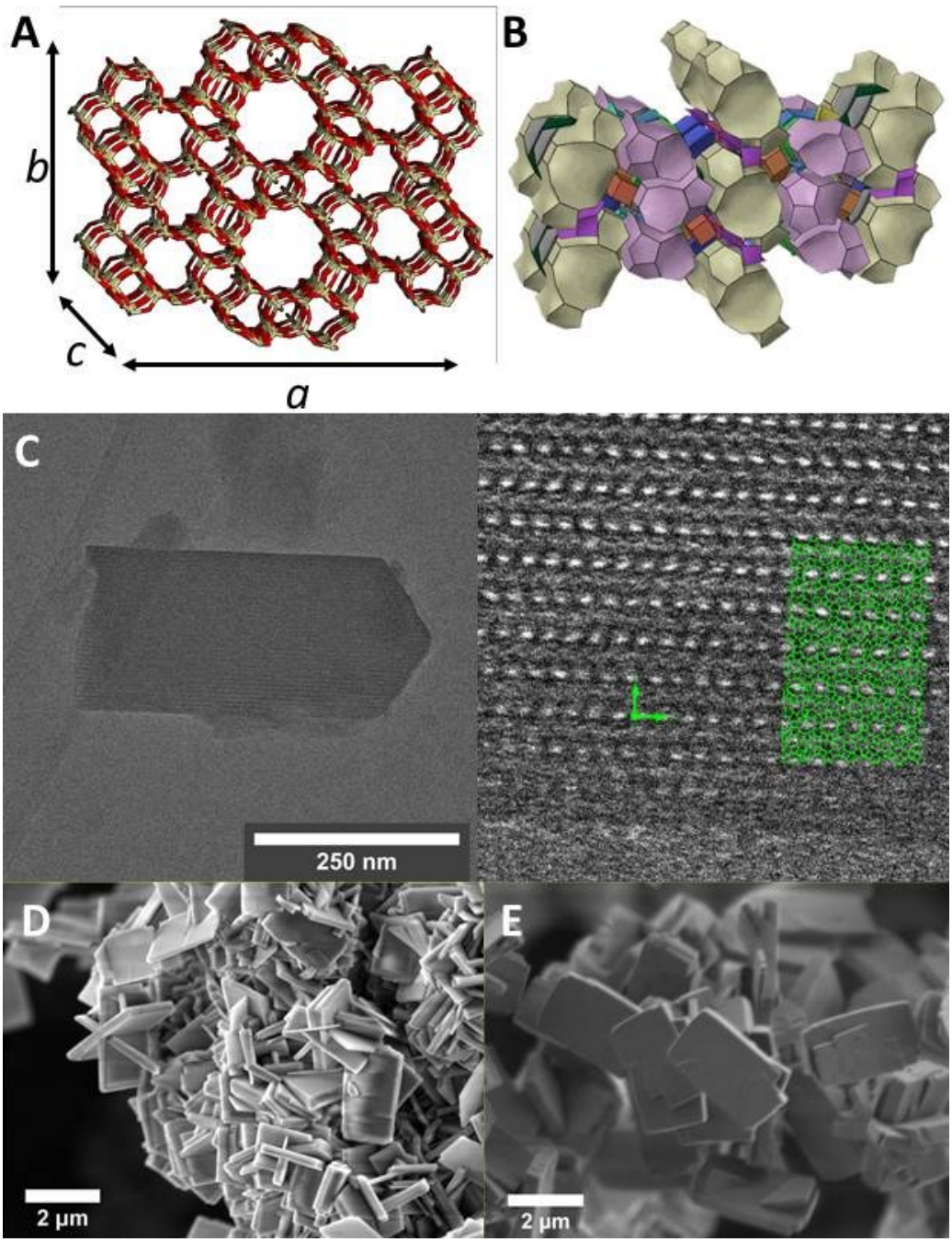

Figure 12: a) **IWW** structure; b) arrangement of the building units in the **IWW** structure; c) TEM image of **IWW** crystal with projection of **IWW** topology along ab-plane; d) SEM image of **IWW** (Si/Ge = 4); e) SEM image of **IWW** (Si/Ge = 6).

5.2. Disassembly – water-vapour adsorption on **UTL** germanosilicates

For the next study, we investigated the hydrolytic stability/lability of the **UTL** germanosilicate and the mechanism of its hydrolysis under varying water content and with varying Si/Ge ratio. We prepared a set of **UTL** zeolites with Si/Ge molar ranging from 2 to 50. **UTL** samples with Si/Ge < 6 were synthetized by direct hydrothermal synthesis. However, the hydrothermal method can only provide **UTL** up to approximately Si/Ge 12.7 (see page 22). Therefore, we prepared the samples with higher Si/Ge molar ratios by repeated post-synthetic stabilisation (degermanation-resilylation) of the directly-synthesised **UTL**. [79] The powder XRD of all samples showed diffraction patterns typical for the **UTL** topology (Figure 13A). Elemental analysis revealed that the directly synthesised samples possess Si/Ge ratios 2.5 and 4.5 and the post-synthetically modified **UTL** Si/Ge = 18.5 and 53.

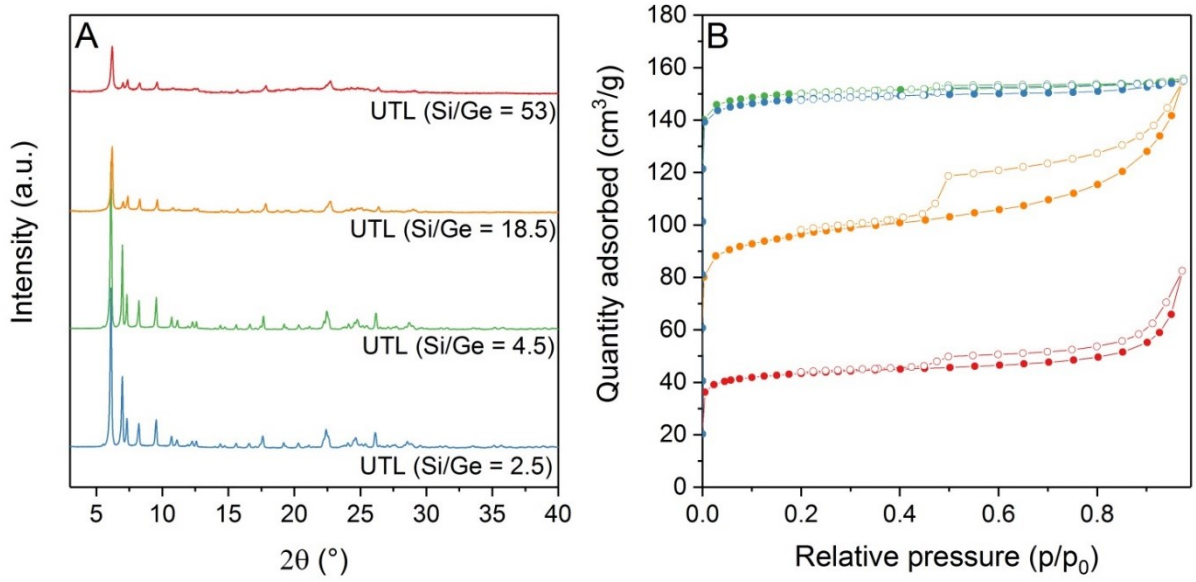

Figure 13: A) powder XRD patterns and B) N_2 adsorption isotherms of **UTL** samples with varying Si/Ge ratio.

Table 4: Si/Ge and textural properties of the **UTL** samples

	Si/Ge	BET (m^2/g)	V_{total} (cm^3/g)	V_{micro} (cm^3/g)
UTL (Si/Ge = 2.5)	2.50	497	0.24	0.21
UTL (Si/Ge = 4.5)	4.52	504	0.24	0.22
UTL (Si/Ge = 18.5)	18.48	327	0.24	0.13
UTL (Si/Ge = 53)	53.15	150	0.13	0.07

UTL (Si/Ge = 2.5) and UTL (Si/Ge = 4.5) also possessed textural properties typical for **UTL** zeolite such as BET area 497 and 504 m^2/g and micropore volume 0.21 and 0.22 cm^3/g, respectively (Table 4). The argon adsorption provided type I isotherms typical for purely microporous materials (Figure 13B). In contrast, UTL (Si/Ge = 18.5) and UTL (Si/Ge = 53) exhibited lower micropore volume 0.13 and 0.07 cm^3/g, respectively. The samples provided type II isotherms with hysteresis loops at higher pressures which implied the presence of structural defects originating from the post-synthetic

treatment. The formation of defects is accompanied by partial decrease of crystallinity of the samples as illustrated by the lower intensities of the XRD reflections and lower micropore volumes (Figure 13, Table 4).

5.2.1. Reversibility of adsorption

The adsorption of water vapour on the UTL (Si/Ge = 2.5) provided an unusual type V isotherm with a wide unclosed hysteresis loop between p/p_0 0.4 and 0.0 (Figure 14A). The adsorption of water on the **UTL** can be divided into three consecutive phases. In the first phase bellow $p/p_0 = 0.35$, only a small amount of water adsorbed on the **UTL**. However, the adsorbed amount abruptly increased after reaching $p/p_0 = 0.35$ (phase II). The steep increase in water adsorption continued until $p/p_0 = 0.45$ where the adsorption isotherm levelled off to a plateau (phase III). The isotherm showed a pronounced hysteresis loop bellow $p/p_0 = 0.45$ during desorption. Moreover, the desorption branch did not close, meaning that significant amount of water remained trapped in the sample after completing the adsorption-desorption cycle.

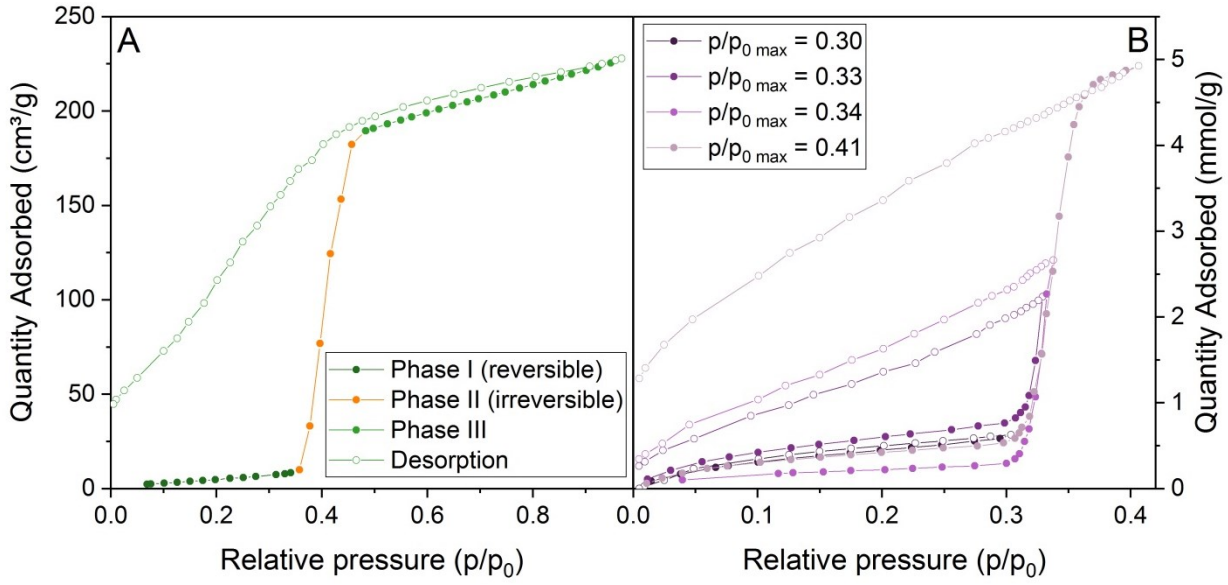

Figure 14: A) Isotherm of water vapour adsorption on UTL (Si/Ge = 2.5) and B) scanning of the isotherm hysteresis with maximum $p/p_0 = 0.30$, 0.33, 0.34 and 0.41.

We performed a scanning of the hysteresis loop in order to examine the reversibility of the water adsorption of the **UTL**. We repeated the water vapour adsorption experiment multiple times with gradually increasing the maximum relative pressure from $p/p_0 = 0.2$ to 0.9. The adsorption-desorption isotherms with maximum $p/p_0 \leq 0.30$ showed no hysteresis and no irreversibly adsorbed water (Figure 14B), meaning that the adsorption was fully reversible. Ergo, we can deduce that the phase I involves only physisorption of water. In contrast, isotherms with $p/p_0 > 0.30$ showed pronounced hysteresis loop with unclosed desorption branch. The amount of irreversibly adsorbed water was proportional to the amount adsorbed at the maximum pressure. This proves that water adsorbs irreversibly onto the **UTL** at $p/p_0 > 0.30$. Characterization of the **UTL** after the experiment by XRD and N_2 adsorption evidenced that the crystallinity as well as micropore volume of the zeolite decreased upon the water-vapour adsorption (Figure 15, Table 5). This shows the water adsorbed at phase II causes changes to the structure of the germanosilicate.

Equatorial mechanism (low water)

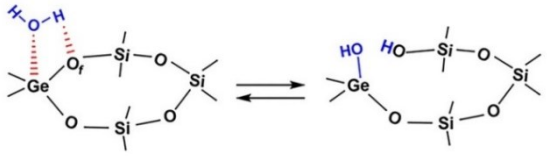

Axial mechanism (high water)

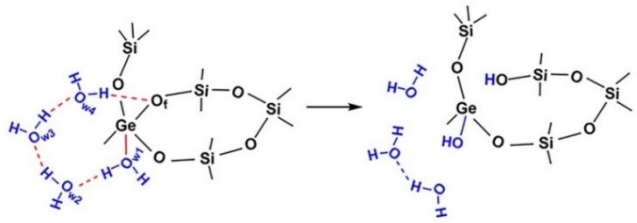

Scheme 2: Illustration of the equatorial and axial mechanism of D4R hydrolysis. [134]

In summary, the experiments on UTL (Si/Ge 2.5) revealed that water adsorbs reversibly onto the germanosilicate at low relative pressure ($p/p_0 < 0.35$). The adsorption becomes irreversible, reactive, only at pressures $p/p_0 > 0.35$. The reactive adsorption of water induces structural changes to the zeolite which eventually result in decrease of its crystallinity. The crystallinity decreases as a result of hydrolysis of labile Ge-O bonds in the Ge-rich D4R units in the **UTL** framework. [74] The hydrolysis of Ge-O bonds consumes water which explains why certain amount of water cannot be desorbed after the adsorption-desorption cycle. We compared our results with theoretical calculations on hydrolytic stability of the **UTL**. From the combined results we disclosed that the hydrolysis at low water content proceeds through equatorial mechanism. This mechanism provides unstable product with two hydroxyl groups in close proximity which are prone to re-condensation (Scheme 2). In contrast, high water content enables axial reaction mechanism which involves proton transfer over a chain of water molecules and provides more stable product where hydroxyl group recondensation is unfavourable. [134]

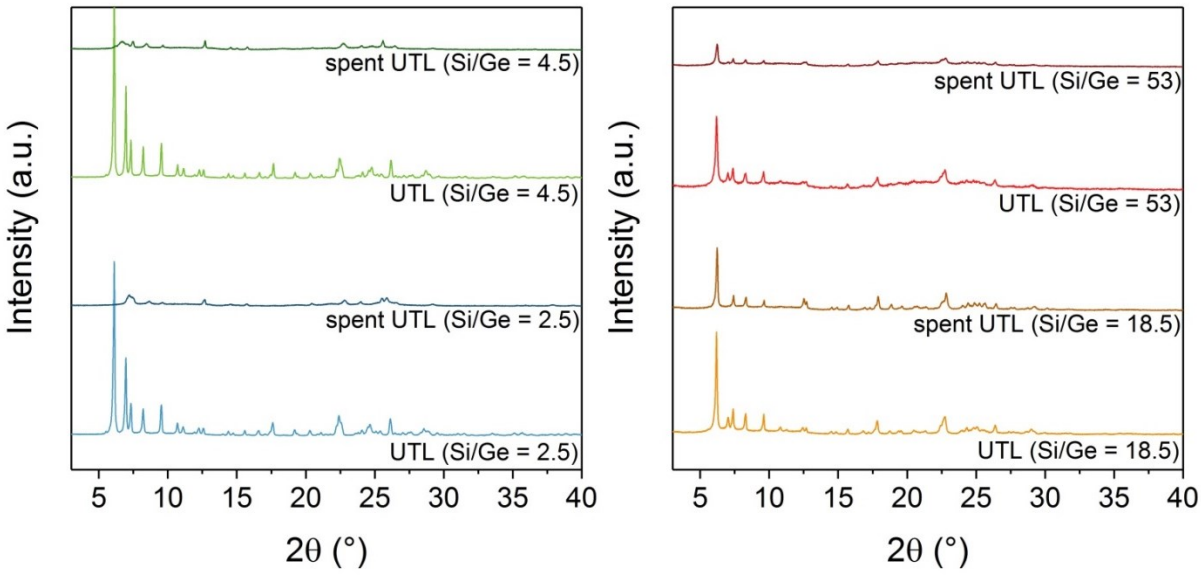

Figure 15: Powder XRD patterns of the **UTL** samples before and after ("spent") 2nd water-vapour adsorption cycle.

5.2.2. Hydrolytic stability and germanium content

Subsequently, we performed the water vapour adsorption on the **UTL** samples with varying Si/Ge molar ratio. The UTL (Si/Ge = 4.5) exhibited analogous behaviour to the UTL (Si/Ge = 2.5); the type V adsorption isotherm with unclosed hysteresis loop bellow p/p_0 = 0.4 (Figure 16A) and loss of crystallinity and micropore volume upon completing the adsorption-desorption cycle (Figure 15, Table 5). In contrast, samples UTL (Si/Ge = 18.5) and UTL (Si/Ge = 53) showed virtually no difference in micropore volume before and after the water adsorption. The XRD also proved that the samples retained the **UTL** structure after the water adsorption-desorption cycle. This bimodal behaviour, with UTL (Si/Ge = 2.5) and UTL (Si/Ge = 4.5) collapsing upon water adsorption on one hand and UTL (Si/Ge = 18.5) and UTL (Si/Ge = 53) being resistant on the other, implies the existence of critical Si/Ge which delimitates hydro-labile Ge-rich **UTL** from hydrolytically stable Ge-poor **UTL**.

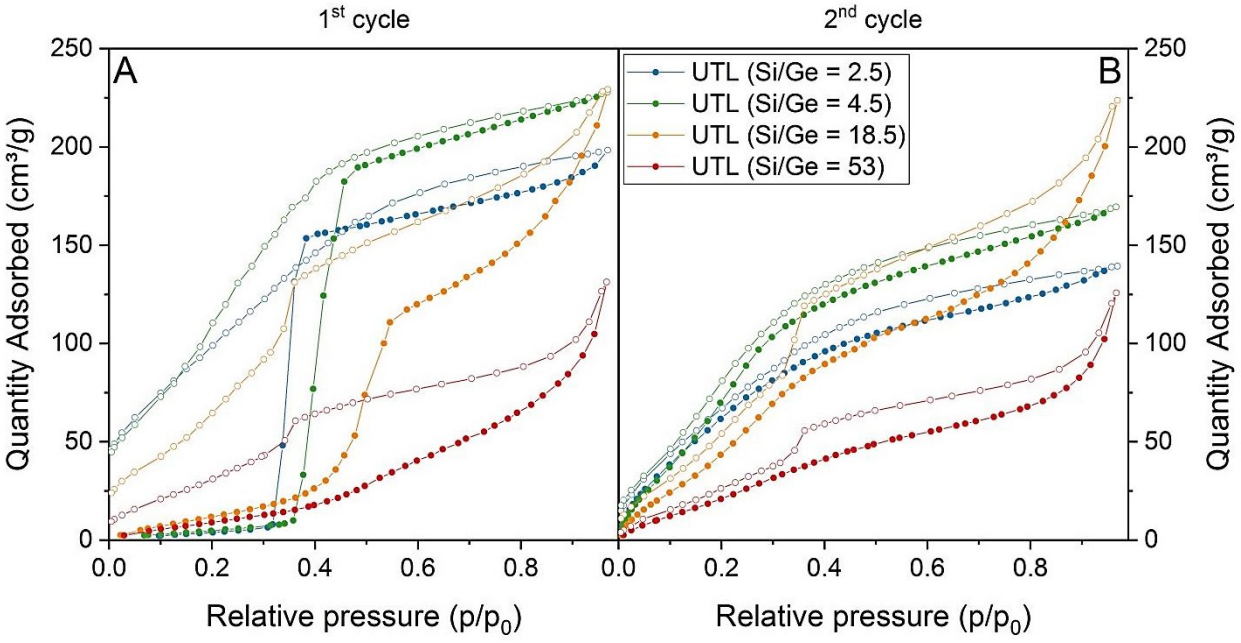

Figure 16: 1st and 2nd cycle of water vapour adsorption-desorption on UTL samples with varying Si/Ge ratio.

The second adsorption-desorption cycle of water vapour provided type I and II isotherms for all samples (Figure 16B). The higher adsorption at low pressure indicates that hydrophilicity of the materials increased after the first cycle. We theorized that the materials became more hydrophilic as a result of hydrolysis of the labile Ge-O bonds in the D4Rs. The hydrolysis of the Ge-O bonds produces two polar Ge(OH) or Si(OH) groups and thereby increases the hydrophilicity of the material. The adsorption isotherms also showed no unclosed hysteresis, meaning that the water adsorption was fully reversibly during the second cycle.

Table 5: Textural properties of the **UTL** samples before and after 1st and 2nd cycle of water vapour adsorption.

	BET (m^2/g)	**V_{micro} (cm^3/g)**	**V_{total} (cm^3/g)**
UTL (Si/Ge = 2.5)	497	0.21	0.24
1st cycle	203	0.09	0.10
2nd cycle	212	0.09	0.10
UTL (Si/Ge = 4.5)	504	0.22	0.24
1st cycle	327	0.15	0.16
2nd cycle	312	0.14	0.15
UTL (Si/Ge = 18.5)	327	0.13	0.24
1st cycle	296	0.12	0.22
2nd cycle	293	0.12	0.22
UTL (Si/Ge = 53)	150	0.07	0.13
1st cycle	136	0.05	0.12
2nd cycle	137	0.05	0.13

Further analysis of the adsorption isotherms from the first cycle revealed that the number of reversibly adsorbed molecules (Phase I) decreased linearly with the number of germanium atoms per unit cell (Figure 17A). The germanium is the source of the framework lability. Therefore, increasing germanium content also raises the susceptibility of the framework to hydrolytic attack and hence reduces its ability to reversibly adsorb water without undergoing structural changes. In addition, the number of irreversibly bound water molecules (after the adsorption-desorption cycle) also varied with the germanium content of the zeolite (Figure 17B). Higher germanium content leads to higher number of water molecules consumed by the Ge-O bond breaking. Nevertheless, the irreversibly adsorbed water amount showed logarithmic dependence on the germanium content suggesting that the relationship is more complex. We hypothesized that the arrangement of the germanium within the D4Rs affects the number of water molecules required for the hydrolysis.

The Si/Ge ratio also affected the relative pressure range at which the major water uptake (Phase II) occurred. The critical relative pressure increased from 0.35 in UTL (Si/Ge = 2.5) to 0.42 in UTL (Si/Ge =53). We calculated the Polanyi adsorption potential distributions from the isotherms in order to quantify the difference between individual samples more accurately. [122] The maximum of the adsorption potential distribution shifted toward lower values with the increasing Si/Ge molar ratio, implying weaker interaction between the adsorbed water and the zeolite (Figure 17C). The adsorption potential distribution of the UTL (Si/Ge = 2.5) resembled narrow Gaussian curve indicating relative homogeneity of the adsorption sites. In contrast, the distribution curves of samples with higher Si/Ge contained shoulders or additional peaks meaning the adsorption sites are more energetically

heterogeneous. The heterogeneity of the adsorption sites in the samples with Si/Ge from 4.5 to 53 likely originates from uneven distribution of the germanium within the D4Rs.

While UTL (Si/Ge = 2.5) contains enough germanium to fill all the D4R positions with germanium, samples with Si/Ge = 4.5 and lower contain both germanium and silicon in the D4R framework positions. Different arrangements of silicon and germanium within the D4Rs create energetically heterogeneous sites. [72, 76]

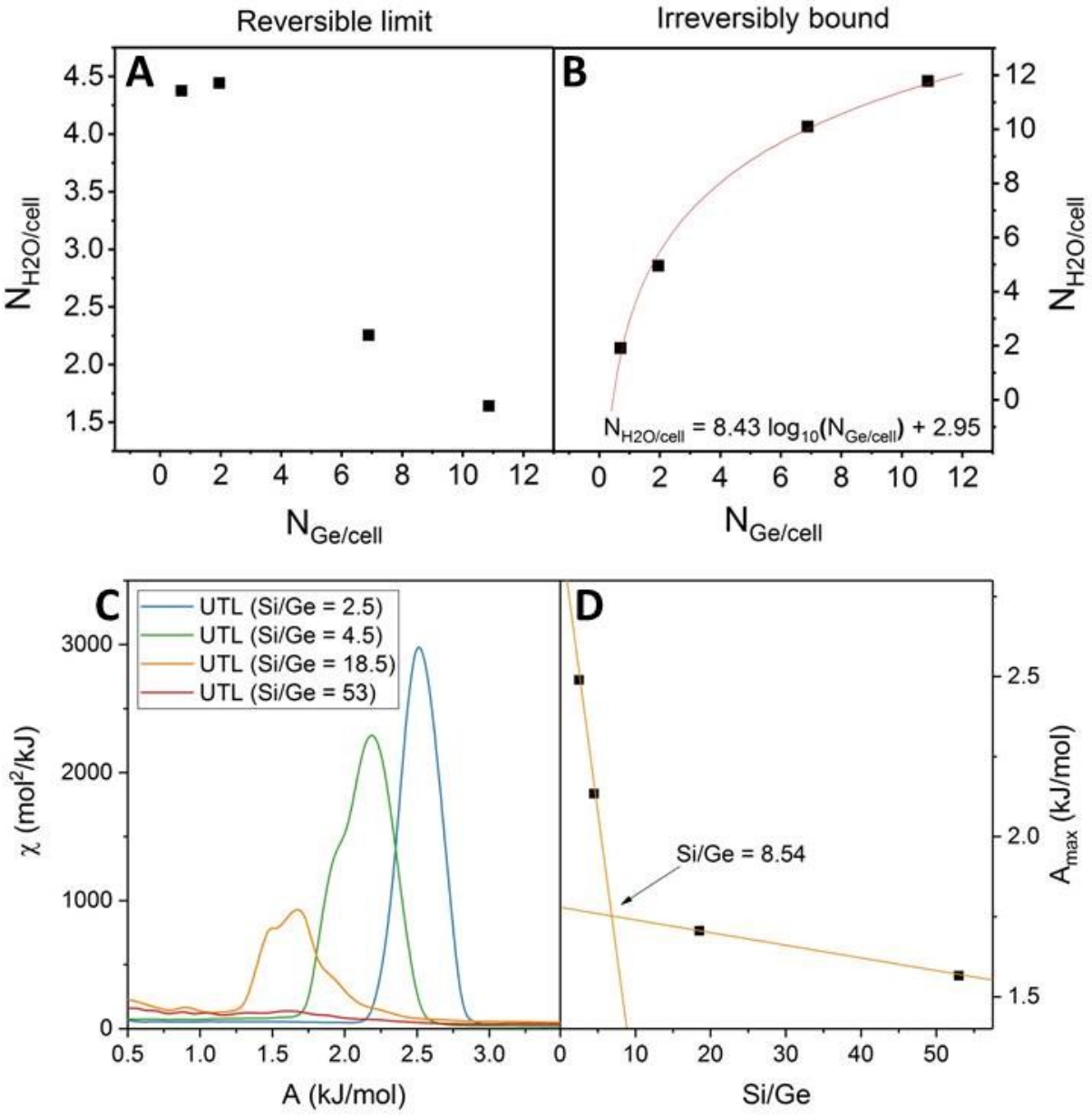

Figure 17: A) Number of reversibly and B) irreversibly adsorbed water molecules as a function of the number of germanium atoms per unit cell; C) adsorption potential distributions of water on **UTL**; D) maxima of adsorption potential distributions against Si/Ge of the sample.

We plotted the maxima of the adsorption potential distributions against the Si/Ge ratio of the samples to show the relation between the relative strength of water adsorption and Si/Ge (Figure 17D). The graph showed a striking difference between the Ge-rich and Ge-poor **UTL** samples. On one hand, the

Ge-rich samples showed strong dependence of the maximum potential value on the Si/Ge. On the other hand, the potential maxima of the Ge-poor samples showed significantly lower dependence. We interpolated the values by a linear fits, which intersected at Si/Ge = 8.54 corresponding to approximately four germanium atoms per D4R. Minimum of four germanium atoms in suitable positions in the D4R are required for successful hydrolysis and separation of the **UTL** into isolated layers. Our results confirm that assumption by showing that Si/Ge = 8.54 is the borderline between hydro-labile Ge-rich and hydrolytically stable Ge-poor **UTL**.

5.3. Slow Disassembly of **UTL** germanosilicate

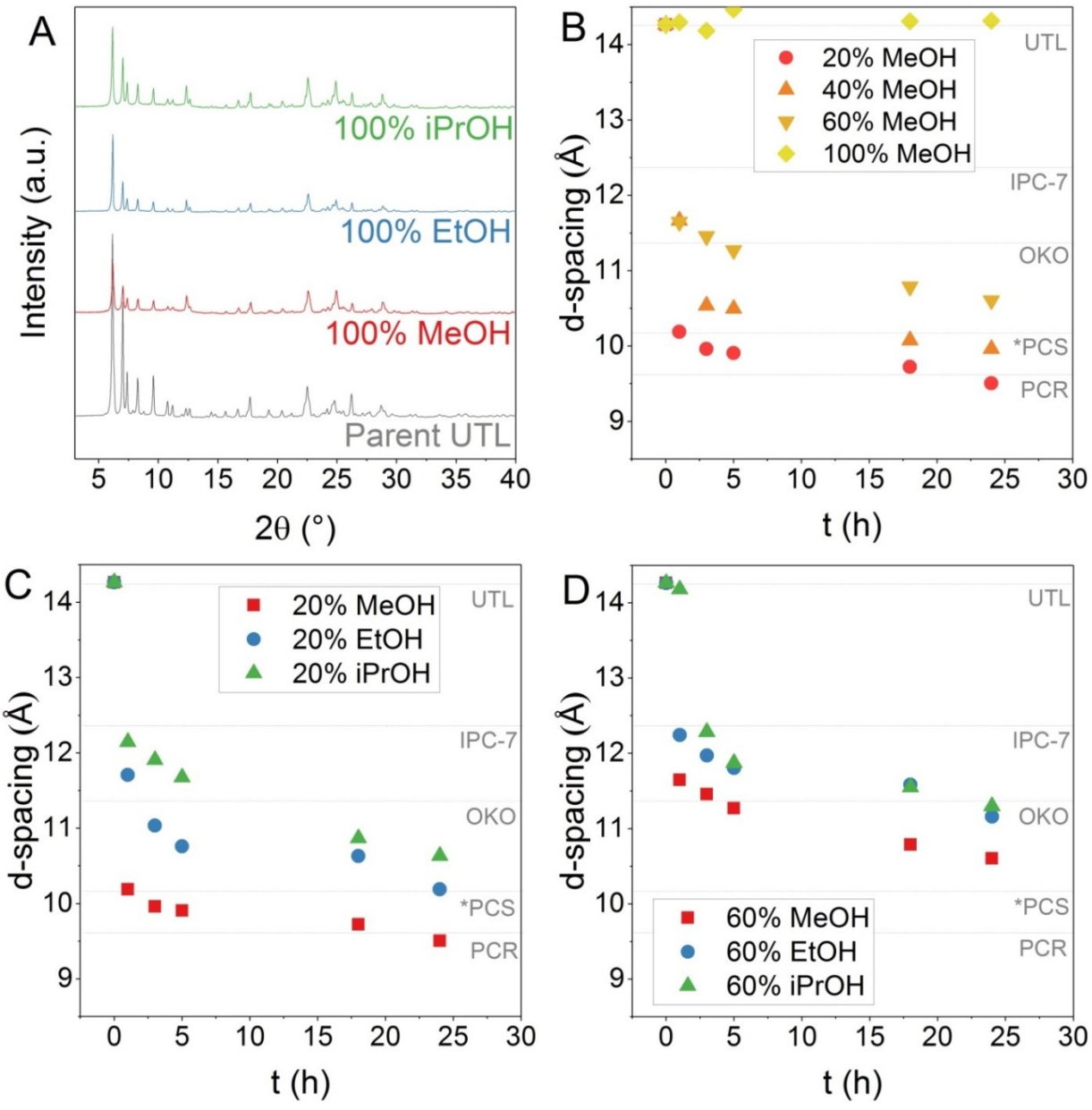

Figure 18: A) XRD patterns of **UTL** treated with pure alcohols for 24 h at 60°C; B) evolution of the d-spacing of **UTL** treated with methanol solution of varying concentrations and in C) 20 % and D) 60 % alcohols.

In the subsequent study we developed a method for controlling the rate of hydrolysis (disassembly) of the **UTL** germanosilicate. The hydrolysis typically proceeds rapidly in water or water-based solution of acid, transforming the **UTL** into the layered IPC-1P within several minutes. The rapid disassembly makes it difficult to control or study. We used **UTL** zeolite with Si/Ge = 4.5 (characterization provided in 5.2.2.) and attempted the disassembly in alternative media including pure alcohols. Treatment with 100 % methanol, ethanol and i-propanol did not cause any structural transformation (Figure 18A) as a result of their lower proton donating ability compared with water. The transformation of **UTL** into the layered precursors is most notably reflected by shift of the 200 reflection in the powder XRD from 6.14° 2 theta to higher values. However, no such shift occurred during the 24h treatment with pure alcohols suggesting the disassembly has been completely suppressed.

Since we observed no disassembly in pure alcohols we hypothesized that diluting the alcohol with defined amount of water would create a solution in which the hydrolysis would proceed in reduced rate correlated with the water content. We prepared solutions of 60, 40 and 20 % methanol and used them for new set of experiments to test the hypothesis. The 200 reflections of the collected samples progressively shifted to higher 2θ values. The evolution of d-spacing calculated from the 200 reflection positions of the calcined samples is depicted in Figure 18B. All experiments showed gradual decrease of d-spacing over 24 h with significantly reduced rate compared to disassembly in water. The solution of 20 % methanol caused the most rapid disassembly of the **UTL** producing IPC-1P after 24 h and subsequently **PCR** zeolite upon calcination. Solutions of 40 and 60 % methanol also caused a disassembly of the **UTL** to layered precursors but with slower rate leading to structures close to IPC-6 (***PCS**) zeolite (Scheme 3).

Table 6: Textural properties of the samples of **UTL** treated with pure i-propanol at 60°C determined by argon adsorption.

Time	BET (m^2/g)	S_{ext} (m^2/g)	V_{tot} (cm^3/g)	V_{mic} (cm^3/g)
/ (parent UTL)	526	41	0.23	0.22
1 h	374	40	0.17	0.16
3 h	326	46	0.15	0.13
5 h	337	41	0.15	0.14
18 h	325	42	0.15	0.13
24 h	319	39	0.15	0.13

The type of the alcohol also affected the rate of the disassembly. The solutions of methanol provided the fastest rate of disassembly followed by ethanol and i-propanol (Figure 18C,D). For example, the d-spacing of zeolite treated with 20% solution of methanol decreased to 9.5 Å after 24 h. In contrast, samples treated with 20% ethanol and i-propanol displayed d-spacing 10.2 and 10.6 Å, respectively. We hypothesized that the kinetic diameter of the alcohol (MeOH (3.6 Å) ≪ EtOH (4.4 Å) < iPrOH (4.7 Å)) may affect the solvation of the leeched Ge species or that the polarity of the alcohol (MeOH (0.76) > EtOH (0.65) > iPrOH (0.55)) may decrease the solubility of the leeched germanium species and thus impede its diffusion from the interlayer space. Alternatively, the acidity of the

respective alcohols may be responsible (pK_a (MeOH) = 15.5 < pK_a (EtOH) = 15.9 < pK_a (iPrOH) = 16.5). [135]

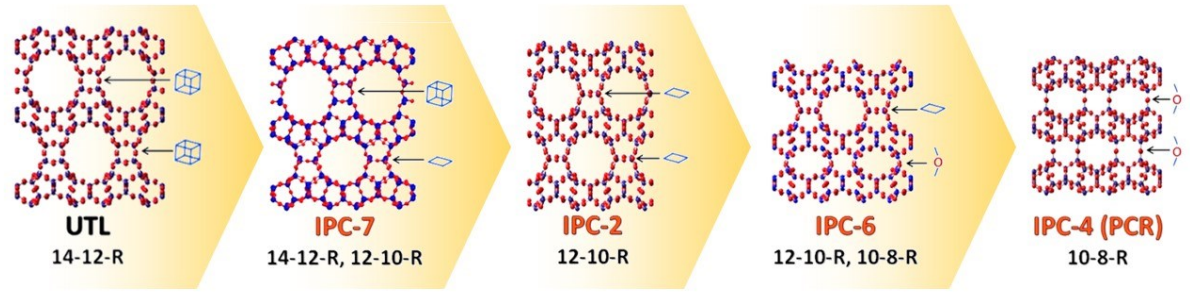

Scheme 3: Slow transformation of **UTL** to IPC-7, IPC-2 (**OKO**), IPC-6 (***PCS**) and IPC-4 (**PCR)** by gradual reduction of the pore size.

The solutions of alcohols with water enabled to decelerate disassembly of the **UTL** which consists of removal of Ge from the framework and gradual reduction of d-spacing and pore size of the zeolite. However, the collected samples suffered from poor textural properties, particularly low pore volumes, due to deposition of the leeched Ge species inside the zeolite channels (Table 6). The leeched germanium formed germanium oxide/hydroxide species which poorly dissolves in the water-alcohol solution. The poor solubility resulted in deposition of the germanium species in the micropores and subsequent blockage of the channel system. In order to tackle this issue, we replaced the water-alcohol solution with water-free solution of HCl in EtOH. The HCl/EtOH reacted with the leeched germanium to form germanium alkoxychlorides and germanium tetrachloride. These compounds are highly soluble in the mixture and therefore do not cause pore blockage in the produced materials. Simultaneously, the HCl/EtOH solution exhibited analogous behaviour to the water-alcohol system, enabling gradual shift of the 200 reflection towards higher values and corresponding decrease in d-spacing of the sample over 16 days (Figure 19A,B).

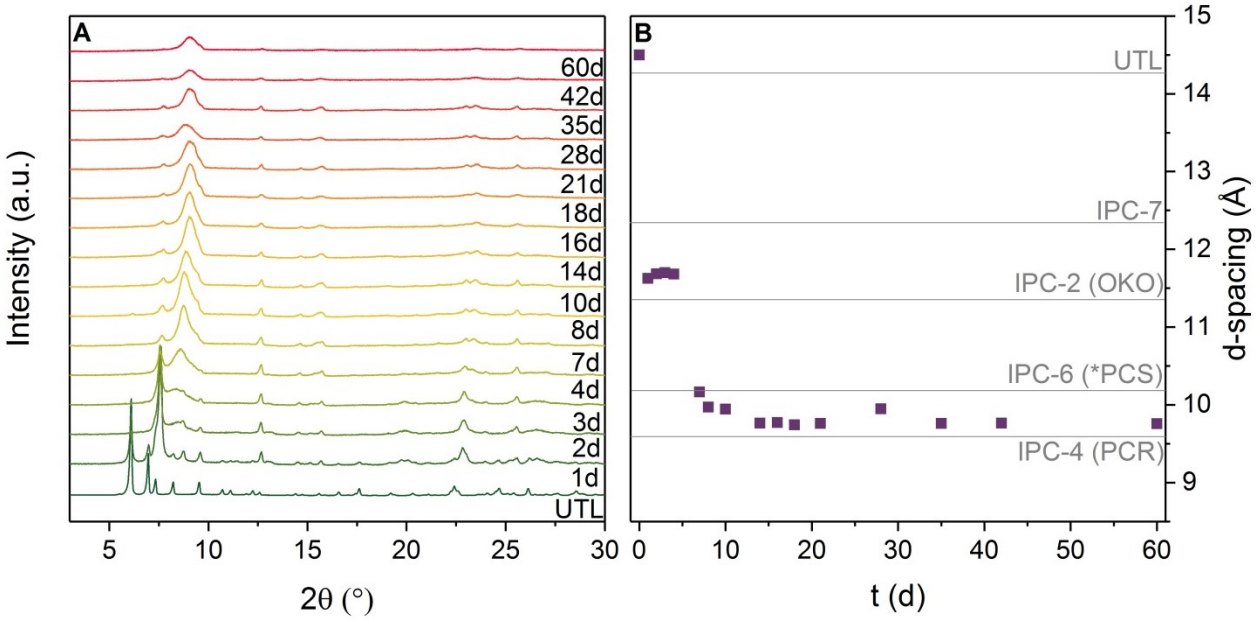

Figure 19: Evolution of A) powder XRD patterns and B) evolution of d-spacing of the samples recovered from hydrolysis of **UTL** in 1.25 HCl/EtOH solution at 0 °C.

The argon adsorption analysis also confirmed the reliability of the method. Each sample provided type I isotherm typical for purely microporous materials. The BET area and micropore volume of the collected samples showed a steady declining trend between 0 and 20 days of the treatment reflecting the gradual decrease of the pore diameter of the produced zeolite. The zeolite structure and pore volume ceased to change after 20 days of treatment. We theorised that at that point, the system reached equilibrium between the leeching of the framework germanium and reinsertion of the leeched germanium from the solution into the structure. This suppresses further structural transformation and provides a material with structure resembling those of **PCR** and IPC-6frameworks.

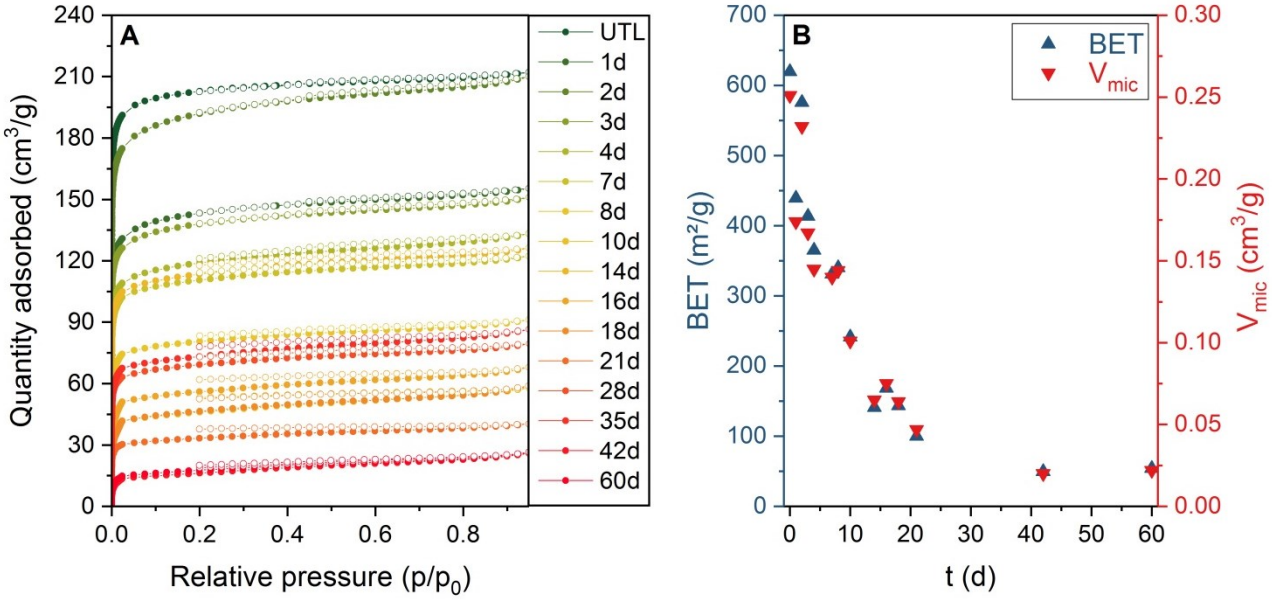

Figure 20: A) Argon adsorption isotherms and B) evolution of BET and micropore volume of the samples recovered from hydrolysis of **UTL** in 1.25 HCl/EtOH solution at 0 °C.

The replacement of water-alcohol solutions with HCl/EtOH thus provided a means to gradually decrease the pore size of **UTL** (Scheme 3) and transform it into daughter zeolites with higher Ge content (i.e. **UTL** (Si/Ge = 4.5) < IPC-7 (Si/Ge = 6.3) < **OKO** (Si/Ge = 8.0) < ***PCS** (Si/Ge = 16.0)) compared to the conventional ADOR transformation (Si/Ge = 80−100) but with similar structural and textural properties. [83, 111]

5.4. Reverse ADOR – reconstruction of **UTL** framework from IPC-1P

Subsequently, we focused on development of "reverse ADOR" transformation of the layered precursor IPC-1P to the three-dimensional **UTL** zeolite. The disassembly of **UTL** zeolite into the layered precursor IPC-1P is accompanied by decrease in the d-spacing between the *pcr* layers from 14.4 Å in the **UTL** to 10.5 Å in the IPC-1P. This manifests as a shift of the interlayer 200 reflection in the XRD pattern from 6.14°to 8.41°. Prolonged treatment may result in re-insertion of the leeched Si species in between the layers and subsequent rearrangement of the IPC-1P to IPC-2P with d-spacing 11.8 Å. [112, 136] Nevertheless, the d-spacing never increases to the original distance of the **UTL** thereby preventing restoration of the structure. Therefore, we aimed to increase the d-spacing artificially in order to make the reconstruction possible.

5.4.1. Expansion of interlayer space

Previous studies have demonstrated that the interlayer spacing of layered materials, including 2D zeolite precursors, can be altered by intercalation of organic agents, most commonly cetyltrimethylammonium, into the interlayer space. [137-139] However, the surfactant molecules with long hydrocarbon chains are flexible and the spacing they provide is sensitive to pH of the environment. It may produce disorders or uneven spacing. Ergo, in our study we chose to use more rigid intercalating agents such as tetrabutylammonium cations.

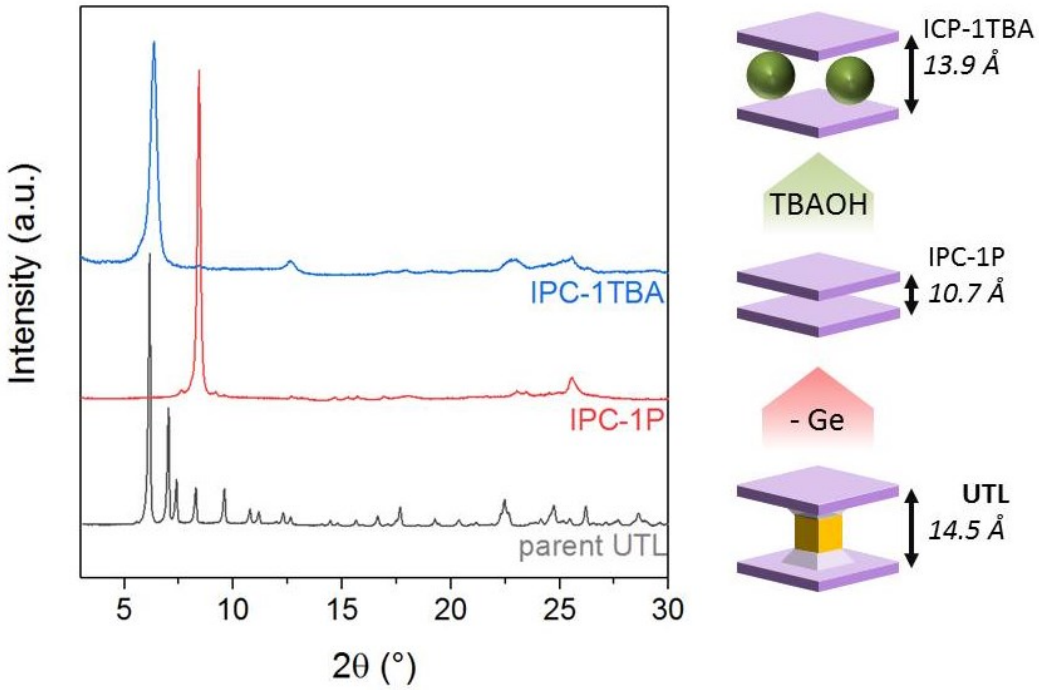

Figure 21: powder XRD patterns of the **UTL** hydrolysis to layered IPC-1P and its intercalation with TBAOH.

The intercalation of tetrabutylammonium hydroxide into the IPC-1P increased its d-spacing from 10.5 to 13.9 Å reflected by shift of the 200 diffraction peak from 8.41 to 6.37° 2θ (Figure 21). The d-spacing of the intercalated material (labelled as IPC-1TBA) is relatively close to that of **UTL** zeolite.

Nevertheless, the intercalation suffered from poor yields and quality of the material as a result of the basic environment during the intercalation. The basic pH is necessary in order to deprotonate the IPC-1P layers and to break the H-bonds between them. However, it also causes desilication of the material. The desilication removes silicon atoms from the framework and creates defects in the material. This method is commonly used for introduction of mesopores into zeolites to enhance their external surface area. However, in our case it detrimentally affects the quality of the material causing a decrease and eventually complete loss of crystallinity.

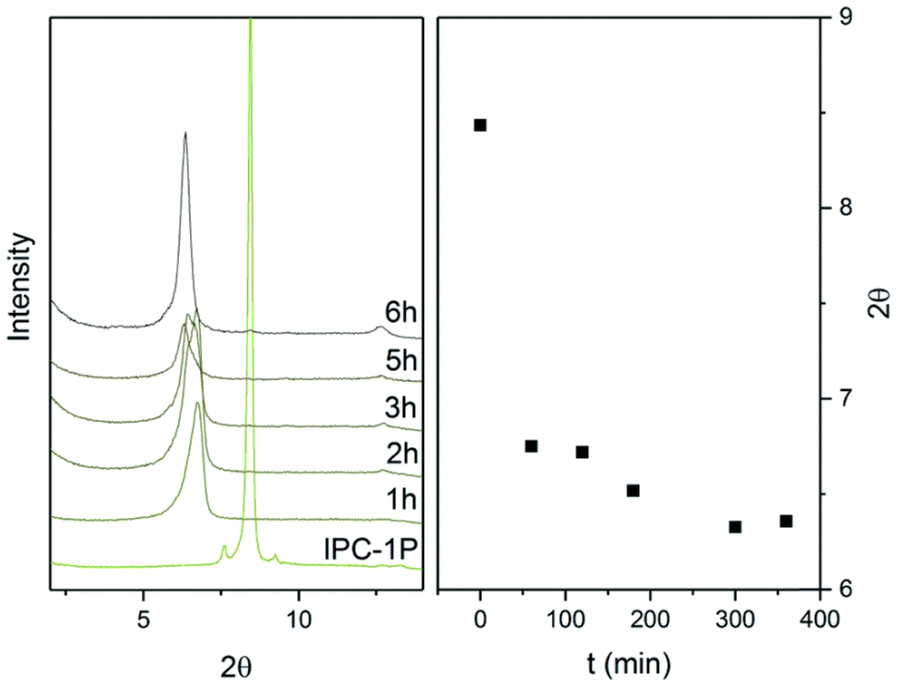

Figure 22: Powder XRD patterns and positions of 200 diffraction lines of the intercalated material as a function of time.

One way for tackling this obstacle includes minimising the contact time of the material with the solution. Our results showed that the position of 200 reflection of the intercalated material gradually increases with treatment time up to 6 hours (Figure 22). After 6 hours of the treatment, the peak position remains constant implying that the intercalation is complete. In essence, longer treatment does not improve the spacing of the IPC-1TBA but only results in deterioration of the crystallinity of the material.

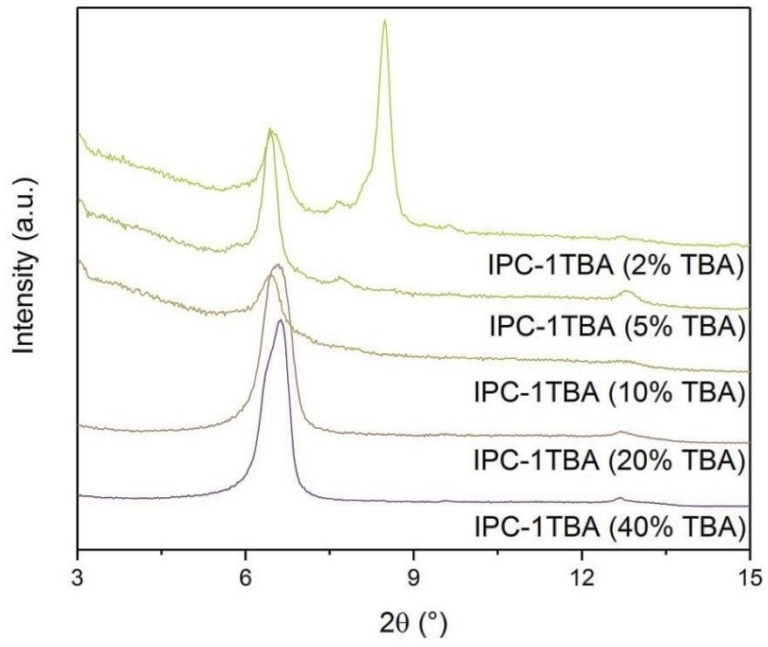

Figure 23: powder XRD patterns of IPC-1P samples intercalated with TBAOH of varying concentrations.

Second, we optimised the concentration of the TBAOH solution (Figure 23). We performed the intercalation with solutions with TBAOH content from 40 to 2 %. Intercalation with 40, 20 and 10 % solution of TBAOH resulted in the IPC-1TBA with d-spacing of 13.9 Å (6.37° 2θ). The 5 % solution also showed a reflection at the same angle; however, another interlayer reflection near 7.1° appeared suggesting incomplete intercalation. The decreasing the TBAOH concentration to 2 % resulted in splitting of the interlayer reflection into two at 6.37° and 8.41°.

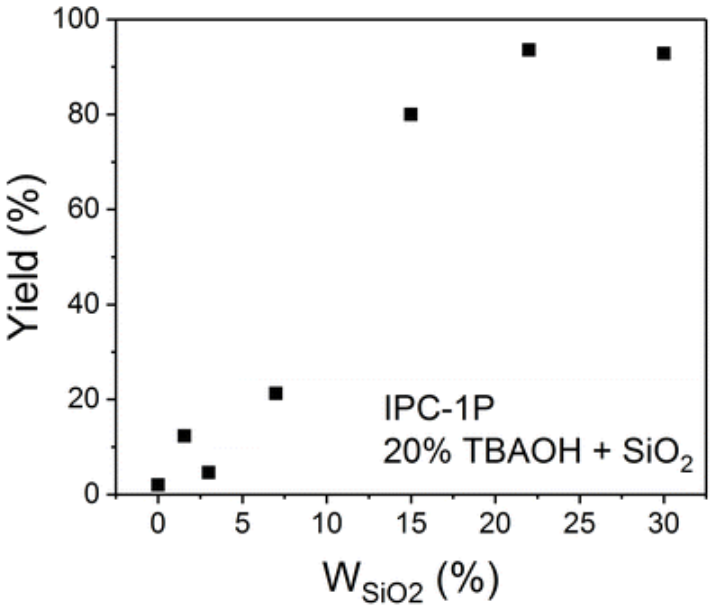

Figure 24: Dependency of the yield of the IPC-1TBA ($m_{IPC\text{-}1TBA}/m_{IPC\text{-}1P}$) on silica content in the solution.

Last but not least, we countered the dissolution of the material by adding colloidal silica into the TBAOH solution. The additional silica saturated the solution with Si species prior to the intercalation. The presence of the Si species in solution changed the chemical equilibrium of the system and decreased the rate of IPC-1P dissolution. We performed a set of intercalation experiments with different SiO_2 content in the mixture to find the optimal concentration. The yield of the intercalated material increased proportionally to the SiO_2 content in the mixture up to 20 % SiO_2 (Figure 24). The mixture with 20 % SiO_2 provided near 100 % yield of the solid (i.e. $m_{IPC\text{-}1TBA}/m_{IPC\text{-}1P}$) and further addition of the colloidal silica did not cause any changes to the yield. Nevertheless, we speculate that excess SiO_2 content may result in deposition of amorphous silica onto the material and interfere with subsequent experiments. Therefore, we settled for 15 % SiO_2 in the solution which provided 80 % yield of the solid but should minimise the silica deposition.

5.4.2. Reconstruction of D4R units

The IPC-1TBA possesses d-spacing similar to that of **UTL** structure but it lacks interlayer connections, the D4Rs. Therefore, the second step in the restoration of the **UTL** structure involves reconstructing the D4R between the layers. We explored several different methods for formation or introduction of the D4Rs into the interlayer space including stabilisation with germanium, stabilisation with fluoride anions and connection with polyhedral silsesquioxanes (POSS).

Stabilisation with germanium

Numerous zeolites with D4R in their structure, including the **UTL**, crystalize as germanosilicates. The germanium can stabilise strained building units such as D4Rs or D3Rs in the zeolite and thereby facilitate the formation of such zeolites. [87] Moreover, cubic precursors to D4R units form in the zeolite synthesis mixture upon addition of germanium almost instantly. [95] Therefore, germanium was a good candidate for reconstruction of the D4R units in between the IPC-1TBA layers.

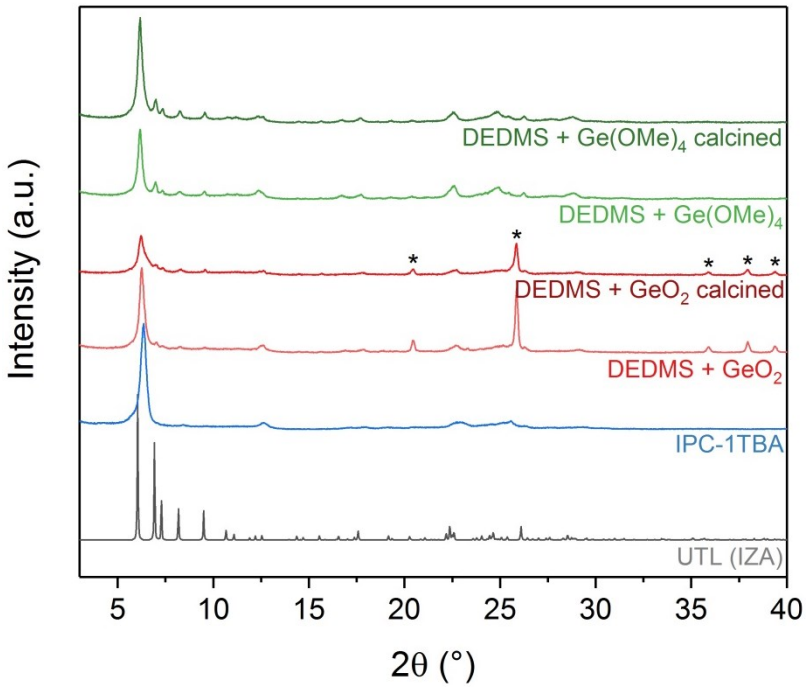

Figure 25: Powder XRD patterns of **UTL** samples stabilised by mixture of DEDMS and germanium oxide or germanium methoxide. Asterisks (*) mark the reflections of GeO_2 phase.

The Ge-O bonds are prone to hydrolytic attack in aqueous environment; therefore, we carried out the reconstruction under anhydrous conditions, using a solution of HCl in ethanol, to protect the newly formed Ge-O bonds from hydrolysis. We tested germanium oxide and germanium methoxide as sources of germanium in combination with diethoxydimethylsilane (DEDMS) in 1:1 molar ratio for the reconstruction. We subsequently calcined the materials to remove the TBA cations. Both Si-Ge mixtures succeeded in restoring the D4R units and the **UTL** structure as evidenced by the powder XRD patterns (Figure 25). The 200 reflection shifted from 6.37° to 6.16° 2θ and new reflections characteristic for the **UTL** framework appeared at 6.99°, 7.35°, 8.27°, 9.55°, 16.7° and 17.7° 2θ. In addition, the XRD pattern of the sample prepared using germanium oxide also showed reflections at 20.4°, 25.8°, 35.9°, 37.9° and 39.4° typical for GeO_2. The **UTL** reflections were also less intense than in the sample reconstructed using germanium methoxide. The low intensity of the reflections and formation of GeO_2 suggests that only portion of germanium successfully incorporated into the zeolite while the rest precipitated as separate GeO_2 phase. The poor incorporation may stem from the lower reactivity or solubility of the germanium oxide in the mixture compared to the germanium methoxide. In contrast, the reactive germanium methoxide incorporated into the zeolite and successfully restored the D4R units without forming the GeO_2 phase.

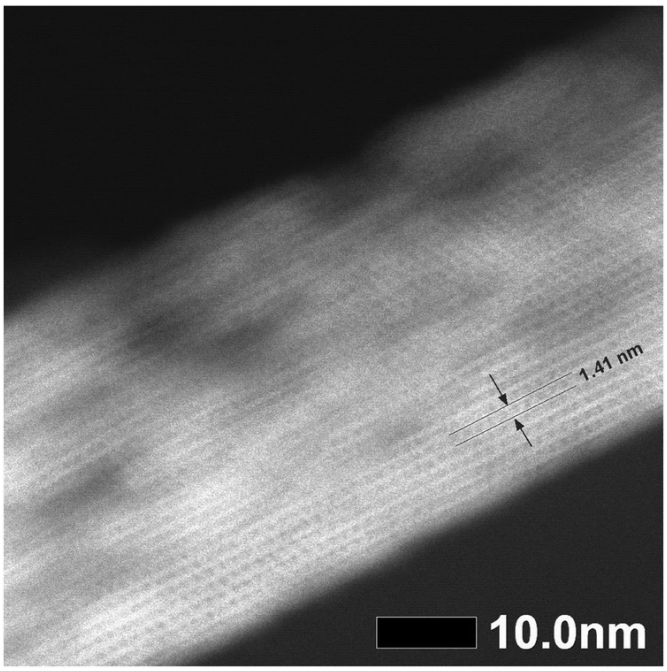

Figure 26: STEM image of the reconstructed **UTL** zeolite rec Si-Ge 1:1

The STEM imaging of the sample reconstructed with DEDMS and germanium methoxide in Si:Ge ratio 1:1 (labelled "rec Si-Ge 1:1") verified that the layers reconnected successfully (Figure 26). The image shows the periodically organised connections between zeolite layers with the uniform spacing 14.1 Å characteristic for the **UTL** structure. The image also shows irregular mesopores in the zeolite crystal introduced by the basic conditions during the intercalation. The mesopore formation is also apparent from the change of textural properties of the reconstructed material (Table 7).

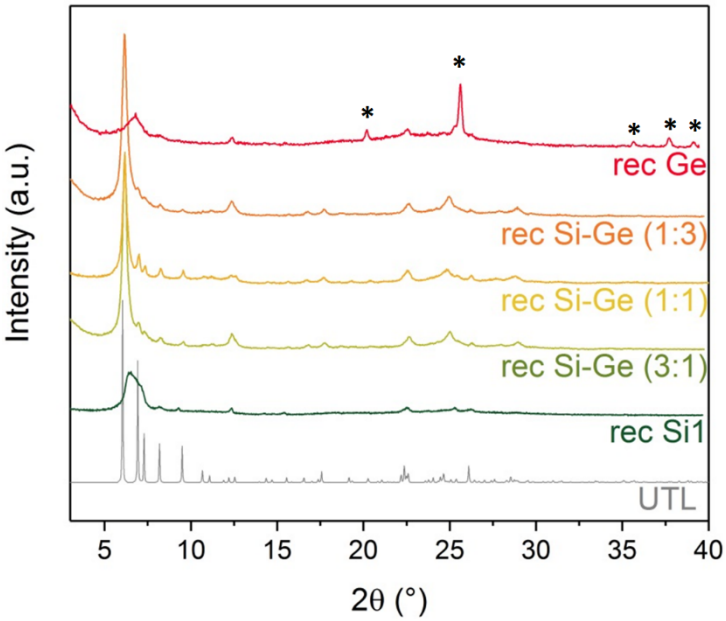

Figure 27: Powder XRD patterns of samples reconstructed using different Si:Ge ratios. Asterisks (*) mark the reflections of GeO_2 phase.

We have demonstrated that the mixture of silicon and germanium sources can restore the D4R units and the **UTL** zeolite. However, it is not clear how much germanium is necessary for the successful reconstruction. Therefore, we carried out additional set of experiments and varied the ratio of Si and Ge sources. The XRD patterns of the obtained samples (Figure 27) revealed that ratios of Si:Ge from 1:3 to 3:1 restored the **UTL** framework. The sample with Si:Ge 1:1 possessed the highest crystallinity and micropore volume 0.15 cm^3/g, the closest to the parent sample with 0.25 cm^3/g (Table 7). The samples with Si:Ge 3:1 and 1:3 exhibited lower volumes of micropores 0.12 and 0.11 cm^3/g, respectively. All three samples exhibited Type II isotherms with hysteresis loops between p/p_0 0.45 and 1 (Figure 28A) and external surface area from 156 to 188 m^2/g in contrast to the parent **UTL** with external surface 52 m^2/g. The increased external surface and the shape of the isotherm stems from the presence of mesopores resulting from the intercalation.

In contrast, the XRD of sample reconstructed in the absence of germanium (rec Si1) showed a broad reflection around 7° signifying non-uniform layer ordering. This experiment proves that the presence of germanium is essential for the reconstruction. However, the sample reconstructed using purely germanium source (rec Ge) also failed to produce the **UTL** structure. On top of that, its XRD pattern also contained additional reflections of GeO_2. It demonstrates that silicon is also necessary for the reconstruction of D4Rs. It is possible that the absence of Si leads to rapid formation of low reactive GeO_2 prior to the D4R reconstruction or that the pure Ge D4Rs are unstable upon calcination.

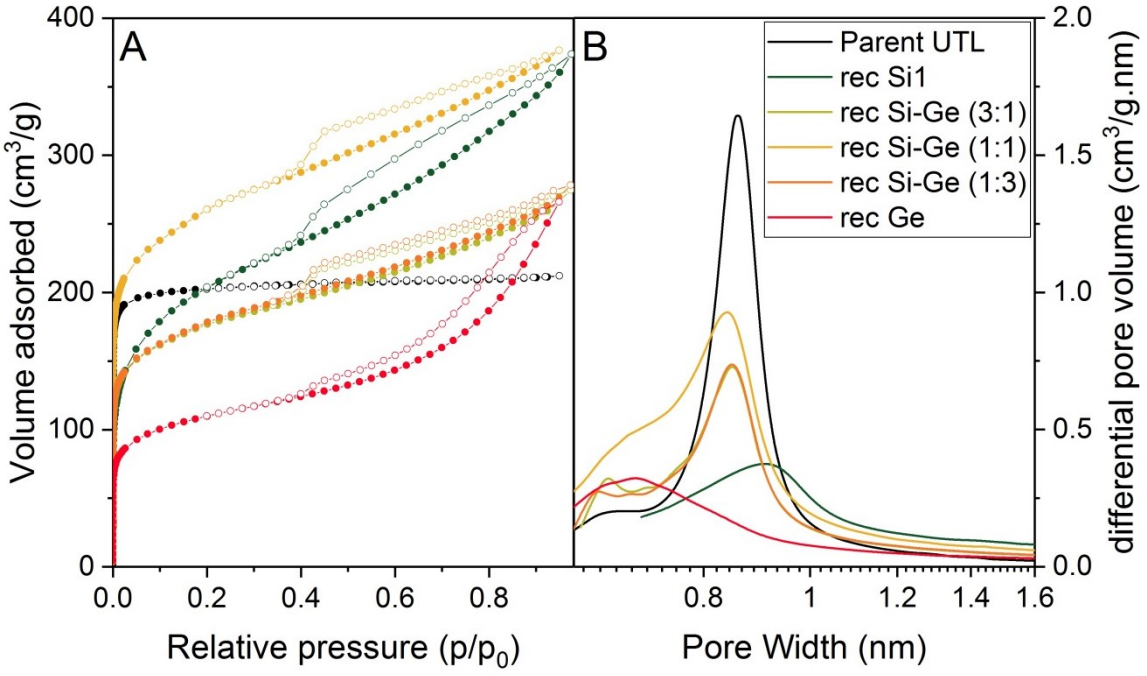

Figure 28: A) argon adsorption–desorption isotherms and B) H–K micropore size distributions of samples reconstructed using different Si:Ge compositions

Table 7: Textural properties of samples reconstructed using different Si:Ge compositions determined by argon adsorption

	BET (m^2/g)	**S_{ext} (m^2/g)**	**V_{tot} (cm^3/g)**	**V_{mic} (cm^3/g)**
Parent UTL	620	52	0.27	0.25
rec Si1	645	334	0.48	0.12
rec Si–Ge (3 : 1)	550	156	0.35	0.12
rec Si–Ge (1 : 1)	808	188	0.48	0.15
rec Si–Ge (1 : 3)	555	165	0.36	0.11
rec Ge	344	139	0.34	0.07

rec Si1 = UTL recostructed with Si source; rec Si-Ge (x:y) = UTL recostructed with Si and Ge sources in x:y molar ratio; rec Ge = UTL recostructed with Ge source.

Stabilisation with fluorides

Besides germanium, fluoride anions are also capable of stabilising cubic D4R units. [140] Numerous extra-large pore zeolites with D4R in their structure, including ***CTH**, **ITH** or **SOR**, crystalize from fluoride gels. [141-143] Accordingly, we performed another set of experiments with **UTL** reconstruction from IPC-1TBA in synthesis mixtures. We used DEDMS, germanium methoxide and mixture of DEDMS and germanium methoxide with Si:Ge 1:1 for reconstruction of the D4Rs. NH_4F was added to each mixture to promote the D4R formation. We verified the crystal structure of the obtained samples by powder XRD. The XRD patterns of all samples exhibited the typical reflections of the **UTL** framework regardless of the Si:Ge composition. This demonstrates that the fluoride anions can stabilise D4Rs during the reconstruction irrespectively of the presence of germanium. Nevertheless, the fluoride anions do not enhance the germanium incorporation into the framework. The sample reconstructed purely with germanium methoxide in the presence of fluoride (labelled “rec F Ge”) also showed reflections of GeO_2 phase implying that significant portion of the germanium failed to incorporate into the structure.

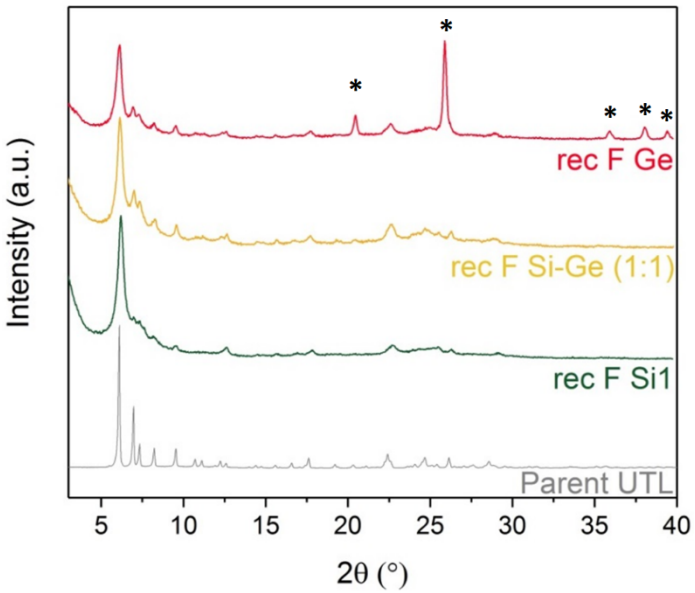

Figure 29: Powder XRD patterns of samples reconstructed using fluoride anions and different Si:Ge ratios. Asterisks (*) mark the reflections of GeO_2 phase.

The samples after fluoride-assisted reconstruction exhibited type II adsorption isotherms (Figure 30) and external surface areas ranging from 101 to 341 m^2/g reflecting the presence of mesopores induced during the intercalation treatment (Table 8). However, the samples reconstructed using fluoride also show significantly lower micropore volumes ranging from 0.05 to 0.07 cm^3/g compared to the samples reconstructed using germanium. The fluoride solutions can etch the zeolite and create vacancies in the framework. The presence of fluorides during the reconstruction likely causes etching which results in the formation of additional defects and overall decrease in crystallinity of the material. The decrease in the crystallinity manifests in the low micropore volumes of the reconstructed samples.

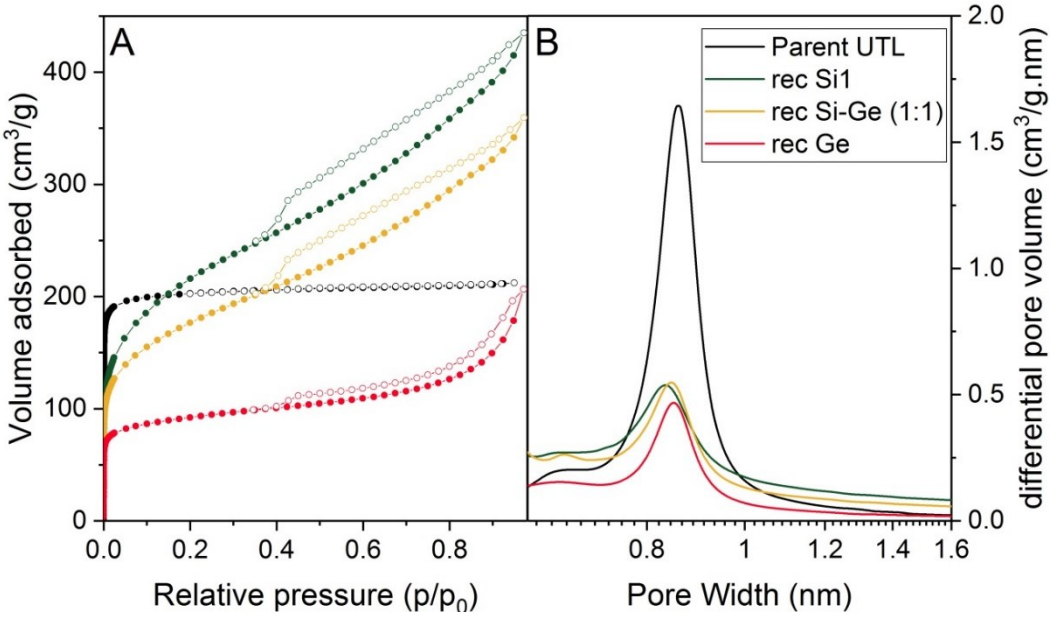

Figure 30: A) argon adsorption–desorption isotherms and B) H–K micropore size distributions of samples reconstructed using fluoride anions and different Si:Ge ratios.

Table 8: Textural properties of samples reconstructed using fluoride anions and different Si:Ge ratios determined by argon adsorption.

	BET (m^2/g)	S_{ext} (m^2/g)	V_{tot} (cm^3/g)	V_{mic} (cm^3/g)
Parent UTL	620	52	0.27	0.25
rec F Si1	691	341	0.56	0.05
rec F Si–Ge (1 : 1)	555	281	0.46	0.06
rec F Ge	280	101	0.26	0.07

rec F Si1 = UTL recostructed with Si source and NH_4F; rec F Si-Ge (1:1) = UTL recostructed with Si and Ge sources in 1:1 molar ratio and NH_4F; rec F Ge = UTL recostructed with Ge source and NH_4F.

Connection with POSS

Using pre-made building blocks, such as polyhedral oligomeric silsesquioxanes (POSS), is a potential alternative to reconstructing the D4Rs within the interlayer space. POSS are cage-like silicate-organic species with general formula $(RSiO_{3/2})_n$ which can take form of various shapes, including $(RSiO_{3/2})_8$ cubes (Scheme 4). We hypothesised that the POSS can intercalate in between the IPC-1TBA layers and connect the layers similarly to the new D4Rs reconstructed using germanium or fluoride route.

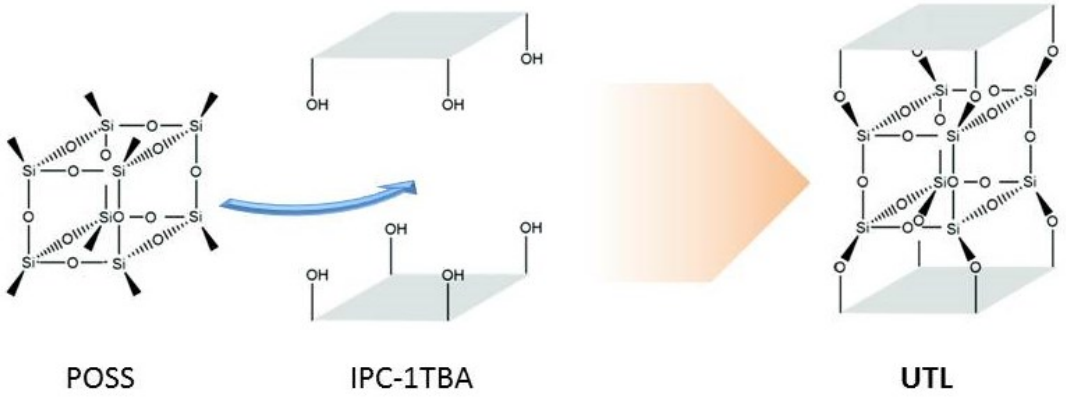

Scheme 4: Intercalation of the POSS in between the IPC-1TBA layers and reconstruction of the **UTL**

We performed the reconstruction of **UTL** zeolite from IPC-1TBA using silicon sources with varying complexity; diethoxydimethyl silane (DEDMS), 1,3-diethoxy-1,1,3,3-tetramethyl-disiloxane (DETMDS), 2,4,6,8-tetramethylcyclotetrasiloxane (TMCTS) and octamethylsilsesquioxane (POSS). The experiments were carried out in the absence of germanium or fluoride anions to assess solely the ability of the silicon source to reconnect the layers. The powder XRD patterns of samples rec Si1 and rec Si2 reconstructed using DEDMS and DETMDS, respectively, exhibited a broad reflection around 7° 2θ (Figure 31). The broadened reflection indicates poor layer ordering resulting from unsuccessful D4R reconstruction. In contrast, samples rec Si4 and rec Si8 reconstructed using TMCTS and POSS, respectively, retained relatively narrow interlayer 200 reflection at 6.16° 2θ. The samples also showed less intense reflections at 6.99°, 7.35°, 8.27° and 9.55° characteristic for the **UTL** structure. These data evidence that complex Si species can also reconnect the IPC-1TBA layers and reconstruct the **UTL** zeolite. The ICP-MS elemental analysis of the rec Si8 revealed that the sample possessed Si/Ge = 481. Si content this high has never been reported for the **UTL** zeolite. The **UTL** with highest Si content,

Si/Ge = 233, reported in the literature was produced by repeated post-synthetic degermanation-resilylation. [79] In contrast, the reconstruction using POSS provided significantly higher Si content in a single step.

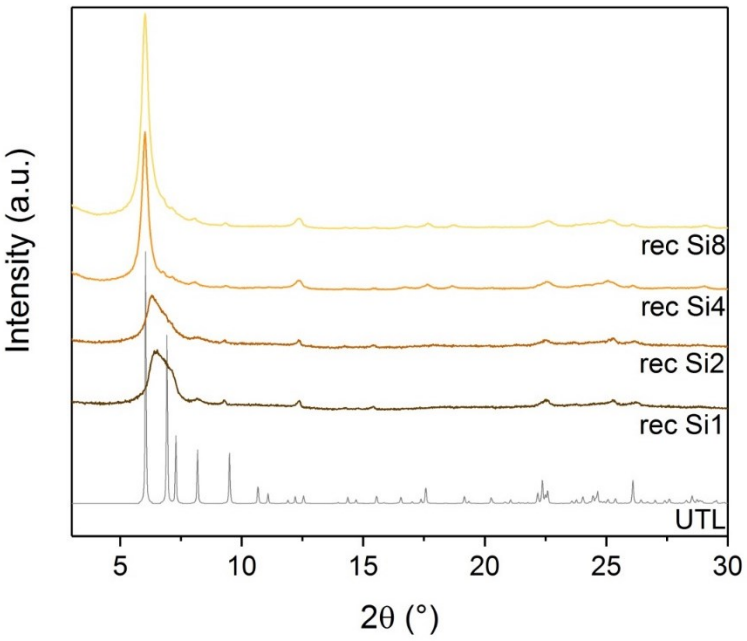

Figure 31: Powder XRD patterns of samples reconstructed using different Si sources.

The decreased intensity of **UTL** framework reflections may originate from low degree of incorporation of the POSS units into the structure or from lower atomic scattering factor of silicon compared to germanium. [144, 145] We can deduce the degree of reconnection of the layers with the D4R units from the textural properties of the reconstructed samples. The rec Si-n (n = 1, 2, 4 or 8) samples exhibited type II adsorption isotherms (Figure 32A). More importantly, samples rec Si4 and rec Si8 possessed micropore volumes 0.14 and 0.13 cm^3/g (Table 9) and mean pore size 8.2 Å (Figure 32B). The micropore volumes and pore size match the textural properties of samples reconstructed using Ge properties and resemble those of the parent **UTL** zeolite (Figure 28, Table 7). In contrast, the mean pore size of rec Si1 and rec Si2 deviated from that of UTL zeolite due to the poor layer ordering. Hence, we can conclude that the TMCTS and POSS reconnected the IPC-1TBA layers to a comparable degree as the germanium-reconstructed D4Rs. Ergo, the lower atomic scattering factor of Si is presumably responsible for the lower intensity of the XRD reflections.

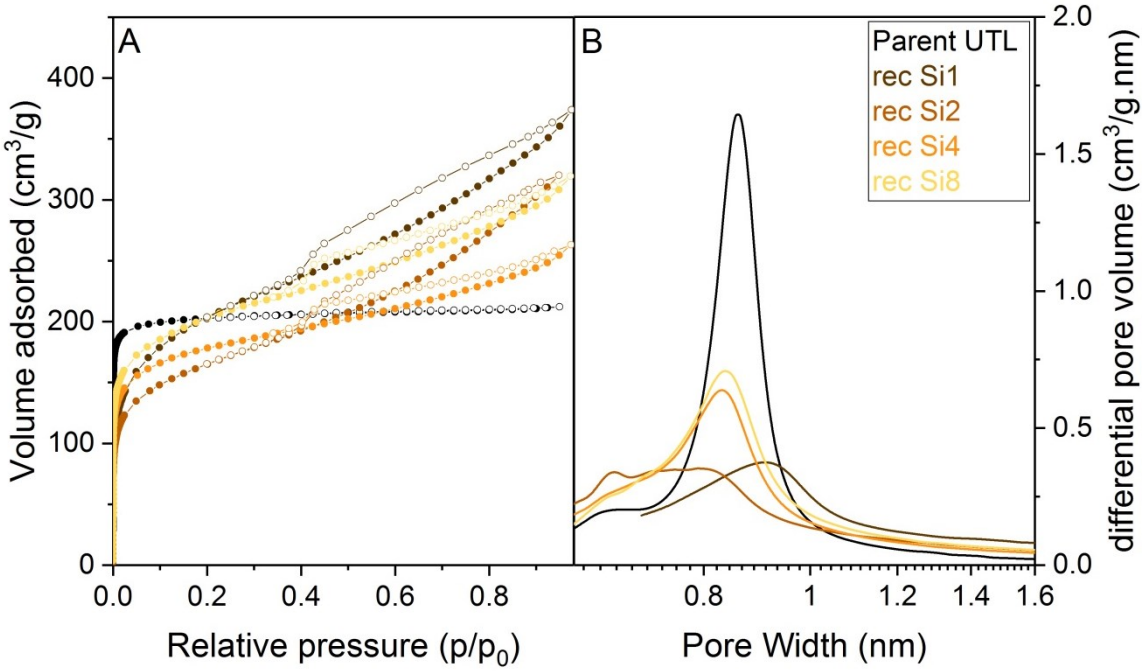

Figure 32: A) argon adsorption–desorption isotherms and B) H–K micropore size distributions of samples reconstructed using different Si sources.

Table 9: Textural properties of samples reconstructed using different Si sources determined by argon adsorption.

	BET (m^2/g)	**S_{ext} (m^2/g)**	**V_{tot} (cm^3/g)**	**V_{mic} (cm^3/g)**
Parent UTL	620	52	0.27	0.25
rec Si1	645	334	0.48	0.12
rec Si2	514	248	0.41	0.08
rec Si4	555	131	0.34	0.14
rec Si8	633	188	0.41	0.13

rec Si1 = UTL reconstructed using DEDMS; rec Si2 = UTL reconstructed using DETMDS; rec Si4 = UTL reconstructed using TMCTS; rec Si8 = UTL reconstructed using POSS.

5.4.3. Introduction of catalytically active elements

Aluminium incorporation

The previous experiments showed that the "Reverse ADOR" protocol enables restoration of the **UTL** zeolite with diverse Si/Ge ratios. The logical next challenge was to adapt the Reverse ADOR to incorporate catalytically active elements into the framework of the **UTL**. Aluminium is presumably the most common catalytically active element in zeolites. It can also be incorporated, albeit with limitations, into the **UTL** through direct synthesis. [81] Therefore we chose aluminium for the demonstration of incorporating active sites into the **UTL** via the Reverse ADOR.

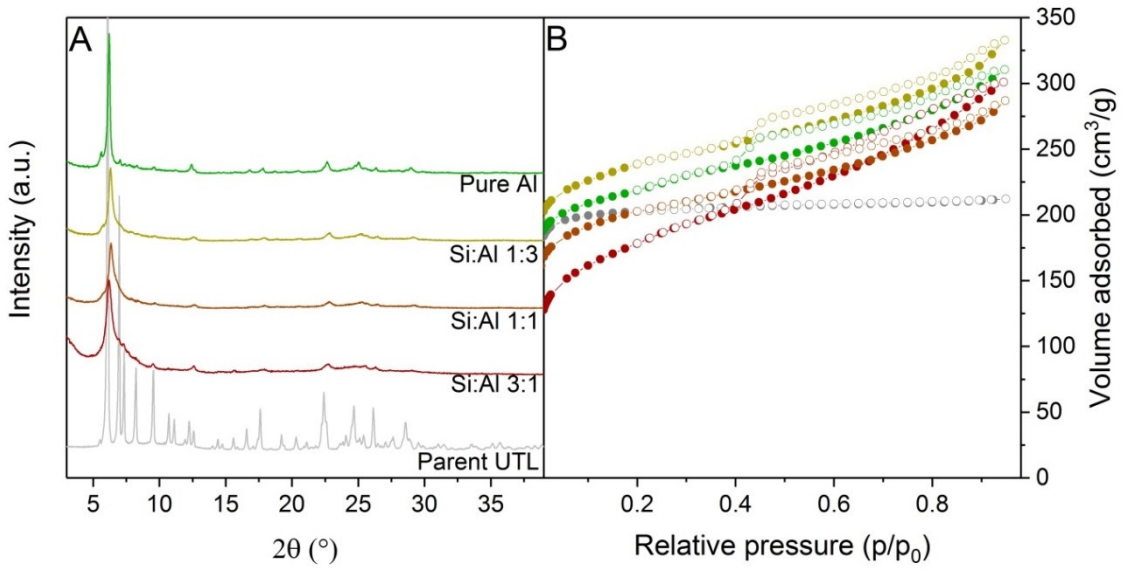

Figure 33: Powder XRD patterns (A) and Ar adsorption isotherms (B) of **UTL** samples reconstructed with varying Si:Al

The fluoride-assisted reconstruction previously showed the ability to reconstruct the **UTL** structure regardless of the Si:Ge composition in the reconstruction synthesis mixture. Ergo, we used the combination of DEDMS and $Al(NO_3)_3$ in ratios 3:1, 1:1, 1:3 and solely $Al(NO_3)_3$ for the reconstruction of D4Rs. The NH_4F was added to the mixtures promote the D4R formation. The XRD patterns of the prepared samples exhibited interlayer 200 reflection at 6.16° 2θ corresponding to the proper layer spacing of the **UTL** topology (Figure 33). Nevertheless, the intensity of the characteristic reflections at 6.99°, 7.35°, 8.27° and 9.55° decreased with the gradual increase of aluminium content from Si:Al = 3:1 to Si:Al = 1:3 suggesting incomplete D4R reconstruction. In contrast, the XRD pattern of the sample reconstructed only using $Al(NO_3)_3$ exhibited relatively narrow 200 reflection and also contained the rest of the characteristic peaks. This implies that the sample possess more uniform layer ordering compared to the samples restored with combination of silicon and aluminium and higher number of D4R.

Nevertheless, reconstruction of the D4R units using only the aluminium source breaks the Loewenstein's rule. The Loewenstein's rule is an empiric rule which states that zeolite frameworks cannot contain direct Al-O-Al bridges. [97] This rule has been derived from empirical observations and also has been supported by a number of theoretical calculations. In essence, zeolites violating the rule should be impossible to synthesize by direct hydrothermal method. In that light, while the reconstruction of the "pure Al" UTL sample may not be outright impossible, it is rather unlikely to say the least. We considered two plausible explanations: either the Loewenstein's rule does not apply to the acidic and anhydrous environment used during the reconstruction, or the aluminium has not fully incorporated and instead migration of silicon from the IPC-1TBA layers aided reconstruction of the D4R units.

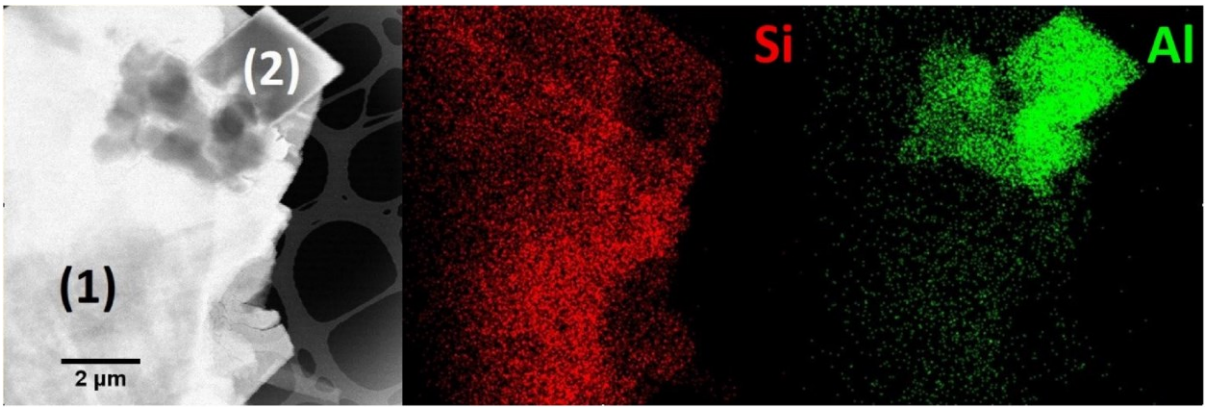

Figure 34: STEM image of “pure Al” reconstructed **UTL** (1) and side-phase (2) and EDX maps of Si (red) and Al (green).

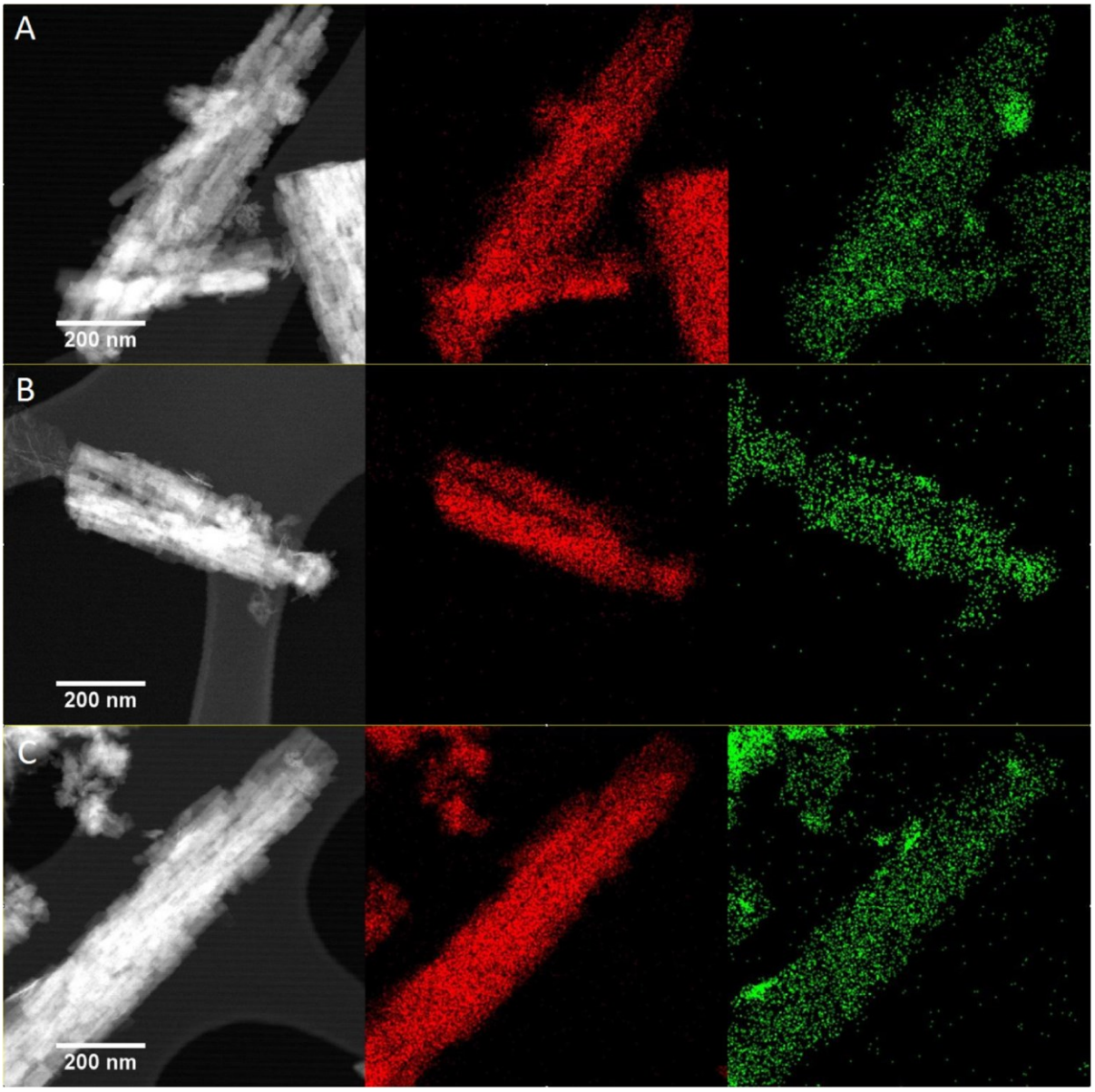

Figure 35: STEM images and Si (red) and Al (green) EDX maps of **UTL** samples reconstructed by fluoride-assisted Reverse ADOR under pHCl = 1 (A), 3 (B) and 5 (C).

The STEM imaging of the Pure Al UTL sample revealed that the sample contains two distinct phases (Figure 34), large flat crystals of the **UTL** (1) and unknown rectangular crystals (2). EDX mapping of the sample further revealed that the **UTL** crystals possess only Si/Al = 21. The high Si/Al molar ratio of the UTL crystals proves our hypothesis of partial incorporation. In contrast, the rectangular particles contained exclusively aluminium but no silicon. Based on these observations, we concluded that aluminium corresponding to the Si/Al = 21 incorporated into the UTL framework and formed the D4R units; whereas, the excess aluminium formed the separate Al-rich phase.

According to literature, the degree of incorporation of various elements (including aluminium) into the zeolite framework depends on the pH. Therefore, we decided to optimise the pH of the synthesis mixture to bolster the aluminium incorporation. We repeated the reconstruction using excess of aluminium and under varying pHCl = 1, 3 and 5, where "pHCl" corresponds to the negative logarithm of the HCl concentration in EtOH. The powder XRD verified the **UTL** crystal structure of the prepared samples and the STEM-EDX imaging revealed the presence of two phases similar to the previous case; the **UTL** and the aluminium-rich phase. The presence of the second phase confirms that the aluminium incorporation into the **UTL** framework reached its maximum under given conditions. We measured the Si/Al of each sample using five separate crystals in order to get an average value. The aluminium content in the **UTL** varied with pHCl showing a maximum Si/Al = 15 at pHCl = 3.

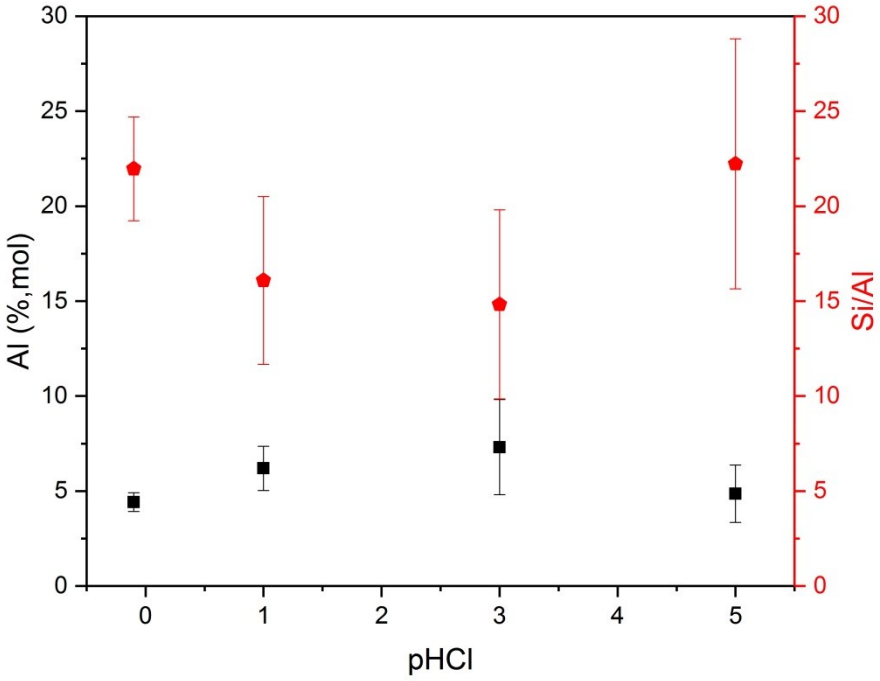

Figure 36: Dependency of aluminium content and Si/Al ratio of the **UTL** zeolites on the pHCl

We also observed a fluctuation of the average pore size with the pHCl. The samples reconstructed under pHCl = -1 possessed the same pore diameter as the parent UTL sample; close to 0.9 nm (Figure 37). However, the increase in pHCl resulted in progressive shift towards lower average pore diameters. We speculate that higher pHCl compromises the ability of fluoride ions to stabilise the D4R units. Insufficient restoration of the D4Rs leads to poor stabilisation of the respective layer distance, to connection of the layers by smaller units on local level and thus to decrease of the average pore size. In order to prove the influence of the fluoride ions and to provide an alternative synthetic pathway,

we performed a second series of reconstruction experiments in the absence of fluorides but with addition of germanium in Si:Ge = 1:1 (see section 4.2.4. and Table 2). The experiments provided a set of reconstructed **UTL** zeolites with average pore size close to that of the parent **UTL**, showing only minor deviation with increasing pHCl (Figure 37). The ability of the germanium to stabilise the D4R units showed no significant dependence on the pHCl and therefore presents more reliable synthesis route for the **UTL** restoration than the use of fluoride anions.

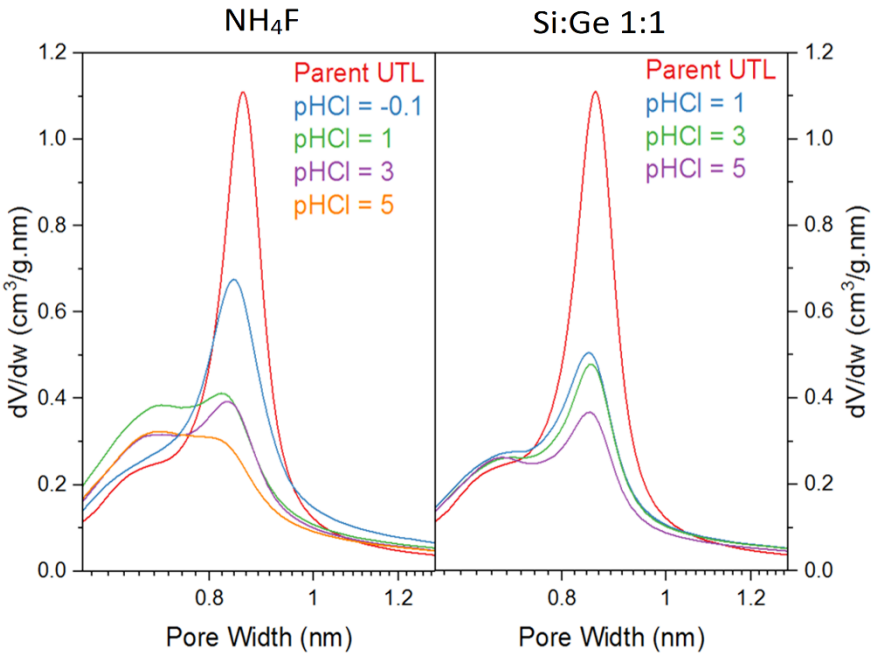

Figure 37: Horwath-Kawazoe pore size distributions of the Al-containing reconstructed **UTL** samples

Catalytic experiments

The aluminium incorporated into the reconstructed **UTL** forms Brønsted acidic Al-(OH)-Si groups or Lewis acid sites in the proximity of structural defects. In addition, the germanium present in the D4R units also exhibits Lewis acidity. Both types of acid sites can provide a source of catalytic activity. We evaluated the catalytic performance of the zeolites using tetrahydropyranylation of 1-decanol as a model reaction. The tetrahydropyranylation can be catalysed by both Brønsted and Lewis sites. The 1-decanol is a bulky compound which cannot penetrate into micropores of common zeolites such as ***BEA**. [110] In contrast, it can enter the extra-large pores of **UTL** and therefore can demonstrate the advantages of extra-large pore zeolites for conversion of bulky substrates. In our experiments, we compared the conversions of 1-decanol over the aluminium-containing **UTL** zeolites reconstructed via both fluoride-assisted route ("Re-UTL (Al)") and germanium-assisted route ("Re-UTL (Al+Ge)"). Additionally, we used directly synthetized alumino-germanosilicate Al-UTL and a commercial aluminosilicate ***BEA** (CP814C Zeolyst, Si/Al = 19) zeolites as benchmark catalysts.

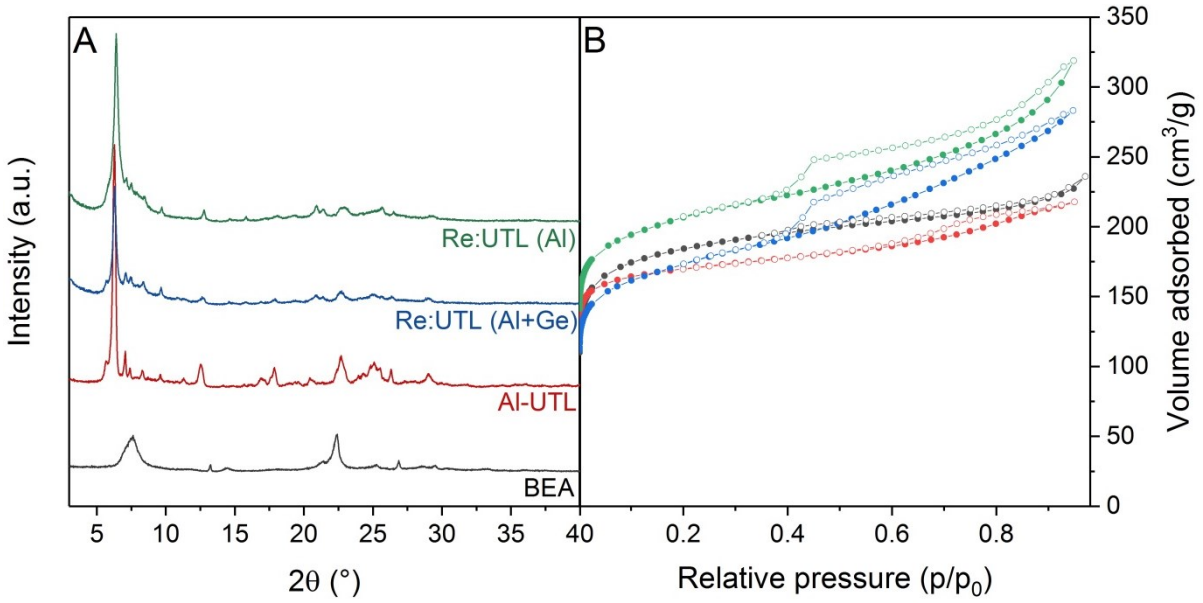

Figure 38: Powder XRD patterns (A) and Ar adsorption isotherms (B) of zeolite catalysts

The X-ray diffraction patterns of used samples (Figure 38A) correspond to the data from IZA database. [19] The Ar adsorption revealed a significant difference between the directly synthetized Al-UTL and the reconstructed Re-UTL samples in their external surface areas (Figure 38B, Table 10). The Re-UTL (Al) and Re-UTL (Al+Ge) exhibited external surface 138 and 180 m^2/g, respectively, while the Al-UTL showed only 64 m^2/g. The high external surface of the reconstructed samples originates from the harsh conditions used during the intercalation and reconstruction procedure. The harsh environment causes etching of the zeolite resulting in formation of mesopores and thus increasing the external surface. The enhanced external surface may boost the mass transfer of the reactants and products during the reaction and thereby increase the reaction rate and reactant conversion.

Table 10: Textural properties and concentration of acid sites of the zeolite catalysts

	BET (m^2/g)	S_{ext} (m^2/g)	V_{tot} (cm^3/g)	V_{mic} (cm^3/g)	c_{Lewis} (µmol/g)	$c_{Brønsted}$ (µmol/g)
BEA	560	170	0.30	0.16	100	300
Al-UTL	454	64	0.25	0.15	74	46
Re-UTL (Al+Ge)	409	180	0.31	0.08	75	25
Re-UTL (Al)	450	138	0.33	0.09	54	21

In order to differentiate between the catalytic activity of the aluminium and germanium sites we tested the reconstructed zeolites both before and after ion exchange to H^+ form. We investigated the concentration of acid sites in both sets of samples by adsorption of pyridine coupled with FTIR spectroscopy. The adsorption of pyridine on the Re-UTL (Al+Ge) before ion exchange revealed no Brønsted acid sites. However, the spectrum also contained a peak at 3677 cm^{-1} characteristic for Brønsted acidic bridging Al-(OH)-Si groups. This implies that the Al sites are inaccessible to the pyridine probe molecule, and we can only observe the vibrations of pyridine interacting with the germanium Lewis acid sites at 1455 cm^{-1}. On the contrary, the signal at 3677 cm^{-1} was not present in the spectrum

of Re-UTL (Al+Ge) ion exchanged to H^+ form. In contrast, the characteristic signal of pyridine interacting with Brønsted acid sites appeared at 1545 cm^{-1}. The samples Re-UTL (Al) and Re-UTL (Al+Ge) possessed similar concentrations of the aluminium Brønsted acid sites 21 and 25 µmol/g, respectively (Table 10). In contrast, the Re-UTL (AL) possessed 54 µmol/g of Lewis sites; whereas, the Re-UTL (Al+Ge) possessed 75 µmol/g due to the additional germanium Lewis sites. [77]

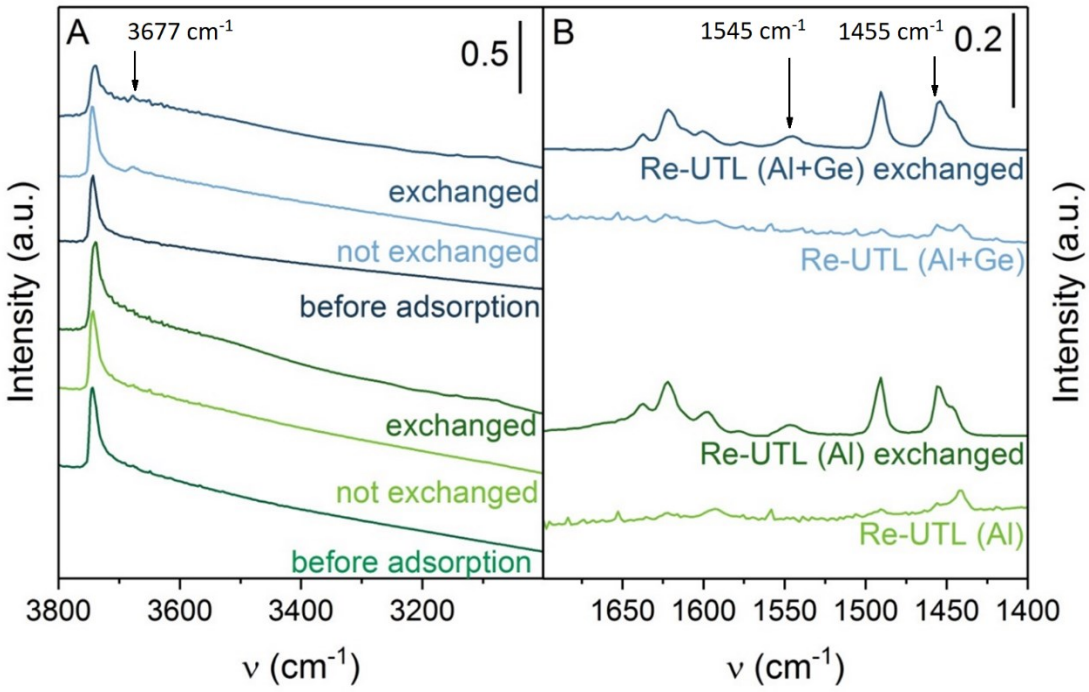

Figure 39: FTIR spectra of hydroxyl groups (A) and adsorbed pyridine (B) of the not exchanged and exchanged reconstructed **UTL** zeolites.

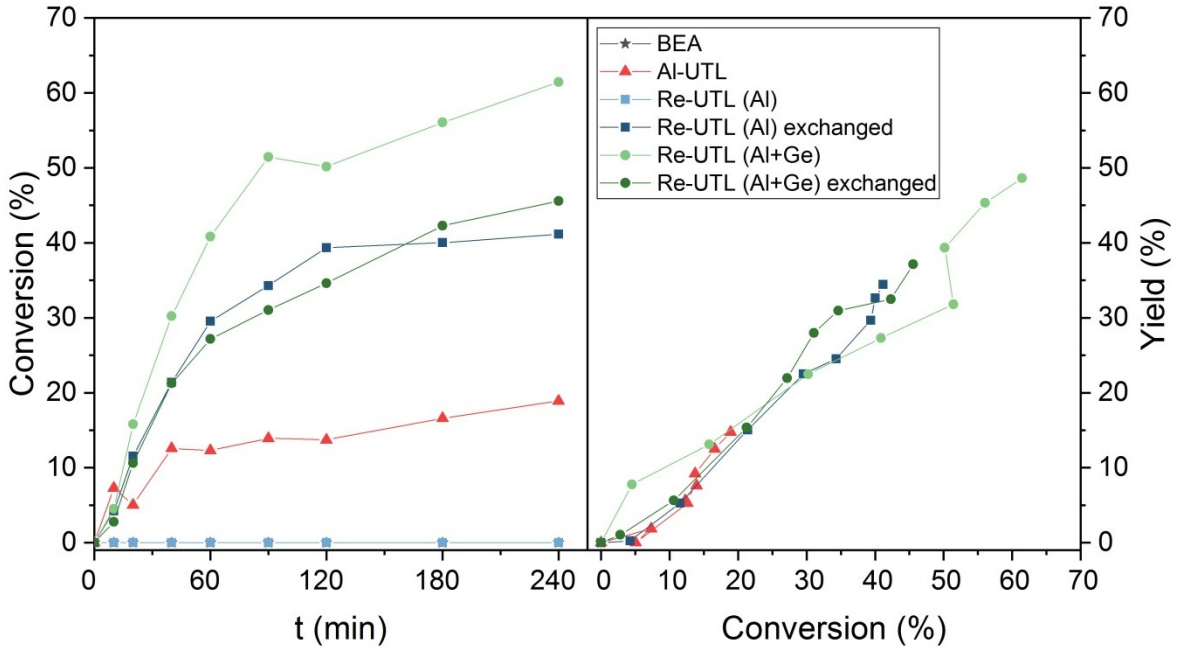

Figure 40: Conversions of 1-decanol and selectivity curves over ***BEA**, Al-UTL and reconstructed **UTL** zeolites.

The ***BEA** zeolite showed no catalytic activity during the tetrahydropyranylation of 1-decanol despite its highest acidity among the catalysts. In contrast, the directly synthetized Al-UTL provided 18.9 % conversion of 1-decanol and 14.8 % yield of tetrahydropyranylated product, 2-decoxytetrahydropyran, after 24 hours, demonstrating the advantage of the extra-large pores for the conversion of bulky substrates such as 1-decanol (Figure 40). The Re-UTL (Al) showed no conversion prior to its ion exchange due to the Brønsted acid sites being inactivated. The ion exchange to H^+ form resulted in 41.2 % conversion of 1-decanol and 34.3 % yield of product. In contrast, the Re-UTL (Al+Ge) provided 61.5 % conversion and 48.5 % yield of product prior to the ion exchange. These data clearly show the advantage of the reconstructed Re-UTL (Al) and Re-UTL (Al+Ge) compared to the directly synthesised Al-UTL. The higher conversion provided by the reconstructed samples mainly stems from their enhanced external surface (Table 10) which facilitates the mass transfer and improves accessibility of the active sites. Furthermore, the synthesis route of the UTL had no effect on the product selectivity (Figure 40) since both directly synthesised Al-UTL and both reconstructed samples provided the desired product with 78 to 83 % selectivity. The results also show that the germanium Lewis acid sites also catalyse the tetrahydropyranylation and can further enhance the catalytic performance of the sample. However, the ion exchange of the Re-UTL (Al+Ge) to H^+ form decreased the conversion to 45.5 % and yield to 37.1 %. We concluded that while the ion exchange activated the aluminium acid sites it simultaneously partially degermanated the zeolite resulting in the decrease of its total acid site concentration and lowered its catalytic performance.

6. Conclusions

This thesis focused on the synthesis and transformation of germanosilicate zeolite **UTL** using the Assembly-Disassembly-Organisation-Reassembly (ADOR) method. The experimental work particularly focused on determining the factors that control the crystal morphology of the **UTL** and on developing a method to control it. It also aimed, on evaluating the hydrolytic stability of the **UTL** germanosilicate depending on the content of germanium in its framework and amount of water in the environment and on developing a method for controlling the rate of hydrolysis and transformation of the **UTL** zeolite into its daughter structures and on reconstructing the **UTL** framework from the hydrolysed product, layered material IPC-1P.

We attempted to alter the zeolite crystal morphology by using growth modifiers and by varying Si/Ge ratio in the synthesis mixture. We observed a progressive change in crystal morphology with increasing Si/Ge molar ratio of the **UTL**. Increase of Si/Ge ratio of the bulk sample from 0.79 to 12.8 caused an increase of the crystal thickness (corresponding to crystallographic *a*-axis) from 0.17 μm to 5.39 μm. In essence, we discovered that the Si/Ge ratio governs the relative growth rate of the **UTL** crystals and that high Si content boosts growth along the *a*-axis which is oriented in perpendicular to the two-dimensional pore system of the **UTL**. On the other hand, none of the growth modifiers (1.5-pentandiol, 1,5-diaminopentane, pentanoic acid and L-lysine) provided any change in UTL crystal morphology. Therefore, we concluded that this strategy is not applicable to the UTL zeolite.

The phenomenon is not limited only to the **UTL** germanosilicate. Other zeolites with one- or two-dimensional pore system, including **AFI**, **IFR**, **LTL** and **MWW,** exhibit analogous evolution of crystal morphology with varying Si/Al ratio. Generally, higher silicon content promotes crystal growth along crystallographic directions perpendicular to the one- or two-dimensional pore system. However, **IWW** zeolite, which contains three-dimensional channel system with large cavities arranged along *b*-axis, also exhibited similar morphology change. The **IWW** with Si/Ge = 4 and 6 revealed that **IWW** crystal size changed from 0.16 x 2.36 x 1.34 μm to 0.38 x 2.79 x 1.50 μm upon increasing its Si/Ge from 4 to 6 in accordance to our observations on the **UTL** zeolite. We concluded that zeolites that possess lower framework symmetry and that contain large building units or cavities continuously and predictably change their crystal morphology depending on their Si/T ratio.

We investigated hydrolytic stability and mechanism of hydrolysis using water vapour adsorption on a set of **UTL** germanosilicate zeolites with varying Si/Ge ratios (Si/Ge = 2.5, 4.5, 18.5 and 53). Adsorption of water vapour on the **UTL** samples provided type V adsorption isotherms with unusual, unclosed hysteresis loop between relative pressures p/p_0 = 0 and 0.35. The adsorption of water on the **UTL** proceeds through 2 stages; first, at low relative pressure $p/p_0 < 0.3$ small amount of water reversibly adsorbs onto the zeolite. No structural changes in the material occur in this stage. The maximum relative pressure for the reversible stage increased with increasing Si/Ge ratio of the sample from 0.3 for Si/Ge = 2.5 to 0.42 for Si/Ge = 53. We also observed that higher Si/Ge ratio enabled higher maximal amount of reversibly adsorbed water due to the increased hydrolytic stability of the framework. Upon exceeding this critical relative pressure, the amount of adsorbed water abruptly increased in the second stage. The adsorption at this stage is partially irreversible. The process represents hydrolysis of Si-O-Ge bonds which results in structural degradation of the sample. This is evidenced by decrease in sample micropore volume from 0.24 to 0.10 cm^3/g for germanium-rich samples (Si/Ge = 2.5 and 4.5) and change of their powder XRD pattern which confirmed that significant structural changes take

place in the zeolite framework. The amount of irreversibly bound water corresponds for the water consumed in breaking the framework Ge-O bonds accompanying the structural transformation and thus it cannot be desorbed. The amount of irreversibly bound water increased logarithmically with the germanium content. Higher content of germanium provides more hydrolytically labile bonds and therefore requires more water for the complete hydrolysis. In contrast, germanium-poor UTL (SI/Ge = 18.5 and 53) exhibited only minor change of micropore volume and retained the **UTL** structure, as evidenced by the XRD. The difference between the two sets of samples implies the existence of critical Si/Ge ratio which delimitates the ability of the **UTL** to hydrolyse into the layered material from the ability to retain the 3D structure.

We further aimed to recover and characterize the intermediates of the transformation and, hence, required to slow down the rate of the hydrolysis. The hydrolysis of **UTL** germanosilicate into the layered precursor IPC-1P is commonly carried out in a large excess of water or acid solution (e.g. 200 ml of solution per 1 g of sample) where the **UTL** completely hydrolyses within several minutes making recovery of the intermediates problematic. In contrast, we established that the **UTL** undergoes no significant structural changes when treated with absolute alcohol (i.e. methanol, ethanol, i-propanol). Thus, the rate of the UTL disassembly can be controlled by diluting water with defined amount of alcohols. Furthermore, we observed that the rate also depends on the type of alcohol in the solution in the respective order MeOH > EtOH > i-PrOH. This phenomenon could originate from the different kinetic diameter, polarity or acidity of the respective alcohols.

The leeched germanium forms germanium oxide/hydroxide poorly soluble in alcohols, which blocks the micropores of the recovered samples. This issue can be overcome by replacing the water-alcohol solutions with solution of HCl in EtOH. The HCl forms more soluble germanium alkoxychlorides and germanium tetrachloride from the leeched germanium. The hydrolysis of the **UTL** in 1.25 M HCl/EtOH solution prolonged the time of the transformation to 20 days. The slow transformation rate enabled recovery of the intermediate samples and characterization of their structure. The structure of the germanosilicate exhibited a gradual decrease of the pore diameter of the zeolite and progressive transformation of the zeolite structure in respective order: **UTL** (14-12R) - IPC-7 (14-12R & 12-10R) - **OKO** (12-10R) - ***PCS** (12-10R & 10-8R).

Last but not least, we developed a method for reconstructing the **UTL** zeolite from the layered precursor IPC-1P. The disassembly of **UTL** to IPC-1P is accompanied by decrease of the interlayer distance from 14.5 to 10.7 Å. The distance cannot spontaneously increase to the original value after the hydrolysis which prevented the restoration of the interlayer D4R units and the **UTL** structure. Hence, we increased the distance between the layers artificially by intercalation of tetrabutylammonium hydroxide (TBAOH) into the interlayer space. On one hand, the TBAOH intercalation successfully increased the interlayer spacing to 13.9 Å. On the other hand, the high pH of the TBAOH solution causes etching of the zeolite which leads to formation of defects, mesopores and eventually complete amorphisation of the material. To counter the issue, we optimised the process on the following parameters: treatment time, TBAOH concentration and concentration of added colloidal SiO_2 in the mixture. The shorter contact time, lower OH^- concentration and pre-saturation of the solution with Si species significantly increased the yields of the intercalated layered precursor. Subsequently we reconstructed the D4R units in between the layers using combinations of DEDMS and germanium methoxide. Combination of both Si and Ge sources resulted in restoration of the **UTL** structure. In contrast, absence of one of the elements prevented the reconstruction. The

reconstruction of **UTL** using only DEDMS or germanium methoxide was enabled only by addition of NH_4F. The fluorides stabilised the D4R units even in the presence of only Si or Ge source. However, the fluorides caused additional etching to the material, yielding samples with poor textural properties including low micropore volume. Alternatively, more complex Si sources such as 2,4,6,8-tetramethylcyclotetrasiloxane or octamethylsilsesquioxane also enabled the **UTL** restoration even in the absence of either germanium or fluorides. This approach yielded high-Si **UTL** zeolite with Si/Ge = 481.

The **UTL** reconstruction protocol, which we labelled “Reverse ADOR”, also enabled also incorporation of catalytically active sites into the zeolite. We illustrated this approach on aluminium incorporation. The fluoride-assisted method yielded samples with **UTL** topology regardless of the aluminium content in the synthesis mixture. However, only portion of aluminium corresponding to Si/Al = 21 successfully incorporated into the zeolite. The excess aluminium formed a separate aluminium oxide phase. We further optimised the degree of incorporation by adjusting the acidity of the synthesis mixture. Increasing the pHCl to 3 resulted in improved aluminium incorporation up to Si/Al = 15. Further increase in the pHCl impeded the incorporation. The reconstructed **UTL** samples prepared by both the fluoride- ("Re-UTL (Al)") and germanium-assisted ("Re-UTL (Al + Ge)") reconstruction were active in tetrahydropyranylation of 1-decanol (41.2 and 48.5 % 1-decanol conversion after 24 h, respectively). In contrast, directly synthetized Al-UTL provided only 14.8 % conversion after 24 h and aluminosilicate ***BEA** zeolite exhibited virtually no catalytic activity. The remarkable catalytic performance of reconstructed **UTL** samples originated mainly from their enhanced external surface area and thus improved accessibility of the acid sites.

7. References

[1] M. Moliner, State of the art of Lewis acid-containing zeolites: lessons from fine chemistry to new biomass transformation processes, Dalton Transactions, 43 (2014) 4197-4208.
[2] M.E. Davis, Ordered porous materials for emerging applications, Nature, 417 (2002) 813-821.
[3] M. Guisnet, Zeolite Catalysts for Cleaner Technologies, ChemInform, 39 (2007) 231-249.
[4] A. Primo, H. Garcia, Zeolites as catalysts in oil refining, Chemical Society Reviews, 43 (2014) 7548-7561.
[5] C. Liu, F. Li, L.-P. Ma, H.-M. Cheng, Advanced Materials for Energy Storage, Advanced Materials, 22 (2010) E28-E62.
[6] H. Fang, J. Yang, M. Wen, Q. Wu, Nanoalloy Materials for Chemical Catalysis, Advanced Materials, 30 (2018) 1705698.
[7] Y. Zhang, H.F. Chan, K.W. Leong, Advanced materials and processing for drug delivery: The past and the future, Advanced Drug Delivery Reviews, 65 (2013) 104-120.
[8] M. Mofarahi, F. Gholipour, Gas adsorption separation of CO_2/CH_4 system using zeolite 5A, Microporous and Mesoporous Materials, 200 (2014) 1-10.
[9] J. Gascon, F. Kapteijn, B. Zornoza, V. Sebastián, C. Casado, J. Coronas, Practical Approach to Zeolitic Membranes and Coatings: State of the Art, Opportunities, Barriers, and Future Perspectives, Chemistry of Materials, 24 (2012) 2829-2844.
[10] J. Weitkamp, Zeolites and catalysis, Solid State Ionics, 131 (2000) 175-188.
[11] M. Anderson, H. Wang, Y.S. Lin, Inorganic membranes for carbon dioxide and nitrogen separation, Reviews in Chemical Engineering, 28 (2012) 101-121.
[12] O.R. Zaborsky, Enzymes: Biological Catalysts, in: J.J. Burton, R.L. Garten (Eds.) Advanced Materials in Catalysis, Academic Press, 1977, pp. 267-291.
[13] R.J.H. Voorhoeve, Perovskite-Related Oxides as Oxidation—Reduction Catalysts, in: J.J. Burton, R.L. Garten (Eds.) Advanced Materials in Catalysis, Academic Press, 1977, pp. 129-180.
[14] H.E. Swift, Catalytic Properties of Synthetic Layered Silicates and Aluminosilicates, in: J.J. Burton, R.L. Garten (Eds.) Advanced Materials in Catalysis, Academic Press, 1977, pp. 209-233.
[15] J.H. Sinfelt, J.A. Cusumano, Bimetallic Catalysts, in: J.J. Burton, R.L. Garten (Eds.) Advanced Materials in Catalysis, Academic Press, 1977, pp. 1-31.
[16] R.B. Levy, Properties of Carbides, Nitrides, and Borides: Implications for Catalysis, in: J.J. Burton, R.L. Garten (Eds.) Advanced Materials in Catalysis, Academic Press, 1977, pp. 101-127.
[17] I. Fechete, Y. Wang, J.C. Védrine, The past, present and future of heterogeneous catalysis, Catalysis Today, 189 (2012) 2-27.
[18] J. Jiang, J.L. Jorda, M.J. Diaz-Cabanas, J. Yu, A. Corma, The Synthesis of an Extra-Large-Pore Zeolite with Double Three-Ring Building Units and a Low Framework Density, Angewandte Chemie International Edition, 49 (2010) 4986-4988.
[19] C. Baerlocher, L.B. McCusker, in, Database of Zeolite Structures: http://www.iza-structure.org/databases/.
[20] J. Li, Z.R. Gao, Q.-F. Lin, C. Liu, F. Gao, C. Lin, S. Zhang, H. Deng, A. Mayoral, W. Fan, S. Luo, X. Chen, M.A. Camblor, F.-J. Chen, J. Yu, A 3D extra-large-pore zeolite enabled by 1D-to-3D topotactic condensation of a chain silicate., Science, 379 (2023) 283-287.
[21] J.F. Haw, Zeolite acid strength and reaction mechanisms in catalysis, Physical Chemistry Chemical Physics, 4 (2002) 5431-5441.
[22] T. Maesen, The Zeolite Scene – An Overview, in: J. Čejka, H. van Bekkum, A. Corma, F. Schüth (Eds.) Studies in Surface Science and Catalysis, Elsevier, 2007, pp. 1-12.
[23] W.J. Roth, P. Nachtigall, R.E. Morris, P.S. Wheatley, V.R. Seymour, S.E. Ashbrook, P. Chlubna, L. Grajciar, M. Polozij, A. Zukal, O. Shvets, J. Čejka, A family of zeolites with controlled pore size prepared using a top-down method, Nature Chemistry, 5 (2013) 628-633.

[24] P. Eliášová, M. Opanasenko, P.S. Wheatley, M. Shamzhy, M. Mazur, P. Nachtigall, W.J. Roth, R.E. Morris, J. Čejka, The ADOR mechanism for the synthesis of new zeolites, Chemical Society Reviews, 44 (2015) 7177-7206.
[25] M.V. Shamzhy, O.V. Shvets, M.V. Opanasenko, P.S. Yaremov, L.G. Sarkisyan, P. Chlubná, A. Zukal, V.R. Marthala, M. Hartmann, J. Čejka, Synthesis of isomorphously substituted extra-large pore UTL zeolites, J. Mater. Chem., 22 (2012) 15793-15803.
[26] R.M. Barrer, P.J. Denny, Hydrothermal chemistry of the silicates. Part IX. Nitrogenous aluminosilicates, Journal of the Chemical Society, (1961) 971-982.
[27] F. Di Renzo, F. Fajula, Introduction to molecular sieves: trends of evolution of the zeolite community, in: J. Ĉejka, H. van Bekkum (Eds.) Studies in Surface Science and Catalysis, Elsevier, 2005, pp. 1-12.
[28] J.-L. Guth, H. Kessler, Synthesis of Aluminosilicate Zeolites and Related Silica-Based Materials, in: J. Weitkamp, L. Puppe (Eds.) Catalysis and Zeolites: Fundamentals and Applications, Springer Berlin Heidelberg, Berlin, Heidelberg, 1999, pp. 1-52.
[29] H.G. Karge, M. Hunger, H.K. Beyer, Characterization of Zeolites — Infrared and Nuclear Magnetic Resonance Spectroscopy and X-Ray Diffraction, in: J. Weitkamp, L. Puppe (Eds.) Catalysis and Zeolites: Fundamentals and Applications, Springer Berlin Heidelberg, Berlin, Heidelberg, 1999, pp. 198-326.
[30] S. Smeets, X. Zou, Zeolite Structures, in: J. Čejka, R.E. Morris, P. Nachtigall (Eds.) Zeolites in Catalysis: Properties and Applications, The Royal Society of Chemistry, 2017, pp. 37-72.
[31] C. Baerlocher, W.M. Meier, D.H. Olson, Atlas of Zeolite Framework Types, in, 2000.
[32] L.B. McCusker, C. Baerlocher, Zeolite Structures, in: J. Čejka, H. van Bekkum, A. Corma, F. Schüth (Eds.) Studies in Surface Science and Catalysis, Elsevier, 2007, pp. 13-37.
[33] S.M. Csicsery, Shape-selective catalysis in zeolites, Zeolites, 4 (1984) 202-213.
[34] E. Roduner, Understanding catalysis, Chemical Society Reviews, 43 (2014) 8226-8239.
[35] B. Smit, T.L.M. Maesen, Towards a molecular understanding of shape selectivity, Nature, 451 (2008) 671-678.
[36] E. Jaramillo, M. Chandross, Adsorption of Small Molecules in LTA Zeolites. NH_3, CO_2, and H_2O in Zeolite 4A, The Journal of Physical Chemistry B, 108 (2004) 20155-20159.
[37] S. Calero, P. Gómez-Álvarez, Effect of the Confinement and Presence of Cations on Hydrogen Bonding of Water in LTA-Type Zeolite, The Journal of Physical Chemistry C, 118 (2014) 9056-9065.
[38] F. Baba, F. Benaliouche, R. Meknaci, Y. Boucheffa, Water adsorption and antibacterial activity studies for characterization of Ca-LTA zeolite/diatomite adsorbents, Colloid and Interface Science Communications, 35 (2020) 100233.
[39] K. Mizukami, H. Takaba, Y. Kobayashi, Y. Oumi, R.V. Belosludov, S. Takami, M. Kubo, A. Miyamoto, Molecular dynamics calculations of CO_2/N_2 mixture through the NaY type zeolite membrane, Journal of Membrane Science, 188 (2001) 21-28.
[40] M.P. Bernal, J. Coronas, M. Menéndez, J. Santamaría, Separation of CO_2/N_2 mixtures using MFI-type zeolite membranes, AIChE Journal, 50 (2004) 127-135.
[41] M. Kacem, M. Pellerano, A. Delebarre, Pressure swing adsorption for CO_2/N_2 and CO_2/CH_4 separation: Comparison between activated carbons and zeolites performances, Fuel Processing Technology, 138 (2015) 271-283.
[42] C. Selzer, A. Werner, S. Kaskel, Selective Adsorption of Propene over Propane on Hierarchical Zeolite ZSM-58, Industrial & Engineering Chemistry Research, 57 (2018) 6609-6617.
[43] C.A. Grande, J. Gascon, F. Kapteijn, A.E. Rodrigues, Propane/propylene separation with Li-exchanged zeolite 13X, Chemical Engineering Journal, 160 (2010) 207-214.
[44] M.J. Climent, A. Corma, A. Velty, M. Susarte, Zeolites for the Production of Fine Chemicals: Synthesis of the Fructone Fragrancy, J. Catal., 196 (2000) 345-351.
[45] D. Aldhayan, K. Kalíková, M.R. Shaik, M.R.H. Siddiqui, J. Přech, Selective Oxidation of Citronellol over Titanosilicate Catalysts, Catalysts, 10 (2020) 1284.

[46] M. Shamzhy, M. Opanasenko, P. Concepción, A. Martínez, New trends in tailoring active sites in zeolite-based catalysts, Chem. Soc. Rev., 48 (2019) 1095-1149.
[47] E.T.C. Vogt, B.M. Weckhuysen, Fluid catalytic cracking: recent developments on the grand old lady of zeolite catalysis, Chemical Society Reviews, 44 (2015) 7342-7370.
[48] P.M.M. Blauwhoff, J.W. Gosselink, E.P. Kieffer, S.T. Sie, W.H.J. Stork, Zeolites as Catalysts in Industrial Processes, in: J. Weitkamp, L. Puppe (Eds.) Catalysis and Zeolites: Fundamentals and Applications, Springer Berlin Heidelberg, Berlin, Heidelberg, 1999, pp. 437-538.
[49] A. de Angelis, P. Ingallina, C. Perego, Solid acid catalysts for industrial condensations of ketones and aldehydes with aromatics, Industrial & Engineering Chemistry Research, 43 (2004) 1169-1178.
[50] P. Botella, A. Corma, R.H. Carr, C.J. Mitchell, Towards an industrial synthesis of diamino diphenyl methane (DADPM) using novel delaminated materials: A breakthrough step in the production of isocyanates for polyurethanes, Applied Catalysis a-General, 398 (2011) 143-149.
[51] D. Kubička, O. Kikhtyanin, Opportunities for zeolites in biomass upgrading—Lessons from the refining and petrochemical industry, Catalysis Today, 243 (2015) 10-22.
[52] Y. Li, L. Li, J. Yu, Applications of Zeolites in Sustainable Chemistry, Chem, 3 (2017) 928-949.
[53] E. Taarning, C.M. Osmundsen, X. Yang, B. Voss, S.I. Andersen, C.H. Christensen, Zeolite-catalyzed biomass conversion to fuels and chemicals, Energy & Environmental Science, 4 (2011) 793-804.
[54] M.J. Climent, A. Corma, S. Iborra, Heterogeneous Catalysts for the One-Pot Synthesis of Chemicals and Fine Chemicals, Chemical Reviews, 111 (2011) 1072-1133.
[55] J.-C. Kim, K. Cho, S. Lee, R. Ryoo, Mesopore wall-catalyzed Friedel–Crafts acylation of bulky aromatic compounds in MFI zeolite nanosponge, Catalysis Today, 243 (2015) 103-108.
[56] M. Bejblova, D. Prochazkova, J. Čejka, Acylation Reactions over Zeolites and Mesoporous Catalysts, Chemsuschem, 2 (2009) 486-499.
[57] C. Gauthier, B. Chiche, A. Finiels, P. Geneste, Influence of acidity in friedel-crafts acylation catalyzed by zeolites, Journal of Molecular Catalysis, 50 (1989) 219-229.
[58] G. Sartori, R. Maggi, Use of Solid Catalysts in Friedel−Crafts Acylation Reactions, Chemical Reviews, 106 (2006) 1077-1104.
[59] J. Přech, Catalytic performance of advanced titanosilicate selective oxidation catalysts – a review, 60 (2018) 71-131.
[60] V. Smeets, E.M. Gaigneaux, D.P. Debecker, Titanosilicate Epoxidation Catalysts: A Review of Challenges and Opportunities, ChemCatChem, 14 (2022) e202101132.
[61] G.M. Lari, P.Y. Dapsens, D. Scholz, S. Mitchell, C. Mondelli, J. Pérez-Ramírez, Deactivation mechanisms of tin-zeolites in biomass conversions, Green Chemistry, 18 (2016) 1249-1260.
[62] H.Y. Luo, L. Bui, W.R. Gunther, E. Min, Y. Román-Leshkov, Synthesis and Catalytic Activity of Sn-MFI Nanosheets for the Baeyer–Villiger Oxidation of Cyclic Ketones, ACS Catalysis, 2 (2012) 2695-2699.
[63] H.Y. Luo, J.D. Lewis, Y. Román-Leshkov, Lewis Acid Zeolites for Biomass Conversion: Perspectives and Challenges on Reactivity, Synthesis, and Stability, Annual Review of Chemical and Biomolecular Engineering, 7 (2016) 663-692.
[64] S. De, S. Dutta, B. Saha, Critical design of heterogeneous catalysts for biomass valorization: current thrust and emerging prospects, Catalysis Science & Technology, 6 (2016) 7364-7385.
[65] Y. Li, J. Yu, New Stories of Zeolite Structures: Their Descriptions, Determinations, Predictions, and Evaluations, Chem. Rev., 114 (2014) 7268-7316.
[66] M. Opanasenko, M. Shamzhy, Y. Wang, W. Yan, P. Nachtigall, J. Čejka, Synthesis and Post-Synthesis Transformation of Germanosilicate Zeolites, Angewandte Chemie International Edition, 59 (2020) 19380-19389.
[67] A. Corma, M.J. Díaz-Cabañas, J. Jiang, M. Afeworki, D.L. Dorset, S.L. Soled, K.G. Strohmaier, Extra-large pore zeolite (ITQ-40) with the lowest framework density containing double four- and double three-rings, Proceedings of the National Academy of Sciences, 107 (2010) 13997-14002.
[68] J.-L. Paillaud, B. Harbuzaru, J. Patarin, N. Bats, Extra-Large-Pore Zeolites with Two-Dimensional Channels Formed by 14 and 12 Rings, Science, 304 (2004) 990.

[69] J.H. Kang, D. Xie, S.I. Zones, M.E. Davis, Transformation of Extra-Large Pore Germanosilicate CIT-13 Molecular Sieve into Extra-Large Pore CIT-5 Molecular Sieve, Chemistry of Materials, 31 (2019) 9777-9787.
[70] S.O. Odoh, M.W. Deem, L. Gagliardi, Preferential Location of Germanium in the UTL and IPC-2a Zeolites, The Journal of Physical Chemistry C, 118 (2014) 26939-26946.
[71] G. Sastre, A. Pulido, A. Corma, An attempt to predict and rationalize relative stabilities and preferential germanium location in Si/Ge zeolites, Microporous and Mesoporous Materials, 82 (2005) 159-163.
[72] J.H. Kang, D. Xie, S.I. Zones, M.E. Davis, Fluoride-free Synthesis of Germanosilicate CIT-13 and Its Inverse Sigma Transformation To Form CIT-14, Chemistry of Materials, 32 (2020) 2014-2024.
[73] E. Verheyen, L. Joos, K. Van Havenbergh, E. Breynaert, N. Kasian, E. Gobechiya, K. Houthoofd, C. Martineau, M. Hinterstein, F. Taulelle, V. Van Speybroeck, M. Waroquier, S. Bals, G. Van Tendeloo, C.E.A. Kirschhock, J.A. Martens, Design of zeolite by inverse sigma transformation, Nature Materials, 11 (2012) 1059-1064.
[74] W.J. Roth, O.V. Shvets, M. Shamzhy, P. Chlubna, M. Kubu, P. Nachtigall, J. Čejka, Postsynthesis Transformation of Three-Dimensional Framework into a Lamellar Zeolite with Modifiable Architecture, Journal of the American Chemical Society, 133 (2011) 6130-6133.
[75] A. Corma, M.J. Díaz-Cabañas, F. Rey, S. Nicolopoulus, K. Boulahya, ITQ-15: The first ultralarge pore zeolite with a bi-directional pore system formed by intersecting 14- and 12-ring channels, and its catalytic implications, Chemical Communications, (2004) 1356-1357.
[76] N. Kasian, A. Tuel, E. Verheyen, C.E.A. Kirschhock, F. Taulelle, J.A. Martens, NMR Evidence for Specific Germanium Siting in IM-12 Zeolite, Chemistry of Materials, 26 (2014) 5556-5565.
[77] I. Podolean, J. Zhang, M. Shamzhy, V.I. Pârvulescu, J. Čejka, Solvent-free ketalization of polyols over germanosilicate zeolites: the role of the nature and strength of acid sites, Catalysis Science & Technology, 10 (2020) 8254-8264.
[78] H. Xu, J. Jiang, B. Yang, H. Wu, P. Wu, Effective Baeyer–Villiger oxidation of ketones over germanosilicates, Catalysis Communications, 55 (2014) 83-86.
[79] H. Xu, J.-g. Jiang, B. Yang, L. Zhang, M. He, P. Wu, Post-Synthesis Treatment gives Highly Stable Siliceous Zeolites through the Isomorphous Substitution of Silicon for Germanium in Germanosilicates, Angewandte Chemie International Edition, 53 (2014) 1355-1359.
[80] M.V. Shamzhy, P. Eliašová, D. Vitvarová, M.V. Opanasenko, D.S. Firth, R.E. Morris, Post-Synthesis Stabilization of Germanosilicate Zeolites ITH, IWW, and UTL by Substitution of Ge for Al, Chemistry – A European Journal, 22 (2016) 17377-17386.
[81] M.V. Shamzhy, O.V. Shvets, M.V. Opanasenko, P.S. Yaremov, L.G. Sarkisyan, P. Chlubna, A. Zukal, V.R. Marthala, M. Hartmann, J. Cejka, Synthesis of isomorphously substituted extra-large pore UTL zeolites, J. Mater. Chem., 22 (2012) 15793-15803.
[82] M.V. Shamzhy, O.V. Shvets, M.V. Opanasenko, L. Kurfiřtová, D. Kubička, J. Čejka, Extra-Large-Pore Zeolites with UTL Topology: Control of the Catalytic Activity by Variation in the Nature of the Active Sites, Chemcatchem, 5 (2013) 1891-1898.
[83] N. Žilková, P. Eliášová, S. Al-Khattaf, R.E. Morris, M. Mazur, J. Čejka, The effect of UTL layer connectivity in isoreticular zeolites on the catalytic performance in toluene alkylation, Catalysis Today, 277 (2016) 55-60.
[84] C. Colella, Natural zeolites, in: J. Čejka, H. van Bekkum (Eds.) Studies in Surface Science and Catalysis, Elsevier, 2005, pp. 13-40.
[85] B. Szczęśniak, S. Borysiuk, J. Choma, M. Jaroniec, Mechanochemical synthesis of highly porous materials, Materials Horizons, 7 (2020) 1457-1473.
[86] I.G. Clayson, D. Hewitt, M. Hutereau, T. Pope, B. Slater, High Throughput Methods in the Synthesis, Characterization, and Optimization of Porous Materials, Advanced Materials, 32 (2020) 2002780.
[87] J. Li, A. Corma, J. Yu, Synthesis of new zeolite structures, Chemical Society Reviews, 44 (2015) 7112-7127.

[88] R.E. Morris, S.L. James, Solventless Synthesis of Zeolites, Angewandte Chemie International Edition, 52 (2013) 2163-2165.
[89] G. Bellussi, A. Carati, C. Rizzo, R. Millini, New trends in the synthesis of crystalline microporous materials, Catalysis Science & Technology, 3 (2013) 833-857.
[90] C.S. Cundy, Synthesis of zeolites and zeotypes, in: J. Čejka, H. van Bekkum (Eds.) Studies in Surface Science and Catalysis, Elsevier, 2005, pp. 65-90.
[91] O. Veselý, R.E. Morris, J. Čejka, Beyond traditional synthesis of zeolites: The impact of germanosilicate chemistry in the search for new materials, Microporous and Mesoporous Materials, (2022) 112385.
[92] K. Asselman, D. Vandenabeele, N. Pellens, N. Doppelhammer, C.E.A. Kirschhock, E. Breynaert, Structural Aspects Affecting Phase Selection in Inorganic Zeolite Synthesis, Chemistry of Materials, 34 (2022) 11081-11092.
[93] J. Yu, Synthesis of Zeolites, in: J. Čejka, H. van Bekkum, A. Corma, F. Schüth (Eds.) Studies in Surface Science and Catalysis, Elsevier, 2007, pp. 39-103.
[94] R.F. Lobo, S.I. Zones, M.E. Davis, Structure-direction in zeolite synthesis, Journal of inclusion phenomena and molecular recognition in chemistry, 21 (1995) 47-78.
[95] B.B. Schaack, W. Schrader, F. Schüth, How are Heteroelements (Ga and Ge) Incorporated in Silicate Oligomers?, Chemistry – A European Journal, 15 (2009) 5920-5925.
[96] B.B. Schaack, W. Schrader, T. Schueth, Detection of Structural Elements of Different Zeolites in Nucleating Solutions by Electrospray Ionization Mass Spectrometry, Angewandte Chemie-International Edition, 47 (2008) 9092-9095.
[97] W. Loewenstein, The distribution of aluminum in the tetrahedra of silicates and aluminates, American Mineralogist, 39 (1954) 92-96.
[98] R. Millini, E. Previde Massara, G. Perego, G. Bellussi, Framework composition of titanium silicalite-1, Journal of Catalysis, 137 (1992) 497-503.
[99] W. Meise, S. FE, Kinetic Studies on Formation of Zeolite-A, Advances in Chemistry Series, (1973) 169-178.
[100] C.S. Cundy, P.A. Cox, The hydrothermal synthesis of zeolites: Precursors, intermediates and reaction mechanism, Microporous and Mesoporous Materials, 82 (2005) 1-78.
[101] A. Korzeniowska, J. Grzybek, K. Kałahurska, M. Kubu, W.J. Roth, B. Gil, The structure-catalytic activity relationship for the transient layered zeolite MCM-56 with MWW topology, Catalysis Today, 345 (2020) 116-124.
[102] M. Kubů, S.I. Zones, J. Čejka, TUN, IMF and -SVR Zeolites; Synthesis, Properties and Acidity, Topics in Catalysis, 53 (2010) 1330-1339.
[103] V. Gábová, J. Dědeček, J. Čejka, Control of Al distribution in ZSM-5 by conditions of zeolite synthesis, Chemical Communications, (2003) 1196-1197.
[104] W. Qin, R. Jain, F.C. Robles Hernández, J.D. Rimer, Organic-Free Interzeolite Transformation in the Absence of Common Building Units, Chemistry – A European Journal, 25 (2019) 5893-5898.
[105] S.I. Zones, S.-J. Hwang, M.E. Davis, Studies of the Synthesis of SSZ-25 Zeolite in a “Mixed-Template” System, Chemistry – A European Journal, 7 (2001) 1990-2001.
[106] O.V. Shvets, A. Zukal, N. Kasian, N. Žilková, J. Čejka, The Role of Crystallization Parameters for the Synthesis of Germanosilicate with UTL Topology, Chemistry – A European Journal, 14 (2008) 10134-10140.
[107] O.V. Shvets, N. Kasian, A. Zukal, J. Pinkas, J. Čejka, The Role of Template Structure and Synergism between Inorganic and Organic Structure Directing Agents in the Synthesis of UTL Zeolite, Chemistry of Materials, 22 (2010) 3482-3495.
[108] O.V. Shvets, M.V. Shamzhy, P.S. Yaremov, Z. Musilova, D. Prochazkova, J. Cejka, Isomorphous Introduction of Boron in Germanosilicate Zeolites with UTL Topology, Chemistry of Materials, 23 (2011) 2573-2585.

[109] N. Remperová, J. Přech, M. Kubů, K. Gołąbek, J.F. Miñambres, M.-F. Hsieh, A. Turrina, M. Mazur, Gas-phase isomerisation of m-xylene on isoreticular zeolites with tuneable porosity, Catalysis Today, 390-391 (2022) 78-91.
[110] Y. Zhou, S.A. Kadam, M. Shamzhy, J. Čejka, M. Opanasenko, Isoreticular UTL-Derived Zeolites as Model Materials for Probing Pore Size–Activity Relationship, ACS Catalysis, 9 (2019) 5136-5146.
[111] P.S. Wheatley, P. Chlubná-Eliášová, H. Greer, W. Zhou, V.R. Seymour, D.M. Dawson, S.E. Ashbrook, A.B. Pinar, L.B. McCusker, M. Opanasenko, J. Čejka, R.E. Morris, Zeolites with Continuously Tuneable Porosity, Angewandte Chemie, 126 (2014) 13426-13430.
[112] S.E. Henkelis, M. Mazur, C.M. Rice, G.P.M. Bignami, P.S. Wheatley, S.E. Ashbrook, J. Čejka, R.E. Morris, A procedure for identifying possible products in the assembly–disassembly–organization–reassembly (ADOR) synthesis of zeolites, Nature Protocols, 14 (2019) 781-794.
[113] C. Isaac, J.-L. Paillaud, T.J. Daou, A. Ryzhikov, Synthesis of BEC-type germanosilicates with asymmetric diquaternary ammonium salts, Microporous Mesoporous Mater., 312 (2021) 110804.
[114] S.E. Henkelis, M. Mazur, C.M. Rice, P.S. Wheatley, S.E. Ashbrook, R.E. Morris, Kinetics and Mechanism of the Hydrolysis and Rearrangement Processes within the Assembly–Disassembly–Organization–Reassembly Synthesis of Zeolites, Journal of the American Chemical Society, 141 (2019) 4453-4459.
[115] G.P.M. Bignami, D.M. Dawson, V.R. Seymour, P.S. Wheatley, R.E. Morris, S.E. Ashbrook, Synthesis, Isotopic Enrichment, and Solid-State NMR Characterization of Zeolites Derived from the Assembly, Disassembly, Organization, Reassembly Process, Journal of the American Chemical Society, 139 (2017) 5140-5148.
[116] M. Mazur, P. Chlubná-Eliášová, W.J. Roth, J. Čejka, Intercalation chemistry of layered zeolite precursor IPC-1P, Catalysis Today, 227 (2014) 37-44.
[117] M. Shamzhy, M. Mazur, M. Opanasenko, W.J. Roth, J. Cejka, Swelling and pillaring of the layered precursor IPC-1P: tiny details determine everything, Dalton Transactions, 43 (2014) 10548-10557.
[118] M. Mazur, P.S. Wheatley, M. Navarro, W.J. Roth, M. Položij, A. Mayoral, P. Eliášová, P. Nachtigall, J. Čejka, R.E. Morris, Synthesis of 'unfeasible' zeolites, Nature Chemistry, 8 (2016) 58-62.
[119] Y. Li, J.H. Yu, R.R. Xu, Criteria for Zeolite Frameworks Realizable for Target Synthesis, Angewandte Chemie-International Edition, 52 (2013) 1673-1677.
[120] X. Li, M.W. Deem, Why Zeolites Have So Few Seven-Membered Rings, The Journal of Physical Chemistry C, 118 (2014) 15835-15839.
[121] V. Zholobenko, C. Freitas, M. Jendrlin, P. Bazin, A. Travert, F. Thibault-Starzyk, Probing the acid sites of zeolites with pyridine: Quantitative AGIR measurements of the molar absorption coefficients, Journal of Catalysis, 385 (2020) 52-60.
[122] M. Jaroniec, K.P. Gadkaree, J. Choma, Relation between adsorption potential distribution and pore volume distribution for microporous carbons, Colloids and Surfaces A: Physicochemical and Engineering Aspects, 118 (1996) 203-210.
[123] A. Zukal, M. Opanasenko, M. Rubeš, P. Nachtigall, J. Jagiello, Adsorption of pentane isomers on metal-organic frameworks Cu-BTC and Fe-BTC, Catalysis Today, 243 (2015) 69-75.
[124] K.E. Wisniewski, R. Wojsz, Description of water vapor adsorption on various cationic forms of zeolite Y, Zeolites, 12 (1992) 37-41.
[125] A.I. Lupulescu, M. Kumar, J.D. Rimer, A Facile Strategy To Design Zeolite L Crystals with Tunable Morphology and Surface Architecture, Journal of the American Chemical Society, 135 (2013) 6608-6617.
[126] C.V. Ramana, G. Carbajal-Franco, R.S. Vemuri, I.B. Troitskaia, S.A. Gromilov, V.V. Atuchin, Optical properties and thermal stability of germanium oxide (GeO2) nanocrystals with α-quartz structure, Materials Science and Engineering: B, 174 (2010) 279-284.
[127] Y.-J. Lee, J.S. Lee, K.B. Yoon, Synthesis of long zeolite-L crystals with flat facets, Microporous and Mesoporous Materials, 80 (2005) 237-246.

[128] L.A. Villaescusa, P.A. Barrett, M. Kalwei, H. Koller, M.A. Camblor, Synthesis and Physicochemical Characterization of an Aluminosilicate Zeolite with IFR Topology, Prepared by the Fluoride Route, Chemistry of Materials, 13 (2001) 2332-2341.
[129] K. Ogorzały, G. Jajko, K. Wolski, S. Zapotoczny, M. Kubů, W.J. Roth, B. Gil, W. Makowski, Catalytic activity enhancement in pillared zeolites produced from exfoliated MWW monolayers in solution, Catalysis Today, 390-391 (2022) 272-280.
[130] O. Kikhtyanin, P. Chlubná, T. Jindrová, D. Kubička, Peculiar behavior of MWW materials in aldol condensation of furfural and acetone, Dalton Transactions, 43 (2014) 10628-10641.
[131] E. Xing, Y. Shi, W. Xie, F. Zhang, X. Mu, X. Shu, Temperature-controlled phase-transfer hydrothermal synthesis of MWW zeolites and their alkylation performances, RSC Advances, 6 (2016) 29707-29717.
[132] S.A. Schunk, D.G. Demuth, B. Schulz-Dobrick, K.K. Unger, F. Schüth, Element distribution and growth mechanism of large SAPO-5 crystals, Microporous Materials, 6 (1996) 273-285.
[133] A. Corma, F. Rey, S. Valencia, J.L. Jorda, J. Rius, A zeolite with interconnected 8-, 10- and 12-ring pores and its unique catalytic selectivity, Nature Materials, 2 (2003) 493-497.
[134] M. Jin, O. Veselý, C.J. Heard, M. Kubů, P. Nachtigall, J. Čejka, L. Grajciar, The Role of Water Loading and Germanium Content in Germanosilicate Hydrolysis, The Journal of Physical Chemistry C, 125 (2021) 23744-23757.
[135] J.I. Brauman, L.K. Blair, Gas-phase acidities of alcohols, Journal of the American Chemical Society, 92 (1970) 5986-5992.
[136] S.E. Henkelis, S.A. Morris, M. Mazur, P.S. Wheatley, L.N. McHugh, R.E. Morris, Monitoring the assembly–disassembly–organisation–reassembly process of germanosilicate UTL through in situ pair distribution function analysis, Journal of Materials Chemistry A, 6 (2018) 17011-17018.
[137] W.J. Roth, Cation size effects in swelling of the layered zeolite precursor MCM-22-P, Polish Journal of Chemistry, 80 (2006) 703-708.
[138] P. Chlubna, W.J. Roth, A. Zukal, M. Kubu, J. Pavlatova, Pillared MWW zeolites MCM-36 prepared by swelling MCM-22P in concentrated surfactant solutions, Catalysis Today, 179 (2012) 35-42.
[139] M. Mazur, P. Chlubná-Eliášová, W.J. Roth, J. Čejka, Intercalation chemistry of layered zeolite precursor IPC-1P, Catalysis Today, 227 (2014) 37-44.
[140] N. Sato, T. Hayashi, K. Tochigi, H. Wada, A. Shimojima, K. Kuroda, Synthesis of Organosilyl-Functionalized Cage-Type Germanoxanes Containing Fluoride Ions, Chemistry – A European Journal, 25 (2019) 7860-7865.
[141] D.S. Firth, S.A. Morris, P.S. Wheatley, S.E. Russell, A.M.Z. Slawin, D.M. Dawson, A. Mayoral, M. Opanasenko, M. Položij, J. Čejka, P. Nachtigall, R.E. Morris, Assembly–Disassembly–Organization–Reassembly Synthesis of Zeolites Based on cfi-Type Layers, Chemistry of Materials, 29 (2017) 5605-5611.
[142] A. Corma, M. Puche, F. Rey, G. Sankar, S.J. Teat, A Zeolite Structure (ITQ-13) with Three Sets of Medium-Pore Crossing Channels Formed by9- and 10-Rings, Angewandte Chemie International Edition, 42 (2003) 1156-1159.
[143] Y. Luo, S. Smeets, F. Peng, A.S. Etman, Z. Wang, J. Sun, W. Yang, Synthesis and Structure Determination of Large-Pore Zeolite SCM-14, Chemistry – A European Journal, 23 (2017) 16829-16834.
[144] J.J. DeMarco, R.J. Weiss, Absolute X-Ray Scattering Factors of Silicon and Germanium, Physical Review, 137 (1965) A1869-A1871.
[145] B.L. Henke, P. Lee, T.J. Tanaka, R.L. Shuimabukuro, B.K. Fujikawa, The Atomic Scattering Factor, f1+if2, for 94 Elements and for the 100 to 2000 eV Photon Energy Region, AIP Conference Proceedings, 75 (1981) 340-340.

8. Appendix

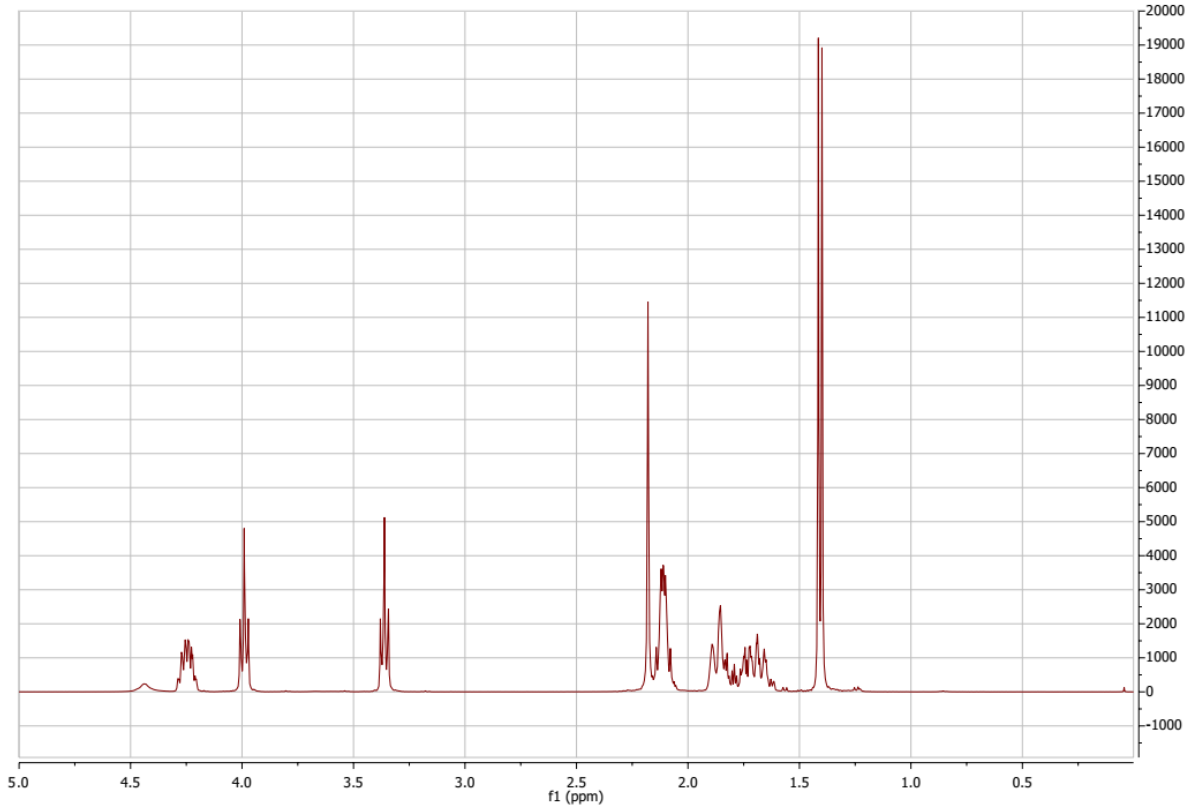

Figure A1: ^{1}H NMR spectrum of the 2,6 dimethyl 5 anizospiro[4.5]decane (DMASD) bromide in D_2O.

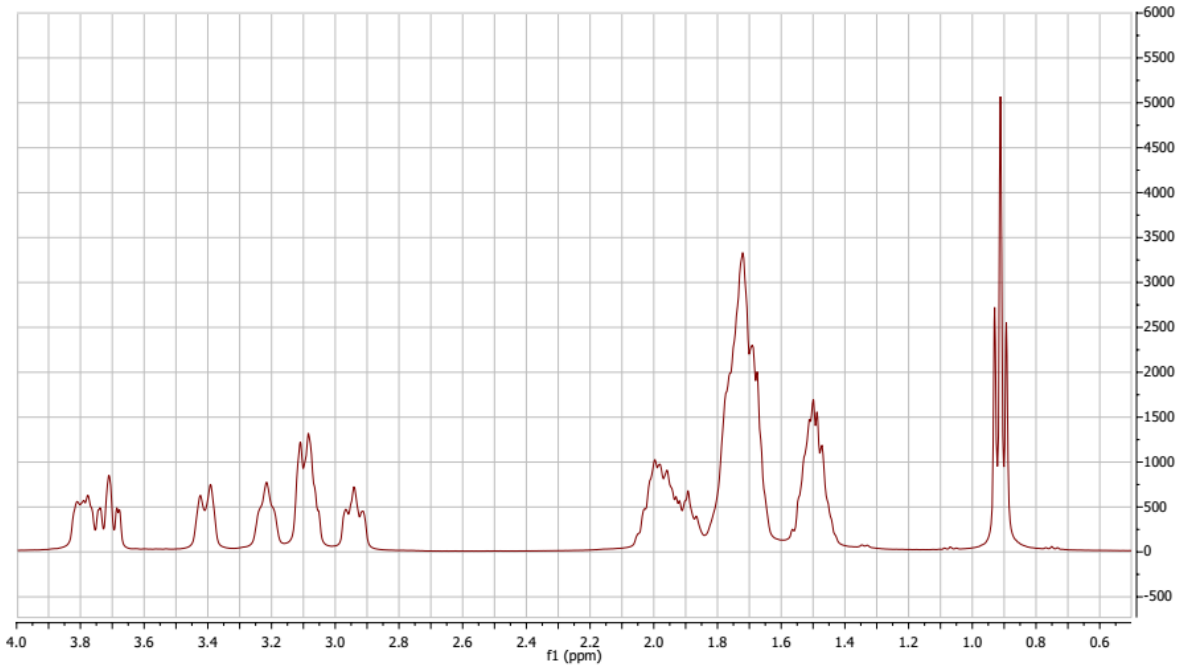

Figure A2: ^{1}H NMR spectrum of the 7-ethyl-6-azoniaspiro[5.5]undecane (EASuD) bromide in D_2O.

8. Publications

Publication 1:

Menting Jin, Ondřej Veselý, Christopher J. Heard, Martin Kubů, Petr Nachtigall, Jiří Čejka, Lukáš Grajciar

The Role of Water Loading and Germanium Content in Germanosilicate Hydrolysis

Journal of Physical Chemistry C, 125 (2021) 43 23744–23757

DOI: 10.1021/acs.jpcc.1c06873

Contribution: Water-vapour adsorption measurements, evaluation and interpretation of the adsorption data, calculation of the adsorption potential distributions and writing of the experimentally-oriented part of the manuscript.

THE JOURNAL OF PHYSICAL CHEMISTRY C
A JOURNAL OF THE AMERICAN CHEMICAL SOCIETY

pubs.acs.org/JPCC

Article

The Role of Water Loading and Germanium Content in Germanosilicate Hydrolysis

Mengting Jin, Ondřej Veselý, Christopher James Heard, Martin Kubů, Petr Nachtigall, Jiří Čejka,* and Lukáš Grajciar*

Cite This: *J. Phys. Chem. C* 2021, 125, 23744−23757

Read Online

ACCESS | Metrics & More | Article Recommendations | Supporting Information

ABSTRACT: The Assembly−Disassembly−Organization−Reassembly (ADOR) process has been used extensively to prepare new zeolite frameworks based on germanosilicate precursors. The disassembly step exploits the lability of the bonds in the presence of water to selectively disconnect the framework, prior to reorganization into new framework topologies. However, a mechanistic understanding of this crucial step is lacking: specifically, the roles of heteroatom (germanium) content and water loading in zeolite hydrolytic instability. In this work, *ab initio* free energy simulations, coupled with water vapor adsorption measurements reveal that collectivity effects control the reactivity of the archetypal ADORable zeolite UTL toward water. A transition between reversible and irreversible water adsorption occurs as water loading is increased, leading to reactive transformations. Clustering of germanium is observed to activate hitherto unreported favorable hydrolysis mechanisms beyond a threshold concentration of three atoms per double four ring unit, demonstrating that the heteroatom distribution and collectivity in the hydrolysis mechanism can drastically influence zeolite framework instability. These findings suggest that control over heteroatom content, distribution, and hydration level is important to achieve the controlled partial hydrolysis of zeolitic frameworks and is likely to apply not only to other ADORable germanosilicate zeolites but also to Lewis acidic zeolites in general.

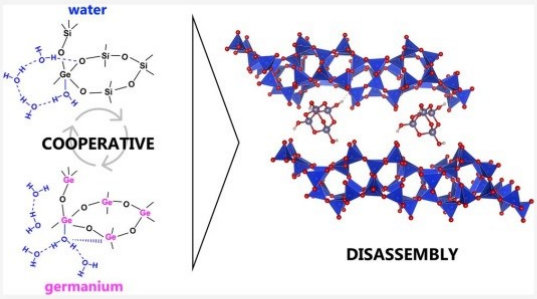

1. INTRODUCTION

Zeolites are crystalline microporous silicate materials with a wide range of applications in adsorption, gas separation, and catalysis.[1,2] New zeolitic frameworks are commonly synthesized under hydrothermal conditions. However, this hydrothermal synthesis has several constraints, including the limited number of zeolite structures that can be produced via this route.[3] Moreover, the relationship between synthesis conditions and the structure of the resulting material is still poorly understood. For this reason, new zeolite structures are often discovered by using a trial-and-error approach.

Notwithstanding these difficulties, the Assembly−Disassembly−Organization−Reassembly (ADOR) process enables us to prepare new zeolites in a controlled and predictable way.[4] ADOR exploits the lability of Ge−O bonds in germanosilicate zeolites containing double-four-ring units (D4R) (along with the tendency to remove germanium from the material). These Ge-rich D4R units can be thus hydrolyzed, leaving only the Si-rich layers intact.[5] In turn, these layers can be subsequently reorganized and reconnected into a new structure. Several germanosilicate zeolites, including UTL, *CTH, and UOV, undergo ADOR transformations,[6,7] and hydrolysis of germanium-rich UTL under mildly acidic or neutral conditions produces a stable layered material, denoted by IPC-1P.[8,9] Conversely, germanium-poor UTL does not undergo such a structural transformation, but germanium can be substituted for other elements (e.g., Al, B, and Ga) without compromising the structure.[10] Therefore, improving our understanding of the germanosilicate zeolite disassembly mechanisms upon contact with water will help us to develop targeted syntheses of ADORable frameworks. Furthermore, knowing the factors that affect hydrolytic pathways will allow us to tailor experimental conditions to optimize the process.

For such purposes, several computational studies have classified the energetic trends of Ge distributions in Ge-zeolites,[11−15] including BEC and UTL. These studies confirmed that D4R units are the most stable substitution sites for Ge. In addition, density functional calculations predict that Ge clustering in D4R likely prevails[12,16] over separated Ge

Received: August 3, 2021
Revised: October 11, 2021
Published: October 25, 2021

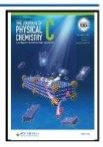

atoms. However, the collective effect of Ge clustering on the hydrolytic stability of germanosilicates remains unknown, thus requiring further research.

The hydrolysis mechanisms of several zeolites have been investigated in detail by combining *in situ* experimental (particularly infrared and NMR spectroscopy) and computational (density functional theory) research.[17] The hydrolytic behavior can also be analyzed by water vapor adsorption under various water loadings and temperatures, thereby gaining a fine control over reactive conditions inside the zeolite. This technique is commonly used to assess the hydrolytic stability/lability of zeolites or their separation properties, but few studies have examined their structural changes.[18−20] Yet, water vapor adsorption can even be used to describe the energetics of sites that participate in the hydrolysis process and thus identify the distribution of reactive sites and the hydrolysis mechanism. For example, Simonot-Grange used water vapor adsorption to differentiate adsorption sites and to investigate irreversible structural transformations of natural zeolites.[21] As germanosilicates also undergo structural transformations upon contact with water, a similar method should be suitable for investigating water vapor interactions with germanosilicates to determine their behavior under varying water loadings.

Complementary density functional theory molecular dynamics simulations have recently been used to probe the effects of water on zeolite framework stability,[22] heteroatom distributions,[23] and hydrolysis mechanisms.[24,25] Several authors observed that the water concentration markedly affects the mechanism and, consequently, the energetics of zeolite hydrolysis.[24−26] For non-aluminosilicates, nevertheless, only a few studies have examined the reactive interaction of Sn- and Ti-substituted zeolites with water, showing that new, catalytically active, open sites may be formed through hydrolysis in zeolites such as BEC,[13] BEA,[13,27,28] or MFI.[29] However, the hydrolysis mechanisms of germanosilicates remain mostly unknown even though they are the most common ADOR parent materials.

Considering the above, we aim to investigate the disassembly of germanosilicate UTL by combining water vapor adsorption and biased *ab initio* molecular dynamics simulations. In this study, we monitored the adsorbed amounts of water in relation to the germanium content and described its behavior using adsorption potential distributions. Water vapor adsorption isotherms revealed two adsorption modes: one reversible, at low partial pressure (low water content), and the other irreversible, at high partial pressure (high water content). The simulations at the density functional level, including biased molecular dynamics, linked the two-modal behavior to water physisorption at low water content and to the reactive hydrolytic transformation at high water content. The adsorbed amounts, in both modes, clearly depended on the germanium content. Moreover, this experimental observation was confirmed upon identifying a previously unknown mechanism at a high Ge content, which was contingent on the presence of a critical concentration of Ge in the double-four-ring sites.

2. METHODS AND MODELS

2.1. Experimental Section. *2.1.1. Materials.* UTL-zeolites (UTL-2.5 and UTL-4.5; the number corresponds to molar ratio Si/Ge determined by ICP-OES) were synthesized based on procedures described in the literature.[30,31] The syntheses were performed under agitation in Teflon-lined stainless-steel autoclaves at high temperature and autogenous pressure. Subsequently, the autoclaves were cooled to room temperature, and the solid product was filtered off, washed with distilled water, and dried in an oven at 60 °C overnight. The samples were calcined under flowing air at 580 °C for 8 h at a heating rate of 1 °C min^{-1}. UTL-18.5 and UTL-53 were prepared by degermanation of as-made UTL-2.5.[32] The as-made UTL was mixed with 1 M HNO_3 and heated to 190 °C for 24 h in a Teflon-lined, stainless-steel autoclave. The procedure resulted in UTL-18.5. UTL-18.5 was subsequently degermanated by using the same procedure, yielding UTL-53. Both samples were calcined under flowing air at 580 °C for 8 h at a heating rate of 1 °C min^{-1}.

2.1.2. Characterization. The structure and crystallinity of all samples, before and after adsorption measurements, were determined by X-ray powder diffraction (XRD) on a Bruker AXS D8 Advance diffractometer equipped with a graphite monochromator and a Vântec-1 position-sensitive detector with Cu Kα radiation in Bragg−Brentano geometry, in a continuous scan mode and in the range of 3°−40° (2θ). Adsorption measurements were performed on an ASAP 2020 (Micromeritics, USA) adsorption analyzer. For the necessary accuracy in accumulating adsorption data over a wide range of pressures, the instrument was equipped with three pressure transducers (13.3 Pa, 1.33 kPa, and 133 kPa). Before the adsorption experiments, the samples were outgassed under turbomolecular pump vacuum; starting at room temperature, the zeolites were heated to 110 °C until reaching the residual pressure of 0.5 Pa. After further heating to 110 °C for 1 h, the temperature was increased (1 °C min^{-1}) to 300 °C and maintained for 8 h. This procedure was repeated after collecting the N_2 isotherms of the parent samples.

The whole sequence covered the N_2−H_2O−N_2−H_2O−N_2 analysis. The N_2 adsorption measurements were performed in a liquid nitrogen bath at −195.8 °C, whereas the H_2O adsorption experiments were conducted at 20 °C in a thermostat. The specific surface area was evaluated by using the BET method, and adsorption data in the relative pressure (p/p_0) range from 0.05 to 0.20. The volume of micropores (V_{mic}) and the external surface area (S_{ext}) were calculated by using the *t*-plot method. The adsorbed amount at $p/p_0 = 0.95$ reflects the total adsorption capacity (V_{tot}). On the basis of the DFT_{PSD} pore size distribution, we assessed the pore size of the samples (the subscript "PSD" is used throughout the text to prevent confusion with density functional theory calculations used for electronic structure problems).

The values of irreversibly bound water molecules were calculated from the adsorbed amounts per unit cell at $p/p_0 = 0.008$ on the desorption branch of the isotherm. The maximum numbers of reversibly adsorbed water molecules were extrapolated from the "knee" of the adsorption branches of the isotherms, between the low and high water-intake regions (Supporting Information Figure S1). The estimation error is negligible given the good linearity and gentle slope of the first step of the water adsorption isotherm.

For individual samples, the water adsorption potential distributions, χ, were calculated based on eq 1:

$$\chi = \frac{dn}{dA} \tag{1}$$

where n stands for the amount adsorbed and A is the adsorption potential.

The adsorption potential[33,34] is described by eq 2:

https://doi.org/10.1021/acs.jpcc.1c06873
J. Phys. Chem. C 2021, 125, 23744−23757

$$A = -RT \ln\left(\frac{p}{p_0}\right) \quad (2)$$

where T is the thermodynamic temperature of the measurement, R is the universal gas constant, and p_0 is the saturation pressure of water at 20 °C equal to 2.333 kPa.

2.2. Computational Section. *2.2.1. Models.* The UTL framework can be described as a set of dense layers containing primarily 5-rings connected via D4R units to form a two-dimensional network of perpendicular 12- and 14-ring channels. The structure of the zeolite UTL was retrieved from the IZA database,[35] transformed to the primitive cell via Niggli reduction, and optimized in siliceous form, keeping the volume fixed. This primitive unit cell of UTL, used throughout the study, contains 114 atoms, and the lattice constants are a = 16.29 Å, b = 14.04 Å, c = 12.44 Å, α = 90.00°, β = 103.80°, and γ = 64.46°. UTL has 12 T sites, each of which connected to four inequivalent oxygen atoms. We investigated three representative T sites located in D4R units (T1 and T2), T sites adjacent to D4R units (T7), and located in the UTL layer (T4, T8, and T12) (see Figure 1), following the naming convention from the IZA database. In the low water-loading simulations, a single water molecule was added to the UTL unit cell. In the high water-loading simulations, the solvent (water) was included in the pore structure, with a density of ∼1 g cm^{-3}, which corresponds to 18 molecules per unit cell. This amount falls within the range of adsorbed water amounts at high p/p_0 experimentally determined from water vapor isotherms (see below), which report between 12 and 24 water molecules/UC, depending on the Si/Ge ratio of the sample. Details on the water insertion procedure are provided in the Supporting Information (section S2.1).

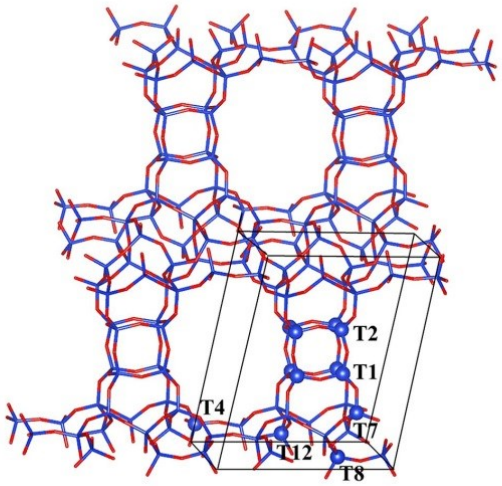

Figure 1. Structural model of the UTL zeolite, highlighting both the primitive unit cell and the T sites considered for the germanium substitution and depicting oxygen and silicon atoms in red and blue, respectively.

2.2.2. Methods. All calculations are performed by using density functional theory as implemented in the VASP 5.4 code,[36,37] with the exchange correlation functions of Perdew, Burke, and Ernzerhof,[38] and a D3 dispersion correction, with Becke–Johnson damping.[39,40] Wave functions are described by a plane-wave basis with a kinetic energy cutoff of 400 eV. The Brillouin zone (BZ) was sampled by gamma-centered Monkhorst–Pack grids, and the electronic structure was calculated at the gamma point only. Local minimization of geometry was performed with the conjugate gradient method, and convergence was defined by an energy and force tolerance of 10^{-6} eV and 0.01 eV/Å, respectively. The stabilities of reactants and products were determined based on *ab initio* molecular dynamics (AIMD) simulations. These simulations were performed in the NVT ensemble, at a target temperature of 370 K, controlled by the Nosé–Hoover thermostat. The duration of all AIMD simulations was 20–40 ps, with a time step of 0.75 fs.

The barriers to the static *equatorial* (*inversion*) and static *geminal* mechanisms were calculated by using the climbing image nudged elastic band method of Henkelman et al.[41] Transition states were verified via diagonalization of the approximate Hessian matrix, which was constructed by using finite differences. For the more complex reaction environments, especially for the high water-loading regime with *axial* and *S2R* mechanisms, slow growth (SG) and thermodynamic integration (TI)[42] simulations were used to identify the (Helmholtz) free energy barriers. One-dimensional collective variables (CV) were used in SG and TI to describe the reaction path between reactants and products. The CV were formed by a combination of bond distances describing the formation and breakage of the chemical bonds, with details provided in the Supporting Information (section S2.2, Figure S6).

The water adsorption energies in UTL were calculated via eq 3:

$$E_{ads} = E_{UTL+nH_2O} - E_{UTL} - nE_{H_2O} \quad (3)$$

where E_{UTL+nH_2O} is the total energy of water adsorbed in the unit cell of UTL, E_{UTL} is the total energy of the UTL unit cell without water, and E_{H_2O} is the energy of a single isolated water molecule in the gas phase.

The energetics of reaction steps are described by reaction energy (E_r) and reaction barrier (activation energy E_a) according to eqs 4 and 5:

$$E_r = E_{FS} - E_{IS} \quad (4)$$

$$E_a = E_{TS} - E_{IS} \quad (5)$$

where E_{IS} is the total energy of the initial state, E_{FS} is the total energy of the hydrolysis product final state, and E_{TS} is the total energy of the transition state. We will also use effective (apparent) barriers, E_a^{eff}, which we define as eq 6:

$$E_a^{eff} = E_{TS*} - E_{IS} \quad (6)$$

where E_{TS*} is the highest energy transition state along the multiple step pathways from reactants to products.

3. RESULTS

3.1. Sample Characterization and Water Vapor Adsorption. Water adsorption experiments were performed with four different UTL samples at Si/Ge ratios ranging from 2.5 to 53. Adsorption isotherms were taken for parent and partly hydrolyzed samples. The structure and crystallinity of all synthesized and hydrolyzed UTL germanosilicates were verified by powder XRD (Figure S2), in addition to assessing

https://doi.org/10.1021/acs.jpcc.1c06873
J. Phys. Chem. C 2021, 125, 23744–23757

Table 1. Textural Properties of the UTL Samples before Water Adsorption Cycle (Ads_0) and Samples after the First and Second Cycle of Water Vapor Adsorption (Ads_1 and Ads_2, Respectively)

	BET[a]			V_{mic}[b]			V_{tot}[b]		
	Ads_0	Ads_1	Ads_2	Ads_0	Ads_1	Ads_2	Ads_0	Ads_1	Ads_2
UTL-2.5	497	203	212	0.21	0.09	0.09	0.24	0.10	0.10
UTL-4.5	504	327	312	0.22	0.15	0.14	0.24	0.16	0.15
UTL-18.5	327	296	293	0.13	0.12	0.12	0.24	0.22	0.22
UTL-53	150	136	137	0.07	0.05	0.05	0.13	0.12	0.13

[a]Surface area in [$m^2\ g^{-1}$]. [b]Microporous and total porous volumes in [$cm^3\ g^{-1}$].

their elemental composition by ICP-OES and textural properties by N_2 adsorption (Figure S3). Textural properties derived from N_2 adsorption experiments of parent germanosilicates and from the first and second water-adsorption cycles are summarized in Table 1. The BET area and volume of micropores reported for UTL-2.5 and UTL-4.5 (samples obtained without a postsynthetic degermanation step) are in good agreement with previously reported values.[8,43] All samples provided a powder XRD pattern corresponding to the UTL structure,[35] but the reflections lost intensity with the decrease in germanium content. This decreased intensity of diffraction patterns (Figure S2) resulted from the lower germanium content and degree of layer connectivity after hydrolysis. All parent samples exhibited a type I N_2 adsorption isotherm; however, samples with a high Si/Ge ratio showed a small hysteresis loop at p/p_0 above 0.45 (Figure S3), which is likely the result of defects in the framework introduced by the postsynthetic degermanation.[44−46] DFT_{PSD} pore size distribution further confirmed the purely microporous nature of the material (Figure S4).

The adsorption isotherms of parent samples (first adsorption cycle) qualitatively differed from those of samples after the first adsorption cycle (Figure 2a). The first adsorption cycle (Figure 2a) is formally a type V isotherm. Regardless of Si/Ge ratio, all UTL samples show similar water adsorption isotherms at low p/p_0 (below 0.3), and the adsorbed amounts are small, corresponding to weak interactions between adsorbate and adsorbent. However, at p/p_0 above 0.3, considerable differences are observed in adsorbed amounts, hysteresis loops, and relative pressures at which water adsorption steeply increases (Figure 2a). All isotherms exhibit pronounced hysteresis upon desorption. The unclosed desorption branches of the isotherms imply that some water remains within the framework even after completing the adsorption−desorption cycle and that this amount increases with the increase in the concentration of framework germanium.

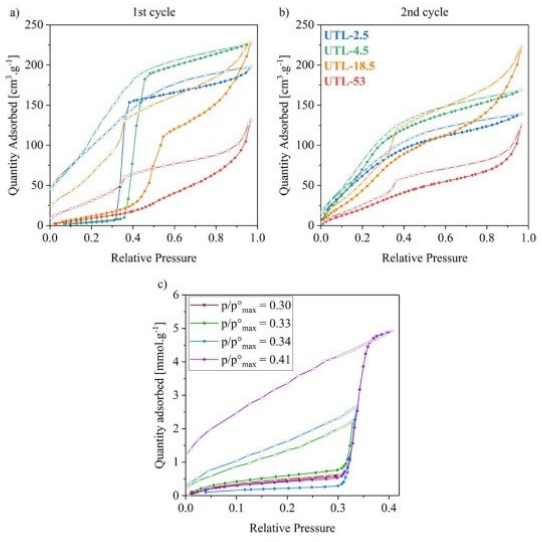

Figure 2. First (a) and second cycle (b) of the experimental water vapor adsorption (●) and desorption (○) on UTL samples at 20 °C and (c) water vapor adsorption−desorption isotherms of UTL-2.5 at 20 °C with maximum p/p_0 = 0.30, 0.33, 0.34 and 0.41.

Each adsorption isotherm contains a low-pressure region, where little adsorption occurs, followed by an increase in water uptake at higher relative pressures (Figure 2a). Adsorption isotherms of germanium-rich samples (UTL-2.5 and UTL-4.5) show a steep increase in the amount of adsorbed water within a narrow range of relative pressure between p/p_0 = 0.3 and 0.4, followed by a plateau. For further insight, the hysteresis loop was scanned to assess the reversibility/irreversibility as a function of the amount of water adsorbed in UTL-2.5 (Figure 2c and Figure S5). Water adsorption was reversible up to approximately p/p_0 = 0.3, qualitatively changing above p/p_0 = 0.3. From this point, adsorption became irreversible, leaving a significant amount of strongly bound water in the zeolite upon desorption. The amount of irreversibly bound water is proportional to the maximum p/p_0 reached in the adsorption experiment. As shown by the adsorption isotherms, Ge-poor samples (UTL-18.5 and UTL-53) show significantly smaller water uptake at $p/p_0 > 0.30$ and amounts of irreversibly bound water than Ge-rich samples.

The irreversibly bound water indicates that some structural changes occurred during the adsorption−desorption cycle, in line with the extent of changes in micropore volumes (Table 1 and Figure S3) and in XRD patterns (Figure S2) observed in parent and hydrolyzed materials. In Ge-rich samples, both the micropore volume and the intensity of XRD reflections significantly decreased. In Ge-poor samples (UTL-18.5 and UTL-53), conversely, only minor decreases were detected in micropore volumes, and the XRD pattern remained virtually unchanged. However, after the second adsorption−desorption cycle, all water vapor isotherms changed to type I (Figure 2b), with a sizable water uptake in all samples from low relative pressures and with no irreversible adsorption. Combined, these findings suggest that hydrophilic defects were formed in both Ge-poor and Ge-rich samples during the initial water adsorption, albeit with significant structural change only in Ge-rich samples. In addition, all samples became hydrolytically more stable after the initial water adsorption (presumably due to germanium leaching), and any further hydrolysis is reversible.

https://doi.org/10.1021/acs.jpcc.1c06873
J. Phys. Chem. C 2021, 125, 23744−23757

To quantify the effect of germanium content, we calculated the following characteristics from the adsorption isotherms: (i) the number of reversibly and irreversibly bound water molecules and (ii) adsorption potential distributions. In Figure 3, the number of reversibly and irreversibly bound water

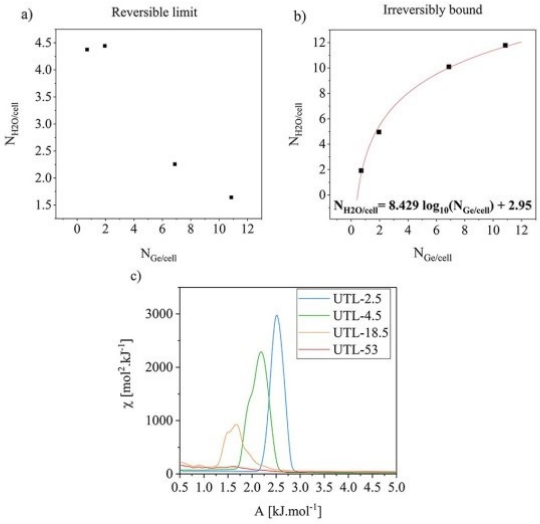

Figure 3. Experimental number of (a) reversibly and (b) irreversibly bound water molecules as a function of the number of germanium atoms per unit cell. (c) Adsorption potential distributions of UTL samples.

molecules (Table S1) is plotted against the number of germanium atoms per unit cell (for unit cell definition see section 2.2.1) in each sample. We found that the number of reversibly bound molecules is indirectly proportional to the number of germanium atoms per unit cell (Figure 3a), whereas the number of irreversibly bound water molecules varies linearly with the natural logarithm of the number of Ge atoms per unit cell (Figure 3b).

The germanium content also affects the pressure range at which the major water uptake occurs (Figure 2a), and this is reflected by the adsorption potential distributions (Figure 3c) that measure the rate of adsorption as a function of water vapor chemical potential, that is, as a function of a negative logarithm of the relative pressure (see section 2.1.2). The largest maxima in adsorption potential distribution A_{max} corresponds to the major peak in the water uptake and shifts to higher relative pressures as the Ge content decreases. In addition, the modality of adsorption potential distributions increases with Si/Ge; only one maximum is clearly discernible for UTL-2.5, whereas multiple local maxima are identified in UTL-4.5, UTL-18.5, and UTL-53, thus suggesting that the heterogeneity of water interaction sites/modes increased with the decrease in Ge content. Lastly, adsorption potential distribution modes corresponding to the heterogeneous interaction sites/modes in UTL-4.5, UTL-18.5, and UTL-53 samples overlap, indicating that water interacts with them simultaneously. In summary, the water vapor adsorption experiments revealed that water adsorption on germanosilicate UTL samples proceeds in two modes: a reversible mode at relatively low water vapor pressures up to about 0.3 p/p_0 and an irreversible mode at higher water vapor pressures, from which point a portion of adsorbed water molecules remain in the zeolite framework even when the water partial pressure drops to zero.

3.2. Mechanistic Analysis. To assess the effect of Ge content and water loading on water adsorption, we performed simulations for UTL models with various Si/Ge ratios, considering both low- and high-water regimes in micropores (1 and 18 water molecules per UTLunit cell, respectively) and both nonreactive (physisorption) and reactive (chemisorption) water interactions with the framework. The results showed an intriguing variability in water−framework interactions with respect to water loading and Ge content.

3.2.1. Physisorption at a Low-Water Regime. Ge-Poor UTL. We evaluated water physisorption near an isolated Ge atom in the UTL framework for the 1Ge-UTL pristine (nondefective) model (see section S2.3 for details) considering germanium located in framework positions of the D4R unit, near the D4R unit, and in the 2D layer (Figure 1). After calculating the adsorption energies of single water molecules adsorbed near the Ge atom at a particular T site and in a similar position in the purely siliceous model of UTL (0Ge-UTLmodel), we determined that the adsorption affinity near an isolated germanium atom was relatively low (Table S2). In our modeling, we identified two types of water adsorption complexes: (i) *O-down* complexes (close O_w−Ge contact in the range 2.34−2.83 Å) in which germanium acts as a Lewis acid site, extending its coordination sphere to five,[47] and (ii) *H-down* complexes, which show no specific germanium−water interaction and are characterized only by one or two close H_w−O_f contacts (2.04−2.52 Å). These structures are similar to local minima of water adsorbed in the purely siliceous UTL framework, not only in geometry but also in adsorption energies (see Table S2 and Figure S7b). *O-down* water complexes, when allowed by the framework, are typically 5−10 kJ mol^{-1} more stable than *H-down* complexes. The most stable water complex is the *O-down* water complex on the T4 site, with an adsorption energy of −38 kJ mol^{-1}. The average water adsorption energy on 1Ge-UTL models amounts to −28 ± 6 kJ mol^{-1} (in line with previously reported values for Ge-BEA[47]), which is approximately 2−3 kJ mol^{-1} higher than the average water stabilization in the purely siliceous UTL framework. In addition, including temperature effects in *ab initio* molecular dynamics (AIMD) simulations confirms that water affinity to germanium Lewis sites is similar to that of a purely siliceous sample (see details about AIMD simulations and their analysis in section S2.3, Figures S8−S10 in particular). Hence, we conclude that parent, defect-free germanium-substituted UTL with a low germanium concentration (Si/Ge > 37) should be almost as hydrophobic as a purely siliceous framework because the isolated germanium atoms are not particularly strong water-adsorption sites.

Ge-Rich UTL. We assessed the framework Ge content effect on water physisorption in UTL considering Ge substitution in D4R unit which contained 1, 2, 3, 4, and 8 Ge atoms (Figure S7). We observed an increase in physisorption energy of up to 10 kJ mol^{-1} over 1Ge-UTL models containing single Ge in D4R sites. The enhanced stabilization may be related to changes in the structure of the water adsorption complex. Starting from the 3Ge-UTL model, water can interact with two Ge atoms, forming two pentacoordinated Ge centers (Figures S7d−f and S11).

https://doi.org/10.1021/acs.jpcc.1c06873
J. Phys. Chem. C 2021, 125, 23744−23757

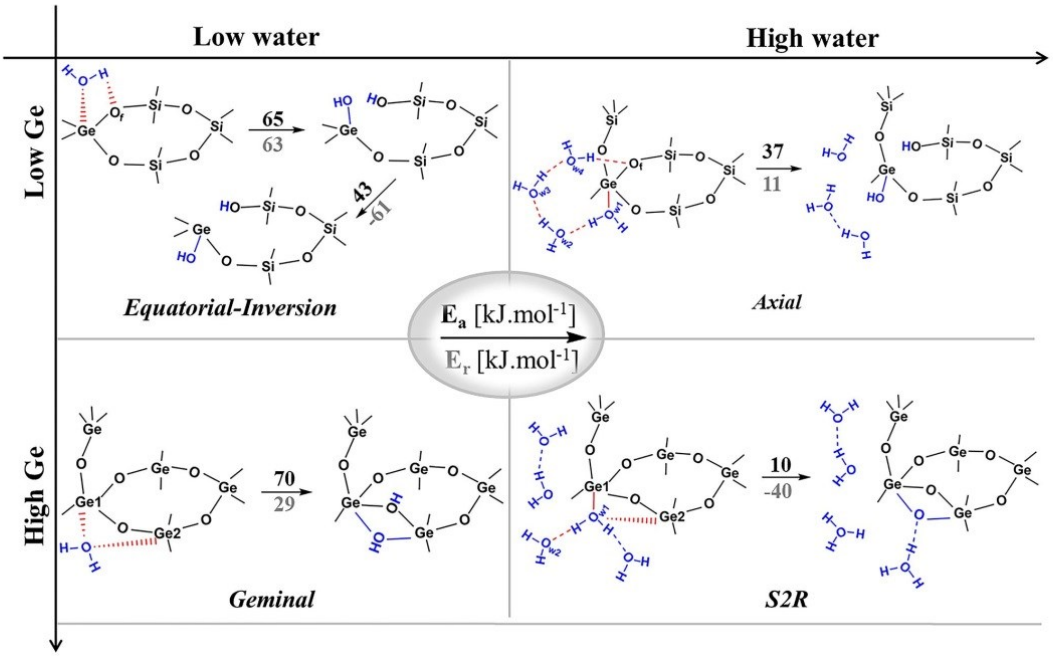

Figure 4. Scheme summarizing mechanisms identified in this study as a function of water loading and germanium content. The corresponding activation and reaction energies for each mechanism are provided above and below the reaction arrows, respectively. Atoms initially present in the zeolite framework are written in black, and atoms originating from the water solvent are highlighted in blue.

3.2.2. Hydrolysis at a Low-Water Regime. We considered the hydrolysis of Ge−O bonds in both Ge-poor and Ge-rich environments and found that, unlike physisorption, hydrolysis proceeds via qualitatively different mechanistic routes in both environments (see Figure 4).

Ge-Poor UTL. We analyzed the mechanism of Ge−O bond hydrolysis for three different locations of Ge atoms, always considering all four adjacent framework oxygen atoms (Figure S12). Hydrolysis starts via an *equatorial* step (Figure 4), as previously described in the literature for the hydrolysis of Si−O bonds,[17,48−51] with reaction barriers of at least 65 kJ mol^{-1}. The equatorial mechanism starts with the approach of a water molecule to the Ge−O bond. The water oxygen (O_w) atom interacts weakly with the Ge atom, with a local minimum on the potential energy surface corresponding to adsorption (see previous section). A four-center transition state is reached, in which a bond is formed between O_w and Ge, and a second bond is formed between a water hydrogen (H_w) and the framework oxygen (O_f) adjacent to Ge. These new bonds are formed as the intramolecular water O−H bond and the framework Ge−O bonds are weakened. The reaction product is an unstable Q^3Ge species (Figure 5). In this configuration, germanol and silanol groups partly repel each other attempting to occupy the same position in space with hydrogen bonding unable to compensate for the induced strain. In addition, their alignment is optimal for the reverse dehydroxylation. Thus, the equatorial reaction step is endothermic, and its products are unstable (reaction energies above 33 kJ mol^{-1}, Figure S12).

Both reaction energies and activation barriers vary between individual Ge−O bonds (33−130 and 65−134 kJ mol^{-1}, respectively), but they do not depend significantly on the location of the framework Ge atom (in the D4R unit, next to D4R, and in the 2D layer, Figure S12) when comparing minimum-energy paths for each T site. The equatorial products are somewhat less unstable for layer (T4) and D4R-adjacent (T7) sites than for the D4R T1 site, which could be related to the larger strain in D4R sites. A similar observation about instability of the equatorial Q^3Ge products was reported earlier for Ge-poor BEC zeolite.[13] Given the

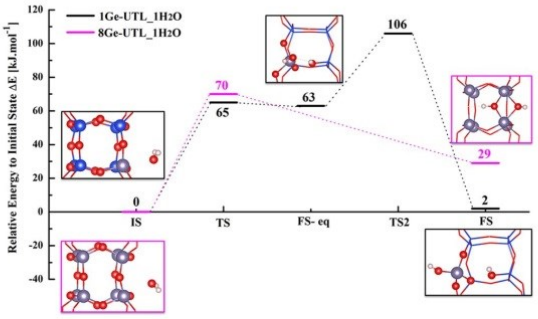

Figure 5. Calculated reaction profiles of the initial phase of UTLhydrolysis in the low-water regime (1 H_2O/UC) in Ge-rich and Ge-poor models. Only the reaction profile of the most labile Ge−O bonds are depicted (see the Supporting Information for the reaction profiles of other bonds). The black line represents the reaction profile of the Ge-poor UTL model, with one Ge atom substituted at the T1 site. The pink line represents the reaction profile of the Ge-rich UTL model, with all T sites in the D4R unit substituted by germanium atoms. The structures of the initial, intermediate, and final states are shown in the inset. Energies are expressed as kJ mol^{-1}. Germanium atoms are highlighted in violet.

https://doi.org/10.1021/acs.jpcc.1c06873
J. Phys. Chem. C 2021, 125, 23744−23757

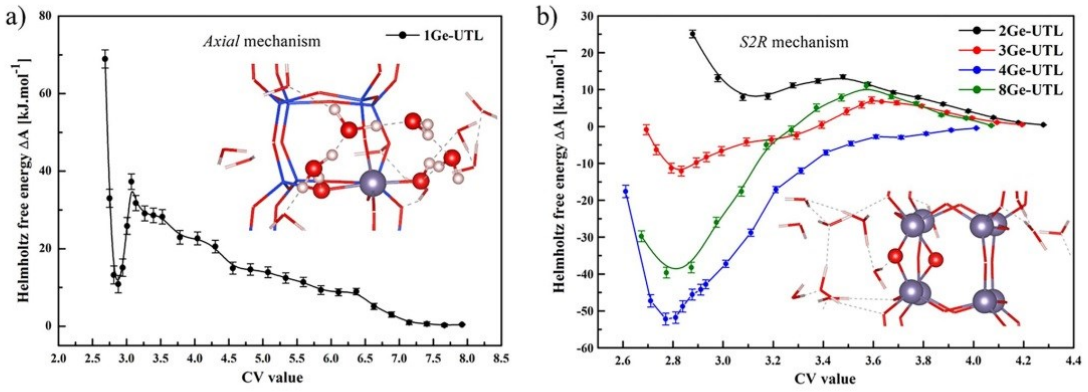

Figure 6. Calculated free energy profiles of the first hydrolysis step at a high-water content according to the (a) *axial* mechanism with a low Ge content and to the (b) *S2R* mechanism at a high Ge content. Insets correspond to representative structures of the (a) transition state at a low Ge content and the (b) final *S2R* product for the 8Ge-UTL model.

instability of the equatorial Q^3Ge products, we considered further transformations. The equatorial Q^3Ge product (Figure 5) can be inverted (when allowed by the topology; see section S2.4) into an axial Q^3Ge product (Figure 5) by Ge−OH group transfer to an axial position with respect to the initially adjacent silanol group. Hence, we identified this two-step process as an *equatorial-inversion* (EI) mechanism.

Regardless of the location of framework Ge, axial products are only 2−14 kJ mol^{-1} above reactants, and hydrolysis may accordingly proceed further. Similar inversion mechanisms have been previously proposed for tin-containing zeolites.[27,28] The inversion barriers vary significantly between Ge−O bonds (see section S2.4 for more details). In a feasible inversion step at the T1 site, the inversion is associated with an activation barrier of ∼43 kJ mol^{-1}. As a result, the overall effective barrier for breaking the first Ge−O bond in UTL can be as high as 106 kJ mol^{-1}. Moreover, evaluations of further hydrolysis steps ($Q^3 \rightarrow Q^2$, $Q^2 \rightarrow Q^1$, and $Q^1 \rightarrow Q^0$ steps) also show that at the low water limit the initial $Q^4 \rightarrow Q^3$ step is the rate-limiting step (Figure S13).

Ge-Rich UTL. The hydrolysis of Ge-rich UTL proceeds via a (double) *geminal* germanol mechanism (Figure 4 and Figure S14), with an activation barrier of 70 kJ mol^{-1} and a reaction energy of 29 kJ mol^{-1} for the 8Ge-UTL model (D4R unit consisting of eight Ge atoms). The *geminal* mechanism starts with water adsorption between two Ge atoms of a D4R edge (Figure 5). In the transition state, the incoming water deposits one of its hydrogens (H_w) on the framework oxygen (O_f) of the Ge−O_f−Ge unit, with the remaining OH group attaching to one of the Ge atoms in the Ge−O_f−Ge unit. The reaction ends with a distortion of the D4R unit that allows the OH group of water to bridge to the second germanium in the Ge−O_f−Ge unit. The final double *geminal* product (Figure 5) contains the Ge−(O_fH_w)(O_wH_w)−Ge motif in which both Ge centers are five-coordinated, with all Ge−O bonds mildly elongated (by about 0.15 Å).

Similar *geminal* mechanisms have been reported earlier for aluminosilicate zeolites by Malola et al.,[17,52] termed the *vicinal* disilanol mechanism, albeit with much higher reaction barriers when forming either double geminal silanols or geminal aluminol and silanol pairs. From the *geminal* product, the hydrolysis can proceed via the standard equatorial-inversion mechanism (Figure S14b), but the overall effective barriers (70 kJ mol^{-1}) are lower and the reaction energies (−49 kJ mol^{-1}) more favorable than in Ge-poor UTL. Hence, even under low-water concentration conditions, the probability of germanosilicate UTL hydrolysis increases with the germanium content. However, the activation barriers are still high, and the initial reactions are endothermic.

Limits of the Low-Water Regime Model. Under low-water conditions, the model becomes less realistic as hydrolysis proceeds (or in the second adsorption/desorption cycle) because hydrolytic intermediates/products significantly increase the hydrophilicity of the UTL framework. For quantitative purposes, we considered models in which a single water molecule adsorbs on the double *geminal* product of the 8Ge-UTL model and on the *axial* and *equatorial-inversion* products of the 1Ge-UTL model (see Figure 5 and Table S3). The hydrogen bonds between hydrolytic intermediates and water are strong, with stabilization ranging from 52 kJ mol^{-1}, in the double geminal product of the 8Ge-UTL model, to 68 kJ mol^{-1}, in the Q^1 equatorial-inversion product of 1Ge-UTL (see section S2.4 for more details). This stabilization is already comparable to that of a water molecule in liquid water,[53,54] increasing the affinity of UTL to water almost 2-fold over pristine UTL (see section 3.2.1). Hence, once the hydrolysis associated with the formation of hydrophilic intermediates starts, the equilibrium water loading in such an incipiently defective UTL should rise steeply (see also experimental data in Figure 2a,b).

3.2.3. Hydrolysis at a High-Water Regime. Experimental adsorption isotherms show that at relative water pressures p/p_0 = 0.3−0.4 UTL samples abruptly adsorb large amounts of water, increasing the mean water concentration from 1 to 2 to approximately 12−24 water molecules per unit cell, depending on the Si/Ge ratio of the sample. Therefore, in the next step, we considered models with a significantly increased water concentration inside the UTL channels using biased AIMD simulations. We focused on a single, high-water loading model with 18 waters/UC, which we used for all our Ge-UTL models with varying Si/Ge ratios. As in section 3.2.2, we considered water interactions with the *germanium-poor* and *germanium-rich* framework, limiting our investigation to Ge exchanged in T sites in the D4R unit. The results showed that water interactions are qualitatively different in these regimes (see Figure 4).

https://doi.org/10.1021/acs.jpcc.1c06873
J. Phys. Chem. C 2021, 125, 23744−23757

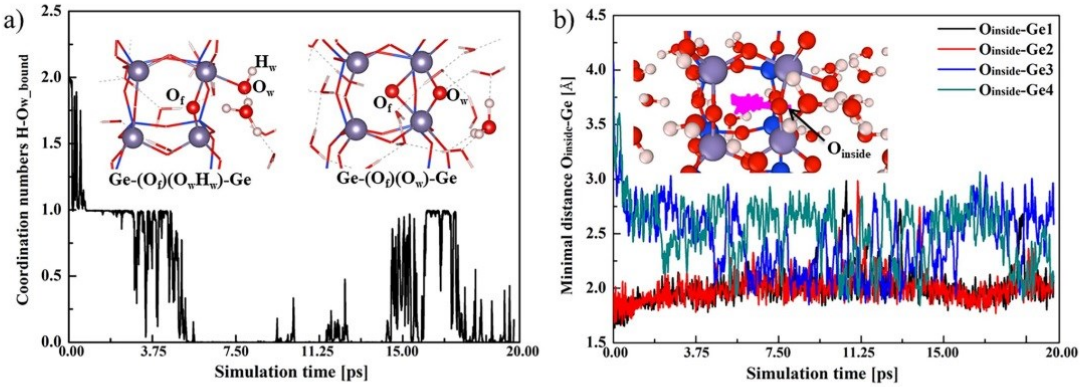

Figure 7. Time evolution of multiple characteristics derived from equilibrium AIMD simulations of the 4Ge-UTL model with 18 H_2O/UC: (a) Number of O_w−H bonds between the oxygen atom of water, O_w, inserted into the Ge−O_f−Ge unit, during the AIMD simulations, and the hydrogens in the unit cell. The insets show representative snapshots of the trajectory depicting structures with one O_w−H bond, i.e., Ge−(O_f)(O_wH_w)−Ge unit, and without a O_w−H bond, i.e., Ge−(O_f)(O_w)−Ge unit. (b) Minimal distance between the oxygen atom (formally O_f, termed O_{inside}) inside the ring and all four Ge atoms when the S2R product, i.e., Ge−(O_f)(O_w)−Ge unit, is formed during AIMD simulations. The inset shows movement of the oxygen atom O_{inside} the D4R unit during the AIMD simulations using trajectory lines (in pink).

Ge-Poor UTL. Short equilibrium AIMD simulations (40 ps) performed with the 1Ge-UTL model (Ge in T1 site) revealed an increased water affinity to germanium Lewis sites. During its trajectory, a water molecule binds to germanium (see Figure S15)) in an O-down fashion, and the O_w−Ge bond is much shorter (as low as 1.956 Å) in this complex than even in the most stable *O-down* complexes (at least 2.3 Å long; see Figures S10 and S11) at the low-water regime (see section 3.2.1). Hence, the Ge atom becomes five-coordinated with five almost equivalent Ge−O bonds (see Figure S15). The five-coordinated germanium does not last throughout the trajectory. However, water molecules stay close to the Ge site (average O_w−Ge distance is below 4 Å) and attempt to adsorb intermittently. Accordingly, increasing the water content of the *Ge-poor* UTL framework will likely increase the water affinity of germanium Lewis acid sites, thereby inducing, at least intermittently, the formation of five-coordinated Ge centers.

These five-coordinate Ge centers are actually intermediates in a novel, low-barrier Ge−O hydrolysis mechanism, which directly leads to the formation of stable axial Q^3 products (Figure 4). The free energy barrier, $\Delta A^{\ddagger}$, of the *axial* mechanism can be as low as 37 kJ mol^{-1} (based on the thermodynamic integration of constrained AIMD simulations; see Table S4 and Figure 6a). The *axial* reaction mechanism at the O3 framework oxygen starts with water adsorption on Ge and the formation of the five-coordinated Ge center. Subsequently, a proton is detached from the adsorbing water and shuttled via a chain of solvent water molecules between this interacting water and the adjacent framework oxygen in an axial position. The proton shuttled via the Grotthuss mechanism helps to break the Ge−O bond, which is followed by inversion of the GeO_3OH tetrahedron. The mechanism ends with the formation of silanol and germanol groups, which are in antipositions to each other, i.e., the axial Q^3 product.

This axial Q^3 product is as in the low-water regime, only a few kJ mol^{-1} (11 kJ mol^{-1}) less stable than the reactants (see Figures 4 and 6a). The activation barrier is lower in the *axial*- than in the *equatorial-inversion* mechanism because the framework oxygen in the axial position is more labile, as confirmed by population analysis, electrostatic potential maps, and projected density of states (see Figures S17 and S18, Table S5) of the five-coordinated Ge center. In summary, increasing water loading in UTL channels opens up a new hydrolysis path, the *axial* mechanism, by decreasing the activation barrier to the first Ge−O hydrolysis step.

Ge-Rich UTL. Increasing the water content in *germanium-rich* UTL models (above 1Ge/UC) boosts water affinity to germanium sites and, above a critical germanium concentration (approximately 3−4 Ge/UC), leads to an almost barrier-free water molecule insertion into the Ge−O_f−Ge unit (see Figure 6b). We performed short (at least 20 ps) equilibrium AIMD simulations of water adsorbed in multiple UTL models with increasing germanium content in D4R units (2, 3, 4, and 8 germanium atoms in D4R unit), with clustered Ge to probe cooperativity effects (see Figure S7 for considered germanium distributions within D4R).

In 2Ge-UTL and 3Ge-UTL models, after a few picoseconds of MD simulation (see Figures S21 and S22), a water molecule spontaneously adsorbs on germanium in either T1 or T2 sites, forming a five-coordinate Ge center, as observed in the *Ge-poor* model. This five-coordinate Ge center then remains stable throughout the simulation (more than 15 ps). In addition, the adsorbed water is intermittently deprotonated, thus forming a short-lived OH group (for a few hundred femtoseconds) with a hydroxonium nearby, i.e., another precursor of the *axial* mechanism described above. The reactivity of the D4R unit undergoes a step change when further increasing the germanium content in D4R to 4 and 8 germaniums, following a *geminal*-like mechanism, termed the *S2R* mechanism for involving the formation of Ge−$(O)_2$−Ge species.

In 4Ge-UTL and 8Ge-UTL models, water almost immediately inserts itself into the Ge−O_f−Ge unit, loses a proton, and pushes the framework oxygen O_f (of Ge−O_f−Ge unit) inside the D4R unit (see Figure 7a and Figures S23−S26). After a few picoseconds, the newly formed Ge−(O_f)(O_wH_w)−Ge unit is further deprotonated, forming the Ge−(O_f)(O_w)−Ge unit, with both protons from the incipient water now solvated in the channel, significantly acidifying the solution nearby. However, one of the protons tends to intermittently reattach to the Ge−

https://doi.org/10.1021/acs.jpcc.1c06873
J. Phys. Chem. C 2021, 125, 23744−23757

$(O_f)(O_w)$−Ge unit. Yet, the framework oxygen O_f inside the D4R is not firmly attached to the incipient Ge−$(O_f)(O_w)$−Ge unit. Instead, this D4R unit is mobile, hopping between Ge−O−Ge units in the D4R, and its mobility is higher in the 8Ge-UTL model than in the 4Ge-UTL model (see Figure 7b and Figures S23−S26).

The presence of such species inside the D4R unit is reminiscent of the well-known case of F^- anions observed in D4R units after zeolite synthesis in hydrofluoric acid.[55−57] Moreover, our tests show that the orientation of germanium-filled S4R ring in D4R unit does not qualitatively change the reported findings (see Figure S25). In conclusion, in line with the experimental observations discussed above (see section 3.1), our simulations indicate that the framework reactivity to water increases with the germanium content and that the hydrolysis dynamics abruptly change after a critical germanium content of approximately 3−4 Ge/UC wherefrom the *S2R* mechanism prevails.

To quantify the favorability of the *S2R* mechanism (Figure 4) as a function of the germanium content, we calculated free energy reaction profiles for this mechanism by thermodynamic integration of constrained AIMD simulations (see Table S4 and Figure 6b). We considered all UTL models with varying degrees of germanium exchange employed in previous sections (1, 2, 3, 4, and 8 germanium atoms in the D4R unit). The *S2R* mechanism in the 1Ge-UTL model does not lead to a stable *S2R* (or even *geminal*) product but instead to an *equatorial* product after short equilibration (see Figure S27). In all the other models with higher Ge content, the *S2R* mechanism leads, at least, to metastable products, and all activation barriers are very low (below 15 kJ mol^{-1}). The main difference between low-Ge (2Ge- and 3Ge-UTL) and high-Ge (4Ge- and 8Ge-UTL) models lies in the stability of the *S2R* products; the reactions are very exergonic in models with a high Ge content ($\Delta A_{rxn} < -30$ kJ mol^{-1}), whereas they are almost free energy neutral in models with a low Ge content ($\Delta A_{rxn} = 0 \pm 10$ kJ mol^{-1}). Hence, with enough germanium in the D4R unit, the *S2R* step can provide excess energy to the system (between 30 and 50 kJ mol^{-1}; see Table S4), which may be used for further reactive transformations, such as hydrolysis of Ge−O bonds, e.g., by using *axial* and *equatorial-inversion* mechanisms.

Based on our preliminary tests for further decomposition steps, starting at the *S2R* product (see Figure S28), the apparent activation barrier to the *S2R* step followed by Ge−O hydrolysis becomes negligible ($\Delta A^{\ddagger}_{app} \sim 0-20$ kJ mol^{-1}), with Ge−O hydrolysis proceeding via either the *axial* or *equatorial* mechanism. Overall, these findings indicate that the UTL framework should become much less hydrolytically stable when enough germanium is clustered in S4Rs (as a part of D4R) and that the water solution inside the zeolite channels becomes extremely acidic (with two protons solvated in 17 waters, i.e., pH ∼ −1, corresponding to a solution of ∼6 M strong acid).

4. DISCUSSION

4.1. Experiment vs Theory: (Ir)reversible Adsorption. Water adsorption in pristine Ge-UTL proceeds in two modes (depending on the water relative partial pressures), one reversible and the other irreversible, in which a portion of adsorbed water is fixated in the zeolite framework even when the water partial pressure drops to zero. The reversible mode, at low water partial pressures, results from the physisorption of water molecules in the interior of pristine Ge-UTL samples. The interior of Ge-UTL is only mildly less hydrophobic than that of its purely siliceous counterpart, in line with meagre water uptakes (approximately 1−2 waters per UC) up to relatively high water partial pressures (from 0.36 to 0.53 for UTL-2.5 and UTL-53, respectively).

Upon increasing the water partial pressure, the irreversible regime sets in accompanied by a steep increase in water loading, most likely associated with the reactive hydrolytic processes that generate hydrophilic defects containing silanol and germanol groups. These hydrophilic defects draw more water into the Ge-UTL channel system. As shown in our biased molecular dynamics simulations, this increased water loading decreases the reaction barriers to and energies of hydrolysis of Ge−O bonds, which generates further hydrophilic defects. In turn, these defects draw even more water inside, thereby establishing a positive feedback loop. However, as Ge-UTL micropores fill up, and all available hydrolytically labile bonds are already broken, the adsorption isotherm starts to level off. Because a step increase in water uptake is associated with reactive events that consume water molecules, the desorption branches are not closed, thus matching the irreversible regime of water adsorption.

A similar irreversibility has been observed in high-pressure water intrusion−extrusion experiments, in some zeosils (LTA, BEC, and BEA).[46] The second water vapor adsorption cycle, however, shows almost no irreversibility (Figure 2), indicating that the irreversible adsorption regime is exclusive to pristine Ge-UTL samples. Any further interaction between water and the framework is completely reversible.[25] In other words, after the first water vapor adsorption cycle, no specific irreversible adsorption sites are available to water.

4.2. Experiment vs Theory: The Role of the Ge Content. In addition to the clear water loading-dependent behavior of all Ge-UTL samples, the germanium content also plays a key role in hydrolysis. First, the water loading necessary for the irreversible regime to set in is inversely proportional to the germanium content. However, this experimentally observed function is more adequately framed in terms of the water density per UC necessary for the irreversible regime to set in in two modes: (i) more than two waters/UC on average for Ge-poor samples (UTL-53 and UTL-18.5) and (ii) only a single water/UC on average for Ge-rich samples (UTL-2.5 and UTL-4.5). This finding broadly agrees with our mechanistic data, which also indicate that the hydrolytic lability of UTL samples depends on the Ge content.

In both low- and high-water regimes, the effective activation barriers and reaction energies are significantly more favorable in Ge-rich than in Ge-poor models (see sections 3.2.2 and 3.2.3). Although computationally determining the exact water density required for the irreversible regime is still beyond the scope of this study, our data suggest that irreversibility is unlikely to occur without the collective action of multiple water molecules at a Ge site, in both Ge-poor and Ge-rich samples. In Ge-poor samples, the average experimental values of critical water density per UC are lower (∼2.2 waters/UC) than the length of the water chain, based on our calculations (∼5−6). However, water−water interactions are much stronger than water−(pristine)−zeolite interactions (see also section 3.2.1).[17,46] Therefore, water should form clusters rather than remain homogeneously distributed throughout the channel system, thus leading to heterogeneous water density in pristine Ge-UTL samples in which the water density may

https://doi.org/10.1021/acs.jpcc.1c06873
J. Phys. Chem. C 2021, 125, 23744−23757

locally cross the threshold necessary for (collective) mechanisms.

The extent of irreversibility, that is, how many waters are irreversibly bound to the framework, is positively correlated to the germanium content. In particular, experimental data highlight a logarithmic variation as a function of the germanium content. This logarithmic function indicates that the irreversibility tends to saturate as the Ge content increases and can be separated into approximately two modes (see section 3.1). To link this observation to our simulations, we normalized the number of irreversibly bound water molecules to the germanium content, that is, to the number of water molecules (irreversibly) consumed per Ge during hydrolysis. These values also show two Ge-content-dependent modes: (i) approximately 1.3−1.4 water molecules consumed per Ge in Ge-poor samples (UTL-53 and UTL-18.5) and (ii) approximately 0.55−0.75 water molecules consumed in Ge-rich samples (UTL-2.5 and UTL-4.5).

To put these values into context, excision of a single, isolated Ge from the framework requires breaking four Ge−O bonds and thus consuming four water molecules per Ge. In contrast, dissecting the whole D4R unit packed with Ge atoms from the UTL layers, despite breaking eight Ge−O bonds, requires only one water per Ge, and the number of water molecules per Ge drops even more as germanium oxide aggregates. Lastly, layer reconnection, i.e., dehydroxylation, could release water, decreasing the amount of water consumed per Ge. Combined, these findings indicate that during the irreversible regime of water adsorption in Ge-UTL samples, either large Ge oxide clusters (tetramers and larger) are formed as the end-products of complete hydrolysis, possibly associated with the layer reconnection, or Ge is only partly hydrolyzed, with Ge atoms retaining some connectivity with the framework, as shown in Sn-zeolites.[27,28]

The formation of large Ge clusters as the end-product of complete hydrolysis[58] is supported by evidence from previous theoretical and experimental (NMR) studies on the stability of "magic number" hydroxylated silicon and germanium clusters, in particular $(SiO_2)_4{\cdot}2H_2O$ and $(SiO_2)_8{\cdot}4H_2O$,[59] which are essentially the hydroxylated forms of the D4R and S4R building units.[60−62] In turn, partial Ge hydrolysis is supported by our preliminary simulation data (Figure S19) on the additional hydrolysis step ($Q^3 \rightarrow Q^2$) in low-Ge models, showing an increase in reaction barriers for the axial mechanism of approximately 70−80 kJ mol^{-1}, which therefore competes with the equatorial mechanism. A possible explanation is the interference of silanol/germanol groups in the Grotthuss proton transfer (Figure S19), which hinders further hydrolysis of isolated Ge atoms. We have previously observed incomplete hydrolysis of the aluminosilicate framework in liquid water under ambient conditions when studying the oxygen exchange mechanism in Al-CHA.[25] Hence, as shown in Sn-zeolites,[17] the number of water molecules consumed per Ge (∼1.3) indicates that partial hydrolysis prevails in Ge-poor UTL samples with mostly isolated Ge atoms.[16] In Ge-rich UTL samples (0.55−0.75), the much lower water consumption per Ge can be related to the excision of larger clusters (D4R-like octamers and S4R-like tetramers, among others) from the framework (see Figure S29), possibly followed by further agglomeration and partial reconnection of delaminated layers.

The presence of two Ge-content-dependent modes (in the number of irreversibly bound water molecules and in the water loading necessary for the irreversible mode to set in; see discussion above) implies the existence of a critical Ge concentration at which the mode switches. On the basis of a simple piecewise linear fitting of available data points for each mode (see Figure 3), we determined that this critical concentration is approximately 4 Ge/UC (Si/Ge ∼ 8.5). Furthermore, as well documented in the literature,[12,16] germanium in UTL preferentially occupies the D4R units, and the occupation of S4R units parallel to the layer may enable UTL delamination.[16] Our analysis of such a preferential clustering of Ge atoms in our computational models (see section 3.2.3) clearly shows that increasing the Ge content in S4R (as a part of D4R unit) from two to four atoms not only lowers the reaction barriers to the first hydrolytic step but also significantly stabilizes (by ∼60 kJ mol^{-1}) the resulting S2R products. As a result, the reaction becomes highly exothermic and may provide the necessary surplus energy for further reaction steps. Hence, the critical Ge concentration of ∼4 Ge/UC is linked to the formation of germanium clusters in UTL S4R units (within D4R units).

4.3. Generality of the Reaction Mechanisms. The hydrolytic mechanisms discussed in this study of the Ge-UTL model should be applicable to other zeolites with Lewis acid sites, such as tin and titanium zeolites for several reasons. First, we have previously observed the *axial* mechanism in Si−O−Si hydrolysis, in a purely siliceous CHA model,[25] confirming the general nature of such a mechanism. Second, this expectation is corroborated by recent reports of the formation of stable Q^3 axial products in Sn-BEA based on static DFT calculations.[27,28] In addition to the *axial* mechanism, the *geminal* and *S2R* mechanisms could also be theoretically generalized for tin or titanium zeolites given the propensity of these atoms, similar to germanium, to increase their coordination beyond four. However, tin and titanium zeolites can be typically prepared only with a very low heteroatom content. Therefore, such mechanisms may not be applicable to the selective hydrolysis of these zeolites.

The hydrolytic mechanisms identified in this study should also be applicable to other zeolite frameworks. The *axial* mechanism is favored when (i) T sites are accessible and (ii) a stable Q^3Ge axial product can be formed without strong steric hindrance within the framework (see section S2.4). In particular, the T site must be well accessible to water to allow, on the one hand, water adsorption followed by the formation of a pentacoordinated Ge center and, on the other hand, a proton attack to the framework oxygen in the axial position. Taking UTL as an example (see section S2.4 and Figure S12), the D4R and adjacent T sites are well accessible to axial attack but not most T sites in the UTL layer. This example further supports the (observed) increase in the hydrolytic stability of UTL layers in comparison with the interlayer.

This concept of accessibility can be extended to other zeolites and used to gauge their propensity to selective hydrolysis, justifying, for example, difficulties in the delamination of zeolites with three-dimensional channel systems.[63] In addition to the *axial* mechanism, the *geminal* and *S2R* mechanisms should also be applicable to other topologies. However, our calculations show that the *S2R* mechanism requires densely clustered germanium, e.g., in S4R rings. Accordingly, topologies unfavorable to such a dense germanium clustering may be hydrolytically stable even at low Si/Ge ratios, whereas the contrary will likely be true for

https://doi.org/10.1021/acs.jpcc.1c06873
J. Phys. Chem. C 2021, 125, 23744−23757

topologies favoring germanium clustering such as UTL. Furthermore, during the *S2R* mechanism, the water in the channel system should be strongly acidic (pH ∼ −1), which could help to explain, following le Chatelier's principle, why treating Ge-rich zeolites with strong acids[63] hinders excessive degermanation and enables controlled degermanation without a loss of crystallinity.

All novel reactive water−framework mechanisms discovered in this study are cooperative[17,24−26] and depend on germanium or water content nonlinearly. In other words, these low-energy mechanisms are very difficult to predict *a priori*, and (i) the *S2R* mechanism becomes viable only at a specific threshold of four Ge atoms clustered in S4R, whereas (ii) the *axial* mechanism becomes available only once enough water molecules can shuffle a proton toward the more reactive framework oxygen in the axial position O_{ax}. We can more easily understand and justify the viability of these mechanisms, for example, by analyzing the charge distribution on O_{ax} or by visualizing the cooperative bonding of germanium atoms in S4R to the additional oxygen embedded in the D4R unit. However, this is typically possible only in hindsight. Therefore, open-ended dynamical simulations must be used to both avoid our biases regarding expected reaction paths and investigate models under realistic conditions. Various types of *reactive* molecular dynamics simulations[64,65] stand out as ideal solutions to this problem, particularly in the mechanism exploration step, despite its significant computational costs at present. Nevertheless, these costs will most likely plummet in the future with the advent of accurate reactive machine learning potentials.[66−68]

4.4. Potential of Water Vapor Adsorption as a Characterization Method. Water vapor adsorption on UTL-zeolite revealed the complex nature of the hydrolysis of germanosilicates. Other methods, such as *in situ* solid state NMR,[5] have been previously used to investigate the hydrolysis of germanosilicates. However, only the water vapor adsorption has enabled us to directly observe the response of the zeolite to water loading. Using this method, we were able to determine the threshold of water loading (or partial pressure of water vapor) needed for the irreversible hydrolysis mechanism to set in.

The irreversible interaction occurs within a relatively narrow range of partial pressures, as illustrated by the adsorption potential distributions derived from the isotherms. This narrow range implies that the water interaction sites are energetically similar, as found in Ge-rich UTL samples with an almost unimodal adsorption potential distribution. These findings correlate with the preferential location of Ge in the D4R units and could be connected to the ability of Ge-rich samples to undergo delamination, i.e., very selective hydrolysis. Conversely, in Ge-poor samples, the adsorption potential distributions are multimodal, suggesting heterogeneous water interaction sites. These modes also overlap significantly. Consequently, the hydrolysis of Ge-poor UTL samples cannot be highly selective.

Considering the above, the location and content of Ge are crucial for the successful preparation and stability of germanosilicates and for their ability to undergo ADOR transformation.[32] The water vapor adsorption provides key insights into the response of germanosilicates to water and may prove valuable for assessing the stability of new materials and for estimating the most suitable conditions for their transformations. As such, water vapor adsorption will likely become a standard characterization method for ADORable germanosilicates and other related materials.

5. CONCLUSIONS

We investigated the hydrolysis mechanism of germanosilicate UTL using combined experimental and computational methods. The experimental water vapor adsorption isotherms revealed that adsorption consists of two different modes: one reversible, at low partial pressures, and the other irreversible, at high partial pressures. The amounts of water adsorbed in both modes depend on the germanium content, displaying a step change in the amount of irreversibly adsorbed water molecules approximately at Si/Ge = 8.5, which is equivalent to ∼4 germaniums per unit cell. The simulations at the density functional level, including biased molecular dynamics, clearly related such two-modal behavior to water physisorption at low water partial pressures and to reactive hydrolytic transformation at high partial pressures.

Reactive hydrolysis proceeds along newly established, energetically favorable mechanisms involving collective action of water molecules, which require sufficient water loading in micropores. Furthermore, simulations confirm the existence of an abrupt change in framework reactivity toward water in high-germanium models, which we relate to the availability of a novel, highly exergonic *S2R* mechanism involving water splitting, solution acidification in the micropores, and formation of Ge−$(O)_2$−Ge species. The clustering of germanium in S4R rings is essential for stabilizing Ge−$(O)_2$−Ge species and for making the *S2R* mechanism highly exergonic. This implies that germanium distribution in D4R units plays a key role in the propensity to delamination of zeolite layers. Although the importance of germanium distribution for delamination has been acknowledged before,[16,63] the underlying mechanistic remained unknown until now.

Based on our results, we also hypothesize that germanium tends to be leached from Ge-rich UTL samples in the form of large clusters (e.g., tetramers or octamers), whereas Ge-poor UTL samples undergo different transformations such as (i) complete hydrolysis of a germanium in specific T sites ending up with small hydroxylated germanium clusters or (ii) partial, possibly reversible, hydrolysis of germanium in most T sites. However, further studies are required to test these hypotheses.

This study not only identifies previously unknown hydrolysis mechanisms for germanium-substituted zeolites, which will likely be generalized to other Lewis acid zeolites, but also explains the observable disassembly behavior of ADORable zeolites at the microscopic level. Furthermore, we also provide compelling evidence of the importance of realistic, open-ended, molecular dynamics simulations to discover the complex cooperative mechanisms that occur at the interface between zeolite and water. Ultimately, our work may also help find conditions for the controlled disassembly of ADORable zeolites and, consequently, for the targeted synthesis of novel zeolites.

■ ASSOCIATED CONTENT

Supporting Information

The Supporting Information is available free of charge at https://pubs.acs.org/doi/10.1021/acs.jpcc.1c06873.

Powder XRD patterns; nitrogen and water isotherms of UTL samples; pore size distribution measurement;

https://doi.org/10.1021/acs.jpcc.1c06873
J. Phys. Chem. C 2021, 125, 23744−23757

details of free energy calculations; water physisorption in Ge-rich models from AIMD simulations; effect of germanium content on water adsorption complex structure; reaction profiles for $Q^4 \rightarrow Q^3$ step at different T sites for Ge-poor model at low water loading; reaction profiles for further degermanation steps ($Q^3 \rightarrow Q^2$, $Q^2 \rightarrow Q^1$, and $Q^1 \rightarrow Q^0$) toward full degermantion in Ge-poor model at low water loading; further hydrolysis steps for Ge-rich model at low water loading; assessment of the framework hydrophilicity after the first hydrolysis step; analysis of the lability of Ge−O bond in the axial position; further hydrolytic steps in Ge-poor models at high water loading; multiple analyses of the S2R mechanism (e.g., time evolution of Ge coordination number, partial distribution functions, etc.); results for 4Ge-UTL model with germanium atoms in S4R parallel to the UTL layer; stability of the plausible hydrolysis products in the UTL channels (PDF)

AUTHOR INFORMATION

Corresponding Authors

Jiří Čejka − *Department of Physical and Macromolecular Chemistry, Charles University, 12496 Prague 2, Czech Republic;* orcid.org/0000-0003-1400-1031; Email: jiri.cejka@natur.cuni.cz

Lukáš Grajciar − *Department of Physical and Macromolecular Chemistry, Charles University, 12496 Prague 2, Czech Republic;* orcid.org/0000-0001-9464-7769; Email: lukas.grajciar@natur.cuni.cz

Authors

Mengting Jin − *Department of Physical and Macromolecular Chemistry, Charles University, 12496 Prague 2, Czech Republic*

Ondřej Veselý − *Department of Physical and Macromolecular Chemistry, Charles University, 12496 Prague 2, Czech Republic*

Christopher James Heard − *Department of Physical and Macromolecular Chemistry, Charles University, 12496 Prague 2, Czech Republic;* orcid.org/0000-0001-8034-6121

Martin Kubů − *Department of Physical and Macromolecular Chemistry, Charles University, 12496 Prague 2, Czech Republic*

Petr Nachtigall − *Department of Physical and Macromolecular Chemistry, Charles University, 12496 Prague 2, Czech Republic;* orcid.org/0000-0002-1628-7275

Complete contact information is available at: https://pubs.acs.org/10.1021/acs.jpcc.1c06873

Author Contributions

M.J. and O.V. made equal contributions to this work.

Notes

The authors declare no competing financial interest.

ACKNOWLEDGMENTS

O.V. and M.K. acknowledge Yong Zhou for providing the starting materials. Charles University Centre of Advanced Materials (CUCAM) (OP VVV Excellent Research Teams, project number CZ.02.1.01/0.0/0.0/15_003/0000417) is acknowledged. P.N. acknowledges the Czech Science Foundation (19-21534S). L.G. acknowledges the support of the Primus Research Program of Charles University (PRIMUS/20/SCI/004). O.V., M.K., and J.Č. acknowledge the support of the Czech Science Foundation to the project EXPRO (19-27551X). This work was supported by The Ministry of Education, Youth and Sports from the Large Infrastructures for Research, Experimental Development and Innovations project "IT4Innovations National Supercomputing Center − LM2015070". The authors thank Carlos V. Melo for editing the manuscript. We are also grateful to Prof. Russell E. Morris for stimulating discussions.

REFERENCES

(1) Li, Y.; Li, L.; Yu, J. Applications of Zeolites in Sustainable Chemistry. *Chem.* **2017**, *3*, 928−949.

(2) Prech, J.; Pizarro, P.; Serrano, D. P.; Cejka, J. From 3D to 2D Zeolite Catalytic Materials. *Chem. Soc. Rev.* **2018**, *47*, 8263−8306.

(3) Li, X.; Deem, M. W. Why Zeolites Have So Few Seven-Membered Rings. *J. Phys. Chem. C* **2014**, *118* (29), 15835−15839.

(4) Mazur, M.; Wheatley, P. S.; Navarro, M.; Roth, W. J.; Položij, M.; Mayoral, A.; Eliášová, P.; Nachtigall, P.; Čejka, J.; Morris, R. E. Synthesis of 'Unfeasible' Zeolites. *Nat. Chem.* **2016**, *8*, 58−62.

(5) Morris, S. A.; Bignami, G. P. M.; Tian, Y.; Navarro, M.; Firth, D. S.; Čejka, J.; Wheatley, P. S.; Dawson, D. M.; Slawinski, W. A.; Wragg, D. S.; Morris, R. E.; Ashbrook, S. E. In Situ Solid-State NMR and XRD Studies of the ADOR Process and the Unusual Structure of Zeolite IPC-6. *Nat. Chem.* **2017**, *9*, 1012−1018.

(6) Kasneryk, V.; Shamzhy, M.; Opanasenko, M.; Wheatley, P. S.; Morris, S. A.; Russell, S. E.; Mayoral, A.; Trachta, M.; Čejka, J.; Morris, R. E. Expansion of the ADOR Strategy for the Synthesis of Zeolites: The Synthesis of IPC-12 from Zeolite UOV. *Angew. Chem., Int. Ed.* **2017**, *56*, 4324−4327.

(7) Firth, D. S.; Morris, S. A.; Wheatley, P. S.; Russell, S. E.; Slawin, A. M. Z.; Dawson, D. M.; Mayoral, A.; Opanasenko, M.; Položij, M.; Čejka, J.; et al. Assembly−Disassembly−Organization−Reassembly Synthesis of Zeolites Based on Cfi-Type Layers. *Chem. Mater.* **2017**, *29*, 5605−5611.

(8) Roth, W. J.; Shvets, O. V.; Shamzhy, M.; Chlubna, P.; Kubu, M.; Nachtigall, P.; Čejka, J. Postsynthesis Transformation of Three-Dimensional Framework into a Lamellar Zeolite with Modifiable Architecture. *J. Am. Chem. Soc.* **2011**, *133*, 6130−6133.

(9) Opanasenko, M.; Parker, W. O.; Shamzhy, M.; Montanari, E.; Bellettato, M.; Mazur, M.; Millini, R.; Čejka, J. Hierarchical Hybrid Organic−Inorganic Materials with Tunable Textural Properties Obtained Using Zeolitic-Layered Precursor. *J. Am. Chem. Soc.* **2014**, *136*, 2511−2519.

(10) Opanasenko, M.; Shamzhy, M.; Wang, Y.; Yan, W.; Nachtigall, P.; Čejka, J. Synthesis and Post-Synthesis Transformation of Germanosilicate Zeolites. *Angew. Chem., Int. Ed.* **2020**, *59*, 19380−19389.

(11) Kamakoti, P.; Barckholtz, T. A. Role of Germanium in the Formation of Double Four Rings in Zeolites. *J. Phys. Chem. C* **2007**, *111*, 3575−3583.

(12) Odoh, S. O.; Deem, M. W.; Gagliardi, L. Preferential Location of Germanium in the UTL and IPC-2a Zeolites. *J. Phys. Chem. C* **2014**, *118*, 26939−26946.

(13) Montejo-Valencia, B. D.; Curet-Arana, M. C. DFT Study of the Lewis Acidities and Relative Hydrothermal Stabilities of BEC and BEA Zeolites Substituted with Ti, Sn, and Ge. *J. Phys. Chem. C* **2015**, *119*, 4148−4157.

(14) Sastre, G.; Gale, J. D. Derivation of an Interatomic Potential for Germanium- and Silicon-Containing Zeolites and Its Application to the Study of the Structures of Octadecasil, ASU-7, and ASU-9 Materials. *Chem. Mater.* **2003**, *15*, 1788−1796.

(15) Sastre, G.; Vidal-Moya, J. A.; Blasco, T.; Rius, J.; Jorda, J. L.; Navarro, M. T.; Rey, F.; Corma, A. Preferential Location of Ge Atoms in Polymorph C of Beta Zeolite (ITQ-17) and Their Structure-

Directing Effect: A Computational, XRD, and NMR Spectroscopic Study. *Angew. Chem., Int. Ed.* **2002**, *41*, 4722−4726.
(16) Kasian, N.; Tuel, A.; Verheyen, E.; Kirschhock, C. E. A.; Taulelle, F.; Martens, J. A. NMR Evidence for Specific Germanium Siting in IM-12 Zeolite. *Chem. Mater.* **2014**, *26*, 5556−5565.
(17) Heard, C. J.; Grajciar, L.; Uhlík, F.; Shamzhy, M.; Opanasenko, M.; Čejka, J.; Nachtigall, P. Zeolite (In)Stability under Aqueous or Steaming Conditions. *Adv. Mater.* **2020**, *32*, 2003264.
(18) Zhu, W.; Gora, L.; van den Berg, A. W. C.; Kapteijn, F.; Jansen, J. C.; Moulijn, J. A. Water Vapour Separation from Permanent Gases by a Zeolite-4A Membrane. *J. Membr. Sci.* **2005**, *253*, 57−66.
(19) Wang, Y.; LeVan, M. D. Adsorption Equilibrium of Carbon Dioxide and Water Vapor on Zeolites 5A and 13X and Silica Gel: Pure Components. *J. Chem. Eng. Data* **2009**, *54*, 2839−2844.
(20) Zhang, K.; Lively, R. P.; Dose, M. E.; Brown, A. J.; Zhang, C.; Chung, J.; Nair, S.; Koros, W. J.; Chance, R. R. Alcohol and Water Adsorption in Zeolitic Imidazolate Frameworks. *Chem. Commun.* **2013**, *49*, 3245−3247.
(21) Simonot-Grange, M.-H. Thermodynamic Properties of Adsorbed Water in Zeolites and Comparison with Clay Minerals. *Sci. Géo., Mém.* **1990**, *87*, 25−33.
(22) Wang, M.; Jaegers, N. R.; Lee, M.-S.; Wan, C.; Hu, J. Z.; Shi, H.; Mei, D.; Burton, S. D.; Camaioni, D. M.; Gutiérrez, O. Y.; et al. Genesis and Stability of Hydronium Ions in Zeolite Channels. *J. Am. Chem. Soc.* **2019**, *141*, 3444−3455.
(23) Heard, C. J.; Grajciar, L.; Nachtigall, P. The Effect of Water on the Validity of Löwenstein's Rule. *Chem. Sci.* **2019**, *10*, 5705−5711.
(24) Nielsen, M.; Hafreager, A.; Brogaard, R. Y.; De Wispelaere, K.; Falsig, H.; Beato, P.; Van Speybroeck, V.; Svelle, S. Collective Action of Water Molecules in Zeolite Dealumination. *Catal. Sci. Technol.* **2019**, *9*, 3721−3725.
(25) Heard, C. J.; Grajciar, L.; Rice, C. M.; Pugh, S. M.; Nachtigall, P.; Ashbrook, S. E.; Morris, R. E. Fast Room Temperature Lability of Aluminosilicate Zeolites. *Nat. Commun.* **2019**, *10*, 4690.
(26) Stanciakova, K.; Ensing, B.; Göltl, F.; Bulo, R. E.; Weckhuysen, B. M. Cooperative Role of Water Molecules during the Initial Stage of Water-Induced Zeolite Dealumination. *ACS Catal.* **2019**, *9*, 5119−5135.
(27) Bukowski, B. C.; Bates, J. S.; Gounder, R.; Greeley, J. First Principles, Microkinetic, and Experimental Analysis of Lewis Acid Site Speciation during Ethanol Dehydration on Sn-Beta Zeolites. *J. Catal.* **2018**, *365*, 261−276.
(28) Josephson, T. R.; Jenness, G. R.; Vlachos, D. G.; Caratzoulas, S. Distribution of Open Sites in Sn-Beta Zeolite. *Microporous Mesoporous Mater.* **2017**, *245*, 45−50.
(29) To, J.; Sokol, A. A.; French, S. A.; Catlow, C. R. A. Formation of Active Sites in TS-1 by Hydrolysis and Inversion. *J. Phys. Chem. C* **2007**, *111*, 14720−14731.
(30) Shvets, O. V.; Shamzhy, M. V.; Yaremov, P. S.; Musilova, Z.; Prochazkova, D.; Cejka, J. Isomorphous Introduction of Boron in Germanosilicate Zeolites with UTL Topology. *Chem. Mater.* **2011**, *23*, 2573−2585.
(31) Shvets, O. V.; Kasian, N.; Zukal, A.; Pinkas, J.; Cejka, J. The Role of Template Structure and Synergism between Inorganic and Organic Structure Directing Agents in the Synthesis of UTL Zeolite. *Chem. Mater.* **2010**, *22*, 3482−3495.
(32) Xu, H.; Jiang, J.; Yang, B.; Zhang, L.; He, M.; Wu, P. Post-Synthesis Treatment Gives Highly Stable Siliceous Zeolites through the Isomorphous Substitution of Silicon for Germanium in Germanosilicates. *Angew. Chem., Int. Ed.* **2014**, *53*, 1355−1359.
(33) Wisniewski, K. E.; Wojsz, R. Description of Water Vapor Adsorption on Various Cationic Forms of Zeolite Y. *Zeolites* **1992**, *12*, 37−41.
(34) Zukal, A.; Opanasenko, M.; Rubeš, M.; Nachtigall, P.; Jagiello, J. Adsorption of Pentane Isomers on Metal-Organic Frameworks Cu-BTC and Fe-BTC. *Catal. Today* **2015**, *243*, 69−75.
(35) Database of Zeolite Structures; http://www.iza-structure.org/databases/ (accessed2021-03-02).
(36) Kresse, G.; Hafner, J. Ab Initio Molecular-Dynamics Simulation of the Liquid-Metal−Amorphous-Semiconductor Transition in Germanium. *Phys. Rev. B: Condens. Matter Mater. Phys.* **1994**, *49*, 14251.
(37) Kresse, G.; Hafner, J. Ab Initio Molecular Dynamics for Liquid Metals. *Phys. Rev. B: Condens. Matter Mater. Phys.* **1993**, *47*, 558.
(38) Perdew, J. P.; Burke, K.; Ernzerhof, M. Generalized Gradient Approximation Made Simple. *Phys. Rev. Lett.* **1996**, *77*, 3865.
(39) Grimme, S.; Antony, J.; Ehrlich, S.; Krieg, H. A Consistent and Accurate Ab Initio Parametrization of Density Functional Dispersion Correction (DFT-D) for the 94 Elements H-Pu. *J. Chem. Phys.* **2010**, *132*, 154104.
(40) Grimme, S.; Ehrlich, S.; Goerigk, L. Effect of the Damping Function in Dispersion Corrected Density Functional Theory. *J. Comput. Chem.* **2011**, *32*, 1456−1465.
(41) Henkelman, G.; Uberuaga, B. P.; Jónsson, H. A Climbing Image Nudged Elastic Band Method for Finding Saddle Points and Minimum Energy Paths. *J. Chem. Phys.* **2000**, *113*, 9901−9904.
(42) Bucko, T. Ab Initio Calculations of Free-Energy Reaction Barriers. *J. Phys.: Condens. Matter* **2008**, *20*, 064211.
(43) Shamzhy, M. V.; Shvets, O. V.; Opanasenko, M. V.; Yaremov, P. S.; Sarkisyan, L. G.; Chlubna, P.; Zukal, A.; Marthala, V. R.; Hartmann, M.; Cejka, J. Synthesis of Isomorphously Substituted Extra-Large Pore UTL Zeolites. *J. Mater. Chem.* **2012**, *22*, 15793−15803.
(44) Liu, X.; Kasian, N.; Tuel, A. New Insights into the Degermanation Process of ITQ-17 Zeolites. *Microporous Mesoporous Mater.* **2014**, *190*, 171−180.
(45) Eroshenko, V.; Regis, R.-C.; Soulard, M.; Patarin, J. Energetics: A New Field of Applications for Hydrophobic Zeolites. *J. Am. Chem. Soc.* **2001**, *123*, 8129−8130.
(46) Fraux, G.; Coudert, F.-X.; Boutin, A.; Fuchs, A. H. Forced Intrusion of Water and Aqueous Solutions in Microporous Materials: From Fundamental Thermodynamics to Energy Storage Devices. *Chem. Soc. Rev.* **2017**, *46*, 7421−7437.
(47) Yang, G.; Zhou, L. Active Sites of M(IV)-Incorporated Zeolites (M = Sn, Ti, Ge, Zr). *Sci. Rep.* **2017**, *7*, 16113.
(48) Xiao, Y.; Lasaga, A. C. Ab Initio Quantum Mechanical Studies of the Kinetics and Mechanisms of Silicate Dissolution: $H^+(H_3O^+)$ Catalysis. *Geochim. Cosmochim. Acta* **1994**, *58*, 5379−5400.
(49) Cypryk, M.; Apeloig, Y. Mechanism of the Acid-Catalyzed Si-O Bond Cleavage in Siloxanes and Siloxanols. A Theoretical Study. *Organometallics* **2002**, *21*, 2165−2175.
(50) Pelmenschikov, A.; Strandh, H.; Pettersson, L. G. M.; Leszczynski, J. Lattice Resistance to Hydrolysis of Si-O-Si Bonds of Silicate Minerals: Ab Initio Calculations of a Single Water Attack onto the (001) and (111) β-Cristobalite Surfaces. *J. Phys. Chem. B* **2000**, *104*, 5779−5783.
(51) Hühn, C.; Erlebach, A.; Mey, D.; Wondraczek, L.; Sierka, M. *Ab Initio* Energetics of Si-O Bond Cleavage. *J. Comput. Chem.* **2017**, *38*, 2349−2353.
(52) Malola, S.; Svelle, S.; Bleken, F. L.; Swang, O. Detailed Reaction Paths for Zeolite Dealumination and Desilication From Density Functional Calculations. *Angew. Chem., Int. Ed.* **2012**, *51*, 652−655.
(53) Smith, J. D.; Cappa, C. D.; Wilson, K. R.; Messer, B. M.; Cohen, R. C.; Saykally, R. J. Energetics of Hydrogen Bond Network Rearrangements in Liquid Water. *Science* **2004**, *306*, 851−853.
(54) Kuo, I.-F. W.; Mundy, C. J. An Ab Initio Molecular Dynamics Study of the Aqueous Liquid-Vapor Interface. *Science* **2004**, *303*, 658−660.
(55) Caullet, P.; Paillaud, J.-L.; Simon-Masseron, A.; Soulard, M.; Patarin, J. The Fluoride Route: A Strategy to Crystalline Porous Materials. *C. R. Chim.* **2005**, *8*, 245−266.
(56) Villaescusa, L. A.; Lightfoot, P.; Morris, R. E. Synthesis and Structure of Fluoride-Containing GeO2 Analogues of Zeolite Double Four-Ring Building Units. *Chem. Commun.* **2002**, *19*, 2220−2221.

(57) Wragg, D. S.; Morris, R. E. Anionic Gallium Phosphate Double Four-Ring Units Containing Occluded Oxygen. *J. Am. Chem. Soc.* **2000**, *122*, 11246−11247.
(58) Zhang, J.; Yue, Q.; Mazur, M.; Opanasenko, M.; Shamzhy, M. V.; Čejka, J. Selective Recovery and Recycling of Germanium for the Design of Sustainable Zeolite Catalysts. *ACS Sustainable Chem. Eng.* **2020**, *8*, 8235−8246.
(59) Jelfs, K. E.; Flikkema, E.; Bromley, S. T. Hydroxylation of Silica Nanoclusters $(SiO_2)M(H_2O)N$, M = 4, 8, 16, 24: Stability and Structural Trends. *Phys. Chem. Chem. Phys.* **2013**, *15*, 20438−20443.
(60) Belton, D. J.; Deschaume, O.; Perry, C. C. An Overview of the Fundamentals of the Chemistry of Silica with Relevance to Biosilicification and Technological Advances: Fundamentals of Silica Chemistry. *FEBS J.* **2012**, *279*, 1710−1720.
(61) Schaack, B. B.; Schrader, W.; Schüth, F. How Are Heteroelements (Ga and Ge) Incorporated in Silicate Oligomers? *Chem. - Eur. J.* **2009**, *15*, 5920−5925.
(62) Pelster, S. A.; Schrader, W.; Schüth, F. Monitoring Temporal Evolution of Silicate Species during Hydrolysis and Condensation of Silicates Using Mass Spectrometry. *J. Am. Chem. Soc.* **2006**, *128*, 4310−4317.
(63) Morris, R. E.; Čejka, J. Exploiting Chemically Selective Weakness in Solids as a Route to New Porous Materials. *Nat. Chem.* **2015**, *7*, 381−388.
(64) Van Speybroeck, V.; Hemelsoet, K.; Joos, L.; Waroquier, M.; Bell, R. G.; Catlow, C. R. A. Advances in Theory and Their Application within the Field of Zeolite Chemistry. *Chem. Soc. Rev.* **2015**, *44*, 7044−7111.
(65) Grajciar, L.; Heard, C. J.; Bondarenko, A. A.; Polynski, M. V.; Meeprasert, J.; Pidko, E. A.; Nachtigall, P. Towards Operando Computational Modeling in Heterogeneous Catalysis. *Chem. Soc. Rev.* **2018**, *47*, 8307−8348.
(66) Artrith, N. Machine Learning for the Modeling of Interfaces in Energy Storage and Conversion Materials. *J. Phys. Energy* **2019**, *1*, 032002.
(67) Mueller, T.; Hernandez, A.; Wang, C. Machine Learning for Interatomic Potential Models. *J. Chem. Phys.* **2020**, *152*, 050902.
(68) Erlebach, A.; Nachtigall, P.; Grajciar, L. Accurate Large-Scale Simulations of Siliceous Zeolites by Neural Network Potentials. *arXiv:2102.12404 [cond-mat]*, 2021; https://arxiv.org/abs/2102.12404 (accessed 2021-10-11).

https://doi.org/10.1021/acs.jpcc.1c06873
J. Phys. Chem. C 2021, 125, 23744−23757

Publication 2:

Jin Zhang, Ondřej Veselý, Zdeněk Tošner, Michal Mazur, Maksym Opanasenko, Jiří Čejka, Mariya Shamzhy

Toward Controlling Disassembly Step within the ADOR Process for the Synthesis of Zeolites

Chemistry of Materials 33 (2021) 4 1228–1237

DOI: 10.1021/acs.chemmater.0c03993

Contribution: Synthesis of the parent UTL germanosilicate, treatment of the UTL with water-alcohol solutions, apparatuses construction and development of the slow deintercalation method in HCl-EtOH solution, argon sorption measurements, evaluation of the obtained data and writing of the manuscript.

CHEMISTRY OF MATERIALS

pubs.acs.org/cm

Article

Toward Controlling Disassembly Step within the ADOR Process for the Synthesis of Zeolites

Jin Zhang, Ondřej Veselý, Zdeněk Tošner, Michal Mazur, Maksym Opanasenko, Jiří Čejka, and Mariya Shamzhy*

Cite This: https://dx.doi.org/10.1021/acs.chemmater.0c03993

Read Online

ACCESS | Metrics & More | Article Recommendations | Supporting Information

ABSTRACT: The application of the Assembly−Disassembly−Organization−Reassembly (ADOR) protocol to the synthesis of germanosilicate zeolites has become a major milestone in material design by enabling the preparation of previously unknown "isoreticular" zeolites with tunable building units (i.e., *-d4r-, -s4r-, -O-*) connecting crystalline layers. Two processes operating in the disassembly step, deconstructive "deintercalation" and reconstructive "rearrangement", determine the structure of ADOR-derived zeolites. However, independent management of these key ADOR processes, which would be desirable to regulate the characteristics of the products, has remained elusive thus far. Herein, we report a new method for controlling the primary steps of the ADOR process and present the first example of a "cycled" structural transformation of interlayer units (*d4r* → *s4r* → *d4r*) in the germanosilicate **UTL** zeolite under "slow deintercalation"/"fast rearrangement" conditions. The "slow deintercalation" mode of ADOR enabled us to prepare the previously known **OKO**, ***PCS**, IPC-7 zeolites via gradual reduction of interlayer units in **UTL** (*d4r* → *d4r*/*s4r* → *s4r* → *s4r*/-O-), in contrast to conventional rearrangement-driven synthesis (-O- → *s4r*/-O- → *s4r*...). X-ray powder diffraction (XRD), sorption, and solid-state NMR time-resolved studies revealed that the "slow deintercalation/fast rearrangement" modification of ADOR makes it possible to adjust the pore architecture of germanosilicate zeolites toward increasing their micropore size, which has never been achieved before in the classical ADOR mechanism. Therefore, "slow deintercalation" or "slow deintercalation/fast rearrangement" routes provide a tool for controlling the "isoreticular" zeolite structure. Ultimately, the results from this study may facilitate the design of previously predicted but inaccessible members of the ADORable zeolite family.

1. INTRODUCTION

Zeolites are microporous crystalline elementosilicates (E = Al, Ti, Sn, Ge, among others) widely used in adsorption, separation, and catalysis. Hydrothermal crystallization, the traditional method for the preparation of zeolites via a sequence of reversible polymerization/depolymerization steps, has made it possible to synthesize most of the 252 zeolite framework types known thus far.[1] However, the high lattice energies of most theoretically predicted frameworks have precluded the direct synthesis of zeolites with unusual structural and textural characteristics (e.g., those with odd-membered rings).[2] The recently discovered ADOR strategy (involving Assembly−Disassembly−Organization−Reassembly steps) applicable to germanosilicate zeolites benefits from the irreversibility of the final material-forming step and thus has allowed synthetic chemists to expand the number of zeolites.[3] The fascinating chemistry of germanosilicate zeolites, particularly the postsynthesis modification of their framework structure and chemical composition,[4−8] has been comprehensively reviewed in ref 9

The success of the ADOR approach in the preparation of new zeolites has been already exemplified by the disassembly−organization−reassembly of **UTL**,[10,11] **UOV**,[12,13] **IWW**,[14−16] and ***CTH**[17−19] germanosilicate frameworks composed of silica layers connected with Ge-enriched *d4r* units selectively removable upon hydrolysis (Scheme 1). Studies[20−22] on **UTL** germanosilicate revealed that two key processes operating in the disassembly step determine the structure/pore architecture of a zeolite formed upon ADOR transformation: (i) "deintercalation", that is, breaking of Ge−O(Ge) or Ge−O(Si) bonds and diffusion of some or all species that left the zeolite framework off the interlayer space and (ii) "rearrangement" of some species, which might not have diffused out of the interlayered space to form various interlayer-connecting units in a "daughter" zeolite. The concentration of water molecules inside the pores plays a key role in both the breaking and making of the T−O bonds in zeolites[23] during the disassembly step. High-water experiments (liquid-to-solid ratio >100 ml/g) have shown that (1) the complete deintercalation of *d4r* units off **UTL** framework leading to the IPC-1P layered precursor of **PCR** zeolite (containing −O− interlayer linkages) is completed within ca. 5 min, regardless of pH and temperature, while (2) rearrangement of IPC-1P (kinetic product of hydrolysis) into an IPC-2P precursor of the **OKO** zeolite containing −*s4r*− interlayer

Received: October 12, 2020
Revised: January 20, 2021

Scheme 1. Controlling the Rate of Rearrangement within "Fast Deintercalation/Rearrangement" Mode of the ADOR Strategy for the Synthesis of UTL-Derived Zeolites (Based on the Results of Refs 20−22, 24, 26)

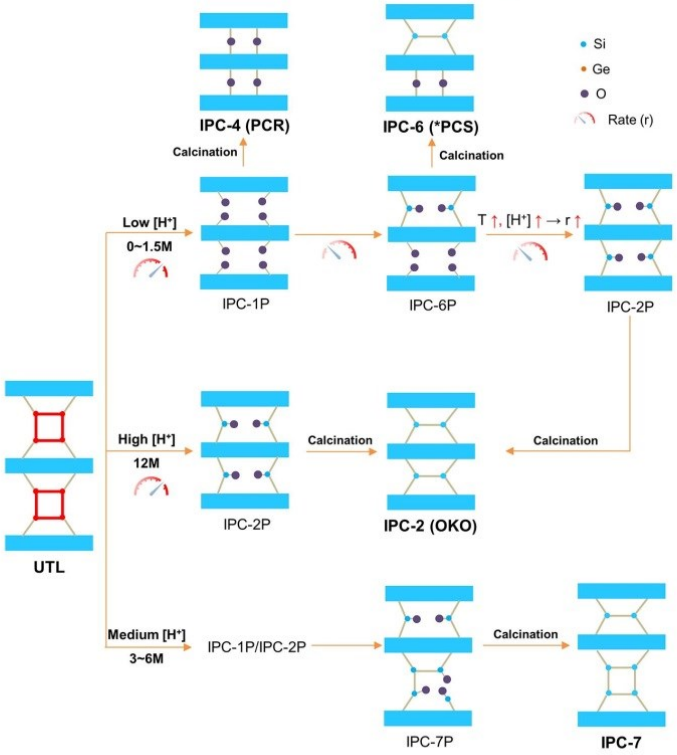

linkages (thermodynamic product) proceeds through an IPC-6P intermediate, the precursor of the stage-structured ***PCS** zeolite containing both **PCR**- and **OKO**-type linkages in a 1:1 ratio. The IPC-1P rearrangement has been shown to accelerate with the acidity/temperature (Scheme 1, top).[22] Thus, varying the rate of rearrangement process in highly liquid systems by adjusting the pH of **UTL** disassembly has made it possible to synthesize a series of "isoreticular" zeolites with the same crystalline layers but different connectivity (Scheme 1):[24−26] 10 × 8-ring **PCR**, 12 × 10-ring **OKO**, 12 × 10-ring and 10 × 8-ring ***PCS**, and 14 × 12-ring and 12 × 10-ring IPC-7.

Although fully hydrolyzing to IPC-1P in high-water experiments, **UTL** was recently reported to disassemble into IPC-2P when the water-to-solid ratio was decreased to 0.2−50 mL/g.[27] The latter, noncomplete **UTL** disassembly can be related to the deceleration of the Ge−O(Si) bond cleavage with the decrease in the water content (low-water conditions) and to the inhibiting transport of leached species in highly viscous, low-liquid systems. Such species trapped in the interlayer space not only negatively affect the textural characteristics of daughter IPC-*n* zeolites[27] but also contribute to the uncontrolled rearrangement of interlayer linkages. Conversely, controlling both deconstructive and reconstructive processes operating on the disassembly step provides a way to synthesize the previously predicted but inaccessible families of "isoreticular" zeolites.[28,29]

Continuous control over the porosity of the **UTL**-derived ADORable zeolites is crucial for applications in separation and shape-selective catalysis.[24] In contrast to **UTL**, the fast "deintercalation/rearrangement" mode of ADOR was not efficient in tuning the interlayer linkages in zeolites formed upon the disassembly of **UOV**,[12,13] **IWW**,[15] **ITH**, and **ITR**[30] germanosilicates. Herein, we report for the first time the synthesis of **UTL**-derived "isoreticular" zeolites via a gradual reduction of the *d4r* interlayer units (*d4r* → *d4r*/*s4r* → *s4r* → *s4r*/*-O-*), a mechanism markedly different from the "fast deintercalation/rearrangement" mode of the ADOR strategy (Scheme 1) that was used so far.[12,13,17,18,29,30] HCl-induced, slow **UTL** deintercalation in water-free alcohol medium enabled the preparation of previously known IPC-*n* (*n* = 2, 6, 7) zeolites with typical structural and textural characteristics. In turn, the "slow deintercalation"/"fast rearrangement" regime operating in a water−alcohol medium in the presence of a framework-building element source promoted the "cycled" structural transformation of the interlayer units (*d4r* → *s4r* → *d4r*) in the **UTL** zeolite. In contrast to classical ADOR, which allows us to control the decrease in the pore size of daughter zeolites (e.g., **UTL** → IPC-*n* transformation), the approach reported here may be useful for adjusting the pore architecture of germanosilicate zeolites toward increasing their micropore size.

2. EXPERIMENTAL SECTION

2.1. Synthesis of UTL Zeolite. **UTL** zeolite characterized by Si/Ge = 4.5 was synthesized using SDA of (6R,10S)-6,10-dimethyl-5-azoniaspiro decane (DMAD) hydroxide, according to ref 31. A gel with a composition of 0.67 SiO_2/0.33 GeO_2/0.25DMAD/30 H_2O was heated to 175 °C for 7 days under agitation (60 rpm). The solid products were recovered by filtration, washed with deionized water, and

https://dx.doi.org/10.1021/acs.chemmater.0c03993
Chem. Mater. XXXX, XXX, XXX−XXX

dried overnight at 70 °C. Then, the zeolites were calcined at 550 °C for 6 h in the air flow.

2.2. Postsynthesis of UTL Zeolite. *2.2.1. Treatment with Water–Alcohol Solutions.* The **UTL** zeolite was treated with pure alcohol (methanol, ethanol, i-propanol) and 20, 40, and 60% solutions of the respective alcohols in water (Table 1).

Table 1. Water–Alcohol Solutions Used for Slow Disassembly of the UTL Zeolite

alcohol concentration, wt %	*m* (water), g	*m* (alcohol), g
0	160	0
20	128	32
40	96	64
60	64	96
100	0	160

In total, 160 mL of each solution was heated to 60 °C and 1 g of **UTL** added. The samples were collected after 1, 3, 5, 18, and 24 h. The solid was separated by centrifugation, washed with pure alcohol (respective to each solution), and dried at room temperature. The dried samples were calcined at 550 °C for 6 h in an air flow.

2.2.2. Treatment with a HCl–Ethanol Solution. The **UTL** zeolite was treated with a 1.25 M solution of HCl in EtOH (Sigma Aldrich). As the HCl in ethanol is highly flammable at high temperatures, the experiment must be performed at temperatures below 16 °C or in a closed autoclave. To suppress the rearrangement process, we chose to perform the disassembly in an open vessel at 0 °C. Thus, 160 ml of the solution was cooled down to 0 °C and 1 g of **UTL** added. The samples were collected periodically for 60 days. The solid was separated by centrifugation, washed with absolute ethanol, and dried at room temperature. The dry samples were calcined at 550 °C for 6 h in an air flow.

2.2.3. Treatment with Al-Containing Water–Methanol Solutions. Aluminum nitrate nonahydrate (98%, Aldrich) was used as the Al source. In total, 134 mL of methanol was mixed with 38 ml of water and heated to 60 °C. Then, 34.1 g of aluminum nitrate nonahydrate was dissolved in a water–methanol mixture, subsequently adding 1 g of **UTL** to 160 mL of the 1 M $Al(NO_3)_3$ water–methanol solution (water-to-methanol w/w 40/60). The samples were collected periodically for 60 days. The solid was separated by centrifugation, washed with absolute methanol, and dried at room temperature. The dried samples were calcined at 550 °C for 6 h in an air flow.

2.3. Characterization. The structure and crystallinity of the materials were examined by X-ray powder diffraction (XRD) on a Bruker AXS D8 Advance diffractometer with a Vantec-1 detector in the Bragg–Brentano geometry using Cu Kα radiation (1.54056 Å). Before the measurements, the samples were ground gently and packed into the holder to decrease the effect of the preferential orientation of individual crystals.

The morphology of the crystals was determined by scanning electron microscopy (TESCAN Vega microscope).

High-resolution transmission electron microscopy (HRTEM) images were acquired using a JEOL NEOARM 200 F microscope equipped with a Schottky-type field emission gun at an accelerating voltage of 200 kV. The samples were ultrasonically dispersed in ethanol and then dropped onto the carbon-coated copper grids before the measurements.

ICP-OES (ThermoScientific iCAP 7000) analysis was used to determine the Si, Ge, and Al content of the materials. For this purpose, a mixture of measured samples (50 mg), HF (1.8 mL), HNO_3 (1.8 mL), and HCl (5.4 mL) were placed in the microwave in a closed vessel at T = 140 °C for 35 min. Then, a saturated solution of H_3BO_3 (5.4 mL) was added to ensure the complexation of the excess HF. After digestion, the solutions under analysis were collected in 250 mL flasks, measuring the volume with ultrapure water.

The Ar adsorption/desorption isotherms were collected at −186 °C using a 3Flex (Micromeritics) static volumetric apparatus. All samples were degassed using SmartVac Prep (Micromeritics) at 300 °C under a vacuum for 8 h before the sorption measurements. The specific surface area was evaluated using the Brunauer–Emmett–Teller (BET) method and the adsorption data in the range of a relative pressure from p/p^0 = 0.05–0.25.[32] The t-plot method was applied to determine the volume of micropores (V_{mic}).[33] The adsorbed amount at a relative pressure p/p^0 = 0.975 reflects the total adsorption capacity (V_{tot}). The pore size distributions were calculated using the density functional theory (DFT) model.[34]

Solid-state ^{27}Al NMR spectra were recorded on a Bruker Advance III HD spectrometer working with a 9.4 T standard-bore superconducting magnet (^{27}Al Larmor frequency of 104.26 MHz). The samples were packed into a thin-wall 3.2 mm zirconia rotor and rotated at a MAS rate of 15 kHz using a Bruker 3.2 mm HX CP-MAS probe. A pulse of 1.0 μs (B1 field approximately 95 kHz) with a relaxation delay of 1 s was applied, averaging 2048 transients. The spectra were referenced to a saturated solution of $Al(NO_3)_3$ in D_2O.

The concentrations of Lewis (cL) and Brønsted (cB) acid sites were determined after pyridine (Py) adsorption, followed by Fourier transform infrared (FTIR) spectroscopy on a Nicolet iS50 spectrometer with a transmission MCT/B detector. The zeolite was pressed into self-supporting wafers with a density of ∼10 mg/cm^2 and activated in situ at 450 °C for 4 h. Pyridine adsorption was performed at 150 °C for 20 min at a partial pressure of 600–800 Pa, followed by desorption for 20 min. Before adsorption, pyridine was degassed in a series of freezing and thawing cycles. All spectra were recorded with a resolution of 4 cm^{-1} by collecting 128 scans for a single spectrum at room temperature. cL and cB values were evaluated from the integral intensities of bands at 1454 cm^{-1} (cL) and at 1545 cm^{-1} (cB) using the molar absorption coefficients $\varepsilon(L)$ = 2.2 cm/μmol and $\varepsilon(B)$ = 1.7 cm/μmol.[35]

3. RESULTS AND DISCUSSION

3.1. From Complete Suppression to Slow Deintercalation: Water–Alcohol Systems. The XRD patterns of the parent **UTL** zeolite (with Si/Ge = 4.5) and the samples treated with different alcohols (liquid-to-solid ratio = 160 mL/g) showed the same positions and relative intensities of the characteristic diffraction lines (Figure 1), revealing the lack of the disassembly in water-free alcohol medium.

Once the water was added, the **UTL** zeolite began to transform into IPC-*n* materials (Scheme 1), as revealed by the development of the XRD patterns over time (Figure S1). To assess the effect of the water-to-solid ratio on the progress of the **UTL** disassembly, the zeolite samples were treated with water–

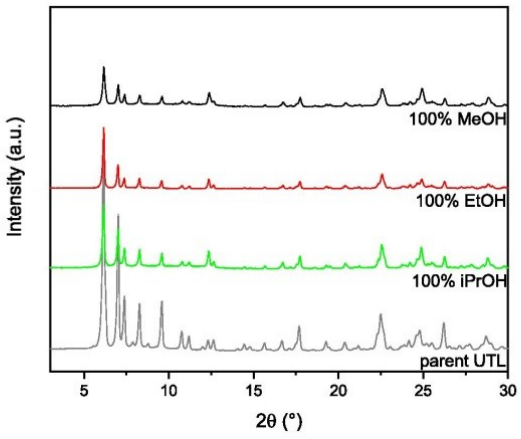

Figure 1. Powder XRD patterns of **UTL** after 24 h treatment in pure MeOH, EtOH, and iPrOH at 60 °C, liquid-to-solid ratio = 160 mL/g.

https://dx.doi.org/10.1021/acs.chemmater.0c03993
Chem. Mater. XXXX, XXX, XXX–XXX

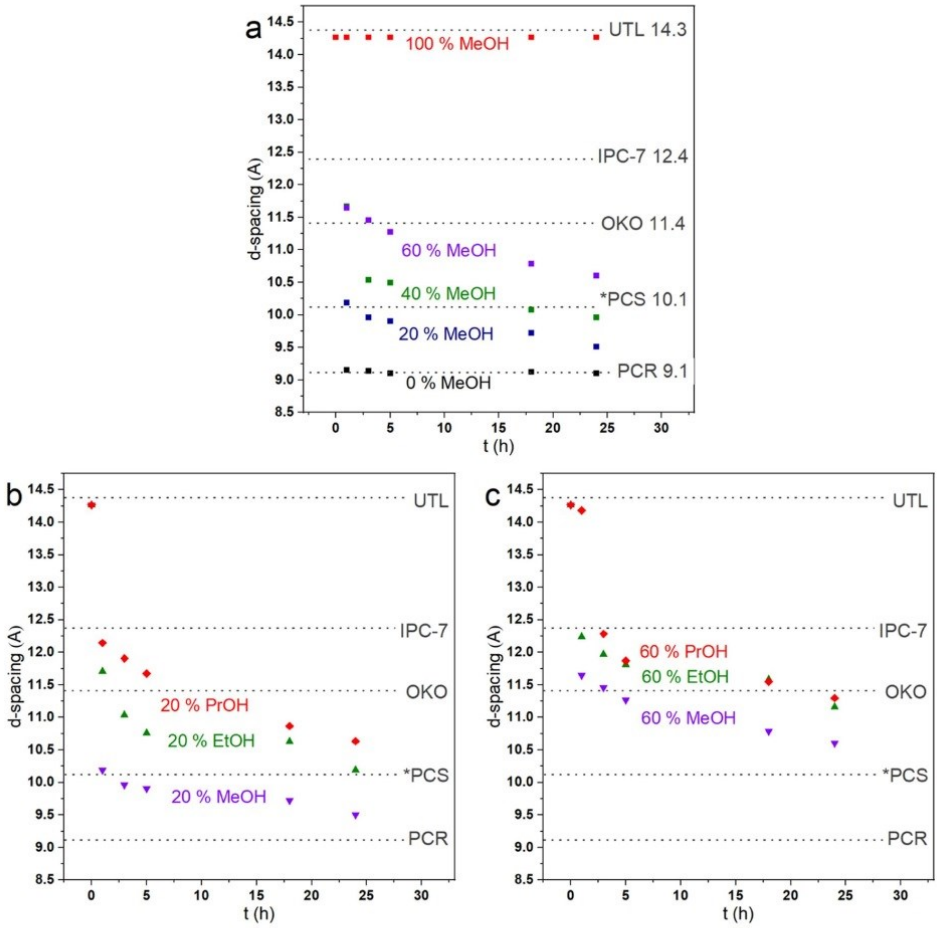

Figure 2. Evolution of the (200) *d*-spacings in zeolites recovered from water−alcohol solutions and subsequently calcined vs MeOH concentration (a) or the type of 20% (b) or 60% alcohol solution (c) at 60 °C; liquid-to-solid ratio = 160 mL/g.

alcohol solutions of different concentrations (Table 1) while keeping the liquid-to-solid ratio high. Figure 2 shows how the interlayer (200) d-spacing in calcined samples changes from 14.4 Å (characteristic of **UTL**) to 11.4 Å (characteristic of **OKO**), 10.1 Å (characteristic of ***PCS**), or 9.1 Å (characteristic of **PCR**), depending on the composition of the liquid medium and on the duration of the treatment. Full deintercalation of *d*4*r* units off the **UTL** framework with a formation of **PCR** zeolite (Scheme 1) was observed only in 0% MeOH (water-to-solid ratio = 160 ml/g), while the ***PCS** zeolite was formed in 20% MeOH (water-to-solid ratio = 128 mL/g) in 1 h (Figure 2a). The lack of **PCR**-to-***PCS** (or **OKO**) transformation in pure water highlights the efficient suppression of the rearrangement process under the conditions used for this purpose. Decreasing the water-to-solid ratio decelerated the process of **UTL**-to-***PCS** transformation, completed after 1 and 18 h in 20 and 40% MeOH, respectively. The strong effect of the water content on the progress of the **UTL** disassembly (first shown here under rearrangement-suppressing conditions) univocally demonstrates that even a small change in the water content affects how fast the Ge−O(Si) bonds are cleaved.

The type of alcohol used as a solvent is another factor that affects the time required for the completion of the **UTL** deintercalation, decreasing in the following sequence (Figure 2b,c): iPrOH > EtOH > MeOH. Increasing the kinetic diameter of the alcohol (MeOH (3.6. Å) ≪ EtOH (4.4 Å) < iPrOH (4.7 Å)) may limit the formation of the solvation shell around leached Ge species in zeolite pores. Moreover, lowering the polarity of the alcohol in the same sequence (MeOH (0.76) > EtOH (0.65) > iPrOH (0.55)) may hinder the transport of leached species from the interlayer space due to the decreased solubility of germanium oxide.[36]

A stepwise decrease in the zeolite (200) d-spacing with treatment time, observed in all studied **UTL**−water−alcohol systems (Figure 2), suggests that the formation of the IPC-*n* zeolites occurs according to the "slow deintercalation" mechanism, that is, through the gradual reduction of the interlayer units in the germanosilicate zeolite (*d*4*r* → *d*4*r*/*s*4*r* → *s*4*r* → *s*4*r*/-*O*-). In contrast, the previously reported approach for the preparation of the IPC-*n* zeolites is based on the rearrangement of −*O*− units in the rapidly formed IPC-1P layered precursor (i.e., -*O*- → *s*4*r*/-*O*- → *s*4*r* transforma-

https://dx.doi.org/10.1021/acs.chemmater.0c03993
Chem. Mater. XXXX, XXX, XXX−XXX

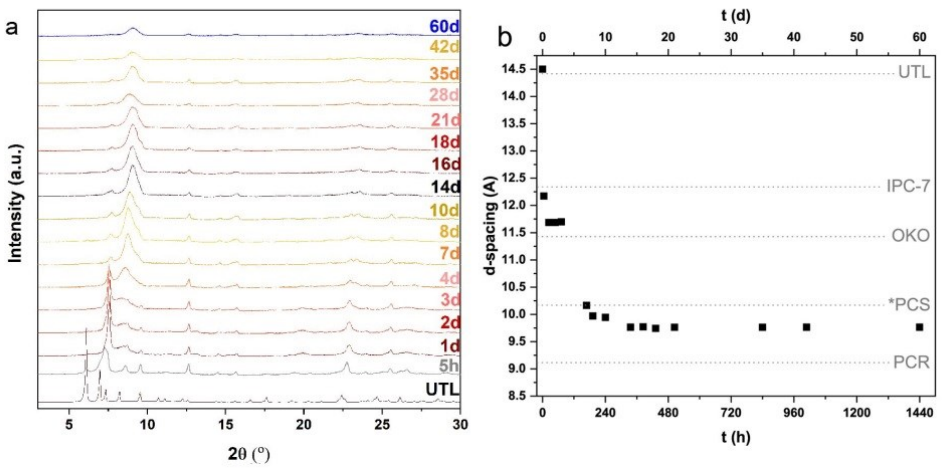

Figure 3. Evolution of powder XRD patterns (a) and the (200) d-spacings (b) in IPC-*n* zeolites recovered from an anhydrous HCl/EtOH solution (T = 0 °C) and subsequently calcined.

tion).[20−22,24,25] The XRD patterns (Figure S1) of IPC-7, **OKO**, and ***PCS** zeolites prepared here for the first time via the "slow deintercalation" of **UTL** in a water−alcohol medium showed phase purity and high crystallinity, albeit with poorer textural properties (Table S1) than their previously reported analogues.[10,24,25,27,37,38] Lower BET area and micropore volume may be caused by a partial blockage of zeolite pores with leached germanium oxide species.

Considering these preliminary results and the ability of Cl^- anions to break the Ge−O(Si) bonds, thereby forming $GeCl_4$, highly soluble in alcohols, the following study has focused on studying the **UTL** disassembly in a water-free Cl^-−EtOH system.

3.2. Slow Deintercalation at Suppressed Rearrangement: Synthesis of "Isoreticular" Zeolites in Water-Free [Cl^-]−Ethanol Systems. To control the removal of leached species from the pores of IPC-*n* zeolites while slowing down the breakage of Ge-O(Si) bonds, **UTL** disassembly was attempted in a water-free ethanolic HCl solution. Importantly, both germanium alkoxychlorides and tetrachloride, formed in such a **UTL**−HCl/EtOH system, are highly soluble in ethanol. The treatment was performed at a temperature (T = 0 °C) low enough to slow down the rearrangement process.

Analysis of the change in the (200) *d*-spacing of zeolite samples (Figure 3) recovered from the HCl/ethanol medium after 5 h to 10 days highlights the "slow deintercalation" regime of the **UTL** disassembly. Indeed, similarly to the water−alcohol systems, *d4r* interlayer linkages in **UTL** were gradually destroying to form IPC-7 (5 h), **OKO** (1−3 days), and finally ***PCS** (7−10 days) zeolites. The process of **UTL**-to-***PCS** conversion upon low-temperature Cl^--assisted deintercalation is clearly slower than that of the water-induced disassembly discussed above (Figures 2 and 3). In agreement with the "slow deintercalation" mechanism of IPC-*n* formation and the facile diffusion of the leached Ge species out of the interlayer space in a water-free HCl/ethanol medium, the decrease in the d-spacings of "isoreticular" zeolites is accompanied by an increase in the Si/Ge ratio (Table S1): **UTL** (Si/Ge = 4.5) < IPC-7 (Si/Ge = 6.3) < **OKO** (Si/Ge = 8.0) < ***PCS** (Si/Ge = 16.0 after 10 days of the treatment). STEM-EDS map analysis (Figure S2) shows a uniform distribution of Ge in the parent **UTL** and treated samples, suggesting that the transformation occurs evenly in crystals. No signs of the final product of **UTL** deintercalation (**PCR** zeolite) are detected, but the (200) diffraction line characteristic of the ***PCS** zeolite decreased in intensity and widened in water-free HCl/ethanol with the prolonging of the treatment, even up to 60 days (Figure 3). The rearrangement process, accelerating with time due to the accumulation of leached species, may explain the stability of ***PCS** against further deintercalation. This assumption is in line with the increase in the Ge concentration of ***PCS** samples over time (Si/Ge = 16.0 and 13.4 after 10 and 35 days, respectively).

Consistent with the XRD results, the TEM images of the samples recovered from the **UTL**−HCl/EtOH system showed layer spacings characteristic of the respective IPC-*n* zeolites. The crystalline material formed after 5 h (Figure 4a) was characterized by lattice fringe separations of 1.4 and 1.2 nm, corresponding to alternate *d4r* and *s4r* interlayer linkages typical of the IPC-7 zeolite, while the sample treated for 1 day (Figure 4b) exhibited the *d*-spacing corresponding exclusively to *s4r* connections of crystalline layers indicative of the **OKO** zeolite.

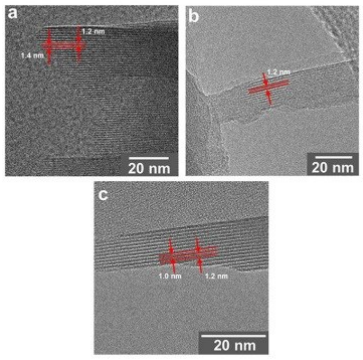

Figure 4. TEM images of the samples recovered from the **UTL**−anhydrous HCl/EtOH systems after 5 h (a), 1 day (b), and 10 days (c) and subsequently calcined.

https://dx.doi.org/10.1021/acs.chemmater.0c03993
Chem. Mater. XXXX, XXX, XXX−XXX

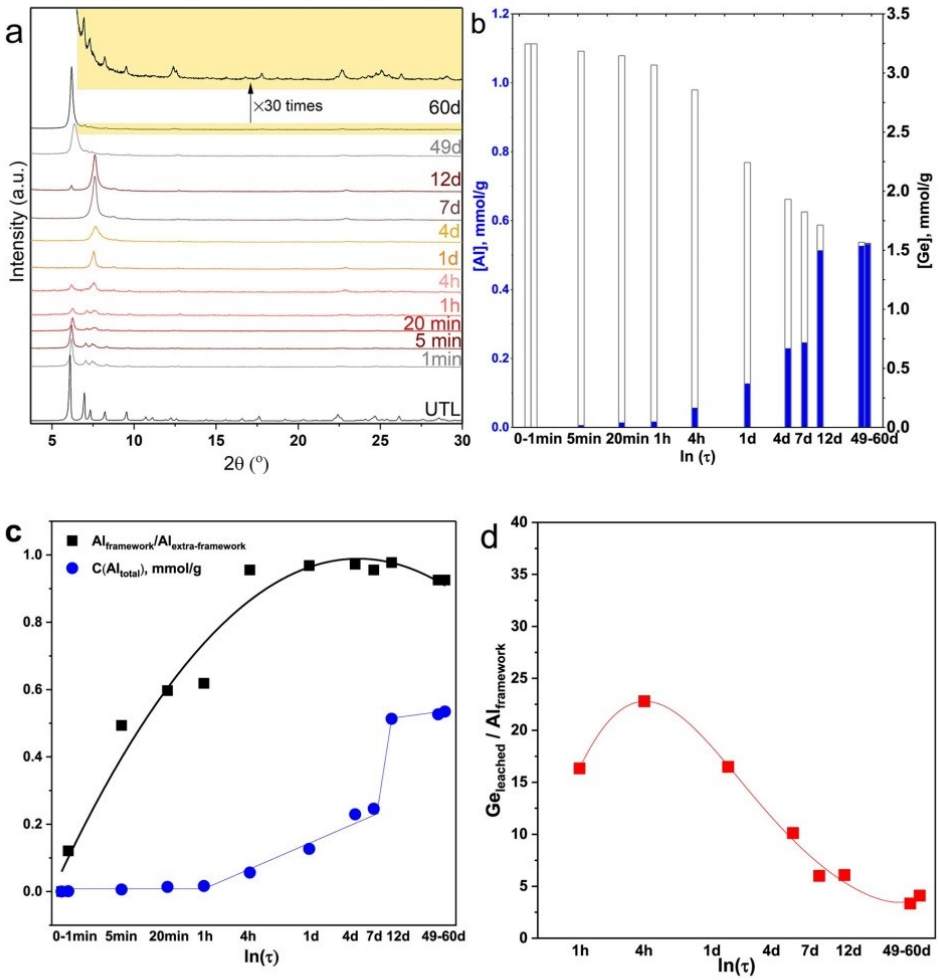

Figure 5. Evolution of XRD patterns (a), Al and Ge contents (b), total concentrations of Al and fractions of framework Al atoms (c), ratios between Ge leached from **UTL** framework and Al incorporated (d) for the samples recovered from Al-containing water−methanol solution (T = 60 °C) and subsequently calcined.

Lastly, the product recovered after 10 days (Figure 4c) demonstrated two distinct interlayer spacings of 1.2 and 1.0 nm characteristic of ***PCS**. A detailed analysis of the TEM image of stage-structured IPC-7 (Figure S3) revealed a higher ordering of the sample prepared via "slow deintercalation" route than the previously reported analogue formed in 5 M HCl aqueous solution.[24] Similarly to ref 24, the ***PCS** zeolite prepared in this study (Figure S4) showed a small degree of faulting, but the overall ratio of characteristic interlayer spacings in the sample was close to 1:1.

The IPC-*n* zeolites synthesized via a "slow deintercalation" of **UTL** showed the BET area and micropore volume similar to those of the previously reported analogous zeolites prepared in aqueous HCl solutions via conventional "fast deintercalation/rearrangement" route (Table S1), albeit with a higher Ge content (Si/Ge = 6.3−16 vs 80−100). The chemical composition of these IPC-*n* materials prepared via the "slow deintercalation" of **UTL** reflects different mechanisms of **UTL** disassembly despite leading to the same "isoreticular" zeolites with typical structural and textural properties.

3.3. "Slow Deintercalation/Fast Rearrangement": Cycled Structural Transformation of UTL in Water−Alcohol Systems Containing a Source of T-Atoms. Controlling the rates of the deintercalation and rearrangement processes within the ADOR strategy is particularly relevant for the rational engineering of new materials. Regulating the rate of the rearrangement at the "fast deintercalation" has already been successfully applied to prepare different **UTL**-derived ADOR-able zeolites,[26,39] but the potential of the rearrangement process to accompany the "slow deintercalation" of germanosilicate zeolites has never been exploited for material design and is therefore addressed below.

In low-water, high-liquid systems (i.e., water−alcohol or HCl/ethanol solutions), sufficiently high concentrations of silicate species involved in the rearrangement process are difficult to reach within a reasonable pH range of stability of

https://dx.doi.org/10.1021/acs.chemmater.0c03993
Chem. Mater. XXXX, XXX, XXX−XXX

zeolite layers.[40,41] For this reason, Al was used as an additive to promote the rearrangement of interlayer linkages and (optionally) to generate acid sites in IPC-*n* zeolites. The XRD patterns of the samples recovered after 1 min to 1 h from an Al-containing water−methanol solution were similar to those of the parent **UTL** zeolite, albeit showing a remarkable decrease in the intensities of diffraction lines (Figure 5a). These results reveal a disordering of the **UTL** framework. In turn, no change was found in the Ge concentration of the corresponding samples with respect to the parent **UTL** zeolite (Figure 5b), thus indicating that no Ge leached out of zeolite pores.

The XRD pattern of the material sampled after 4 h contained two visible (200) diffraction lines related to **UTL** (6.2°) and **OKO** (7.8°),[10] while prolonging the treatment not only removed the interlayer peak of **UTL** (after 1 day) but also increased the intensity of the (200) reflection of **OKO**, peaking after 7 days. After 12 days of treatment, the (200) reflection of **OKO** decreased sharply and the (200) diffraction line corresponding to **UTL** recovered. The increase in the intensity and the narrowing of the interlayer reflection over time (12−60 days) indicate an increasing structure ordering in the renovating zeolite. Unprecedentedly, the full restoration of the **UTL** framework was observed after 60 days under the "slow disassembly"/fast rearrangement conditions applied. It is evident from the XRD pattern of the respective sample showing diffraction lines characteristic of **UTL**, although of lower intensities and larger widths compared to that of the parent zeolite (Figure 5a). The latter result is consistent with a smaller size of the crystals of zeolite (Figure S5) recovered after long-term treatment. Similarly, the crushing of the zeolite crystals was reported in ref 27 upon mechanochemically assisted hydrolysis of **UTL**. Consistently with XRD, the TEM images of both the parent and the restored **UTL** samples demonstrated stacked layers with a 1.4 nm repeat, which is characteristic of **UTL** (Figure 6).

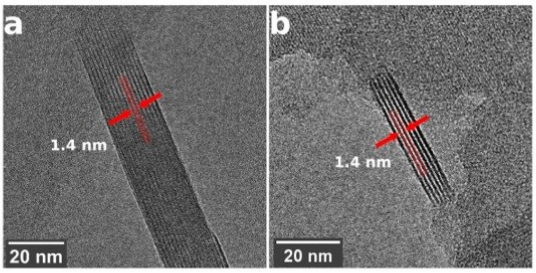

Figure 6. TEM images of the parent **UTL** zeolite (a) and the sample recovered from an Al-containing water−methanol solution after 60 days and subsequently calcined (b).

The gradual decrease in the Ge content of the zeolite during the 4 h to 12 day period was accompanied by an increase in the Al concentration (Figure 5b). Accordingly, the ^{27}Al MAS NMR spectra (Figure S6) revealed a progressive incorporation of Al atoms into the zeolite frameworks as the intensity of the peak corresponding to the extraframework Al (0 ppm) slightly decreased, while the intensity of the peak assigned to the tetrahedrally coordinated framework Al atoms (~54 ppm) increased markedly (Figure S6). The analysis of the variation of the ratio between Ge leached from the **UTL** framework and Al incorporated (Figure 5d) shows the delayed character of the rearrangement process. While the $Ge_{leached}/Al_{framework}$ ratio reached 15−25 during 1−4 h, it gradually decreased over time to 4 after 49−60 days. The **UTL**-like material restored after 60 days of the treatment had Si/Al = 24 and Si/Ge = 9 and was characterized by the uniform distribution of Al in the crystal, as shown in the STEM-EDS maps (Figure S7).

The structural transformations of **UTL** in the Al-containing water−methanol system were also highlighted by the change in pore size distribution (PSD; Figure 7a) and micropore volume (Figures 7b and S8). The **UTL**-to-**OKO** conversion (20 min to 12 days of the treatment) was reflected in the change from bimodal to monomodal PSD.[27] In turn, **OKO**-to-**UTL** restoration was accompanied by the re-emergence of the peak related to larger (14-ring) pores in the PSD curve. However, the exact positions and the relative areas of the peaks shown in the PSD curves of the original and restored **UTL** zeolites should be carefully analyzed because the framework composition and therefore the probe−framework interactions decisive for the evaluation of pore size[27] significantly change upon the **UTL**-to-Al-**UTL** transformation. The decrease in crystallinity (Figure 5a) and the evident blockage of zeolite pores with Ge species (Figure 5b) match the substantially reduced micropore volumes of the **UTL** samples after 1−20 min of treatment (from 0.21 cm^3/g for the parent **UTL** to 0.08−0.09 cm^3/g; Figure 7b). Increasing the structure ordering of **OKO** within 1−7 days increased the V_{micro} (up to 0.11 cm^3/g, which is slightly lower than V_{micro} characteristic for the typical **OKO** samples).[10,24,25,37,38,42] The renovated Al-**UTL**-like material surpasses the previously reported Al-substituted **UTL** zeolites[7,43−45] with respect to the number of strong Brønsted (0.30 mmol/g) and Lewis (0.20 mmol/g) acid centers (Figure S9) serving as active sites in a number of important catalytic transformations,[1,46] albeit with a slightly lower V_{micro} (0.18 cm^3/g) than the values characteristic of the hydrothermally synthesized zeolites (0.19−0.23 cm^3/g).[43−45,47,48]

Overall, the results presented in Figures 5−7 suggest the following plausible mechanism of **UTL** → Al-**OKO** → Al-**UTL** transformation (Scheme 2):

1. Slow hydrolysis of Ge−O(Si) linkages results in the distortion of the **UTL** framework and temporary blockage of the pore system with the leached Ge species (1 min to 1 h under the conditions used in this study).
2. Progressively leached germanium is removed from the pores and while the concentration of extra-framework Al species increased. The resulting Al-poor **OKO** zeolite (1 h to 1 day) is characterized by low crystallinity and a high fraction of octahedral Al.
3. Al incorporation into the framework along with self-organization of zeolite layers (1−12 days) leads to higher crystallinity of the resulting Al-enriched **OKO** zeolite with Al predominantly in framework positions.
4. Al-assisted rearrangement continues at suppressed deintercalation and results in the reconstruction of the *d4r* units characteristic of **UTL** zeolite (12−60 days).

4. CONCLUSIONS

Deintercalation upon germanosilicate zeolite hydrolysis (disassembly) can be efficiently decelerated in water−alcohol or anhydrous HCl−ethanol media. The "slow deintercalation" mode of ADOR was successfully used to synthesize previously known **UTL**-derived "isoreticular" zeolites with typical structural and textural properties, but with a higher content of Ge. In

https://dx.doi.org/10.1021/acs.chemmater.0c03993
Chem. Mater. XXXX, XXX, XXX−XXX

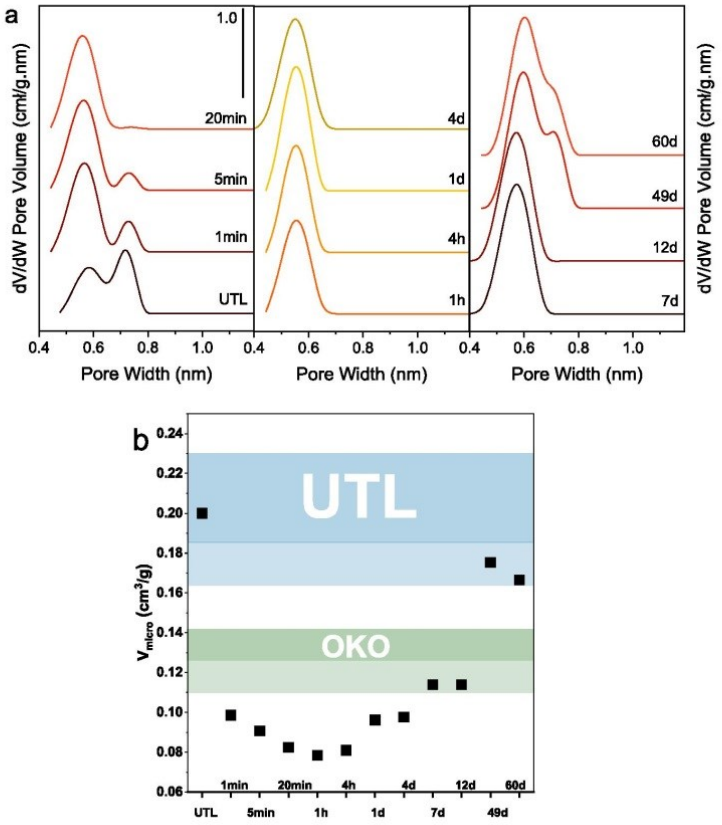

Figure 7. Evolution of the pore-size distribution (a) and micropore volume (b) for the samples recovered from Al-containing water−methanol solutions (T = 60 °C) and subsequently calcined. The ranges of V_{micro} for **UTL** and **OKO** zeolites previously reported in the literature[42,43,47,48] are shown as blue and green rectangles, respectively.

Scheme 2. "Slow Deintercalation/Fast Rearrangement" of UTL Germanosilicate in Al-Containing Water−Methanol Solution

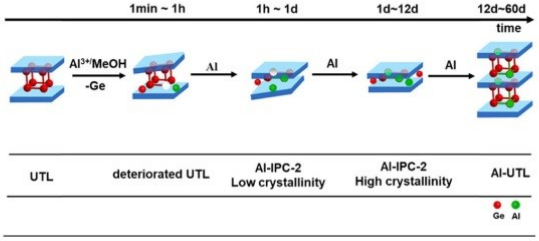

contrast to conventional synthesis of IPC-*n* materials based on building up the interlayer units (*-O-* → *s4r*/*-O-* → *s4r*...) in rapidly deintercalated zeolite, the "slow deintercalation" approach enables the preparation of ADORable zeolites via a gradual reduction of original interlayer units (*d4r* → *d4r*/*s4r* → *s4r* → *s4r*/*-O-*), a mechanism suitable for the structural transformation of most germanosilicate zeolites.

By promoting heteroelement-induced rearrangement while decelerating the deintercalation in the water−alcohol systems containing a source of T-atoms, we showed for the first time the cycled structural transformation of interlayer units (*d4r* → *s4r* → *d4r*) in the **UTL** zeolite. This result reveals the potential of "deintercalation/fast rearrangement" modification of ADOR for adjusting the pore architecture of germanosilicate zeolites toward increasing their micropore size. Moreover, heteroatoms efficiently incorporated as potential active sites in the germanosilicate framework (up to 0.5 mmol/g), thereby highlighting the usefulness of this new approach for catalyst engineering.

■ ASSOCIATED CONTENT

Supporting Information

The Supporting Information is available free of charge at https://pubs.acs.org/doi/10.1021/acs.chemmater.0c03993.

XRD patterns of **UTL** zeolites treated with alcohol aqueous solutions; textural characteristics and chemical analysis of IPC-*n* zeolites; STEM images and EDS mapping of parent **UTL** and IPC-*n* zeolites; TEM images of IPC-7 and ***PCS** zeolites; SEM images and FTIR spectra of parent **UTL** zeolite and UTL-60d sample recovered from Al-containing water−methanol solution after 60 days; ^{27}Al MAS NMR, STEM images, EDS mapping, and Ar adsorption/desorption isotherms of samples recovered from Al-containing water−methanol solution after 1 min to 60 days (PDF)

https://dx.doi.org/10.1021/acs.chemmater.0c03993
Chem. Mater. XXXX, XXX, XXX−XXX

AUTHOR INFORMATION

Corresponding Author

Mariya Shamzhy − *Department of Physical and Macromolecular Chemistry & Charles University Center of Advanced Materials, Faculty of Science, Charles University, 12843 Prague, Czechia;* orcid.org/0000-0002-1979-6817; Email: mariya.shamzhy@natur.cuni.cz

Authors

Jin Zhang − *Department of Physical and Macromolecular Chemistry & Charles University Center of Advanced Materials, Faculty of Science, Charles University, 12843 Prague, Czechia*

Ondřej Veselý − *Department of Physical and Macromolecular Chemistry & Charles University Center of Advanced Materials, Faculty of Science, Charles University, 12843 Prague, Czechia*

Zdeněk Tošner − *Department of Physical and Macromolecular Chemistry & Charles University Center of Advanced Materials, Faculty of Science, Charles University, 12843 Prague, Czechia*

Michal Mazur − *Department of Physical and Macromolecular Chemistry & Charles University Center of Advanced Materials, Faculty of Science, Charles University, 12843 Prague, Czechia;* orcid.org/0000-0001-5044-5284

Maksym Opanasenko − *Department of Physical and Macromolecular Chemistry & Charles University Center of Advanced Materials, Faculty of Science, Charles University, 12843 Prague, Czechia*

Jiří Čejka − *Department of Physical and Macromolecular Chemistry & Charles University Center of Advanced Materials, Faculty of Science, Charles University, 12843 Prague, Czechia;* orcid.org/0000-0003-1400-1031

Complete contact information is available at: https://pubs.acs.org/10.1021/acs.chemmater.0c03993

Notes

The authors declare no competing financial interest.

ACKNOWLEDGMENTS

We thank Dr. Carlos Henrique Vieira Melo for editing this manuscript. This work was supported by the Czech Science Foundation through projects No. 20-12099S (Z.T. and M.S.) and EXPRO No. 19-27551X (O.V. and J.Č.). J.Z. acknowledges the support of the Grant Agency of Charles University for the project 1398119. M.O. thanks the Primus Research Program of the Charles University (project number PRIMUS/17/SCI/22 "Soluble zeolites"). Support by OP VVV "Excellent Research Teams", project No. CZ.02.1.01/0.0/0.0/15_003/0000417—CUCAM is also acknowledged.

REFERENCES

(1) Shamzhy, M.; Opanasenko, M.; Concepción, P.; Martínez, A. New trends in tailoring active sites in zeolite-based catalysts. *Chem. Soc. Rev.* **2019**, *48*, 1095−1149.

(2) Li, X.; Deem, M. W. Why Zeolites Have So Few Seven-Membered Rings. *J. Phys. Chem. C* **2014**, *118*, 15835−15839.

(3) Eliášová, P.; Opanasenko, M.; Wheatley, P. S.; Shamzhy, M.; Mazur, M.; Nachtigall, P.; Roth, W. J.; Morris, R. E.; Čejka, J. The ADOR mechanism for the synthesis of new zeolites. *Chem. Soc. Rev.* **2015**, *44*, 7177−7206.

(4) Burel, L.; Kasian, N.; Tuel, A. Quasi All-Silica Zeolite Obtained by Isomorphous Degermanation of an As-Made Germanium-Containing Precursor. *Angew. Chem., Int. Ed.* **2014**, *53*, 1360−1363.

(5) Xu, H.; Jiang, J. G.; Yang, B. T.; Zhang, L.; He, M. Y.; Wu, P. Post-Synthesis Treatment gives Highly Stable Siliceous Zeolites through the Isomorphous Substitution of Silicon for Germanium in Germanosilicates. *Angew. Chem., Int. Ed.* **2014**, *53*, 1355−1359.

(6) Liu, X.; Xu, H.; Zhang, L.; Han, L.; Jiang, J. G.; Oleynikov, P.; Chen, L.; Wu, P. Isomorphous Incorporation of Tin Ions into Germanosilicate Framework Assisted by Local Structural Rearrangement. *ACS Catal.* **2016**, *6*, 8420−8431.

(7) Shamzhy, M. V.; Eliašová, P.; Vitvarová, D.; Opanasenko, M. V.; Firth, D. S.; Morris, R. E. Post-Synthesis Stabilization of Germanosilicate Zeolites ITH, IWW, and UTL by Substitution of Ge for Al. *Chem. Eur. J.* **2016**, *22*, 17377−17386.

(8) Opanasenko, M.; Parker, W. O.; Shamzhy, M.; Montanari, E.; Bellettato, M.; Mazur, M.; Millini, R.; Čejka, J. Hierarchical Hybrid Organic-Inorganic Materials with Tunable Textural Properties Obtained Using Zeolitic-Layered Precursor. *J. Am. Chem. Soc.* **2014**, *136*, 2511−2519.

(9) Opanasenko, M.; Shamzhy, M.; Wang, Y.; Yan, W.; Nachtigall, P.; Čejka, J. Synthesis and Post-Synthesis Transformation of Germanosilicate Zeolites. *Angew. Chem., Int. Ed.* **2020**, *59*, 19380−19389.

(10) Roth, W. J.; Nachtigall, P.; Morris, R. E.; Wheatley, P. S.; Seymour, V. R.; Ashbrook, S. E.; Chlubná, P.; Grajciar, L.; Polozij, M.; Zukal, A.; Shvets, O.; Čejka, J. A family of zeolites with controlled pore size prepared using a top-down method. *Nat. Chem.* **2013**, *5*, 628−633.

(11) Mazur, M.; Wheatley, P. S.; Navarro, M.; Roth, W. J.; Položij, M.; Mayoral, A.; Eliášová, P.; Nachtigall, P.; Čejka, J.; Morris, R. E. Synthesis of 'unfeasible' zeolites. *Nat. Chem.* **2016**, *8*, 58−62.

(12) Kasneryk, V.; Shamzhy, M.; Opanasenko, M.; Wheatley, P. S.; Morris, S. A.; Russell, S. E.; Mayoral, A.; Trachta, M.; Čejka, J.; Morris, R. E. Expansion of the ADOR Strategy for the Synthesis of Zeolites: The Synthesis of IPC-12 from Zeolite UOV. *Angew. Chem., Int. Ed.* **2017**, *56*, 4324−4327.

(13) Kasneryk, V.; Shamzhy, M.; Opanasenko, M.; Wheatley, P. S.; Morris, R. E.; Čejka, J. Insight into the ADOR zeolite-to-zeolite transformation: the UOV case. *Dalton Trans.* **2018**, *47*, 3084−3092.

(14) Chlubná-Eliášová, P.; Tian, Y. Y.; Pinar, A. B.; Kubů, M.; Čejka, J.; Morris, R. E. The Assembly-Disassembly-Organization-Reassembly Mechanism for 3D-2D-3D Transformation of Germanosilicate IWW Zeolite. *Angew. Chem., Int. Ed.* **2014**, *53*, 7048−7052.

(15) Kasneryk, V.; Shamzhy, M.; Zhou, J.; Yue, Q.; Mazur, M.; Mayoral, A.; Luo, Z.; Morris, R. E.; Čejka, J.; Opanasenko, M. Vapour-phase-transport rearrangement technique for the synthesis of new zeolites. *Nat. Commun.* **2019**, *10*, No. 5129.

(16) Lu, K.; Huang, J.; Jiao, M.; Zhao, Y.; Ma, Y.; Jiang, J.; Xu, H.; Ma, Y.; Wu, P. Topotactic conversion of Ge-rich IWW zeolite into IPC-18 under mild condition. *Microporous Mesoporous Mater.* **2021**, *310*, No. 110617.

(17) Firth, D. S.; Morris, S. A.; Wheatley, P. S.; Russell, S. E.; Slawin, A. M. Z.; Dawson, D. M.; Mayoral, A.; Opanasenko, M.; Polozij, M.; Čejka, J.; Nachtigall, P.; Morris, R. E. Assembly-Disassembly-Organization-Reassembly Synthesis of Zeolites Based on cfi-Type Layers. *Chem. Mater.* **2017**, *29*, 5605−5611.

(18) Liu, X.; Mao, W.; Jiang, J.; Lu, X.; Peng, M.; Xu, H.; Han, L.; Che, S.-A.; Wu, P. Topotactic Conversion of Alkali-Treated Intergrown Germanosilicate CIT-13 into Single-Crystalline ECNU-21 Zeolite as Shape-Selective Catalyst for Ethylene Oxide Hydration. *Chem. Eur. J.* **2019**, *25*, 4520−4529.

(19) Kang, J. H.; Xie, D.; Zones, S. I.; Davis, M. E. Transformation of Extra-Large Pore Germanosilicate CIT-13 Molecular Sieve into Extra-Large Pore CIT-5 Molecular Sieve. *Chem. Mater.* **2019**, *31*, 9777−9787.

(20) Morris, S. A.; Bignami, G. P. M.; Tian, Y.; Navarro, M.; Firth, D. S.; Čejka, J.; Wheatley, P. S.; Dawson, D. M.; Slawinski, W. A.; Wragg, D. S.; Morris, R. E.; Ashbrook, S. E. In situ solid-state NMR and XRD studies of the ADOR process and the unusual structure of zeolite IPC-6. *Nat. Chem.* **2017**, *9*, 1012−1018.

https://dx.doi.org/10.1021/acs.chemmater.0c03993
Chem. Mater. XXXX, XXX, XXX−XXX

(21) Henkelis, S. E.; Morris, S. A.; Mazur, M.; Wheatley, P. S.; McHugh, L. N.; Morris, R. E. Monitoring the assembly−disassembly−organisation−reassembly process of germanosilicate UTL through in situ pair distribution function analysis. *J. Mater. Chem. A* **2018**, *6*, 17011−17018.
(22) Henkelis, S. E.; Mazur, M.; Rice, C. M.; Wheatley, P. S.; Ashbrook, S. E.; Morris, R. E. Kinetics and Mechanism of the Hydrolysis and Rearrangement Processes within the Assembly−Disassembly−Organization−Reassembly Synthesis of Zeolites. *J. Am. Chem. Soc.* **2019**, *141*, 4453−4459.
(23) Heard, C. J.; Grajciar, L.; Uhlík, F.; Shamzhy, M.; Opanasenko, M.; Čejka, J.; Nachtigall, P. Zeolite (In)Stability under Aqueous or Steaming Conditions. *Adv. Mater.* **2020**, *32*, No. 2003264.
(24) Wheatley, P. S.; Chlubná-Eliášová, P.; Greer, H.; Zhou, W. Z.; Seymour, V. R.; Dawson, D. M.; Ashbrook, S. E.; Pinar, A. B.; McCusker, L. B.; Opanasenko, M.; Čejka, J.; Morris, R. E. Zeolites with Continuously Tuneable Porosity. *Angew. Chem., Int. Ed.* **2014**, *53*, 13210−13214.
(25) Verheyen, E.; Joos, L.; Van Havenbergh, K.; Breynaert, E.; Kasian, N.; Gobechiya, E.; Houthoofd, K.; Martineau, C.; Hinterstein, M.; Taulelle, F.; Van Speybroeck, V.; Waroquier, M.; Bals, S.; Van Tendeloo, G.; Kirschhock, C. E. A.; Martens, J. A. Design of zeolite by inverse sigma transformation. *Nat. Mater.* **2012**, *11*, 1059−1064.
(26) Henkelis, S. E.; Mazur, M.; Rice, C. M.; Bignami, G. P. M.; Wheatley, P. S.; Ashbrook, S. E.; Čejka, J.; Morris, R. E. A procedure for identifying possible products in the assembly−disassembly−organization−reassembly (ADOR) synthesis of zeolites. *Nat. Protoc.* **2019**, *14*, 781−794.
(27) Rainer, D. N.; Rice, C. M.; Warrender, S. J.; Ashbrook, S. E.; Morris, R. E. Mechanochemically assisted hydrolysis in the ADOR process. *Chem. Sci.* **2020**, *11*, 7060−7069.
(28) Trachta, M.; Bludský, O.; Čejka, J.; Morris, R. E.; Nachtigall, P. From Double-Four-Ring Germanosilicates to New Zeolites: In Silico Investigation. *ChemPhysChem* **2014**, *15*, 2972−2976.
(29) Hermann, J.; Trachta, M.; Nachtigall, P.; Bludský, O. Theoretical investigation of layered zeolite frameworks: Surface properties of 2D zeolites. *Catal. Today* **2014**, *227*, 2−8.
(30) Shamzhy, M.; Opanasenko, M.; Tian, Y. Y.; Konysheya, K.; Shvets, O.; Morris, R. E.; Čejka, J. Germanosilicate Precursors of ADORable Zeolites Obtained by Disassembly of ITH, ITR, and IWR Zeolites. *Chem. Mater.* **2014**, *26*, 5789−5798.
(31) Shvets, O. V.; Shamzhy, M. V.; Yaremov, P. S.; Musilova, Z.; Procházková, D.; Čejka, J. Isomorphous Introduction of Boron in Germanosilicate Zeolites with UTL Topology. *Chem. Mater.* **2011**, *23*, 2573−2585.
(32) Brunauer, S.; Emmett, P. H.; Teller, E. Adsorption of Gases in Multimolecular Layers. *J. Am. Chem. Soc.* **1938**, *60*, 309−319.
(33) Lippens, B. C.; de Boer, J. H. Studies on pore systems in catalysts: V. The t method. *J. Catal.* **1965**, *4*, 319−323.
(34) Jagiello, J.; Thommes, M. Comparison of DFT characterization methods based on N_2, Ar, CO_2, and H_2 adsorption applied to carbons with various pore size distributions. *Carbon* **2004**, *42*, 1227−1232.
(35) Emeis, C. A. Determination of Integrated Molar Extinction Coefficients for Infrared Absorption Bands of Pyridine Adsorbed on Solid Acid Catalysts. *J. Catal.* **1993**, *141*, 347−354.
(36) Hohman, J. N.; Kim, M.; Bednar, H. R.; Lawrence, J. A.; McClanahan, P. D.; Weiss, P. S. Simple, robust molecular self-assembly on germanium. *Chem. Sci.* **2011**, *2*, 1334−1343.
(37) Zukal, A.; Shamzhy, M.; Kubů, M.; Čejka, J. The effect of pore size dimensions in isoreticular zeolites on carbon dioxide adsorption heats. *J. CO_2 Util.* **2018**, *24*, 157−163.
(38) Jagiello, J.; Sterling, M.; Eliášová, P.; Opanasenko, M.; Zukal, A.; Morris, R. E.; Navaro, M.; Mayoral, A.; Crivelli, P.; Warringham, R.; Mitchell, S.; Perez-Ramirez, J.; Čejka, J. Structural analysis of IPC zeolites and related materials using positron annihilation spectroscopy and high-resolution argon adsorption. *Phys. Chem. Chem. Phys.* **2016**, *18*, 15269−15277.
(39) Bignami, G. P. M.; Dawson, D. M.; Seymour, V. R.; Wheatley, P. S.; Morris, R. E.; Ashbrook, S. E. Synthesis, Isotopic Enrichment, and Solid-State NMR Characterization of Zeolites Derived from the Assembly, Disassembly, Organization, Reassembly Process. *J. Am. Chem. Soc.* **2017**, *139*, 5140−5148.
(40) Iler, R. K.; K, I. R. *The Chemistry of Silica: Solubility, Polymerization, Colloid and Surface Properties and Biochemistry of Silica*; Wiley, 1979; pp 30−49.
(41) Baes, C. F.; Mesmer, R. E., *The Hydrolysis of Cations*; Wiley, 1976, pp 112−349.
(42) Zhou, Y.; Kadam, S. A.; Shamzhy, M.; Čejka, J.; Opanasenko, M. Isoreticular UTL-Derived Zeolites as Model Materials for Probing Pore Size−Activity Relationship. *ACS Catal.* **2019**, *9*, 5136−5146.
(43) Shamzhy, M. V.; Shvets, O. V.; Opanasenko, M. V.; Yaremov, P. S.; Sarkisyan, L. G.; Chlubna, P.; Zukal, A.; Marthala, V. R.; Hartmann, M.; Čejka, J. Synthesis of isomorphously substituted extra-large pore UTL zeolites. *J. Mater. Chem.* **2012**, *22*, 15793−15803.
(44) Shamzhy, M. V.; Shvets, O. V.; Opanasenko, M. V.; Kurfirtova, L.; Kubicka, D.; Čejka, J. Extra-Large-Pore Zeolites with UTL Topology: Control of the Catalytic Activity by Variation in the Nature of the Active Sites. *Chemcatchem* **2013**, *5*, 1891−1898.
(45) Žilková, N.; Shamzhy, M.; Shvets, O.; Čejka, J. Transformation of aromatic hydrocarbons over isomorphously substituted UTL: Comparison with large and medium pore zeolites. *Catal. Today* **2013**, *204*, 22−29.
(46) Přech, J.; Pizarro, P.; Serrano, D. P.; Čejka, J. From 3D to 2D zeolite catalytic materials. *Chem. Soc. Rev.* **2018**, *47*, 8263−8306.
(47) Paillaud, J. L.; Harbuzaru, B.; Patarin, J.; Bats, N. Extra-large-pore zeolites with two-dimensional channels formed by 14 and 12 rings. *Science* **2004**, *304*, 990−992.
(48) Corma, A.; Diaz-Cabanas, M. J.; Rey, F.; Nicolooulas, S.; Boulahya, K. ITQ-15: The first ultralarge pore zeolite with a bi-directional pore system formed by intersecting 14- and 12-ring channels, and its catalytic implications. *Chem. Commun.* **2004**, *12*, 1356−1357.

https://dx.doi.org/10.1021/acs.chemmater.0c03993
Chem. Mater. XXXX, XXX, XXX−XXX

Publication 3:

Ondřej Veselý, Pavla Eliášová, Russel E. Morris, Jiří Čejka

Reverse ADOR: reconstruction of UTL zeolite from layered IPC-1P

Materials Advances, 2 (2021) 3862-3870

DOI: 10.1039/D1MA00212K

Contribution: Synthesis of the parent UTL germanosilicate and hydrolysis to the IPC-1P, Intercalation experiments, development and carrying out the reconstruction experiments, argon sorption measurements, evaluation of the data and writing of the manuscript.

Materials Advances

ROYAL SOCIETY OF CHEMISTRY

PAPER

View Article Online
View Journal | View Issue

Cite this: *Mater. Adv.*, 2021, 2, 3862

Reverse ADOR: reconstruction of UTL zeolite from layered IPC-1P†

Ondřej Veselý,[a] Pavla Eliášová,[a] Russell E. Morris *[b] and Jiří Čejka*[a]

Received 10th March 2021,
Accepted 2nd April 2021

DOI: 10.1039/d1ma00212k

rsc.li/materials-advances

The assembly–disassembly–organisation–reassembly (ADOR) process has led to the discovery of numerous zeolite structures, albeit limited to materials with decreased pore size in relation to the parent germanosilicate zeolite. This limitation stems from the rapid decrease in *d*-spacing upon hydrolysis (disassembly). Nevertheless, we have artificially increased the *d*-spacing of layered IPC-1P by intercalating organic species. Furthermore, we have reconstructed double four rings (D4R) between layers, thus transforming IPC-1P back into the parent **UTL** zeolite. This reconstruction has provided not only germanosilicate but also a new, high-silica **UTL** zeolite (Si/Ge = 481). Therefore, our "reverse ADOR" opens up new synthetic routes towards promising extra-large-pore zeolite-based materials with new chemical compositions.

1. Introduction

Zeolites are crystalline silicate-based microporous materials. The micropore size of common zeolites is similar to the kinetic diameters of small organic molecules.[1] For this reason, zeolites are extensively used in separation and shape-selective catalysis processes. For example, they are commonly applied as heterogeneous catalysts in petrochemistry.[2–4] Moreover, zeolites have also been modified to catalyse biomass conversion[5–7] and fine chemical synthesis,[8,9] highlighting the wide range of industrial uses of these materials.

Zeolites are commonly prepared by solvothermal (mostly hydrothermal) synthesis[10] in the presence of structure directing agents (SDAs) and mineralising agents (OH^- or F^-).[11] While the hydrothermal method is versatile and easy to perform, its mechanism remains difficult to generalise. As a result, new zeolites are often discovered by trial and error. In contrast, the assembly–disassembly–organisation–reassembly (ADOR) method has been developed to prepare new zeolites and to predict their structure based on theoretical calculations and experimental conditions.[12,13] The ADOR process exploits labile Ge-rich double-four ring (D4R) units in germanosilicates, such as **UTL** or ***CTH**.[14,15] The structure of these zeolites consists of Si-rich layers connected by Ge-rich D4Rs. Upon selective hydrolysis of D4Rs, layered materials are formed, thus preserving their original structure. Subsequently, these layers undergo topotactic condensation to a new 3D structure and hence a new zeolite. Accordingly, the ADOR is a tool for the rational design of new zeolites by controlled 3D-2D-3D transformation.[14]

The ADOR process was first studied on the **UTL** germanosilicate, which hydrolyses to layered IPC-1P.[16] Further manipulations of IPC-1P layers have resulted in a whole new family of materials (**PCR**, **OKO**, ***PCS**, IPC-7, IPC-9 and IPC-10; Fig. 1).[17–20] The IPC materials contain the same Si-rich layers as the parent **UTL** but differ in the connections between layers and consequently in pore size. The average pore size of IPC materials, 12-ring and 10-ring, is usually smaller than that of the parent structure (14-ring). However, no **UTL** or other structure with 14-ring pores has been formed after full 3D-2D-3D transformation until now.

The kinetics of **UTL** hydrolysis has been described in detail by Henkelis *et al.*[21] **UTL** rapidly disassembles into IPC-1P, thereby decreasing the interlayer distance (as measured by the d_{200}-spacing in XRD) from 1.45 nm to 1.05 nm. As the IPC-1P layers slowly rearrange, an IPC-2P with 1.18 nm *d*-spacing is formed, but this IPC-2P is never fully reconverted into **UTL** under such conditions.[22] Conversely, Xu *et al.* succeeded in doing so when using another Ge-rich **UTL**, which was transformed back to **UTL** through isomorphous substitution of Ge by Si. This Ge-rich **UTL**, however, still contained the SDA. The SDA molecules were necessary to preserve the structure throughout the process, otherwise **UTL** would quickly disassemble into layered IPC-1P. Once the layered precursor was formed, the UTL structure could not be restored,[23] so **UTL** restoration from layered IPC-1P remains a challenge. Wu *et al.* have also reported a 2D–3D transformation of the layered material MCM-22P.[24,25] After expanding the interlayer distance by intercalating organic agents, they connected the expanded layers through silanes,

[a] *Department of Physical and Macromolecular Chemistry & Charles University Center of Advanced Materials, Faculty of Science, Charles University, Hlavova 8, 12843 Prague, Czech Republic. E-mail: jiri.cejka@natur.cuni.cz*
[b] *School of Chemistry, EaStChem, University of St. Andrews, North Haugh, St. Andrews, Fife, KY16 9ST, UK*

† Electronic supplementary information (ESI) available. See DOI: 10.1039/d1ma00212k

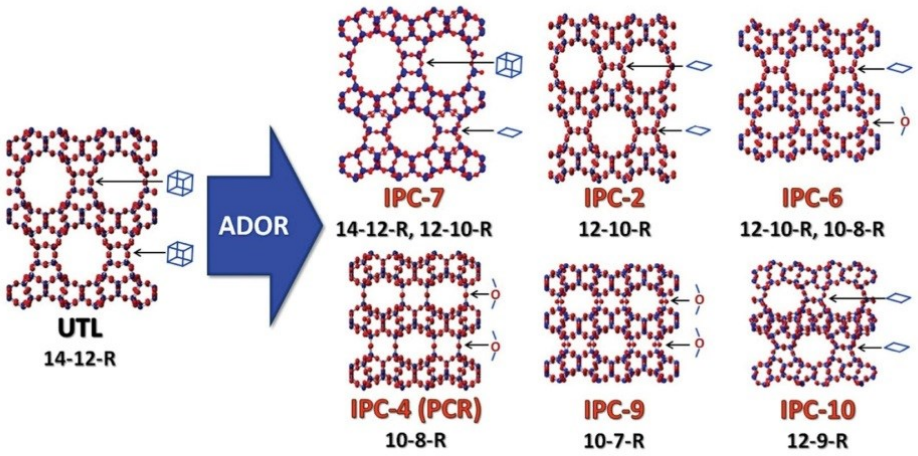

Fig. 1 Zeolite UTL and its daughter structures prepared using the ADOR method, highlighting the connecting units between the layers in the different materials.

thus forming MCM-IEZ. These authors used a similar approach to transform the layered HUS-2 to ECNU-19. However, in both MCM-IEZ and ECNU-19, the layers were not connected by D4R units, which are present in **UTL**, but instead by individual Si linkages. Therefore, by definition, these materials are not zeolites.[26]

Considering the above, in this study we have developed a method for reversing the ADOR process and fully restoring the **UTL** zeolite from layered IPC-1P for the first time. In this approach, **UTL** reconstruction relies on the formation of D4R units between layers. D4Rs form either in a favourable ratio of Si and Ge or in the presence of additional agents, such as fluorides. The process results in a **UTL** zeolite with Si/Ge ratios ranging from 8 to 400, depending on synthesis design.

2. Experimental section

2.1 Synthesis of the structure-directing agent (SDA) for UTL

(6*R*,10*S*)-6,10-Dimethyl-5-anizosporo[4.5]decane hydroxide was used as the SDA to synthetize the UTL germanosilicate.[27] In total, 60 mL of 1,4-dibromobutane, 82.9 g of K_2CO_3 and 500 mL of acetonitrile were mixed in a round-bottom flask. Subsequently, 67 mL of 2,6-dimethylpiperidine was added dropwise, and the mixture was heated to 85 °C and kept refluxing overnight. The acetonitrile was evaporated, and the solid product was dissolved in ethanol. Insoluble compounds were filtered off. Ethanol was evaporated to create an almost saturated solution. Then, the product was precipitated by adding diethyl ether, filtered off, washed with ether, and dried under vacuum overnight. The identity of the SDA structure was confirmed by ^{1}H NMR spectroscopy. The product was ion exchanged to the hydroxide form using the Ambersep 900(OH) ion exchange resin.

2.2 UTL synthesis

UTL was prepared using the hydrothermal method.[28] Germanium dioxide was dissolved in SDA solution in water. Then, silica (Cab–O–Sil M5) was added to the solution, and the mixture was stirred at room temperature until completely dissolved. The resulting mixture, with a molar composition of $0.67SiO_2$:$0.33GeO_2$:0.4SDA:$33.3H_2O$, was charged into a 1000 mL Parr autoclave and heated to 175 °C for 6 days with agitation (200 rpm). The solid product was recovered by filtration, washed out with a copious amount of distilled water and dried in the oven at 60 °C. The SDA was removed by calcination in air at 550 °C for 6 h, with a temperature ramp of 1 °C min^{-1}.

2.3 IPC-1P synthesis

Calcined **UTL** zeolite was hydrolysed in 1 M CH_3COOH (250 mL per g of sample) at 85 °C for 16 h. The product was isolated by filtration, washed with water and dried at 60 °C.

2.4 Intercalation

IPC-1P was treated with a 20% solution of tetrabutylammonium hydroxide (TBAOH) for 6 hours at room temperature.[27] The product was recovered by centrifugation and washed with distilled water to neutral pH. The intercalated precursor (IPC-1TBA) was dried at 60 °C overnight.

2.5 D4R restoration

In total, 0.1 g of IPC-1TBA was added to a 25 mL Teflon-lined steel autoclave with 5 mL of 1.25 M HCl in ethanol and the respective sources of silicon and germanium (see Table 1). The autoclave was heated to 170 °C for 20 hours. The product was filtered off, washed with ethanol and dried at 60 °C. The TBA was removed by calcination in air at 550 °C for 6 h, with a temperature ramp of 1 °C min^{-1}.

2.6 Characterisation

The crystalline structure of the samples was determined by X-ray powder diffraction (XRD) on a Bruker AXS D8 Advance diffractometer with a Vantec-1 detector in the Bragg–Brentano geometry using Cu Kα radiation (1.54056 Å).

Table 1 Molar ratios of the Si and Ge sources in the individual reaction mixtures and their respective labelling

Sample	$(EtO)_2Me_2Si$	$(EtO)_2Me_4Si_2O$	$Me_8Si_4O_4$	POSS	$(MeO)_4Ge$
rec Si1	65.8 mg	—	—	—	—
rec Si2	—	49.4 mg	—	—	—
rec Si4	—	—	26.7 mg	—	—
rec Si8	—	—	—	29.8 mg	—
rec Si–Ge (3 : 1)	49.4 mg	—	—	—	21.9 mg
rec Si–Ge (1 : 1)	32.9 mg	—	—	—	43.7 mg
rec Si–Ge (1 : 3)	16.5 mg	—	—	—	65.6 mg
rec Ge	—	—	—	—	87.3 mg

$(EtO)_2Me_2Si$ = Diethoxydimethylsilane. $(EtO)_2Me_4Si_2O$ = 1,3-diethoxy-1,1,3,3-tetramethyl-disiloxane. $Me_8Si_4O_4$ = 2,4,6,8-tetramethylcyclotetrasiloxane. POSS = octamethylsilsesquioxane. $(MeO)_4Ge$ = germanium methoxide.

High-resolution transmission electron microscopy (HRTEM) images and energy dispersive X-ray (EDX) spectra were acquired under a JEOL NEOARM 200 F microscope with a Schottky-type field emission gun at an accelerating voltage of 200 kV. The samples were dispersed onto the carbon-coated copper grids before the measurements.

Ar adsorption/desorption isotherms were collected at −186 °C on a 3Flex (Micromeritics) static volumetric apparatus. All samples were degassed on a SmartVac Prep (Micromeretics) at 300 °C under vacuum for 8 h before the sorption measurements. The surface area was calculated using the BET method and adsorption data on a relative pressure range of p/p°_0 = 0.05–0.25. The *t*-plot method was applied to determine the micropore volume (V_{mic}). The adsorbed amount at a relative pressure of p/p°_0 = 0.975 reflects the total micropore volume and interparticle adsorption (V_{tot}). The pore size distributions were calculated using the Horwath–Kawazoe method.

3. Results and discussion

3.1 Intercalation

The *d*-spacing between the respective layers in the **UTL** structure is 1.44 nm (which corresponds to reflection at 6.14° in X-ray diffraction using Cu Kα radiation). Hydrolysis of the D4R units in **UTL** results in the layered material IPC-1P. IPC-1P consists of silica-rich layers with a *d*-spacing of 1.05 nm (corresponding to reflection at 8.41°). The first challenge in reconverting IPC-1P into **UTL** was to increase the spacing between IPC-1P layers to 1.44 nm; however, the distance between IPC-1P layers cannot spontaneously increase to the original value (ref. 21; Fig. S1, ESI†). Hence, we adjusted this distance by intercalation. Intercalation, or swelling, of layered silicates and zeolites commonly involves surfactants, such as cetyltrimethylammonium hydroxide.[29–31] However, their long hydrocarbon chains are flexible, and their structure between the layers is sensitive to the pH of the environment. Because this may produce disorder and irregularities in the reconstructed material,[32] we decided to intercalate the layers with more rigid species, such as the tetrabutylammonium cation (TBA^+).[27] TBA^+ intercalation into IPC-1P shifted the interlayer 200 reflection from XRD from 8.4° to 6.37°, which is relatively close to 6.14° (Fig. 2) – the position of the 200 reflection of the UTL material.[33] Accordingly, TBA^+ is suitable for increasing the *d*-spacing of IPC-1P to a distance close to that of the **UTL** zeolite.

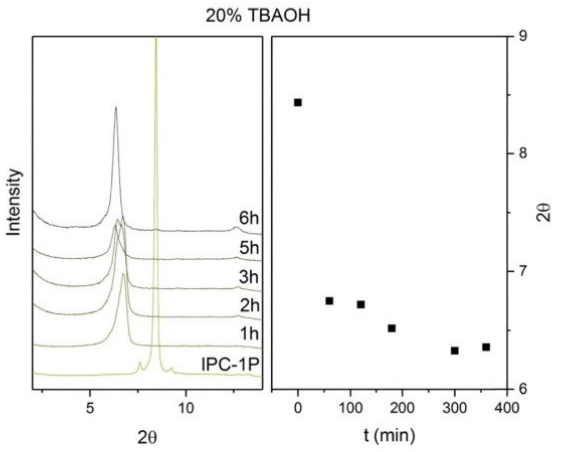

Fig. 2 Powder XRD patterns and positions of 200 diffraction lines of IPC-1P intercalated with TBA^+ over time.

To optimise the intercalation time, we performed a kinetic experiment with a 20% TBAOH solution. This solution has a basic pH, which is necessary to deprotonate the IPC-1P layers, to form silanolates, and to break the H-bonds between the layers.[34] However, high pH also causes desilication,[35–38] creating defects and mesopores in the material, which loses layer crystallinity. To preserve the crystallinity of the IPC-1P layers, we shortened the intercalation time. Fig. 2 shows the stabilisation of the 200 reflection at 6.37° for 6 hours. After 6 hours, the 200 peak position remains constant under the conditions of the treatment, thus indicating that the intercalation has ended.

3.2 Reconstruction

The aim, and the main challenge, of this study was to restore the **UTL** structure by reconstructing D4R units between IPC-1TBA layers. Numerous D4R-containing zeolites, including UTL, crystallise mainly as germanosilicates; therefore, we reconstructed UTL using silicon and germanium alkoxides and their combination for their good reactivity and solubility (see Section 3.3). After silicon and germanium incorporation, the 200 diffraction shifted from 6.37° to 6.16° (Fig. 3). New diffraction lines also appeared at 6.99, 7.35, 8.27, 9.55, 16.7 and 17.7°. These diffraction lines match the XRD pattern of the **UTL** structure. Moreover, these reflections remained unchanged after calcining the sample to remove the TBA^+. These findings suggest that the reconstructed **UTL** is stable without the support of organic agents.

The STEM image (Fig. 4) confirmed that the distance between the layers is 1.41 nm and that the layers are visibly connected as a three-dimensional framework. However, STEM also revealed that the treatments caused some etching of the

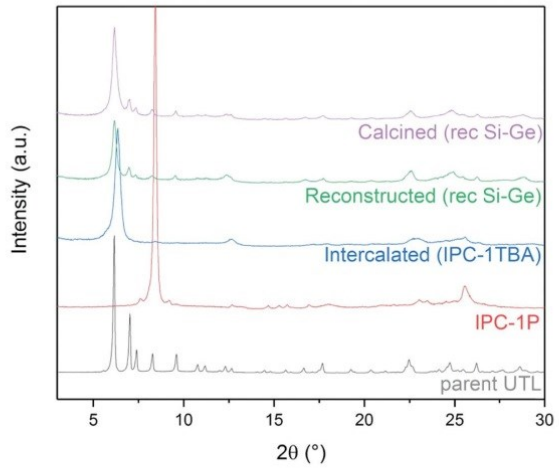

Fig. 3 Powder XRD patterns of individual stages in the IPC-1P-to-**UTL** reconstruction, using the rec Si–Ge (1 : 1) sample as an example.

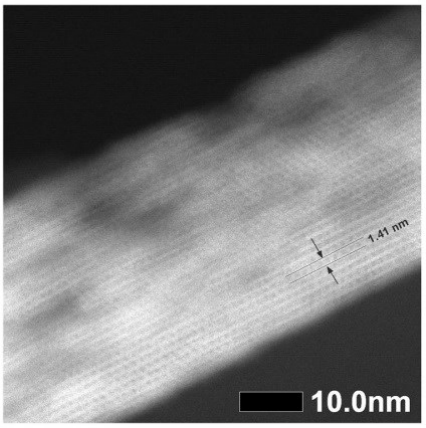

Fig. 4 STEM image of the reconstructed **UTL** sample.

Table 2 Textural properties of the parent **UTL** and reconstructed **UTL** material determined by Ar adsorption

	BET ($m^2\ g^{-1}$)	S_{ext} ($m^2\ g^{-1}$)	V_{tot} ($cm^3\ g^{-1}$)	V_{mic} ($cm^3\ g^{-1}$)	Si/Ge
Parent **UTL**	620	52	0.27	0.25	4.47
Reconstructed **UTL**	808	188	0.48	0.15	7.50

crystal, thereby forming mesopores in the zeolite. The formation of these mesopores is further supported by the changes in textural properties outlined in Table 2.

3.3 Ge content effect

Germanium can stabilise D4R units in zeolites.[39,40] The results shown above illustrate the structure directing effect of germanium on **UTL** reconstruction. We investigated how the germanium content affects the result in a series of similar reconstruction experiments with varying Si : Ge molar ratios (we use the "Si : Ge" notation to express the ratio of Si and Ge sources that we added to the reconstruction mixture to differentiate this ratio from the overall Si/Ge ratio of bulk samples).

XRD showed a broad diffraction peak at 7° (Fig. 5) in the sample reconstructed without germanium. The broad peak is caused by a non-uniform interlayer distance, thus implying that the layers lost their ideal ordering upon calcination. The loss of ordering likely stems from unsuccessful or incomplete reconstruction of the D4R units that connect individual layers. The samples reconstructed with both Si and Ge resulted in **UTL** structures. The peaks in XRD are less pronounced in the samples with 1 : 3 and 3 : 1 Si : Ge, mainly in the region from 5 to 10 °C. These patterns suggest that the interlayer ordering contains some defects. The sample with 1 : 1 Si : Ge produced the powder XRD pattern closest to that of the parent UTL zeolite. When we used only germanium for the reconstruction, the structure also collapsed upon calcination. Moreover, the diffraction pattern also contained new peaks at 25.7, 35.7, 37.7 and 39.2° belonging to germanium oxide. The germanium oxide species also appeared in the STEM image of the sample (Fig. S2, ESI†), which had a very low micropore volume (0.07 $cm^3\ g^{-1}$; Table 3). The formation of germanium oxide may result from the high reactivity of germanium methoxide, which forms the oxide before it can be incorporated into the framework.

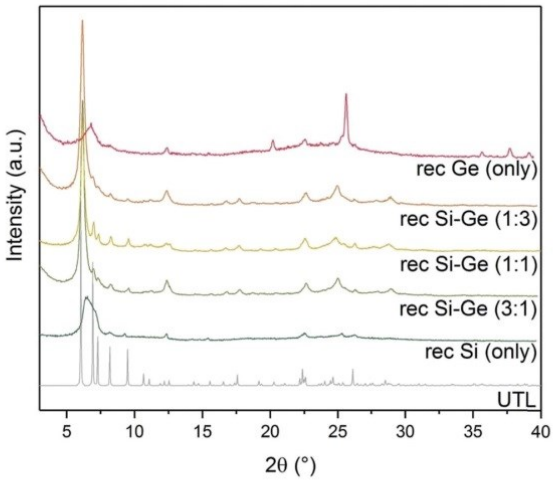

Fig. 5 Powder XRD patterns of calcined samples after reconstruction with different Si:Ge compositions.

Table 3 Textural properties of samples after reconstruction with different Si:Ge compositions determined by Ar adsorption

	BET ($m^2\ g^{-1}$)	S_{ext} ($m^2\ g^{-1}$)	V_{tot} ($cm^3\ g^{-1}$)	V_{mic} ($cm^3\ g^{-1}$)
UTL	620	52	0.27	0.25
rec Si (only)	645	334	0.48	0.12
rec Si–Ge (3 : 1)	550	156	0.35	0.12
rec Si–Ge (1 : 1)	808	188	0.48	0.15
rec Si–Ge (1 : 3)	555	165	0.36	0.11
rec Ge (only)	344	139	0.34	0.07

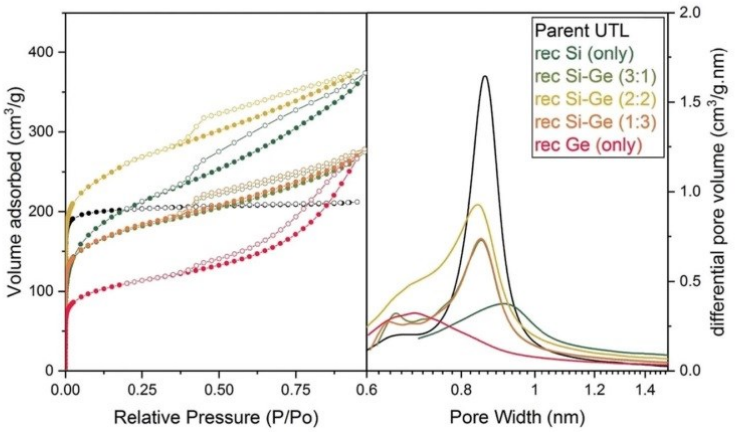

Fig. 6 Argon adsorption–desorption isotherms (left) and H–K micropore size distributions (right) of samples after reconstruction with different Si:Ge compositions.

Alternatively, the purely Ge-based D4Rs may be unstable under the current conditions, but this assumption requires further investigation, which is beyond the scope of this article.

The micropore volume of the reconstructed **UTL** samples ranges from 0.11 to 0.15 $cm^3\ g^{-1}$ (Fig. 6) and is thus smaller than the micropore volume of the parent **UTL** (0.25 $cm^3\ g^{-1}$). These poor textural properties may be caused by incomplete D4R reconstruction because intercalated TBA^+ occupy some D4R positions. Consequently, D4R reconstruction does not proceed until the intercalant is removed. To test this hypothesis, we performed D4R reconstruction with 1 : 1 Si : Ge, as described above, calcined the sample and repeated the reconstruction under the same conditions. However, we observed only negligible differences in powder XRD patterns (Fig. S3, ESI†) and adsorption behaviour (Fig. S4, ESI†). Nevertheless, the pore volume of the samples decreased after the second reconstruction cycle (Table S1, ESI†) due to further damage under such harsh conditions. This experiment disproved that TBA^+ significantly hinders D4R reconstruction.

Considering the presence of germanium in its D4R, we theorised that the reconstructed **UTL** may be able to undergo hydrolysis to IPC-1P. To test this hypothesis, we performed a hydrolysis of the reconstructed sample in water and in solution of acetic acid at 85 °C. In both cases the 200 reflection on the XRD pattern shifted to higher angles (Fig. S5, ESI†). The shift suggests that the material transformed during the hydrolysis. However, neither of the experiments produced the IPC-1P, probably due to low germanium content or uneven germanium distribution which prevented complete disassembly into layers.

3.4 Stabilisation by fluorides

Fluoride anions can also stabilise D4R units in zeolites. In fact, numerous D4R-containing extra-large-pore zeolites have been prepared in fluoride medium.[39,41,42] Based on the above, we assessed the effect of fluorides on D4R reconstruction. We performed another set of experiments with varying Si:Ge contents, with and without ammonium fluoride.

The powder XRD patterns (Fig. 7) of samples reconstructed with Si or Ge alone changed significantly after adding ammonium fluoride. The samples that were synthesized with fluoride showed 200 diffraction at 6.16°, similar to **UTL**. This diffraction remained unchanged even after calcination. Other reflections, characteristic of the **UTL**, also appeared at 6.99, 7.35, 8.27 and 9.55° in the sample reconstructed solely with Ge in fluoride-containing medium. However, the powder diffraction pattern of this sample also contained the peaks of germanium oxide. The sample reconstructed with Si alone showed a similar change after adding fluorides, but the other diffraction lines were significantly less intense. The XRD pattern of the sample prepared with 1 : 1 Si : Ge shows no significant difference after adding ammonium fluoride.

Structural changes caused by fluoride addition to the mixture are also identified in the pore-size distribution. The shape of the distribution curves (Fig. 8) of Ge- and Si-only samples

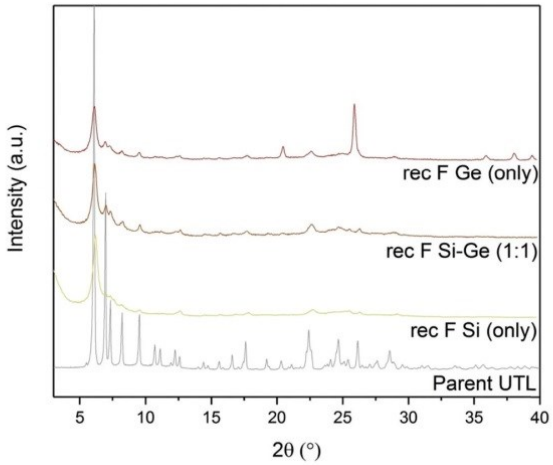

Fig. 7 Powder XRD patterns of calcined samples after D4R reconstruction with different Si:Ge compositions, with and without NH_4F.

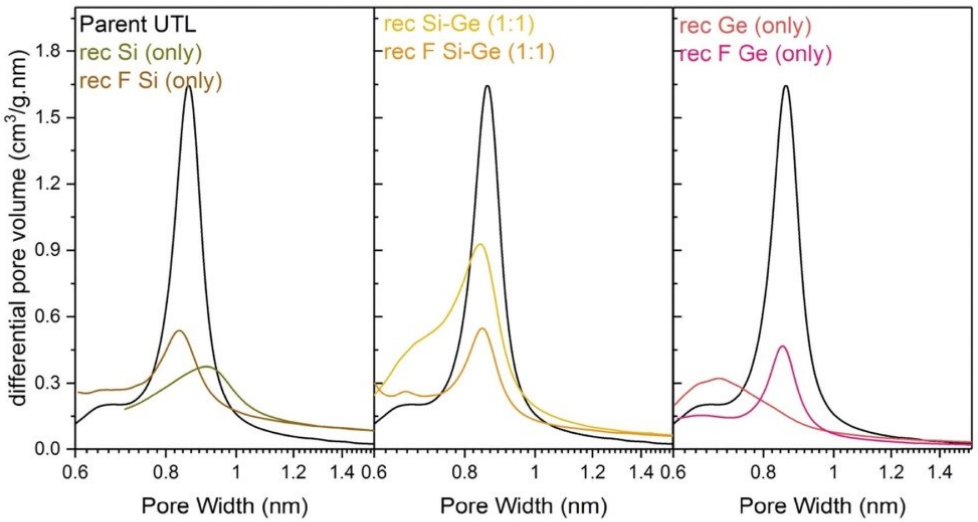

Fig. 8 H–K micropore size distributions of samples after reconstruction with different Si:Ge compositions, with and without NH_4F.

Table 4 Textural properties of the samples after reconstruction with different Si:Ge compositions determined by Ar adsorption, with NH_4F

	BET (m^2 g)	S_{ext} (m^2 g^{-1})	V_{tot} (cm^3 g^{-1})	V_{mic} (cm^3 g^{-1})
UTL	620	52	0.27	0.25
Pure Si	691	341	0.56	0.05
Si : Ge 1 : 1	555	281	0.46	0.06
Pure Ge	280	101	0.26	0.07

narrowed down. Simultaneously, the maxima of the distribution shifted to 0.84 nm, near the 0.85 nm of the parent UTL. However, all samples prepared in fluoride media had micropore volumes smaller than 0.07 cm^3 g^{-1} (Table 4) far lower than that of the parent UTL (0.25 cm^3 g^{-1}; Table 2). This decrease may originate from framework etching by fluoride anions in solution, leading to partial amorphisation of the material (Fig. S7, ESI†) and/or subsequent pore blockage by amorphous framework debris.

In summary, while fluoride anions stabilise D4R units, they simultaneously damage the material, which accounts for the poor micropore volumes of the samples.

3.5 Structure of the silicon source

D4R formation solely from silane molecules is unfavourable without fluoride anions to stabilise these units. For this reason, we investigated whether other Si sources would form D4R units, even without using germanium or fluorides, *e.g.*, diethoxydimethylsilane (Si1), 1,3-diethoxy-1,1,3,3-tetramethyl-disiloxane (Si2), 2,4,6,8-tetramethylcyclotetrasiloxane (Si4) and octamethylsilsesquioxane (Si8) as Si sources. The broad diffraction peak at 7° in both Si1 and Si2 samples (Fig. 9) implies that their relative layer arrangements lack order and that their structure collapsed after calcination. In contrast, samples Si4 and Si8 retained a very narrow 200 diffraction peak at 6.16°, even after the calcination.

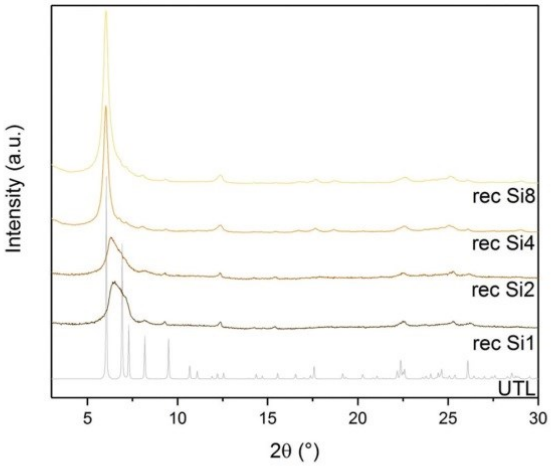

Fig. 9 Powder XRD patterns of calcined samples after D4R reconstruction with different Si sources.

The other diffractions at 6.99, 7.35, 8.27 and 9.55° remained unchanged but were less intense than in the germanium-containing sample, as shown in Fig. 3. This lower intensity may arise from the higher silicon content of the samples Si4 and Si8.

STEM measurements (Fig. 10) further confirmed the structure and interlayer spacing, showing 1.41 nm distances between individual layers. This distance is in line with the **UTL** structure. We analysed the composition of the sample Si4 by EDX. The sample has a Si/Ge ratio of 481. This is an interesting result because D4R-containing zeolites or any extra-large pore zeolite with such a high Si content are seldom prepared without any hetero-element (such as Ge) or fluorides.[43]

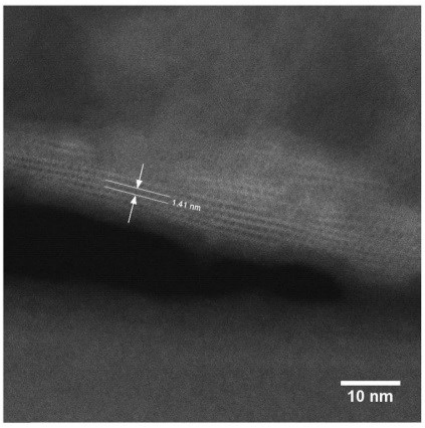

Fig. 10 STEM image of the reconstructed **UTL** sample Si4.

3.6 Tuning the textural properties

Regardless of their elemental composition, all the **UTL** samples that were reconstructed in this study had lower micropore volumes, ranging from 0.11 to 0.15 $cm^3\ g^{-1}$, than their parent **UTL** sample (0.25 $cm^3\ g^{-1}$). Their lower pore volumes stem from their decreased crystallinity inflicted during the intercalation of the samples with TBA^+. The IPC-1TBA crystal shown in Fig. 11 is severely damaged after intercalation because the treatment resulted in formation of defects and mesopores in the crystal. However, this is not necessarily a disadvantage of the method as the formation of defects may be beneficial because mesopores can enhance diffusion in catalytic applications.[44]

The high pH of the treatment solution causes etching but is needed for TBA^+ intercalation. Under optimal conditions, intercalation would proceed at the lowest pH possible to minimise the damage to the crystals, albeit high enough to support TBA^+ intercalation. To find the optimal conditions, we intercalated IPC-1P with 40, 20, 10, 5 and 2% TBAOH solutions and monitored the position of the 200 diffraction (Fig. 12). The position of

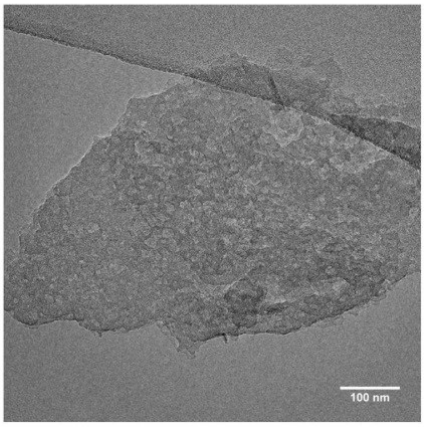

Fig. 11 TEM image of the damaged IPC-1TBA sample crystal.

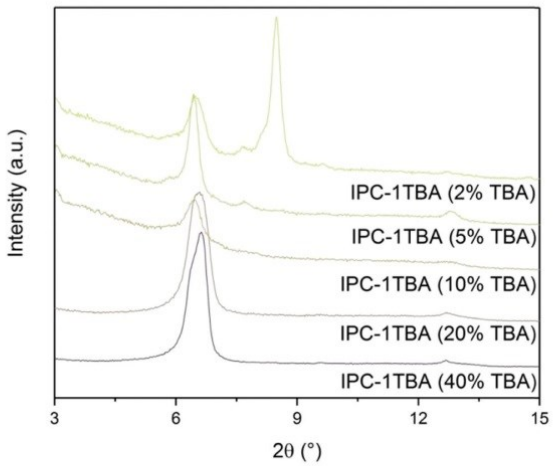

Fig. 12 Powder XRD patterns of IPC-1P samples intercalated with TBAOH of varying concentrations.

200 peak in the samples treated with 40, 20 and 10% TBAOH was identified at 6.37°. The powder XRD pattern of the sample treated with 5% TBAOH also contained a peak at 6.37° but another, minor diffraction appeared at 7.67°. Treatment with 2% TBAOH resulted in three diffractions at 6.37, 7.67 and 8.4°, indicating incomplete intercalation. In summary, 5% is the minimum TBAOH concentration required for successful TBA^+ intercalation into IPC-1P.

We reconstructed all samples with 1 : 1 Si : Ge, including the sample treated with a 2% TBAOH, and subsequently characterised them by adsorption. All isotherms showed large adsorbed amounts at a relative pressure bellow 0.1 (Fig. 13) – filling of micropores. At higher pressures, the intake decreased in all samples; however, the flat plateau observed in the parent

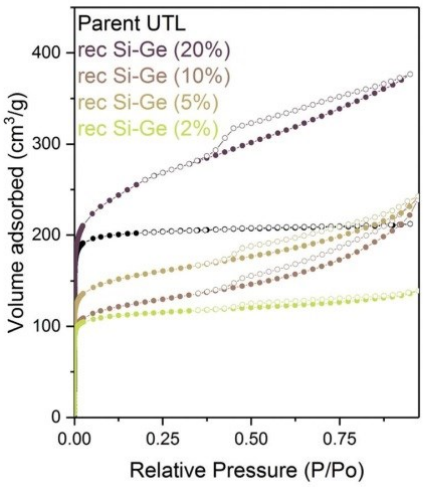

Fig. 13 Argon adsorption–desorption isotherms of reconstructed samples previously intercalated with TBAOH of varying concentrations.

UTL sample was not found, suggesting that the samples contain not only micropore but also some mesopores. Nevertheless, the slope of the isotherm above the relative pressure p/p_0 of 0.1 decreases with the decrease in the concentration of the TBAOH solution. The lower hydroxide concentration mitigates the damage and produces samples with fewer defects.

4. Conclusions

Until now, the ADOR method was limited to decreasing the interlayer distance and, consequently, the pore size of the parent zeolite during the process. In this study, we overcome this limitation by intercalating organic species between IPC-1P layers formed by UTL hydrolysis. TBAOH intercalation increases the *d*-spacing to 1.41 nm, the distance of the original UTL structure. The UTL structure is then restored using varying Si and Ge ratios to rebuild the D4R units between the intercalated IPC-1P layers, and the formation of D4Rs is promoted in the presence of an optimal Ge content or fluoride ions. Moreover, the UTL zeolite can also be restored using structurally more complex compounds, such as cyclotetrasiloxanes or polyhedral silsesquioxanes. In summary, the "Reverse ADOR" produces zeolites with a wide range of various compositions, ranging from the common UTL with a 7.5 Si/Ge to the new high-silica UTL with 481 Si/Ge.

While the intercalation treatment inherently causes the formation of mesopores in the zeolite crystals, we can mitigate its impact by tuning the treatment conditions. Furthermore, these mesopores may, in turn, be advantageous in future catalytic applications. Therefore, the "Reverse ADOR" method opens up opportunities for incorporating other elements towards producing novel zeolite-based catalysts.

Conflicts of interest

There are no conflicts to declare.

Acknowledgements

The authors acknowledge the support of the Czech Science Foundation to the project EXPRO (19-27551X) and OP VVV "Excellent Research Teams", project no. CZ.02.1.01/0.0/0.0/15_003/0000417 – CUCAM. REM thanks the European Research Council for the provision of an Advanced Grant (ADOR – 787073). The authors acknowledge Dr Michal Mazur (Charles University) for the STEM imaging, Dr Martin Kubů (Charles University) for the Ar adsorption measurements, and Dr Carlos V. Melo for editing the manuscript.

References

1 J. Čejka, H. van Bekkum, A. Corma and F. Schueth, *Introduction to Zeolite Molecular Sieves*, Elsevier, Amsterdam, 2007.
2 J. Čejka, E. R. Morris and P. Nachtigall, *Zeolites in Catalysis: Properties and Applications*, The Royal Society of Chemistry, 2017.
3 W. Vermeiren and J. P. Gilson, Impact of zeolites on the petroleum and petrochemical industry, *Top. Catal.*, 2009, **52**, 1131–1161.
4 J. Prech, P. Pizarro, D. P. Serrano and J. Cejka, From 3D to 2D zeolite catalytic materials, *Chem. Soc. Rev.*, 2018, **47**, 8263–8306.
5 T. Ennaert, J. Van Aelst, J. Dijkmans, R. De Clercq, W. Schutyser, M. Dusselier, D. Verboekend and B. F. Sels, Potential and challenges of zeolite chemistry in the catalytic conversion of biomass, *Chem. Soc. Rev.*, 2016, **45**, 584–611.
6 P. Sudarsanam, E. Peeters, E. V. Makshina, V. I. Parvulescu and B. F. Sels, Advances in porous and nanoscale catalysts for viable biomass conversion, *Chem. Soc. Rev.*, 2019, **48**, 2366–2421.
7 E. Taarning, C. M. Osmundsen, X. Yang, B. Voss, S. I. Andersen and C. H. Christensen, Zeolite-catalyzed biomass conversion to fuels and chemicals, *Energy Environ. Sci.*, 2011, **4**, 793–804.
8 M. Shamzhy, M. Opanasenko, P. Concepción and A. Martínez, New trends in tailoring active sites in zeolite-based catalysts, *Chem. Soc. Rev.*, 2019, **48**, 1095–1149.
9 L.-H. Chen, M.-H. Sun, Z. Wang, W. Yang, Z. Xie and B.-L. Su, Hierarchically Structured Zeolites: From Design to Application, *Chem. Rev.*, 2020, **120**, 11194–11294.
10 C. S. Cundy and P. A. Cox, The Hydrothermal Synthesis of Zeolites: History and Development from the Earliest Days to the Present Time, *Chem. Rev.*, 2003, **103**, 663–702.
11 J. Yu, Synthesis of Zeolites, in *Studies in Surface Science and Catalysis*, ed. J. Čejka, H. van Bekkum, A. Corma and F. Schüth, Elsevier, 2007, pp. 39–103.
12 P. Eliášová, M. Opanasenko, P. S. Wheatley, M. Shamzhy, M. Mazur, P. Nachtigall, W. J. Roth, R. E. Morris and J. Čejka, The ADOR mechanism for the synthesis of new zeolites, *Chem. Soc. Rev.*, 2015, **44**, 7177–7206.
13 D. S. Firth, S. A. Morris, P. S. Wheatley, S. E. Russell, A. M. Z. Slawin, D. M. Dawson, A. Mayoral, M. Opanasenko, M. Položij, J. Čejka, P. Nachtigall and R. E. Morris, Assembly–Disassembly–Organization–Reassembly Synthesis of Zeolites Based on cfi-Type Layers, *Chem. Mater.*, 2017, **29**, 5605–5611.
14 M. Opanasenko, M. Shamzhy, Y. Wang, W. Yan, P. Nachtigall and J. Čejka, Synthesis and Post-Synthesis Transformation of Germanosilicate Zeolites, *Angew. Chem., Int. Ed.*, 2020, **59**, 19380–19389.
15 C. J. Heard, L. Grajciar, F. Uhlík, M. Shamzhy, M. Opanasenko, J. Čejka and P. Nachtigall, Zeolite (In)Stability under Aqueous or Steaming Conditions, *Adv. Mater.*, 2020, **32**, 2003264.
16 W. J. Roth, O. V. Shvets, M. Shamzhy, P. Chlubna, M. Kubu, P. Nachtigall and J. Čejka, Postsynthesis Transformation of Three-Dimensional Framework into a Lamellar Zeolite with Modifiable Architecture, *J. Am. Chem. Soc.*, 2011, **133**, 6130–6133.
17 W. J. Roth, P. Nachtigall, R. E. Morris, P. S. Wheatley, V. R. Seymour, S. E. Ashbrook, P. Chlubna, L. Grajciar, M. Polozij, A. Zukal, O. Shvets and J. Čejka, A family of zeolites with controlled pore size prepared using a top-down method, *Nat. Chem.*, 2013, **5**, 628–633.

18 P. S. Wheatley, P. Chlubná-Eliášová, H. Greer, W. Zhou, V. R. Seymour, D. M. Dawson, S. E. Ashbrook, A. B. Pinar, L. B. McCusker, M. Opanasenko, J. Čejka and R. E. Morris, Zeolites with Continuously Tuneable Porosity, *Angew. Chem.*, 2014, **126**, 13426–13430.

19 S. A. Morris, G. P. M. Bignami, Y. Tian, M. Navarro, D. S. Firth, J. Čejka, P. S. Wheatley, D. M. Dawson, W. A. Slawinski, D. S. Wragg, R. E. Morris and S. E. Ashbrook, In situ solid-state NMR and XRD studies of the ADOR process and the unusual structure of zeolite IPC-6, *Nat. Chem.*, 2017, **9**, 1012–1018.

20 M. Mazur, P. S. Wheatley, M. Navarro, W. J. Roth, M. Položij, A. Mayoral, P. Eliášová, P. Nachtigall, J. Čejka and R. E. Morris, Synthesis of 'unfeasible' zeolites, *Nat. Chem.*, 2016, **8**, 58–62.

21 S. E. Henkelis, M. Mazur, C. M. Rice, P. S. Wheatley, S. E. Ashbrook and R. E. Morris, Kinetics and Mechanism of the Hydrolysis and Rearrangement Processes within the Assembly–Disassembly–Organization–Reassembly Synthesis of Zeolites, *J. Am. Chem. Soc.*, 2019, **141**, 4453–4459.

22 S. E. Henkelis, M. Mazur, C. M. Rice, G. P. M. Bignami, P. S. Wheatley, S. E. Ashbrook, J. Čejka and R. E. Morris, A procedure for identifying possible products in the assembly–disassembly–organization–reassembly (ADOR) synthesis of zeolites, *Nat. Protoc.*, 2019, **14**, 781–794.

23 H. Xu, J.-G. Jiang, B. Yang, L. Zhang, M. He and P. Wu, Post-Synthesis Treatment gives Highly Stable Siliceous Zeolites through the Isomorphous Substitution of Silicon for Germanium in Germanosilicates, *Angew. Chem., Int. Ed.*, 2014, **53**, 1355–1359.

24 W. J. Roth, W. Makowski, B. Marszalek, P. Michorczyk, W. Skuza and B. Gil, Activity enhancement of zeolite MCM-22 by interlayer expansion enabling higher Ce loading and room temperature CO oxidation, *J. Mater. Chem. A*, 2014, **2**, 15722–15725.

25 P. Wu, J. Ruan, L. Wang, L. Wu, Y. Wang, Y. Liu, W. Fan, M. He, O. Terasaki and T. Tatsumi, Methodology for Synthesizing Crystalline Metallosilicates with Expanded Pore Windows Through Molecular Alkoxysilylation of Zeolitic Lamellar Precursors, *J. Am. Chem. Soc.*, 2008, **130**, 8178–8187.

26 B. Yang, J.-G. Jiang, H. Xu, H. Wu and P. Wu, Synthesis of Large-Pore ECNU-19 Material (12 × 8-*R*) *via* Interlayer-Expansion of HUS-2 Lamellar Silicate, *Chin. J. Chem.*, 2018, **36**, 227–232.

27 M. Mazur, P. Chlubná-Eliášová, W. J. Roth and J. Čejka, Intercalation chemistry of layered zeolite precursor IPC-1P, *Catal. Today*, 2014, **227**, 37–44.

28 O. V. Shvets, A. Zukal, N. Kasian, N. Žilková and J. Čejka, The Role of Crystallization Parameters for the Synthesis of Germanosilicate with UTL Topology, *Chem. – Eur. J.*, 2008, **14**, 10134–10140.

29 W. J. Roth, Cation size effects in swelling of the layered zeolite precursor MCM-22-P, *Pol. J. Chem.*, 2006, **80**, 703–708.

30 P. Chlubna, W. J. Roth, A. Zukal, M. Kubu and J. Pavlatova, Pillared MWW zeolites MCM-36 prepared by swelling MCM-22P in concentrated surfactant solutions, *Catal. Today*, 2012, **179**, 35–42.

31 M. Shamzhy, M. Mazur, M. Opanasenko, W. J. Roth and J. Cejka, Swelling and pillaring of the layered precursor IPC-1P: tiny details determine everything, *Dalton Trans.*, 2014, **43**, 10548–10557.

32 M. Opanasenko, W. O. N. Parker, M. Shamzhy, E. Montanari, M. Bellettato, M. Mazur, R. Millini and J. Čejka, Hierarchical Hybrid Organic–Inorganic Materials with Tunable Textural Properties Obtained Using Zeolitic-Layered Precursor, *J. Am. Chem. Soc.*, 2014, **136**, 2511–2519.

33 C. Baerlocher and L. B. McCusker, in, Database of Zeolite Structures, http://www.iza-structure.org/databases/.

34 W. J. Roth and J. C. Vartuli, Preparation of exfoliated zeolites from layered precursors: The role of pH and nature of intercalating media, in *Nanoporous Materials Iii*, ed. A. Sayari and M. Jaroniec, 2002, pp. 273–279.

35 B. Gil, Ł. Mokrzycki, B. Sulikowski, Z. Olejniczak and S. Walas, Desilication of ZSM-5 and ZSM-12 zeolites: Impact on textural, acidic and catalytic properties, *Catal. Today*, 2010, **152**, 24–32.

36 D. Verboekend and J. Perez-Ramirez, Desilication Mechanism Revisited: Highly Mesoporous All-Silica Zeolites Enabled Through Pore-Directing Agents, *Chem. – Eur. J.*, 2011, **17**, 1137–1147.

37 M. Kubů, M. Opanasenko and M. Shamzy, Modification of textural and acidic properties of SVR zeolite by desilication, *Catal. Today*, 2014, **227**, 26–32.

38 M. Kubů, M. Opanasenko and D. Vitvarová, Desilication of SSZ-33 zeolite – Post-synthesis modification of textural and acidic properties, *Catal. Today*, 2015, **243**, 46–52.

39 T. Blasco, A. Corma, M. J. Díaz-Cabañas, F. Rey, J. A. Vidal-Moya and C. M. Zicovich-Wilson, Preferential Location of Ge in the Double Four-Membered Ring Units of ITQ-7 Zeolite, *J. Phys. Chem. B*, 2002, **106**, 2634–2642.

40 P. Kamakoti and T. A. Barckholtz, Role of Germanium in the Formation of Double Four Rings in Zeolites, *J. Phys. Chem. C*, 2007, **111**, 3575–3583.

41 J. Jiang, J. L. Jorda, M. J. Diaz-Cabanas, J. Yu and A. Corma, The Synthesis of an Extra-Large-Pore Zeolite with Double Three-Ring Building Units and a Low Framework Density, *Angew. Chem., Int. Ed.*, 2010, **49**, 4986–4988.

42 A. Corma, M. J. Díaz-Cabañas, J. Jiang, M. Afeworki, D. L. Dorset, S. L. Soled and K. G. Strohmaier, Extra-large pore zeolite (ITQ-40) with the lowest framework density containing double four- and double three-rings, *Proc. Natl. Acad. Sci. U. S. A.*, 2010, **107**, 13997–14002.

43 M. Fischer and L. Freymann, Local Distortions in a Prototypical Zeolite Framework Containing Double Four-Ring Cages: The Role of Framework Composition and Organic Guests**, ChemPhysChem, n/a.

44 D. Schneider, D. Mehlhorn, P. Zeigermann, J. Kärger and R. Valiullin, Transport properties of hierarchical micro–mesoporous materials, *Chem. Soc. Rev.*, 2016, **45**, 3439–3467.

Publication 4:

Ondřej Veselý, Michal Mazur, Jan Přech, Jiří Čejka

Modified reverse ADOR assembles Al-rich UTL zeolite from IPC-1P layers

Inorganic Chemistry Frontiers, 9 (2022) 5444-5453

DOI: 10.1039/D2QI01360F

Contribution: Synthesis of the parent UTL germanosilicate and hydrolysis to the IPC-1P, Intercalation experiments, development and carrying out the reconstruction experiments, argon sorption measurements, assistance with the Transmission Electron Microscopy imaging, catalytic experiments, evaluation and interpretation of the data and writing of the manuscript.

INORGANIC CHEMISTRY FRONTIERS

RESEARCH ARTICLE

Cite this: *Inorg. Chem. Front.*, 2022, **9**, 5444

Modified reverse ADOR assembles Al-rich UTL zeolite from IPC-1P layers†

Ondřej Veselý, * Michal Mazur, Jan Přech and Jiří Čejka

Received 25th June 2022,
Accepted 13th August 2022

DOI: 10.1039/d2qi01360f

rsc.li/frontiers-inorganic

Extra-large pore zeolites clear the way for the synthesis of fine chemicals and bulky compounds unable to enter the channels of medium- and large-pore zeolites. However, such extra-large pore zeolites rarely contain catalytically active elements and often show limited stability. In this study, we modified the Reverse assembly–disassembly–organisation–reassembly (ADOR) process to prepare extra-large pore zeolite **UTL** from layered IPC-1P while simultaneously incorporating a high amount of aluminium (reaching Si/Al = 15) into the framework. Using this modified Reverse ADOR approach, we significantly reduced the synthesis time of alumino-germanosilicate **UTL** from the 28 days needed for direct synthesis to only 24 hours for reconstruction and 14 days in total. Furthermore, in the tetrahydropyranylation of 1-decanol over the reconstructed **UTL** zeolite, directly synthesised **UTL** and commercial Beta zeolite, used as a reference, reconstructed **UTL** provided conversion up to 61.4%, outperforming directly synthesised **UTL** and Beta with 14.8 and 0% conversion, respectively. The modified Reverse ADOR procedure enables us to introduce mesoporosity into zeolites, which further improves their catalytic performance by facilitating active site accessibility.

1. Introduction

Zeolites are a group of microporous crystalline tectosilicates whose crystal framework comprises tetrahedral units, with silicon in their centre, connected through oxygen atoms in their corners. Framework tetrahedra may also contain other elements with suitable size and coordination, such as Al, Ge, Ti, Fe or Sn, and some zeolite structures may even require a heteroelement (B or Ge, among others) for their formation.[1] These heteroelements introduce Brønsted and/or Lewis acidity into zeolites and affect their thermal/hydrothermal stability. Trivalent elements (for example, Al^{3+}, Ga^{3+}, and Fe^{3+}) form Brønsted acid sites,[2] whereas tetravalent elements with unoccupied orbitals (Ti, Zr, Ge, and Sn, among others) provide Lewis acid sites.[3] Although the framework stability may decrease in the presence of these substituting elements, including B and Ge,[4–6] we may use this lability for post-synthetic modifications.[1] Selectively removing these atoms creates vacancies for introducing other catalytically active species.[1,7–9]

The Assembly–Disassembly–Organisation–Reassembly (ADOR) process is a notable example of a post-synthetic transformation. ADOR exploits weak spots in the structure of numerous germanosilicate zeolites – Ge-rich double-four ring (D4R) units. Upon chemically selective hydrolysis of D4Rs, only Si-rich zeolitic layers remain intact, but these layers may subsequently be reorganised and reconnected to form new structures.[10] As a case in point, **UTL** germanosilicate,[11,12] the most widely studied zeolite in ADOR, produces layered IPC-1P upon hydrolysis.[13] These IPC-1P layers can act as building blocks for new 3D zeolites.[14–16]

The ADOR transformation of **UTL** germanosilicate can yield a whole family of new zeolites. The daughter materials consist of the same layers connected by S4R units (**OKO**), oxygen bridges (**PCR**) or combination of S4R and D4R (IPC-7) and S4R and oxygen bridges (***PCS**).[10,14,17] In addition to that, shifting the layers in crystallographic b-direction and connecting by S4R or oxygen bridges produces structures with odd-numbered rings (IPC-10 and 9, respectively).[15] However, all aforementioned zeolites contain only large- or medium-size pores. In other words, the ADOR transformation of **UTL** zeolites decreases their pore size. The only exception to this rule is IPC-7 in which some D4R units are preserved during the treatment and the recently developed Reverse ADOR approach.[16,18]

Through Reverse ADOR, we can prepare **UTL** from layered IPC-1P by expanding the layers through the intercalation of cations, thus producing zeolites with extra-large pores (*i.e.*, larger than 12-ring pores) from layered precursors.[18] In addition, Ge atoms from the original positions in d4r units are substituted for Si or other heteroatoms, which considerably increases the hydrothermal stability of the **UTL**.[19] Extra-large pore zeolites are highly desirable[20,21] because they can catalyse the synthesis of fine chemicals, which are often bulky molecules unable to penetrate into medium- and large-pore zeolite

Department of Physical and Macromolecular Chemistry, Faculty of Sciences, Charles University, Hlavova 8, 128 43 Prague 2, Czech Republic.
E-mail: ondrej.vesely@natur.cuni.cz

†Electronic supplementary information (ESI) available. See DOI: https://doi.org/10.1039/d2qi01360f

catalysts. However, these extra-large pore zeolites, including **UTL** zeolite, rarely contain catalytically active elements (*e.g.*, Al, Ga, Fe, and Ti). Several articles have reported the synthesis of Al–, Ga– or Fe– containing **UTL** zeolites, but their content is limited, and introducing these elements significantly prolongs the synthesis time. For example, the introduction of aluminium extends the synthesis time of **UTL** from 8 (Al-free) to 28 (Si/Al = 44) days.[6,22,23] As a result, the synthesis of the alumino-germanosilicate **UTL** is much more tedious and impractical than the synthesis of germanosilicate **UTL**. The Reverse ADOR transforms an intercalated layered precursor to the **UTL** zeolite with varying composition, however; previous study focused only on the incorporation of Si and Ge. Furthermore, the intercalation and reconstruction treatments partially dissolved the precursor resulting in poor yields of final zeolites.[18]

Considering the above, we aimed to overcome limitations of the Reverse ADOR method preventing its wider use by improving the yields of the intercalated precursor IPC1-TBA and by determining the appropriate conditions for incorporating catalytically active elements. For this purpose, we addressed the following key questions: (i) What is the limit of heteroelement incorporation and its variation as a function of the synthesis conditions? (ii) How does heteroelement introduction alter the properties of the final zeolite (*e.g.*, crystallinity and textural properties)? (iii) What are the advantages of a catalyst prepared by Reverse ADOR process over the same catalyst prepared by directly synthesis? To answer these questions, we incorporated aluminium into the **UTL** framework and assessed the catalytic activity of both Reverse ADOR- and directly synthesised **UTL** zeolites in the tetrahydropyranylation reaction of 1-decanol, using commercial **BEA** zeolite as a reference. In addition to introducing mesoporosity into the zeolite, our modified Reverse ADOR approach approximately halved the total synthesis time, increased the aluminium content and thus the concentration of active sites, and the resulting catalyst showed enhanced mass transfer during catalysis, together with increased reactant conversion rates and product yields. Accordingly, this contribution reports another major step forward in Reverse ADOR for the synthesis of aluminosilicate or alumino-germanosilicate **UTL** zeolites.

2. Experimental

2.1. Synthesis of structure directing agents

The structure directing agent (SDA) for the preparation of germanosilicate **UTL**, the 2,6-dimethyl-5-anizospiro[4.5]decane (DMASD) bromide, was synthesized by mixing 60 mL of 1,4-dibromobutane, 82.9 g of K_2CO_3 and 500 mL of acetonitrile in a round-bottom flask. Subsequently, 67 mL of 2,6-dimethylpiperidine was added dropwise, and the mixture was heated to 85 °C and kept refluxing overnight. Once the acetonitrile was evaporated, the solid product was dissolved in ethanol. The insoluble fraction was filtered off and disposed of. The ethanol extract was evaporated to create an almost saturated solution. Then, the product was precipitated by adding diethyl ether, and the solid product was filtered off, washed with diethyl ether, and dried under vacuum overnight. The identity of the SDA structure was confirmed by ^{1}H NMR spectroscopy (Fig. S1†). This SDA was ion exchanged to the hydroxide form using Ambersep 900(OH) ion exchange resin with a 2 : 1 SDA : resin w/w ratio.

The SDA for alumino-germanosilicate **UTL**, 7-ethyl-6-azoniaspiro[5.5]undecane (EASuD) bromide, was synthesized following a procedure similar to that used for 2,6-dimethyl-5-anizosporo[4.5]decane, with 1,4-dibromopentane and 2-ethylpiperidine as the starting compounds. The structure of the SDA was verified by ^{1}H NMR spectroscopy (Fig. S2†). This SDA was ion exchanged to the hydroxide form using the Ambersep 900 (OH) ion exchange resin with a 2 : 1 SDA : resin w/w ratio.

2.2. UTL synthesis

The germanosilicate **UTL** zeolite was prepared following a procedure described in the literature, using DMASD hydroxide as the SDA.[11,24] The molar composition of the synthesis mixture was 0.67 SiO_2: 0.33 GeO_2: 0.4 SDA: 33.3 H_2O. Crystallization in a 1000 mL stainless steel Parr autoclave at 175 °C for 6 days with agitation (200 rpm) resulted in a product which was dried and calcined in air at 550 °C for 6 hours with a ramp 1 °C min^{-1}.

The alumino-germanosilicate **UTL** ("Al-UTL") was prepared following an analogous synthesis using EASuD hydroxide as the SDA and aluminium hydroxide as the aluminium source. The EASuD SDA facilitates aluminium incorporation into the **UTL**, in contrast to the DMASD, which is more suitable for preparation of pure germanosilicate **UTL**[6,23] A synthesis mixture with a molar composition of 1 SiO_2 : 0.5 GeO_2 : 0.012 Al_2O_3 : 0.4 SDA : 33.3 H_2O was placed into 90 mL Teflon lined autoclave and heated under agitation at 175 °C for 28 days. The recovered solid was dried and calcined in air at 550 °C for 6 hours with a ramp of 1 °C min^{-1}.

2.3. Al-UTL stabilisation

As-synthesized Al-UTL was stabilised according to a previously published protocol to increase its hydrothermal stability.[25] For this purpose, 0.15 g of as-synthesized Al-UTL was mixed with 15 mL of 1.25 M HCl solution in ethanol (Sigma-Aldrich) diluted to required concentration with pure ethanol (see section 3.2.) and 33 mg of TEOS in a Teflon-lined autoclave. The mixture was stirred for 15 min and then heated in the closed autoclave to 175 °C for 24 hours under static conditions. Subsequently, the solid was recovered by filtration, dried at 60 °C, and then stirred in 15 mL of 1 M $Al(NO_3)_3$ solution at 80 °C for 24 hours. The sample was recovered by filtration, dried at 60 °C, and calcined in air at 550 °C for 6 hours.

2.4. IPC-1P preparation

Layered IPC-1P was prepared by calcined **UTL** zeolite hydrolysis. In a glass bottle, 250 mL of 1 M CH_3COOH was heated to 85 °C, adding 1 g of a freshly calcined **UTL** to the mixture.

After 24 hours, the solid was recovered by filtration and washed with a copious amount of distilled water. The product was dried at 60 °C.

2.5. Intercalation

IPC-1P was mixed with an aqueous solution of tetrabutylammonium hydroxide (TBAOH) and colloidal silica (Ludox AS-40) in varying ratios using 30 mL of the solution per 1 g of IPC-1P. The mixture was stirred for 6 hours at room temperature. Subsequently, the solid was recovered by centrifugation, washed with distilled water to neutral pH and dried at 60 °C yielding intercalated IPC-1 (IPC-1TBA).

2.6. UTL reconstruction

For **UTL** reconstruction, 0.1 g of IPC-1TBA was added to a 25 mL, Teflon-lined steel autoclave, along with 5 mL of HCl solution and diethoxydimethylsilane, germanium methoxide, aluminium nitrate and ammonium fluoride, which were used as sources of the respective elements. Exact composition for individual samples is listed in Table S1.† **UTL** was reconstructed at 170 °C for 20 hours. The solid was recovered by filtration, washed with ethanol, and dried at 60 °C. TBA was removed by calcination in air at 550 °C for 6 hours.

2.7. Ion exchange

The samples were ion exchanged to their H^+ form by stirring 1 g of sample with 100 mL of a 0.5 M NH_4NO_3 solution in ethanol for 4 hours at room temperature. The solid was recovered by centrifugation, and the procedure was repeated four times. The exchanged samples were dried at 60 °C and subsequently activated at 450 °C for 90 min.

2.8. Characterisation

Sample crystallinity was determined by X-ray powder diffraction (XRD) analysis on a Bruker D8 Advance diffractometer equipped with a Linxeye XE-T detector in the Bragg–Brentano geometry using Cu Kα (λ = 0.15406 nm) radiation. Data were collected over the 2θ range of 3–40° with 0.021° step size and 0.8 s time per step.

Sample morphology, structure and phase purity were analysed by scanning transmission electron microscopy (STEM) under a JEOL NeoARM 200 F microscope equipped with a Schottky-type field emission gun operated at an accelerating voltage of 200 kV. Phase composition was investigated by EDX mapping on an EX-37001 energy dispersive X-ray analyser. The Si/Al molar ratios of the **UTL** samples were calculated as an average Si/Al molar ratio by EDX analysis of four separate **UTL** crystals for each sample. Microscope was aligned using a gold nanoparticles sample as the standard to reach atomic resolution. STEM alignment involves the emission current optimisation, the correction of the condenser lens aperture size and position, and spherical aberration correction (using CEOS ASCOR corrector) based on the structure of a Ronchigram.

Sample surface area, pore volume and pore size distribution were determined from argon adsorption/desorption isotherms measured on a Micromeritics 3Flex volumetric Surface Area Analyser at −186 °C. Before the measurements, the samples were degassed on a Micromeritics Smart Vac Prep instrument under vacuum at 250 °C (heating rate 1 °C min^{-1}) for 8 hours at 3×10^{-2} mmHg minimum pressure. The specific surface area was evaluated using the BET method and adsorption data in the relative pressure range from p/p_0 = 0.05 to p/p_0 = 0.25. The t-plot method was applied to determine the volume of micropores (V_{mic}). The adsorbed amount at relative pressure p/p_0 = 0.98 reflects the total adsorption capacity (V_{tot}). The pore size distributions were calculated using the Horwath–Kawazoe method.

The concentration and type of acid sites were determined by ammonia and pyridine adsorption, which were used as probe molecules. The content of the adsorbed base was quantified on an FTIR spectrometer Nicolet 6700 AEM equipped with a DTGS detector. Prior to probe adsorption, the samples were pressed into self-supporting wafers at a density of 10 mg cm^{-2} and evacuated in a quartz IR cell under vacuum (10^{-4} Pa) at 450 °C for 2 hours. Pyridine adsorption proceeded at 150 °C for 20 min at partial pressure 3 Torr, followed by 20 min evacuation at 150 or 450 °C. The concentrations of Brønsted and Lewis acid sites in aluminosilicate samples were determined from the integral intensities of individual bands characteristic of pyridine on Brønsted acid sites at 1545 cm^{-1} and of the band of pyridine on Lewis acid sites at 1455 cm^{-1} and using the molar absorption coefficients of $\varepsilon(B)$ = 1.67 ± 0.1 cm μmol^{-1} and $\varepsilon(L)$ = 2.22 ± 0.1 cm μmol^{-1}, respectively.[26] The spectra were recorded with a resolution of 4 cm^{-1} after collecting 128 scans for each spectrum.

Solid-state ^{27}Al NMR spectra were collected on a Bruker Advance III HD spectrometer working with a 9.4 T standard-bore superconducting magnet at a resonance frequency of 104.2 MHz using strong and short 1 μs pulses, with 1.5 s repetition time and 4000 scans. The samples were packed into a 3.2 mm zirconia rotor and rotated at a MAS rate of 15 kHz using a Bruker 3.2 mm HX CP-MAS probe.

2.9. Catalytic experiments: 1-decanol tetrahydropyranylation

The catalytic experiments were performed in liquid phase at an atmospheric pressure at 60 °C in a three-neck 25 mL bottle placed on a multi-experiment workstation Starfish™. The catalyst was activated at 450 °C for 90 min before each experiment. Typically, the reaction was performed using 50 mg of catalyst, 4.5 mmol of 1-decanol, 0.25 g of internal standard (mesitylene) and 10 mL of 3,4-dihydro-2*H*-pyran in a two-neck vessel equipped with a condenser and a thermometer.[27] The reaction was initiated by adding 1-decanol. Samples of the reaction mixture were taken periodically and analysed on an Agilent 7890B GC gas chromatograph equipped with an autosampler, an HP-5 column (30 m length, 0.320 mm diameter, and 0.25 μm film thickness) and a flame ionization detector Scheme 1.

3. Results and discussion

In this study, we prepared alumino-germanosilicate **UTL** zeolites using both direct hydrothermal synthesis ("Al-UTL") and

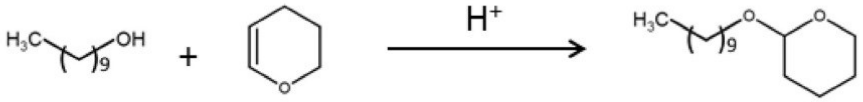

Scheme 1 Tetrahydropyranylation of *n*-decanol.

the Reverse ADOR transformation. The Reverse ADOR process consists of the hydrothermal synthesis of a parent germanosilicate **UTL**, **UTL** hydrolysis to the IPC-1P layered precursor, IPC-1P intercalation with tetrabutylammonium hydroxide and **UTL** reconstruction. The general route towards **UTL** zeolites is depicted in Scheme 2 ("Re-UTL (X)"; X stands for the incorporated heteroelements).

3.1. Intercalation optimisation

The key step of the Reverse ADOR process is the intercalation of tetrabutylammonium (TBA) cations in between IPC-1P layers. The *d*-spacing of the IPC-1P layers (1.05 nm) does not suffice for reconstructing D4R units in the interlayer space. TBA cations increase the interlayer distance and produce an IPC-1TBA precursor with a *d*-spacing similar to that of the parent **UTL** zeolite (1.44 nm).[18] This intercalation requires a basic environment for the deprotonation of the silanol groups on IPC-1P and for the separation of its layers. However, IPC-1P layers gradually deteriorate under basic conditions, which promotes the formation of defects, mesopores, and eventually causes the dissolution of the layers, thus accounting for the poor yields of the intercalated material, IPC-1TBA.[18] We countered this problem by adding colloidal silica (Ludox AS-40) into the TBA solution. The silica saturated the solution with silicate species, changing the chemical equilibrium and, therefore, slowing down the IPC-1P dissolution rate. The yields of the final solid material, IPC-1TBA, increased proportionally to the silica content up to 100% when using 20% w/w of the silica in the solution (Fig. 1). The optimised intercalation produced IPC-1TBA with a *d*-spacing close to that of the **UTL** zeolite in approximately 90–95% yields.

3.2. Aluminium incorporation

We demonstrated aluminium incorporation by Reverse ADOR by reconstructing the **UTL** zeolite from IPC-1TBA using Si and Al sources in a 3 : 1 Si : Al ratio ("Si : Al" stands for the ratio of Si and Al sources used in the reconstruction; not to be confused with the Si/Al molar ratio of the whole zeolite) and fluoride anions to stabilise the D4Rs.[18] The sample provided the

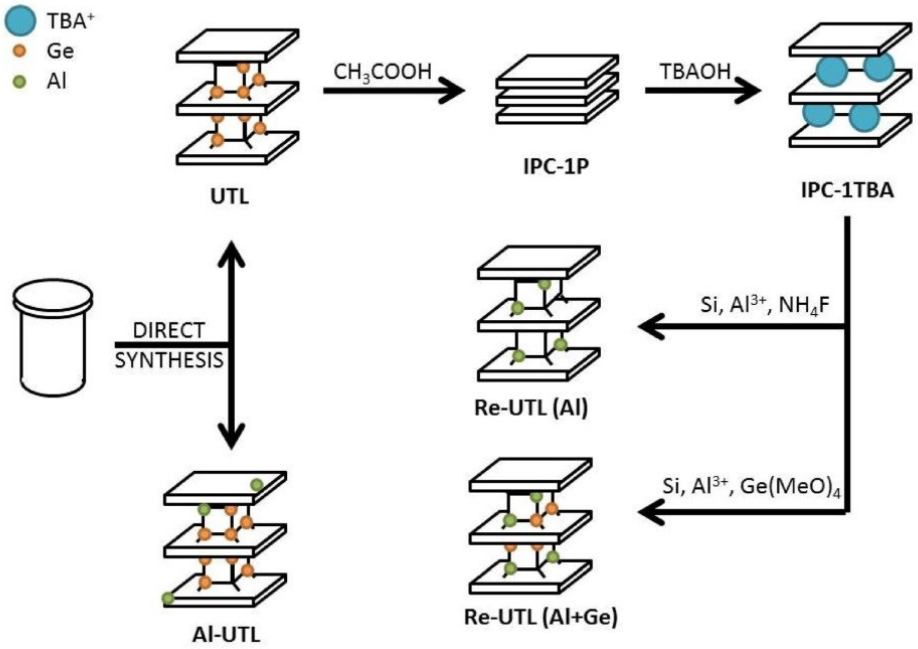

Scheme 2 General scheme of the preparation of in Al-containing **UTL** samples through direct synthesis (Al-UTL) and Reverse ADOR (Re-UTL). Framework heteroelements are depicted as coloured spheres (Al – green, Ge – orange); other framework elements (Si and O) are not depicted.

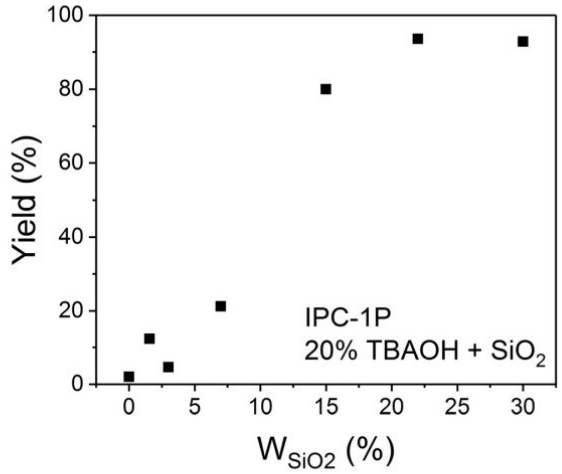

Fig. 1 IPC-1TBA yield increases with the silica content of the solution.

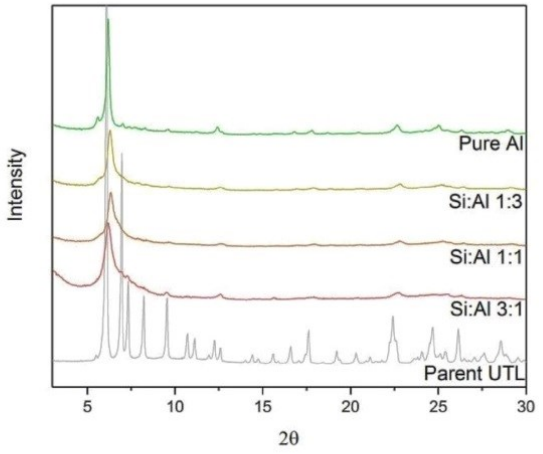

Fig. 2 Powder XRD patterns of **UTL** zeolites reconstructed with varying Si : Al ratios.

characteristic XRD reflections of the **UTL** structure at 6.16, 7.02, 7.38, 8.28, 9.60, 22.48 and 26.20 of 2 theta (Fig. 2).

To address the first research question (i), we probed the limit of Al incorporation for fluoride-assisted Reverse ADOR by gradually increasing the aluminium content in the reconstruction mixture to 3 : 1, 1 : 1, and 1 : 3 Si : Al and "Pure Al". Increasing the aluminium content above Si : Al 1 : 1 resulted in a decline of crystallinity and the 200 reflection in samples Si : Al 1 : 1 and 1 : 3 shifted to higher angles indicating that some S4R connections exist in the samples. Nevertheless, all samples showed high-angle reflections characteristic for the **UTL** structure (Fig. 2) and no signs of competing phases. However, complete aluminium incorporation into D4R units appeared unlikely, especially in the "pure Al" sample because aluminium would have to occupy more than four T-positions

Table 1 Textural properties of **UTL** zeolites reconstructed with varying aluminium content

	BET ($m^2\ g^{-1}$)	S_{ext} ($m^2\ g^{-1}$)	V_{tot} ($cm^3\ g^{-1}$)	V_{mic} ($cm^3\ g^{-1}$)
UTL	506	32	0.25	0.22
3Si : 1Al	597	200	0.39	0.10
1Si : 1Al	528	168	0.34	0.10
1Si : 3Al	509	166	0.34	0.09
Pure Al	389	130	0.28	0.08

in D4R units, which violates the Loewenstein's rule.[28] Instead, we theorised that aluminium either migrated to other framework positions, formed extra-framework species, or failed to incorporate into the zeolite altogether, forming a separate phase.

While aluminium migration cannot be ruled out, incomplete aluminium incorporation is much more likely to occur, as evidenced by textural properties of the samples. The micropore volumes of reconstructed samples gradually decreased with the increase in aluminium content from 0.10 to 0.08 $cm^3\ g^{-1}$ (Table 1 and Fig. S4†). This observation suggests that increasing aluminium content results in an incomplete reconstruction of D4R units. Hence, D4R units cannot be made from aluminium alone.

The ^{27}Al MAS NMR spectrum of the "pure Al" sample revealed a significant portion of pentahedrally and octahedrally coordinated aluminium species, as shown by signals at 30 and 0 ppm (Fig. S3†). Framework aluminium is typically tetrahedrally coordinated (60 ppm), but octahedrally coordinated aluminium is also found in extra-framework species or aluminium oxide phases.[29] Accordingly, a fraction of aluminium does not incorporate into D4R positions of the **UTL**. For this reason, we probed the phase purity and actual aluminium content of "pure Al" **UTL** by STEM with EDX mapping.

STEM imaging of pure Al samples combined with EDX mapping (Fig. 3) supported our hypothesis in revealing two distinct phases, namely large flat crystals of the **UTL** (1)[30] with Si/Al = 17 and (2) an aluminium-rich phase (Fig. 3). These two phases show that only a portion of the aluminium with Si/Al = 21 was incorporated into the zeolite. The excess aluminium crystallized separately as the second phase. Altogether, the presence of a second phase in these sample demonstrates that Si/Al = 21 is the limit of aluminium incorporation into **UTL**.

STEM-EDX analysis of restored **UTL** showed the limit of aluminium incorporation into the **UTL** framework, but according to the literature, the degree of incorporation of various elements depends on the pH‡.[1,31] Therefore, pH optimisation may further lower the limiting Si/Al ratio.

The experiments with **UTL** reconstruction under varying pHCl values proved that the degree of incorporation depends on pHCl. We repeated the synthesis with an excess of the alu-

‡The term "pH" is commonly defined for aqueous solutions. However, **UTL** reconstruction uses an anhydrous solution of HCl in ethanol, in which the pH is not defined. Thus, we adopted the term pHCl equal to the negative logarithm of the HCl concentration.

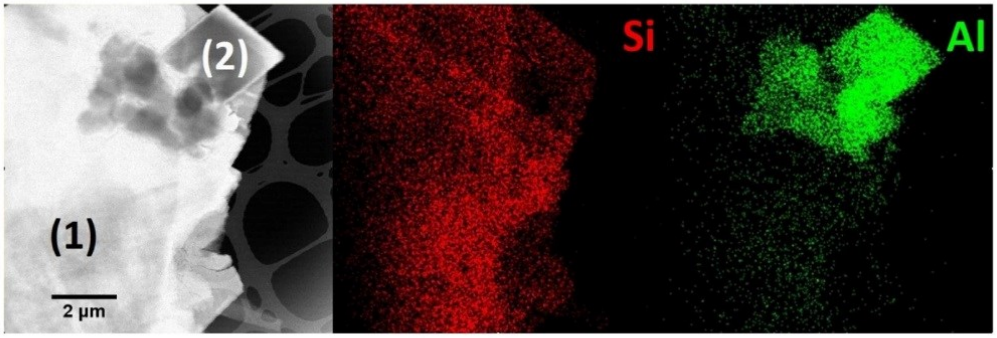

Fig. 3 STEM image of "pure Al" reconstructed **UTL** (1) and side-phase (2) and EDX maps of Si (red) and Al (green).

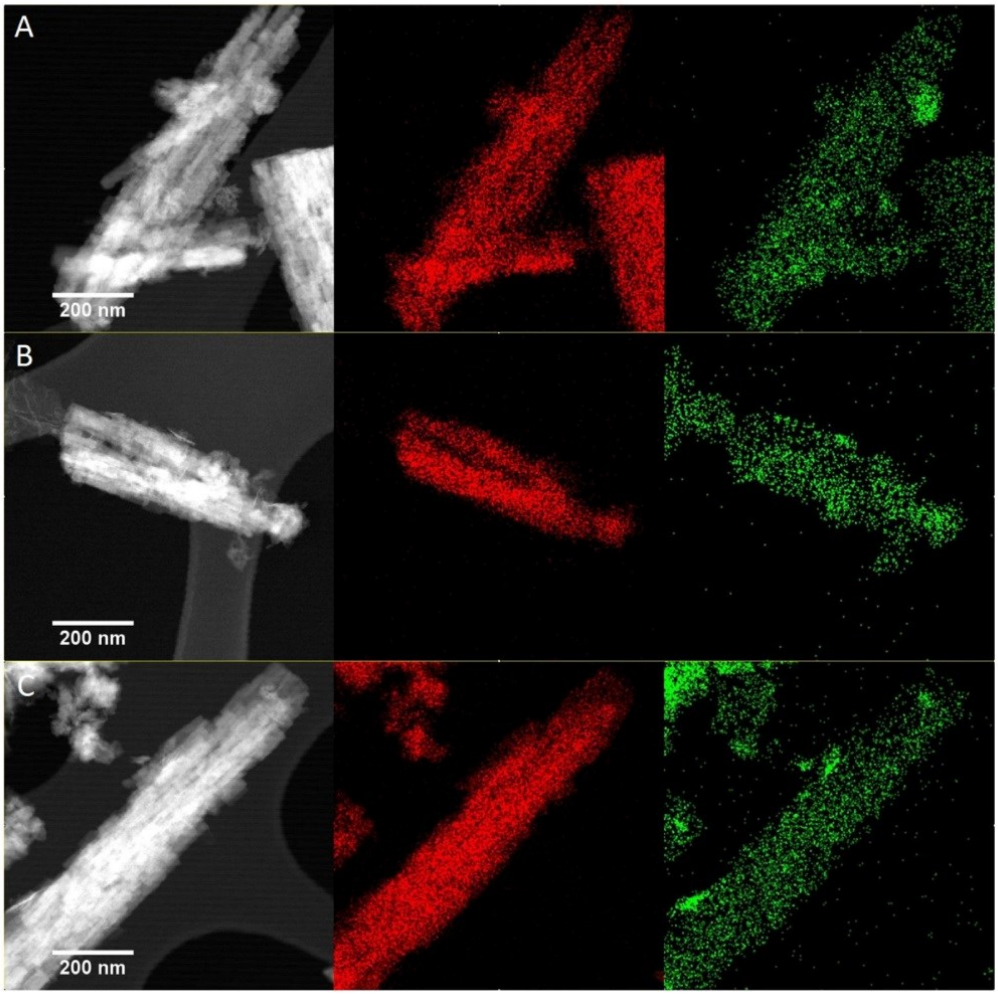

Fig. 4 STEM images and Si (red) and Al (green) EDX maps of **UTL** samples reconstructed by fluoride-assisted Reverse ADOR under pHCl = 1 (A), 3 (B) and 5 (C).

minium source (Si : Al 4 : 1) under pHCl = 1, 3 and 5 and analysed the samples by powder XRD and STEM-EDX. The powder XRD (Fig. S5 and S6†) verified that the samples possess the **UTL** structure with varying degree of crystallinity. The resulting STEM-EDX images (Fig. 4) revealed that all samples consisted of flat **UTL** zeolite crystals and a small amount of the second, aluminium-rich phase. The presence of the second phase confirms that aluminium incorporation reached the limit under these conditions, *i.e.*, the lower limit of the Si/Al ratio in **UTL**. The Si/Al of **UTL** decreased from 21 at pHCl = −0.1 to 15 at pHCl = 3. However, after increasing pHCl to 5, Si/Al increased to 22 (Fig. 5), indicating that the degree of Al incorporation peaks around pHCl = 3, which enables us to prepare **UTL** with Si/Al = 15.

The textural properties of reconstructed **UTL** also varied with the increase in the pHCl of the synthesis when using fluoride ions to stabilise the D4R units. The mean pore size of the samples gradually decreased from 0.84 nm, typical for **UTL**, to 0.69 nm (Fig. 6) when increasing pHCl from −0.1 to 5. This decrease in mean pore size indicates that D4R units are incompletely reconstructed at a higher pHCl and partly and randomly substituted with smaller connecting units, such as S4R, throughout the framework.

We did not observe such a change, nevertheless, when using germanium to direct the reconstruction. Germanium-assisted reconstruction (Si : Ge : Al 2 : 2 : 1) provided a consistent mean pore size close to 0.84 nm under varying pHCl. Hence, the structure-directing ability of germanium is not significantly affected by pHCl, but that of fluorides is, noticeably declining with the increase in pHCl.

On balance, aluminium incorporation by Reverse ADOR provides **UTL** materials with an aluminium content as high as Si/Al = 15, while direct synthesis yields **UTL** with Si/Al = 43.[4] In addition, the synthesis time of reconstructed **UTL** is significantly shorter than that of **UTL** prepared by direct synthesis. **UTL** reconstruction from IPC-1TBA requires 24 hours and in total approximately 14 days when considering all other synthesis steps (*i.e.*, parent **UTL** synthesis, hydrolysis to IPC-1P and TBA intercalation). In contrast, the direct synthesis of Al-UTL with Si/Al = 43 takes 28 days.

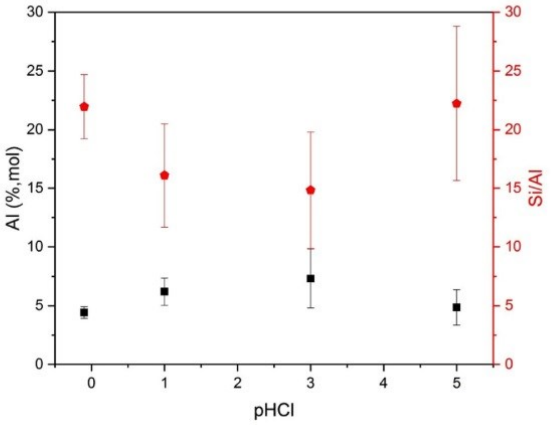

Fig. 5 Variation of aluminium content and Si/Al molar ratio of reconstructed **UTL** as a function of acidity (expressed as pHCl).

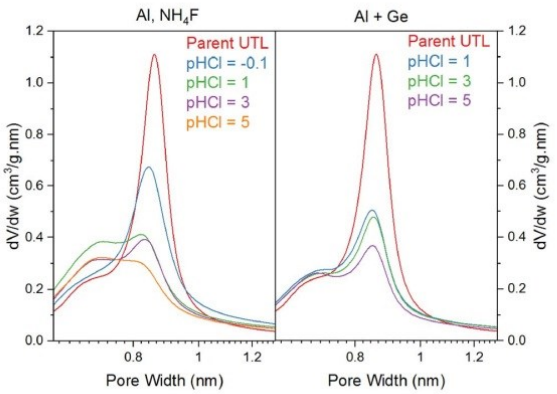

Fig. 6 Horwath-Kawazoe pore size distributions of **UTL** zeolites ((Si + Ge) : Al 4 : 1) reconstructed under varying acidity.

3.3. Catalytic activity

All samples prepared by Reverse ADOR outperformed Al-UTL in catalytic tests when testing **UTL** zeolites ("Re-UTL (Al)" and "Re-UTL (Al + Ge)" reconstructed *via* the fluoride or germanium routes, respectively) in the tetrahydropyranylation of 1-decanol and comparing their results with those of two benchmark catalysts, namely zeolite **BEA** (CP814C Zeolyst, Si/Al = 19) and stabilised Al-UTL prepared by direct synthesis (Fig. S7, S8 and Table S2†). The conversion rates of 1-decanol over Re-UTL (Al) and Re-UTL (Al + Ge) reached 41.1 and 45.6% after 4 hours (Fig. 7), respectively, with 80% selectivity to the tetrahydropyranylation product. In turn, directly synthesised Al-UTL provided conversion rates of only 14.8%, and **BEA** afforded no conversion under the same conditions. The high conversion rates of Re-UTL samples mainly resulted from their enhanced external surface area and mesopores, which boost mass transfer during this reaction. Re-UTL (Al) and Re-UTL (Al + Ge) have an external surface of 138 and 180 $m^2\ g^{-1}$, respectively, while Al-UTL has 64 $m^2\ g^{-1}$ external surface. **BEA** also has a large external surface of 170 $m^2\ g^{-1}$, but its narrower 12-ring channels impede mass transfer during this reaction.

In addition to aluminium, germanium is also used for Re-UTL (Al + Ge) reconstruction and has catalytic activity.[4,32,33] We differentiated the catalytic activity of aluminium and germanium sites by conducting catalytic tests on samples before and after ion exchange to the proton form and measuring the concentration of acid sites in both sets of samples by pyridine adsorption combined with FTIR spectroscopy. By FTIR spectroscopy, no Brønsted acid sites were identified in reconstructed **UTL** samples prior to activation (Fig. 8), but activated **UTL** samples revealed signals of Brønsted and Lewis acid sites at 1545 cm^{-1} and 1455 cm^{-1} in their FTIR spectra, respectively,

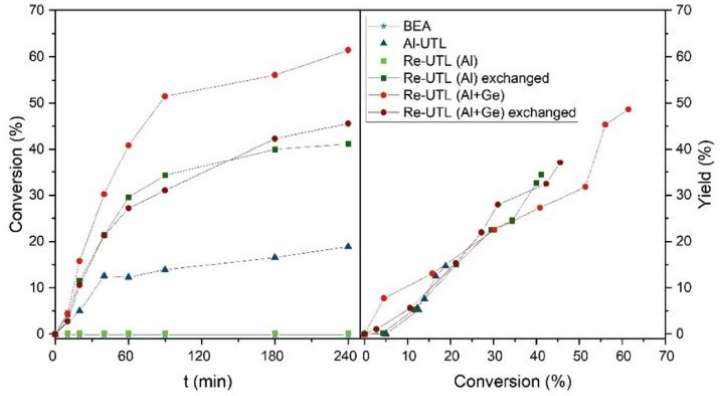

Fig. 7 Conversions of 1-decanol and selectivity curves over **BEA**, Al-UTL and reconstructed **UTL** zeolites.

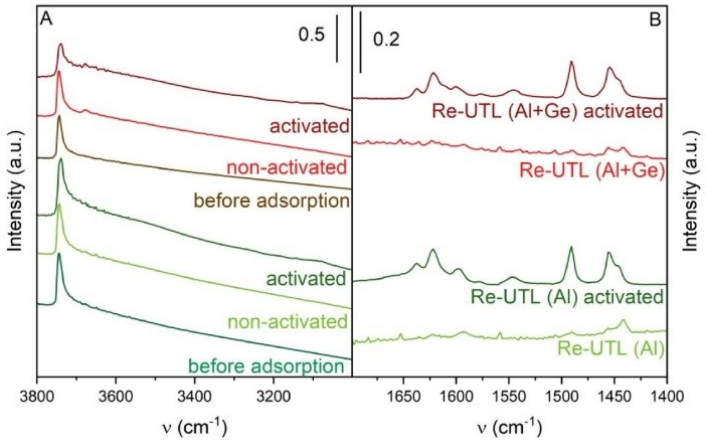

Fig. 8 FTIR spectra of hydroxyl groups (A) and adsorbed pyridine (B) of the non-activated and activated reconstructed **UTL** zeolites.

with concentrations of Brønsted acid sites of 21 and 25 μmol g^{-1} for Re-UTL (Al) and Re-UTL (Al + Ge), respectively (Table S2†).

1-Decanol conversion over non-activated Re-UTL (Al + Ge) reached 61.4% (Fig. 7). Simultaneously, non-activated Re-UTL (Al) provided no conversion, confirming that the catalytic activity of non-activated Re-UTL (Al + Ge) stems solely from germanium Lewis acid sites. Conversion decreased from 61.4 to 45.6% over Re-UTL (Al + Ge) after ion exchange due to partial germanium leaching from framework position upon ion exchange.

In summary, we compared the catalytic properties of reconstructed **UTL** samples against commercially available zeolite **BEA** and stabilised Al-UTL in the tetrahydropyranylation of 1-decanol. Since tetrahydropyranylation can be catalysed by both aluminium and germanium sites, we tested both non-activated and activated forms of each catalyst to discern the effect of each type of catalytic site. We also modified the intercalation step of the protocol by adding colloidal silica into the mixture, which significantly increased the yields of the intercalated material. We subsequently performed the reconstruction of **UTL** zeolites from layered IPC-1P in a controlled stepwise approach following two routes, either fluoride- or germanium-assisted paths. The fluoride route provided purely aluminosilicate **UTL** but was reliable only under highly acidic conditions (pHCl ≤ 1), which are less favourable to aluminium incorporation (Si/Al = 17). By contrast, the germanium-assisted route was reliable even under near-neutral conditions, which are more favourable to the incorporation of a high aluminium content. The results showed a high amount of aluminium incorporated into these reconstructed **UTL** zeolites, reaching up to Si/Al = 15, the lowest Si/Al of any **UTL** reported thus far,[6] and hence a high concentration of active sites. Non-activated germanium-free reconstructed **UTL** was inactive, while germanium-containing non-activated **UTL** showed 61.4% conversion and 80% selectivity, outperforming stabilised Al-UTL, which

reached only 14.8% conversion. Ion exchange increased conversion over germanium-free reconstructed **UTL** to 45.6%, but conversion over germanium-containing **UTL** decreased to 41.9%, most likely due to minor structural damage caused by ion exchange.

4. Conclusions

Our modified Reverse ADOR protocol approximately halves **UTL** synthesis time to 14 days in comparison to direct synthesis. Moreover, in contrast to degermanation followed by substitution with aluminium, modified Reverse ADOR proceeds through 3D–2D–3D transformation, thereby increasing the control over zeolite structure and active site location. These synthesis conditions introduce mesoporosity into the zeolite, enhancing mass transfer during catalysis and increasing reactant conversion rates and product yields, as shown in the tetrahydropyranylation reaction of 1-decanol over Reverse ADOR- and directly synthesised **UTL** zeolites, using commercial **BEA** zeolite as a reference. Although we focused on aluminium incorporation into **UTL** because aluminium is the most common framework heteroelement in zeolite catalysts, we believe that this modified Reverse ADOR method can also enable us to incorporate other T elements. Other T elements will require different conditions, such as pHCl, for incorporation into the zeolite framework, with necessarily different limiting Si/T ratios as well. Nevertheless, this approach may be used as a universal experimental paradigm for the incorporation of other elements commonly found in zeolite frameworks.

Conflicts of interest

There are no conflicts to declare.

Acknowledgements

The authors thank the Czech Science Foundation for funding this research through project EXPRO (19-27551X) and OP VVV "Excellent Research Teams", project no. CZ.02.1.01/0.0/0.0/15_003/0000417 – CUCAM. OV acknowledges the support from the project "Grant Schemes at CU" (reg. no. CZ.02.2.69/0.0/0.0/19_073/0016935), from Dr Kinga Gołąbek, who performed the FTIR measurements, and from Dr Zdeněk Tošner, who performed the ^{27}Al MAS NMR measurements. M. M. acknowledges the Czech Science Foundation for the project 19-21534S. The authors thank Dr Carlos V. Melo for editing the manuscript.

References

1 H. Koller, C.-Y. Chen and S. I. Zones, Selectivities in Post-Synthetic Modification of Borosilicate Zeolites, *Top. Catal.*, 2015, **58**, 451–479.

2 J. Čejka, A. Vondrova, B. Wichterlova, G. Vorbeck and R. Fricke, The Effect of Al, Fe, and In Substitution in the MFI Silicate Structure on the Aromatic Hydrocarbon Transformation - SI-OH-M Site Strength, *Zeolites*, 1994, **14**, 147–153.

3 M. Shamzhy, M. Opanasenko, P. Concepción and A. Martínez, New trends in tailoring active sites in zeolite-based catalysts, *Chem. Soc. Rev.*, 2019, **48**, 1095–1149.

4 N. Kasian, E. Verheyen, G. Vanbutsele, K. Houthoofd, T. I. Koranyi, J. A. Martens and C. E. A. Kirschhock, Catalytic activity of germanosilicate UTL zeolite in bifunctional hydroisomerisation of n-decane, *Microporous Mesoporous Mater.*, 2013, **166**, 153–160.

5 M. V. Shamzhy, C. Ochoa-Hernández, V. I. Kasneryk, M. V. Opanasenko and M. Mazur, Direct incorporation of B, Al, and Ga into medium-pore ITH zeolite: Synthesis, acidic, and catalytic properties, *Catal. Today*, 2016, **277**, 37–47.

6 M. V. Shamzhy, O. V. Shvets, M. V. Opanasenko, P. S. Yaremov, L. G. Sarkisyan, P. Chlubna, A. Zukal, V. R. Marthala, M. Hartmann and J. Cejka, Synthesis of isomorphously substituted extra-large pore UTL zeolites, *J. Mater. Chem.*, 2012, **22**, 15793–15803.

7 X. Liu, H. Xu, L. Zhang, L. Han, J. Jiang, P. Oleynikov, L. Chen and P. Wu, Isomorphous Incorporation of Tin Ions into Germanosilicate Framework Assisted by Local Structural Rearrangement, *ACS Catal.*, 2016, **6**, 8420–8431.

8 X. Liu, L. Zhang, H. Xu, J. Jiang, M. Peng and P. Wu, Pore size-tunable titanosilicates post-synthesized from germanosilicate by structural reorganization and H2TiF6-assisted isomorphous substitution, *Appl. Catal., A*, 2018, **550**, 11–19.

9 R. de Ruite, K. Famine, A. P. M. Kentgens, J. C. Jansen and H. van Bekkum, Synthesis of molecular sieve [B]-BEA and modification of the boron site, *Zeolites*, 1993, **13**, 611–621.

10 P. Eliášová, M. Opanasenko, P. S. Wheatley, M. Shamzhy, M. Mazur, P. Nachtigall, W. J. Roth, R. E. Morris and J. Čejka, The ADOR mechanism for the synthesis of new zeolites, *Chem. Soc. Rev.*, 2015, **44**, 7177–7206.

11 J.-L. Paillaud, B. Harbuzaru, J. Patarin and N. Bats, Extra-Large-Pore Zeolites with Two-Dimensional Channels Formed by 14 and 12 Rings, *Science*, 2004, **304**, 990.

12 A. Corma, M. J. Díaz-Cabañas, F. Rey, S. Nicolopoulus and K. Boulahya, ITQ-15: The first ultralarge pore zeolite with a bi-directional pore system formed by intersecting 14- and 12-ring channels, and its catalytic implications, *Chemical Communications*, 2004, 1356–1357.

13 W. J. Roth, O. V. Shvets, M. Shamzhy, P. Chlubna, M. Kubu, P. Nachtigall and J. Čejka, Postsynthesis Transformation of Three-Dimensional Framework into a Lamellar Zeolite with Modifiable Architecture, *J. Am. Chem. Soc.*, 2011, **133**, 6130–6133.

14 W. J. Roth, P. Nachtigall, R. E. Morris, P. S. Wheatley, V. R. Seymour, S. E. Ashbrook, P. Chlubna, L. Grajciar, M. Polozij, A. Zukal, O. Shvets and J. Čejka, A family of zeolites with controlled pore size prepared using a top-down method, *Nat. Chem.*, 2013, **5**, 628–633.

15 M. Mazur, P. S. Wheatley, M. Navarro, W. J. Roth, M. Položij, A. Mayoral, P. Eliášová, P. Nachtigall, J. Čejka and R. E. Morris, Synthesis of 'unfeasible' zeolites, *Nat. Chem.*, 2016, **8**, 58–62.

16 P. S. Wheatley, P. Chlubná-Eliášová, H. Greer, W. Zhou, V. R. Seymour, D. M. Dawson, S. E. Ashbrook, A. B. Pinar, L. B. McCusker, M. Opanasenko, J. Čejka and R. E. Morris, Zeolites with Continuously Tuneable Porosity, *Angew. Chem.*, 2014, **126**, 13426–13430.

17 E. Verheyen, L. Joos, K. Van Havenbergh, E. Breynaert, N. Kasian, E. Gobechiya, K. Houthoofd, C. Martineau, M. Hinterstein, F. Taulelle, V. Van Speybroeck, M. Waroquier, S. Bals, G. Van Tendeloo, C. E. A. Kirschhock and J. A. Martens, Design of zeolite by inverse sigma transformation, *Nat. Mater.*, 2012, **11**, 1059–1064.

18 O. Veselý, P. Eliášová, R. E. Morris and J. Čejka, Reverse ADOR: reconstruction of UTL zeolite from layered IPC-1P, *Mater. Adv.*, 2021, **2**, 3862–3870.

19 H. Xu, J.-G. Jiang, B. Yang, L. Zhang, M. He and P. Wu, Post-Synthesis Treatment gives Highly Stable Siliceous Zeolites through the Isomorphous Substitution of Silicon for Germanium in Germanosilicates, *Angew. Chem., Int. Ed.*, 2014, **53**, 1355–1359.

20 J. Jiang, J. Yu and A. Corma, Extra-Large-Pore Zeolites: Bridging the Gap between Micro and Mesoporous Structures, *Angew. Chem., Int. Ed.*, 2010, **49**, 3120–3145.

21 S. I. Zones, Translating new materials discoveries in zeolite research to commercial manufacture, *Microporous Mesoporous Mater.*, 2011, **144**, 1–8.

22 J. Zhang, O. Veselý, Z. Tošner, M. Mazur, M. Opanasenko, J. Čejka and M. Shamzhy, Toward Controlling Disassembly Step within the ADOR Process for the Synthesis of Zeolites, *Chem. Mater.*, 2021, **33**, 1228–1237.

23 O. V. Shvets, M. V. Shamzhy, P. S. Yaremov, Z. Musilova, D. Prochazkova and J. Cejka, Isomorphous Introduction of Boron in Germanosilicate Zeolites with UTL Topology, *Chem. Mater.*, 2011, **23**, 2573–2585.

24 O. V. Shvets, N. Kasian, A. Zukal, J. Pinkas and J. Čejka, The Role of Template Structure and Synergism between Inorganic and Organic Structure Directing Agents in the Synthesis of UTL Zeolite, *Chem. Mater.*, 2010, **22**, 3482–3495.

25 M. V. Shamzhy, P. Eliašová, D. Vitvarová, M. V. Opanasenko, D. S. Firth and R. E. Morris, Post-Synthesis Stabilization of Germanosilicate Zeolites ITH, IWW, and UTL by Substitution of Ge for Al, *Chem. – Eur. J.*, 2016, **22**, 17377–17386.

26 V. Zholobenko, C. Freitas, M. Jendrlin, P. Bazin, A. Travert and F. Thibault-Starzyk, Probing the acid sites of zeolites with pyridine: Quantitative AGIR measurements of the molar absorption coefficients, *J. Catal.*, 2020, **385**, 52–60.

27 Y. Zhou, S. A. Kadam, M. Shamzhy, J. Čejka and M. Opanasenko, Isoreticular UTL-Derived Zeolites as Model Materials for Probing Pore Size–Activity Relationship, *ACS Catal.*, 2019, **9**, 5136–5146.

28 W. Loewenstein, The distribution of aluminum in the tetrahedra of silicates and aluminates, *Am. Mineral.*, 1954, **39**, 92–96.

29 G. Engelhardt and D. Michel, *High-resolution solid-state NMR of silicates and zeolites*, 1987.

30 O. V. Shvets, A. Zukal, N. Kasian, N. Žilková and J. Čejka, The Role of Crystallization Parameters for the Synthesis of Germanosilicate with UTL Topology, *Chem. – Eur. J.*, 2008, **14**, 10134–10140.

31 Y. Oumi, S. Kikuchi, S. Nawata, T. Fukushima and T. Sano, Galliation of beta zeolite by the pH control method, in *Studies in Surface Science and Catalysis*, ed. R. Aiello, G. Giordano and F. Testa, Elsevier, 2002, pp. 1833–1840..

32 I. Podolean, J. Zhang, M. Shamzhy, V. I. Pârvulescu and J. Čejka, Solvent-free ketalization of polyols over germanosilicate zeolites: the role of the nature and strength of acid sites, *Catal. Sci. Technol.*, 2020, **10**, 8254–8264.

33 H. Xu, J. Jiang, B. Yang, H. Wu and P. Wu, Effective Baeyer–Villiger oxidation of ketones over germanosilicates, *Catal. Commun.*, 2014, **55**, 83–86.

Publications under revision:

Ondřej Veselý, Maryia Shamzhy, Wiesław J. Roth, Russel E. Morris, Jiří Čejka

Controlling crystal morphology of anisotropic zeolites with elemental composition

(2023)

Contribution: Synthesis of the UTL germanosilicate samples, Scanning Electron Microscopy imaging of the UTL germanosilicate samples, evaluation of the obtained data and writing of the manuscript.